Electron Beam Induced Nanometer Scale Deposition

Natalia **SILVIS-CIVIDJIAN**

Electron Beam Induced
Nanometer Scale Deposition

P r o e f s c h r i f t

ter verkrijging van de graad van doctor
aan de Technische Universiteit Delft,
op gezag van de Rector Magnificus prof. dr. ir. J. T. Fokkema,
voorzitter van het College voor Promoties,
in het openbaar te verdedigen op maandag 22 april 2002 om 13:30 uur

door

Natalia CIVIDJIAN

inginer Automatizări şi Calculatoare
Universitatea din Craiova
geboren te Craiova, Roemenië

Dit proefschrift is goedgekeurd door de promotor:

Prof. dr. ir. P. Kruit

Samenstelling Promotiecommissie:

Rector Magnificus,	*voorzitter*
Prof. dr. ir. P. Kruit	*Technische Universiteit Delft, promotor*
Prof. dr. C. Colliex	*Université Paris-Sud, Frankrijk*
Prof. dr. A. W. Kleijn	*Universiteit Leiden*
Prof. dr. H. W. Zandbergen	*Technische Universiteit Delft*
Prof. dr. C. Dekker	*Technische Universiteit Delft*
Dr. C. W. Hagen	*Technische Universiteit Delft*
Dr. E. W. J. M. van der Drift	*Technische Universiteit Delft/DIMES*

Printed in The Netherlands

Contents

Chapter 1

Introduction

1.1   Energetic beam induced nanoprocessing

It is year 2002 and the prefix "nano" can be applied without surprise to almost anything: wires, lines and dots but also puzzles, nozzles, spirals and glasses. In the common language, "nano" becomes synonym with "small" and replaces the older generation's "micro". But how small is "small"? Nano-structures are defined as assemblies of bonded atoms with dimensions in the range of 1 to 100 nanometers. The label "small" given to a structure depends on the interests of the specific community. For biologists nanostructures like DNA, enzymes, proteins, viruses are considered familiar objects, while for solid-state physicists and electrical engineers, the same sizes are considered extraordinary small and difficult to control or fabricate. At this moment biomolecular science and physics of nanofabrication have met each other in the geometrical dimensions of the considered objects. The smallest features in mass production of integrated circuits are near 100 nm and this is less than 1% of the length of a stretched single DNA molecules ($16\mu m$) [8].

The term "nanotechnology" has been introduced in 1974 by Taniguchi to describe the material processing and manufacturing to accuracies and tolerances in the nanometer regime. One of his conclusions was that in the following decennia, accuracies between $0.1\mu m$ and 1 nm would be needed to cater for the industry's needs [12, 13]. Due to giant efforts in instrumentation development and fundamental physical research, the mid-seventies predictions became reality. Nowadays, structures with sizes between 10 and 500 nm are currently fabricated, offering possibilities to investigate the behaviour of matter at dimensions previously inaccessible (see Fig.1-1).

The trend of miniaturization, developed first in electronics industry aiming for higher packing densities and faster switching, can be summarized in three words: smaller, cheaper, faster. IC industry is characterized by an incredible growth. In 25 years the performance of a microprocessor has been multiplied by 25 000. The need of higher integration will require smaller and smaller resolvable features. Presently 0.35 μm features can be fabricated on industrial scale and 0.25 μm generation is under way.

The miniaturization trend is extending also to other scientific and technical fields, including biology, chemistry, high density data storage, optics and optoelectronics, sensors, photonics, etc. Fascinating applications of nanostructures are visible everywhere in everyday life. Molecular biology and genetic engineering can use nanometric contacts to measure the properties

ACHIEVABLE
MACHINING
ACCURACY

PROCESSES MEASURING INSTRUMENTS

0·1mm

NORMAL MACHINING

LATHES, MILLING MACHINES VERNIER CALIPERS

PRECISION MACHINE TOOLS MECHANICAL COMPARATORS

0·01mm

10μm

5μm

PRECISION JIG BORERS OPTICAL COMPARATORS

1μm

PRECISION MACHINING

1μm

1μm

PRECISION GRINDING MACHINE

ELECTRONIC COMPARATORS (NON-CONTACT)

ULTRAPRECISION MACHINING (EXTREME ACCURATE MACHINING)

0·1μm

0·1μm

0·1μm

PRECISION DIAMOND LATHES

0·05μm

PRECISION DIAMOND GRINDING MACHINES

LASER MEASURING INSTRUMENTS

0·01μm

0·01μm

(ELECTRON BEAM LITHOGRAPHY) SUPER HIGH PRECISION GRINDING

HIGH PRECISION LASER MEASURING INSTRUMENTS

0·005μm

0·01μm,(1nm)

0·001μm

ATOM, MOLECULE OR ION BEAM MACHINING, ATOM OR MOLECULE DEPOSITION

SEM STM AFM

0·3nm

(ATOMIC
LATTICE
DISTANCE) 1900 1920 1940 1960 1980 2000 YEAR

Figure 1-1: The development of achievable processing accuracy (from [13])

2

of proteins, DNA and single molecules. Nanometer scale objects made of inorganic materials can serve in biomedical research, disease diagnosis and therapy. Nanoparticles could be used to deliver drugs just where they are needed, avoiding the harmful side effects that so often result from strong medicines. Artificial nanoscale building blocks may one day be used to help repair tissues as skin, cartilage and bone - and they may even help patients to regenerate organs [1]. The environment will be easier to handle and protect because new biomaterials are synthetised, replacing the manual work in destruction and recycling of toxic waste. Microsensors, microvalves, minirobots and micromotors, in a word - micro electro mechanical systems (MEMS) are fabricated everywhere around the world, drastically reducing the sizes of control and measurement systems.

But it is also true that even smaller features, down to the atomic sizes (0.1 nm) are still waiting to be fabricated and the way to achieve this dream is not easy and requires a lot of research. These small structures can be used for single electron devices, electrical connections to individual molecules and ultra high density storage media. These tiny structures will offer the scientists the possibility to discover mesoscale laws and very intriguing behaviour.

At this moment, the research in nanotechnology on industrial scale aims to explore the basic physics, technology and applications of the ultrasmall structures and devices with dimensions in the sub-100 nm regime.

The fabrication resolution can be improved in two ways: by improving the existing methods or by discovering new methods. In case when the first path is chosen, an analysis of the existing conventional methods for nanofabrication that reveals their pros and cons is necessary.

When the critical dimensions of high-precision material processing are approaching the nanometer scale, the traditional mechanical tools become inadequate, creating room to other fabrication techniques.

Two competing paradigms are pursuing nanotechnology. The approach based on a progressive reduction of dimensions, the so-called "top-down approach", originates from solid state physics. It uses lithography, micromaching and deposition with energetic beams. The "bottom up" approach, inspired from biological sciences, on the contrary relies on the atom per atom or molecule per molecule building of functionalized elements. Still in its infancy, it uses the near field methods and self-assembly properties of atoms and molecules.

The scanning probe lithography (SPL) uses scanning force instruments (STM or AFM) to pattern nanometer features.

In 1981, Binnig and Rohrer and their colleagues at the IBM Research Laboratory in Zürich developed a new kind of surface analytical instrument - the Scanning Tunnelling Microscope (STM) [3]. The STM consists of a conducting needle, held close to a conducting surface. As the needle approaches the surface at a distance smaller than 1 nm, electrons can tunnel with a reasonable probability between the conductors and the current is a sensitive measure of their separation. If the needle is scanned above the surface, the current registered can serve for imaging the surface. In an atomic force microscope (AFM), the imaging signal is the force between the cantilever and the surface.

The STM is normally used as an analytical instrument but it has been proved to be also a useful nanometer scale fabrication tool. How is STM used to fabricate nanometer scale structures?

A first method to create nanostructures with a STM uses manipulation of individual atoms or molecules adsorbed on the target surface into a desired pattern. This directional diffusion is induced by the electrical field at the surface on the dipole moment of adsorbed atoms or molecules. "Hand made" manipulation and arrangement of molecules and atoms in a pattern have been experimented by many authors [2, 7, 6, 14]. Organic molecules could be also pinned

on a graphitic surface by applying a voltage pulse to the tip. The pinned molecules could be later removed or cleaved by another voltage pulse. Both pinning as well as removal of molecules are found to be threshold processes, starting at 3-4 eV. Adsorbed atoms of xenon, iron, silicon, sulfur, cesium could be manipulated and arranged on a surface. For example, Eigler has demonstrated the reproducible manipulation of individual Xe atoms physisorbed on a Ni(100) surface at 4K [6], Whitman demonstrated the fabrication of Cs structures of 1 nm to few tens of nanometers [14]. A new field has thus been opened, the atomic engineering of nanometer scale structures by electric field induced manipulation. The drawback of this techniques remains its throughput, being as low as 1 atom per minute.

Another direction of development in the instrumentation for nanofabrication is the use of energetic beams. Energetic beams are controllable, directional fluxes of particles irradiating a surface and able to modify its physical state. In this category are included photon beams, electron beams, inert and chemically reactive ion beams, cluster ion beams, neutral atom beams and molecular beams. The current research interest is focused nowadays only on the application of photon, electron and ion beams for nanoprocessing and fabrication.

Photon beam processing

Photon beam processing uses photons with wavelengths between 1 and 1000 nm.

Photolithography remains the dominant method of ultra high precision pattern transfer in integrated circuits IC manufacture. The technique illuminates a photosensitive resist with a flood exposure through a mask, followed by an etching procedure. This is a reliable process which produces circuit features with submicrometer resolution. The fabrication resolution of this process is diffraction limited by:

$$r \simeq \frac{0.5\lambda}{NA} \tag{1.1}$$

The numerical aperture NA is related to the depth of focus d, that cannot be reduced unlimited because of mechanical reasons.

$$d \simeq \frac{\pm 1}{2(NA)^2} \tag{1.2}$$

It results that the only possibility to increase the fabrication resolution in the non-laser lithography is to move to shorter wavelengths, like deep UV light, which improves the fabrication resolution down to 250 nm.

X-ray lithography uses wavelengths from 0.2 to 5 nm and therefore can produce features of 100 nm. Despite the efforts made to develop short wavelength X-ray sources (synchrotrons, plasma), there are still problems in mask fabrication technology and defects repair.

Coherent radiation uses excimer lasers, which are pulsed lasers capable of emitting radiation in the deep UV. Examples are ArF, KrF, XeCl and XeF lasers with wavelength of 193 nm, 248 nm, 308 nm and 351 nm.

Micromachining with high power Nd:YAG lasers is possible for material removal, like trimming of thin films, vaporization of redundant contact lines. If the laser beam is focused, it can produce microdeposition, i.e. direct writing of structures on a substrate, localized at sites

of submicron sizes. For gas phase precursors, two techniques are possible: the thermochemical (pyrolytic) deposition and the photochemical (photolytical) deposition, also known as laser chemical vapour deposition (LCVD). In pyrolytic deposition, the substrate is heated by the laser focused beam and the gas is decomposed above the specimen. In photolytic deposition the gas is directly dissociated by the incident beam and deposition on the substrate takes place. The fabrication resolution depends on the diameter of the focused laser, which is just of sub micron size.

High energy 193 nm photons lithography for 130 nm technology is scheduled for 2003. Optical projection systems are designed for manufacturing ICs on 8 or 12 inch wafers of Si, at a rate of 60 wafers per hour [11].

Electron beam processing

Electron beams are widely used in lithography. The pattern is written one pixel at a time with around beam whose diameter is equal to the pixel size. The lithography process consists of the following steps. The substrate is first covered with a thin layer of a radiation sensitive material, the resist. The electron beam induces changes in the resist that alter its solubility. The electron beam illuminates the resist, directly or through a shadow mask, defining a pattern. The resist is afterwards developed. If the exposed resist remains after development, then the resist is named negative resist. If the exposed resist is dissolved, then the resist is called positive resist. Afterwards, the pattern transfer is done by etching, doping or lift-off that eliminates the resist and metal structures are fabricated. The development step has a great influence on the fabrication resolution.

The minimum feature size of the structures fabricated in this way is limited not only by the beam size, but by the electron scattering in the resist and from the substrate, the so-called proximity effect. Typically the commercial electron lithography EBL machines use a beam diameter of 2-3 nm at 50 keV.

Electron beams can be also occasionally used for material nanomachining. Very small focussed beams with 0.5 nm diameter could drill holes with 2 nm diameter in thin films of alumina, aluminium and lithium fluoride.

The process is rather slow compared with X-ray lithography typically 10^7 pixels/second. It is too slow and too expensive for volume manufacturing and it is used only in particular cases like some quick production of ASICs (application specific integrated circuits).

Ion beam processing

Ion beam processing of materials can be divided into non-spatially selective, using a broad or showered ion beam or spatially selective, using a fine focused ion beam or showered beam, with a delimiting mask.

Showered ion beam machining and milling (SIBM) uses low energy ions (50 to 1500 eV). It is used as universal etchant to remove any material, regardless of its mechanical properties. Devices can be fabricated like optical gratings, diamond tips with 10-20 nm radius.

Focused ion beam machines use high beam energies (10-50 keV) and can focus the beam in probes with diameters smaller than 10 nm. Ions can be also used in lithography, with the same resist as in EBL. However, the most advanced commercial application of focussed ion beams (FIB) is in the micromachining by sputtering and milling, failure analysis and repair of ICs and photolithographic masks.

An inconvenience of using FIBs in failure repair is the ion implantation (staining) in device or mask.

Focused charged particles beams produce in laboratories features around 20 nm. The question that now troubles many nanotechnology research groups is which method will make the step to atomic size large scale fabrication? Since electron beam lithography in general provides higher resolution than any other method, except local probe atom manipulation, electrons are one of the main potential candidates.

It is now accepted that the conventional resist based electron beam lithography reached its resolution limits. The minimum sizes of patterned features in PMMA has been confirmed experimentally by several research groups as roughly 10 nm. The resolution limit will stay on this value because it is set by the interaction range of electrons with the resist and/or by the molecular size and development mechanism of the resist (5-10nm) and not by the electron optics, which can approach 0.1 nm [4].

In this context, it is interesting to investigate other non-conventional lithography process, used until now only occasionally but with promising resolution results: the focused beam induced deposition. It is a direct writing process, localized in the area irradiated by the beam.
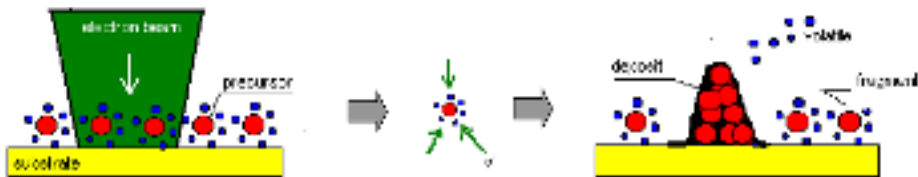
Figure 1-2: Illustration of electron beam induced deposition (EBID) process

The principle of the focused beam induced direct deposition can be described shortly as follows. In a high vacuum chamber, an electron beam is focused on a surface on which precursor gas molecules are adsorbed. The precursor has to be a suitable vapor containing the element to be deposited. Depending on the nature of the deposit, either metallic (Pt, W, Fe, Cu, Au, Al, Ta, Cr) or carbonaceous, the precursor has to be an organometallic compound or a hydrocarbon. As a result of complex beam-induced surface reactions, the precursor molecules situated in- and close to the irradiated area dissociate into nonvolatile and volatile materials. The nonvolatile materials eventually will adhere to the surface, forming the desired deposit, while the volatile components will be evacuated from the chamber, see Fig. 1-2. Complicated 2D and 3D patterns can be fabricated by displacing the beam according to a desired model. Depending on the nature of the energetic beam, one distinguishes three techniques: laser induced deposition, electron beam induced deposition (EBID) and ion beam induced deposition (IBID). All three types of beams, photon, ion and electrons have been demonstrated as suitable to initiate this direct nanodeposition process [9, 10, 5].

The advantage of such a method is that the materials are patterned and deposited simultaneously, making it a one-step technique. Since it is mask-less and resist-less, the method has another advantage over conventional deposition methods, the freedom of choosing any substrate material and geometry (planar and nonplanar). The disadvantage of the method up to this moment is the high electrical resistivity of the deposit and the low throughput.

Nowadays the electron optical instruments (SEM, STEM) can offer the finest focussed electron beam (0.2-2 nm), with very large range of electron energies up to 300 keV in STEM. This

means that the logistics for a high resolution direct fabrication process initiated by electrons exists and there is a reason to believe that this approach could be the key to sub-10 nm fabrication. The main question is why all the useful structures fabricated with EBID are always reported to be around 15-20 nm wide, even though such good electron optical instruments exist already?

1.2   Contents of this thesis

This thesis will investigate the potential of electron beam induced deposition for high resolution sub-10 nm fabrication. To achieve this goal, one needs a theoretical study on EBID spatial resolution and a practical demonstration.

In chapter 2 the results of a detailed literature review on the deposition processes under electron and ion irradiation are presented. First the specimen contamination in electron microscopy is treated, which has been regarded for decades as a nuisance and therefore has been extensively studied. Afterwards, the electron-beam induced-deposition (EBID) of metals is discussed, regarded as a potential nanofabrication method, unfortunately insufficiently understood. The chapter ends with conclusions where the open problems in EBID studies are identified. The problem of EBID spatial resolution is formulated as the main goal of this thesis. The intriguing question in the center of the present research is why electron beam writers with 0.2 nm diameter fabricate EBID structures with 15-20 nm.

Chapter 3 offers all the theoretical tools necessary to study the fabrication resolution problem and answer this question. The relevant interactions between electron and gas precursor are studied, as well as different surface processes that can happen during EBID. The physical aspects of electron scattering in solid matter, followed by a necessary know-how for the programmer of Monte Carlo simulations are systematically described. The conclusion of this chapter will point out the processes that might influence the EBID resolution and therefore will need considerable attention: the secondary electrons emitted as a result of electron bombardment, the delocalization of electron inelastic scattering, the migration of fragments on the surface and the electrical field effects.

Chapter 4 will describe a procedure to estimate the role of secondary electrons in the spatial resolution of EBID. For this purpose, Monte Carlo simulation programs have been written for the electron scattering in the target. Also a profile simulator based on a cellular automata method, adapted for EBID has been designed. The results of this exercise prove the major role that the secondary electrons play in the shapes and sizes of grown dots.

Chapter 5 investigates the role that the delocalization of electron inelastic scattering can play in EBID fabrication resolution. According to our estimations this contribution is negligible compared with the role of secondary electrons.

In Chapter 6 we describe the aspects of building an experimental setup for EBID study in a STEM. The additional elements necessary for a STEM to host EBID : a PC- controlled pattern generator and two possible variants for a gas delivery system are designed and described. A nozzle injector gas delivery system has been designed for the Philips EM 420 electron microscope, as part of a dual beam instrument. In order to perform EBID experiments in another higher resolution STEM, a portable gas cell, that can be used without modifications for the host, is the last issue of this chapter.

Encouraged by the theoretical estimations from the chapters 4 and 5, pointing out that sub 10 nm lithography is possible using EBID, we dedicated Chapter 7 to the optimization of EBID towards high resolution. Some successful high resolution experiments with contamination and

EBID in a state-of-the-art STEM have been performed and the results are presented.

In conclusion we have proven theoretically and practically that EBID can produce 2 nm size structures and that STEM is a tool that can host with success high resolution sub 10 nm electron beam induced deposition.

Bibliography

[1] ALIVISATOS, A. Less is more in medicine. *Scientific American 9* (2001), 59.

[2] BERNHARDT, R., MCGONIGAL, G., SCHNEIDER, R., AND THOMSON, D. Mechanisms for the deposition of nanometer-sized structures from organic fluids using the STM. *Journal of Vacuum Science and Technology A 8* (1990), 667.

[3] BINNING, G., AND ROHRER, H. *Helv. Phys. Acta 55* (1982), 726.

[4] BROERS, A. N., AND HOOLE, A. Electron beam lithography-resolution limits. *Microelectronic Engineering 32* (1996), 131.

[5] EHRLICH, D., OSGOOD, R., SILVERSMITH, D., AND DEUTCH, T. One step repair of transparent defects in hard-surface photolithographic masks via laser photodeposition. *IEEE Electron Devices Letters 1* (1980), 101–103.

[6] EIGLER, D., AND SCHWEITZER, E. Positioning single atoms with a scanning tunneling microscope. *Nature 344* (1990), 524.

[7] FOSTER, J., FROMMER, J., AND ARNETT, P. Molecular manipulation using a tunnelling microscope. *Letters to nature 331*, 28 (1988), 324.

[8] KOHLER, M., AND DIEKMANN, S. Biomolecular nanotechnolgy. *Reviews in molecular biotechnology 82* (2001), 1–2.

[9] KOOPS, H., KRETZ, J., RUDOLPH, M., WEBER, M., DAHM, G., AND LEE, K. Characterization and application of materials grown by EBID. *Japanese Journal of Applied Physics 33* (1994), 7099.

[10] PREWETT, P., AND HEARD, P. Repair of opaque defects in photomask using focused ion beams. *Journal of Physics D 20* (1987), 1207.

[11] SMITH, H. Low cost nanolithography with nanoaccuracy. *Physica E 11* (2001), 104.

[12] TANIGUCHI, N. On thebasic concept of nanotechnology. In *Proc. Int. Conf. Prod. Eng., Tokyo* (1974), vol. 2, JSPE, pp. 18–23.

[13] WHITEHOUSE, D. Trends in instrumentation and nanotechnology. In *From instrumentation to Nanotehcnology*, vol. 1 of *Developments in nanotechnology*. Gordon and Breach science, 1991.

[14] WHITMAN, L., STROSCIO, J., DRAGOSET, R., AND CELOTTA, R. Manipulation of adsorbed atoms and creation of new structures on room temperature surfaces with a STM. *Science 251* (1991), 1206.

Chapter 2

Electron beam induced deposition

"Buiten de zwarigheid om uit zoveel bouwstoffen het nodige uit te zoeken en te rangschikken, kwamen er gedurig in de handschriften woorden en uitdrukkingen voor, die hij niet begreep, en die ook mij vreemd waren."[1]

Multatuli, "Max Havelaar"

2.1 Historical overview

The observation of electron induced deposition is not new. Probably everything started when microscopists observed that the electron beam on the specimen created dark brown films, commonly called contamination.

Beam-induced specimen contamination has been recognized as a problem from the infant times of electron microscopy. In the beginning it has been suspected that the bad vacuum inside the system from oil diffusion pumps, O-rings, grease, etc. was the main reason and this assumption urged the construction of electron microscopes with better vacuum conditions. Nowadays, in conventional electron microscopes the contamination problem can be satisfactory controlled by the use of various anti-contamination devices and good vacuum techniques. Typically the pressures around the specimen are as low as 10^{-7} mbar. However, contamination still occurs, this time from the hydrocarbons already deposited on the specimen and specimen holder during operation in the open air. It seems that an ultra-high vacuum alone does not completely solve the problem of contamination unless the specimen is prepared by cleaving, evaporation or ion beam etching inside the UHV specimen chamber.

The phenomenon of contamination under electron beam irradiation is not completely understood but the current dogma holds that the growth results when adsorbed hydrocarbon contaminants, diffusing rapidly across the surface are cracked and cross-linked to the target surface under the influence of the electron beam. As a result, a carbon rich film, ring or cone grows depending on the beam diameter and exposure method. If the specimen is thin and the majority of electrons are transmitted, then contamination will grow not only on the top but also on its bottom side, as it can be seen in Fig. 2-1. When the electron beam is defocused, a ring is deposited as it can be seen in Fig. 2-2.

---

[1]Beside the difficulty to find and arrange the necessary information from so much material, the manuscript frequently contained words and expressions which he did not understand, and which also seemed strange to me.
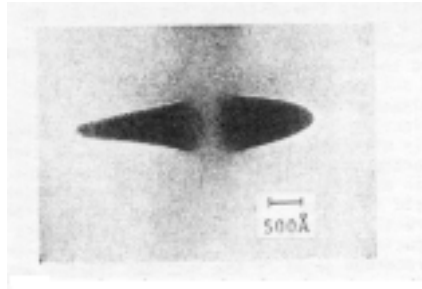
Figure 2-1: TEM image of tilted contamination spots created by a focused electron beam coming from the left (from [30])
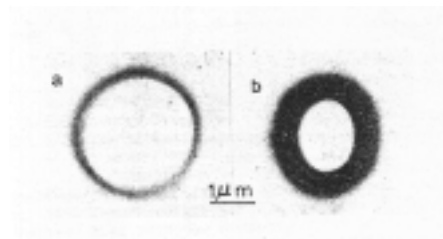
Figure 2-2: TEM image of two contamination rings, created by a defocused electron beam for different specimen temperatures (from [25]).

The morphological analysis of the contaminant films can be determined using EDS and EELS methods. A typical EELS spectrum from the deposits grown in a STEM from pump oil vapor shows a volume plasmon peak at 20-25 eV, specific for carbon, meaning that the deposits contains carbon (see Fig.2-3 from [4]).
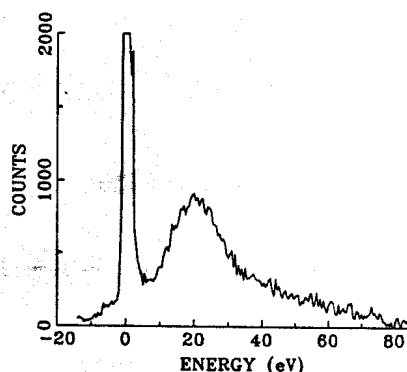
Figure 2-3: Electron energy loss spectrum recorded from a contamination film (from [4])

This electron irradiation induced carbon contamination is a significant barrier to high-resolution microstructural analysis. One of the most serious annoyances is the loss of spatial resolution, especially in the extreme case of a finely focused probe necessary in the scanning mode of a STEM [40]. The degradation in resolution is caused by the beam spreading in the contaminant film or by the charging of the poorly conductive contaminant layer, followed by beam deflection. The contamination layer also affects the measurement of local surface composition, both in EDS and EELS. The contamination rate depends inversely proportional on the electron stopping power and the beam energy, making contamination an actual problem for low energy SEMs. Also ion beam induced deposition of organic molecules has been observed in the past due to the effect of polymer buildup at the target of particle accelerators. Care must be taken to avoid contamination in some photon and electron induced lithography processes.

For these reasons there has been a lot of work done looking for methods to understand, prevent and reduce the contamination build-up on specimen surfaces subject to electron or ion bombardment.

However contamination buildup is not always an undesirable process and can serve as a useful tool in electron beam lithography. The carbonaceous deposits resist subsequent removal by chemical etching or ion bombardment in the same way the photoresist used in solid state microfabrication does.

Searching for new lithography methods, Broers had the idea to use this "annoying" electron-beam cracked hydrocarbon layer as a negative resist (protective mask) during reactive ion etching lithography [10]. The idea turned out to be successful and for the first time 80Å wide metal lines on a thin carbon film were fabricated in a STEM. Thus, the ugly duckling became a swan, the new technique received the name of **contamination lithography** and it has now proved to provide high-resolution structures. As a result of this success, metal-bearing gases as well as various hydrocarbon mixtures started to be introduced on purpose in the focused beam columns as precursor, in order to study a promising lithography technique named **electron-**

beam-induced deposition (EBID). In the last ten years, EBID obtained more technical importance, as a tool for *"additive lithography"* [60], being applied on a small scale in SEMs, TEMs, in dedicated lithography systems, STMs, dual beam instruments and image projection systems.

Specimen contamination in electron microscopy can be interpreted as an electron-beam-induced-deposition of structures from a hydrocarbon mixture precursor. The information accumulated about the physics of this phenomenon can be a relevant help in EBID study. Contamination in electron microscopy and analysis has been the subject of some very good reviews [40].

2.2 Electron beam induced deposition (EBID): a literature survey

2.2.1 Motivation

We decided to perform a literature review on the use of electron beam induced deposition in micro- and nanofabrication.

The study of EBID started later than the study of contamination in electron microscopy so that a very extensive literature review on this subject does not exist at this moment. A start in this direction has been made by Koops in [60]. Also EBID has been in 1994 the subject of a PhD dissertation by M. Weber [110]. We used these sources as model for structuring our review.

Of course a natural question will occur on the usefulness of such an extensive effort. The main reason is that we need this review ourselves, in order to know what has been already done, to establish the problems that remain to be solved and focus our efforts on what is really new. An additional motivation would come if other groups of readers could also benefit from this work.

Who might further benefit from this review? First of all, a review is one of the most effective time savers available. This review will help the reader to acquire in a short time the know-how in EBID, the theoretical and practical aspects necessary at different stages of the research. For example, outsiders reading about exciting EBID applications, can consider to use EBID for their purposes. The review is useful for a novice who already decided to use EBID, but does not have an experimental setup yet. The review offers in this case a set of possible precursors and constructive choices with their advantages and disadvantages. Also it will enable the novice to become familiar with the prevailing knowledge and understanding of the topic.

Some shaky points and still open problems in the theoretical modelling are identified, generating new ideas and approaches to follow for other researchers. Finally more advanced and curious readers, still having questions on EBID can find some of the answers in this review.

The EBID technique is used and reported sometimes under slightly different names, which we will mention, but in order to avoid confusion we will try in the review to keep consequently the most accepted terminology. For example, some authors call the contamination lithography *electron beam induced resist growth (EBIR)* and the related metal deposition as *electron beam induced metal formation (EBIM)* [45]. Because it allows local patterning of small areas of the substrate, EBID is also called *electron beam induced selective chemical vapour deposition* or just *electron beam CVD* [70]. Because etching is also possible as effect of electron beam induced surface reactions, the method can be called by combining these two effects, *Electron beam*

induced selective etching and deposition (EBISED) [68, 102]. A new concept of *environmental EBID* [23] is recently introduced when an environmental SEM hosts the deposition process.

Focused ion beam (FIB) machines are currently used for IC and mask repair as well as for failure analysis of microdevices by milling and sputtering. By introducing gas in such a system, also material deposition can be obtained under ion irradiation, in competition with sputtering. The technique is named **ion-beam-induced-deposition (IBID)** or sometimes *ion beam assisted deposition (IBAD)* [50]. Not only metal but also insulator material can be deposited for integrated circuit repair using IBID [54]. If a reactive precursor is used, etching is observed under ion beam irradiation and a nanostructuring technique is obtained, named *ion beam induced etching* or *gas assisted etching (GAE)*. Nagamachi [77] introduced a new fabrication method named *focused ion beam direct deposition (FIBDD)*. By maintaining a high vacuum (10^{-7} Pa) during deposition, it eliminates the contamination of the specimen with adsorbed gas molecules. By using very low beam energies, high current densities and alloy ion sources, magnetic and super-conducting materials have been deposited using this method. Even if it is not a proper IBID according to our adopted definition, but rather an ion implantation method, we will mention his results because he makes a parallel analysis between IBID and FIBDD.

During the last two decades, several research groups in the world have been using, experimenting or modelling the electron / ion beam induced deposition process. All their research efforts are usually aiming for one or more requirements such as: high deposition rate, high fabrication resolution and high deposit quality (low conductivity and high purity). The relevant work of the mentioned research groups, their results and predictions (1980-2001) are discussed in this literature review. Because we intend to study in detail the electron beam induced direct writing processes, the interest in this review was mainly limited to reports about EBID and we think that this survey is close to exhaustive. Because of similarities in phenomenology and modelling, also some ion beam induced deposition (IBID) articles are discussed. The section about instrumentation and deposit quality analysis can be integrally used also for IBID. In the modelling the effect of material sputtering, which is much stronger for ion beams, should be taken into account.

The level in the review is suitable for a beginner in the EBID and electron optics fields. Because it is addressed to a large spectrum of readers, the amount of information exceeds sometimes the immediate needs of this thesis.The conclusions we present are pointing at the open problems that we could and did solve in this thesis. Other readers might generate their own conclusions.

2.2.2 Instrumentation and techniques

This section presents typical experimental setups where EBID and IBID is studied as well as choices that the builder has at present.

Experimental setups have been built to prove theoretical models, to appreciate the influence of different parameters on the deposition quality or to show possibilities of new applications of these methods. In order to experimentally study EBID and IBID some essential hardware is needed, starting with a vacuum chamber containing a position-controlled focused particle beam, a specimen stage and a gas delivery system with flow control facilities. If more complicated patterns have to be deposited, a pattern generator has to be attached to the beam deflectors. Eventually the deposition results have to be evaluated and this will require imaging, recording and / or in-situ analytical capabilities to be added to the experimental setup.

Given these indispensable elements, EBID began to be studied in modified electron mi-

croscopes, in SEMs more often due to their flexibility and availability, but also in STEMs, commercial EBL systems, dual beam instruments or STMs, most of them with an added possibility to introduce the gas in the specimen area. In cases where the aim is not an application but the clarification of the fundamental mechanisms involved in EBID, special bakeable UHV setups have been built [68, 93, 18]. Their construction is more simple, containing only an electron gun, a gas inlet and a (multispecimen) XYZ translational stage, but they are largely supported by various in-situ surface preparation and analysis apparatus, as ion guns for cleaning, Auger spectrometers, diffraction analysers, quadrupole mass spectrometers, quartz crystal microbalances, etc. (see Fig 2-4).
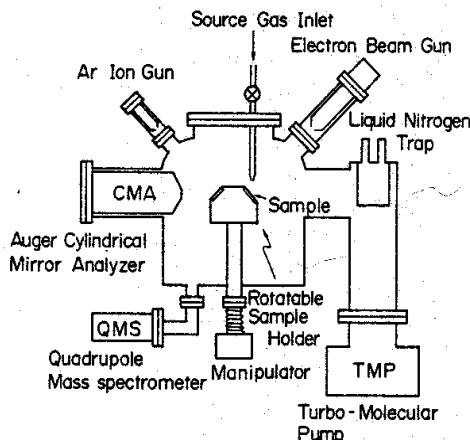
Figure 2-4: EBID apparatus to study fundamental characteristics (from [68])

When designing a gas injection system coupled to an UHV microscope column, care has to be taken to prevent the gas from leaking into the pressure-sensitive gun chamber (the FEG requires pressures lower than 2 x 10^{-9} torr) and to reduce the unwanted deposition in other places except on the specimen itself. The deposition system parameters are determined by the focused probe optics (beam acceleration voltage, probe current and probe size, imaging performance), the specimen (material, temperature, treatment history, electric potential) and the gas delivery system (precursor type, precursor temperature and vapour pressure, pressure and molecular flux at the specimen). Several reported EBID experimental setups and their parameters will be described further on.

2.2.2.1 The environment and the vacuum system

High fabrication and imaging resolution requires very stable focused beams and specimen stages. For this reason, the deposition system can be better situated in an environment, where the temperature is stable maintained to within 0.1° C and shielding from the different environmental influences is provided. For example the floor vibrations decoupling can be realized by situating the whole system on a concrete cube of 5.5 t mass resting on 3 air springs with a designed eigen

frequency of 1 Hz. [43, 9]. The ambient magnetic stray field has to be restricted to below 0.2 mG at 50Hz.

The exhaust line of the vacuum pumps in case of precursors with a health hazard has to be led outside the laboratory space and filters are necessary in some critical cases. Special safety measures for toxic precursors, with suitable manipulation and ventilation facilities, according to the maximum allowed concentrations (mac) or threshold limit values (TLV) [91], together with a hazard analysis are obligatory steps in building an operational EBID experimental setup.

A dry pumping system offers the best vacuum conditions. For this purpose ion getter pumps should be used and the oil diffusion pumps present usually in the original construction of the microscopes should be changed with turbomolecular pumps. If the change is not possible, then Fomblin pump oil has to be used to avoid the hydrocarbon contamination. Of course, in the case of contamination lithography, if the precursor is expected to arrive from the oil diffusion pump vapours and residual vacuum, these changes are not justified. A membrane pump in place of a rotary pump will give less vibrations increasing the specimen stage mechanical stability. Also the membrane pump is oil free and will assure an oil free combination with turbo drag pumps. The vacuum pumps construction has to be compatible with the precursor vapours used, to avoid corrosion problems. The turbopump is safer than a cryopump when potentially hazardous materials are used as precursors. The optical column should be differentially pumped in double aperture construction, to separate the gun chamber from the specimen chamber where gas at high pressure is introduced. Extra gauges have to be mounted in order to monitor the gas inlet pressure and the changes of pressure in sensitive places in the column.

2.2.2.2   The probe formation. Optical focusing columns

Photon, electron and ion beams can be used to induce the deposition, but the photon beams fall out of the discussion from the start because of their low achievable resolution. The electrons can be focused in a much smaller spot than the ions and the current densities can be higher, compensating somehow for their low reaction cross-section. For ion systems, the resolution can be 20 times worse because of the electrostatic lens aberrations and large energy spread of the available liquid metal ion sources (LMIS). Another advantage of electron beams is that they offer, compared with ion beams, a smaller risk of implantation in the specimen and of simultaneous sputtering of the deposited material. Indeed, sputtering becomes a problem in case of high resolution imaging with ion beams. On the other hand, the deposition rate in IBID is much higher than in EBID due to the difference of mass between electron and ion. As a result, the longer exposure time necessary for electron beam induced surface reactions will require higher stability from the electron optical columns and their specimen stage. Ion beams are more advantageous in IC surgery because they allow beside the material deposition, the conductors cutting and layers sputtering in order to reveal buried defects.

a) Electron beam columns

The electron beam columns are usually modified microscopes having as electron source a thermionic gun (W or LaB_6), or a Zr/O/W thermal field emission gun (FEG) or Schottky field emission gun. A better electron source will offer a higher reduced brightness and thus more current in a smaller probe, an essential feature in high-resolution applications. The lenses used are magnetic, the gun lens is electrostatic. The probe sizes vary depending on the microscope performance. In commercial SEMs the beam diameter is 1 nm at best. In TEM/STEM based constructions the electron probes are much smaller, as 0.2 nm. The advantage of a TEM/STEM is that the spot can be imaged at extremely high magnification, allowing the generation of an ideal beam regarding the spot diameter and astigmatism, a fact that will be of importance in
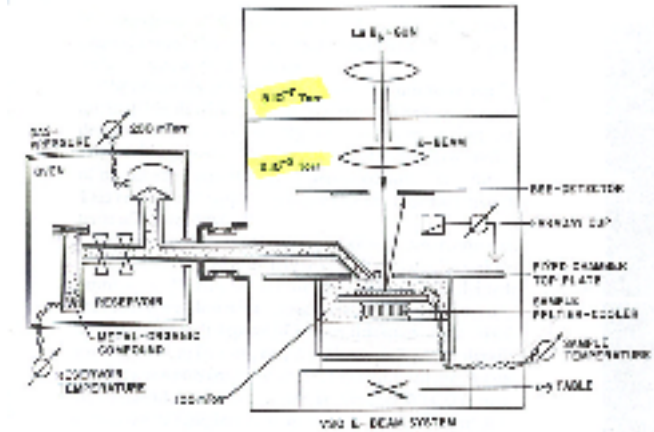
Figure 2-5: A SEM modified to implement EBID (from [62])

patterning. An example of a SEM modified to implement EBID is shown in Fig. 2-5.

The current density in the spot depends on the brightness of the source, on the focus, astigmatism and diffraction aberrations and on the fixed chromatic and spherical aberrations of the objective lens. In systems without automatic alignment it will depend on the skills of the operator, making reproducibility difficult to achieve. The beam current density distribution is usually supposed to be gaussian, or otherwise it can be measured. The commonly used method to measure the beam density profile and diameter is by scanning the beam over a sharp edge and a synchronized detection of the current in a Faraday cup underneath (the transmitted signal) or the secondary electrons (reflected signal), using the so-called Rishton method [86]. The beam diameter is determined by reading the slope of the measured current between 15% and 85% of the total current change. The sharp edge can be the edge of a Faraday cup or a Ni mesh knife edge or a cleaved edge of a 200 μm thick Si wafer [63, 69, 35, 53]. In edge methods, the signal depends strongly on the nanostructure of the edge and the evaluation depends on skills of the user. Weber argues that edge methods are not suitable for high resolution applications being slow and not reproducible and proposes a new faster method to determine the beam current density distribution, by analyzing the SFM image of the deposited dot obtained in spot mode by EBID or contamination growth i.e. the material response to the spot exposure [113].

The probe size of the original microscope can be improved by using a special probe forming objective lens with lower aberration coefficients.

The beam impact energies on the specimen vary usually between 30 and 120 keV, depending on the design of the host microscope, but even lower energies are necessary sometimes for experimental reasons. The problem is that the performance of an electron beam column decreases with the beam energy, the low energy at the gun level increasing the spot size at the specimen. This inconvenience can be solved if along the column the beam is accelerated at high energy and it is retarded between the final lens and the substrate by applying a negative bias on the specimen. In this way, operation down to zero energy can be performed. In this regime, care has to be taken with distances between the eventual gas nozzle and specimen in order to avoid flashovers. Hoyle experimented EBID for different landing energies from 0.06 keV to 20 keV

drawing conclusions about the influence of landing energy on the deposition quality [38]. But high beam energies are preferable, in order to reduce the chromatic aberration, diffraction and beam broadening in a target by forward scattering. In Table 2.4 we summarize some typical parameters of the electron beam columns used for EBID.

b) Ion beam columns

The focused ion beam (FIB) columns used for deposition are UHV chambers with an ion source, a condenser-objective combination of electrostatic lenses, a specimen stage and a gas delivery system. The ions are usually supplied by a liquid metal ion source (LMIS) or less often a gas field ion source (GFIS) and are in most of the cases gallium Ga^+ and less often indium In^+, silicon Si_2^+, gold Au^+, hydrogen H_2^+ or argon Ar^+ ions. Liquid alloy ion sources are also available for conducting, superconducting and magnetic materials. For example Au-Si, Au-Cu, Au-Cu-Si alloy sources for conducting materials, Nb-Au-Cu alloy source for superconducting Nb material and Co-Cu-Nb-Au alloy source for Co magnetic material. A mass E x B Wien filter between the two lenses has to be inserted to separate different ion species when alloy sources are used.

The host system can be a commercial FIB [71] or a custom-built system [9]. The beam accelerating energies can vary between 15 and 60 keV and the probe sizes range from 7 nm to 250nm. The final probe size will depend in high current regime on the spherical aberration, in intermediate regime on chromatic abberrations and at the smallest current values mainly on the source size. Higher resolution can be obtained if special objective lenses are designed in order to minimize the spherical aberration [15] or energy filters are inserted in order to minimize the energy spread of the LMIS (usually around 10 eV) and thus the chromatic aberration. Electrostatic octupoles can be used to correct the astigmatism due to mechanical misalignments [90, 9]. An example of a FIB system modified to implement IBID is shown in Fig.2-6.
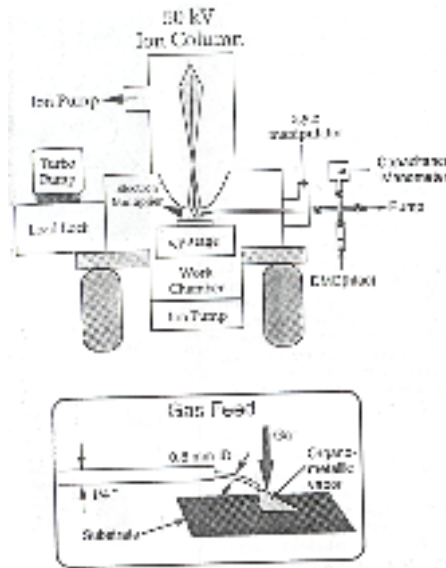

Figure 2-6: A FIB modified to implement IBID (from [9])

Though it is usual to assume that the beam obtained by FIB columns has a gaussian profile, there is evidence of deviations from this. The ion beam current density distribution and diameter can be estimated in the same way as for electron beams, by scanning the beam across a sharp edge and measuring the resulting secondary electrons signal as function of beam displacement or by sputtering of thin films. The beam diameter is then defined by the distance between 10% and 90 % amplitude of this signal.

c) Special EBID setups

Less often encountered but nevertheless very interesting EBID host constructions are:

c1) the environmental SEM (ESEM), with the advantage of allowed high pressures up to 10 Pa in the column [79, 24, 23] so that less precautions have to be taken when the precursor gas is introduced.

c2) the scanning tunneling microscope (STM), that without offering a focused beam is an interesting research environment for low energy electron induced deposition. From a modelling point of view it is useful to separate low and high energy electron excitations. This is in a SEM or a TEM not easy to realize. The STM is used for low energy deposition from organometallic or hydrocarbon precursor, the so called STM CVD. The main application is the improvement of the tip shape [89, 73]. The visualization of fabricated structures can be realized in the same STM, or in a SEM with a higher resolution and speed. Such a combination STM-SEM allowed structures of 10-100 nm to be deposited [87]. The low energy tunnelling electrons decompose the precursor adsorbed molecules on the substrate and produce deposition. Two types of electron beam induced deposition can be experimented in a STM. One is the growth of a structure (hillock, bump or line) on the sample surface and an other process grows a nanowire on the STM tip and improves its shape and imaging ability. These different effects are obtained by simply reversing the polarity of the tip. All experiments shown that if the tip pulse was less than 3 V no visible surface modifications occurred.

The deposition in STM has as well a reverse effect: the molecular removal from the surface. This process also has a threshold at about 3.5 eV. Etching of holes is possible only in air or when water vapour is adsorbed on the sample. In a vacuum environment no holes could be drilled. Holes with 4 nm diameter and 6 nm spacing could be drilled in the graphite substrate situated in air, by applying a voltage pulse of 3-8 eV for 10-100 μs in the presence of water vapour [2].

An example of a STM-CVD system is shown in Fig. 2-7.

c3) the dual beam instruments, where both electron and ion beams are combined in one machine and comparative analysis of electron/ion induced chemistry phenomena (deposition or etching) can be performed [90, 66, 16, 119, 102]. The second advantage offered by a dual beam system is that imaging can be realized in electron microscopy with less specimen damage. The two columns are oriented to aim at the same specimen and their optical axes intersect usually under an angle of 45 degrees. de Jager proposed [16] another relative placement of columns where the ion and electron beams both are normally incident on the specimen. An example of dual beam instrument used for gas assisted etching is shown in Fig. 2-8.

c4) Nagamachi [77] introduces a new technique, the focused ion beam direct deposition, FIBDD. In fact it is an ion implantation technique and not IBID in our strict definition, because it does not use a gas precursor. The FIB system has very low beam energies and high current densities necessary for implantation, with an optimized lens system and a mass filter, maintaining very low residual pressure during deposition, $2 \times 10^{-7} Pa$.
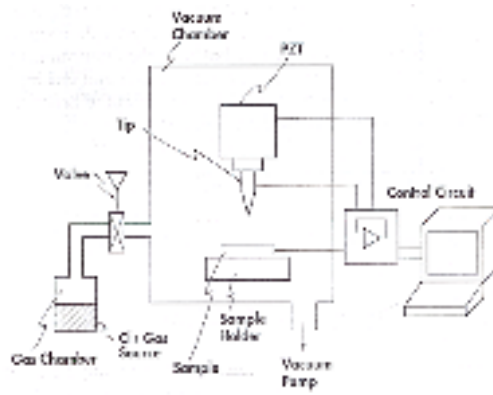
Figure 2-7: STM-CVD microfabrication system (from [69])
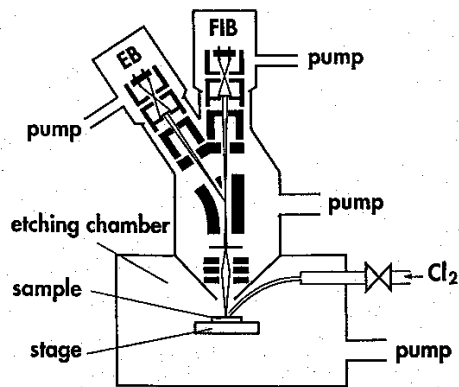
Figure 2-8: Schematic of a dual beam instrument, combining FIB and EB columns and used for etching with Cl_2 (from [102])
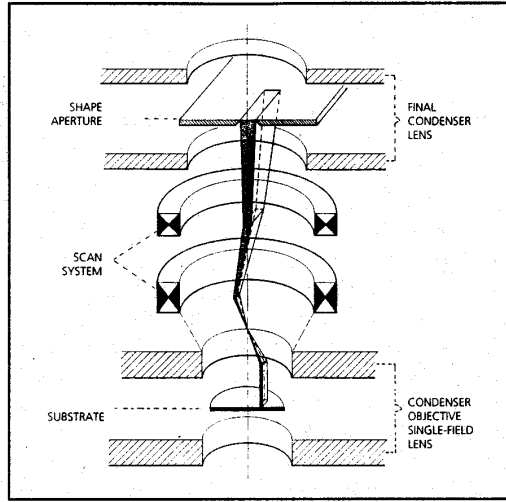
Figure 2-9: Telecentric beam path with Köhler illumination from ([41])

2.2.2.3 Patterning and exposure techniques

In order to deposit a certain pattern, the focused beam has to be positioned and scanned, while applying the precursor gas flux at constant rate. The beam deflection can be done manually or automatically by means of deflectors, usually magnetic for electron beams and electrostatic for ion beams. A blanking facility is necessary to avoid exposure during the return of the beam. A simple construction needs only two deflectors, in the orthogonal X and Y directions. The optimum construction is the double deflector arrangement, which allows a normal beam incidence over the whole exposed area (telecentric beam path) by fixing a favorable pivot point in the backfocal plane of the upper pole piece of the objective lens, (see Fig.2-9).

The pattern is made of discrete points or pixels, and each pixel is exposed for a predefined time called dwell time, t_d. There must be a delay between successive visits of the beam in a certain pixel on the surface to give time for replenishment with precursor molecules and this time is called refresh or loop time, t_l. The loop time depends on the deposited area and on the exposure strategy:

$$t_l = \frac{t_d * L * W}{(D * (1 - OL))^2} \tag{2.1}$$

where D is the beam diameter, L and W are the length and width of the pattern and OL the overlap.

The most common patterns to be deposited are dots, lines and rectangles and they can be obtained by simply using the imaging scan generator available in any SEM to raster the

22

beam. The deflection can be also made by a function generator with fast rastering, but with reduced patterning capabilities and no blanking. The maximum scanning rate (100 kHz) is limited by the response time of the magnetic deflector coils. Beside these analog beam scanning modalities, modern systems use a digital beam scanning facility, assisted by a computer [98, 60]. If more complicated models have to be exposed, a scan generator is not flexible enough and a pattern generator is then necessary. A pattern generator can be a separate hardware module or a computer with a plugged-in digital to analog conversion (DAC) card, controlled by a user interface and attached to the deflecting coils. According to the pattern given as input file, the pattern generator will generate the necessary signals to control the deflectors. The scan field dimensions can vary from 50 $\mu m \times$ 50 μm to over 4 mm x 4 mm. Exposure times per pixel (dwell time) vary from $1\mu s$ to >100 s. The refresh time depends on the exposure order and on the length of the pattern but typically it can be 10 ms. Exposure doses in EBID can vary from a low dose of 0.01 C/m^2 to a high dose of 10000 C/m^2. The electrical noise and instabilities in the deflector signal will reduce the achievable fabrication resolution.

Exposure techniques and recipes

The same pattern can be exposed in different ways (timing, order, step) and it seems that the deposit properties and quality depends on these parameters. For example, the same line can be exposed by a repeated fast exposure or a single slow scanning, see Fig.2-11a) and Fig. 2-11b).

Now we will give some recipes on "how to build" simple structures using EBID. In all cases it is assumed there is enough precursor vapour supply in the irradiated substrate area.

- Deposit a dot, tip or column. First in SEM picture or in TEM defocused mode locate the place where deposition is necessary. Switch the SEM in spot mode (focus the beam) and keep the beam in the same position for a time [42, 1, 52]. If dots are needed, then 10 seconds is enough, for tips 1 minute will be sufficient for a height of $1\mu m$.

- Deposit lines (wires). Localize in low magnification the start or the center point of the needed segment, then focus the beam and scan it using the SEM line scanning mode or in imaging mode by deactivating one of the scan directions. An example of lines and spaces deposited with EBID is shown in Fig. 2-10.

- Deposit rectangles. Rectangles are useful to be deposited instead of lines to ease the width and resistivity measurements and to reduce the influence of the beam drift. The simplest way is to use the scan generator in frame mode. When using a pattern generator, in order to avoid exposure during beam return, the rectangles should be deposited in meander (serpentine) pattern (Fig 2-11.c) The step should be 10% of measured spot size.

- Deposit free-standing structures (nanowires, rods and bridges across a hole in membranes). Start by keeping the beam at the edge of a thin membrane until film nucleation is formed and then move the beam slowly in line scan towards the hole. The deposited layer follows the slow moving e-beam also outside the membrane, across the hole. If the beam sweep rate is too high, the growth cannot follow the beam and the process will be interrupted. On the contrary, if the sweep rate is too slow, a thick sheet and not a rod will be formed. The solution is to start with high sweep rates and decrease them until the growth can follow the beam. The speed has to be around 1-5 nm/sec [8, 49]. Another method to deposit bridges across the hole is to keep the beam in the hole at a distance of a few nm from the edge and wait until the grown wire reaches the beam. This distance growth is explained by delocalization of molecular dissociation or by the tails of the beam current density distribution [49].

- Deposit 3D nanostructures. By controlling the x and y beam positions correlated with time, 3D structures can be deposited by EBID.[60]. A smaller penetration range of the ions
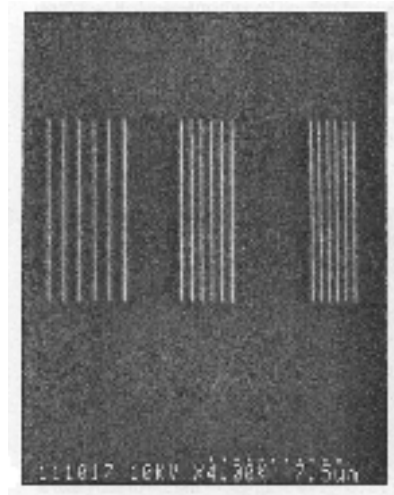
Figure 2-10: Gold lines deposited on Si substrate by EBID ($4 \times 10^{-6} C/cm^2$) (from [65])
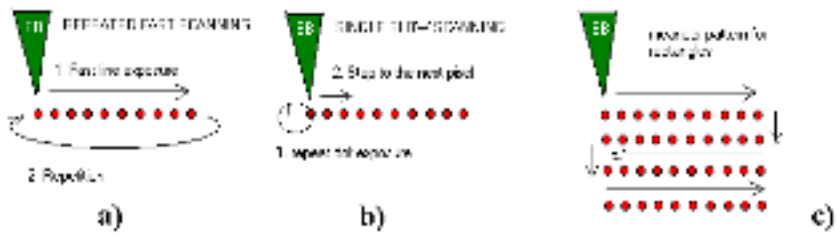
Figure 2-11: Illustration of different scanning methods
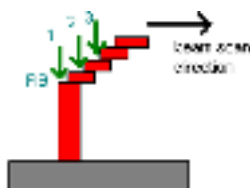
Figure 2-12: Procedure for the fabrication of 3D structures

compared to electrons allows us to fabricate also complex three dimensional structures using IBID, pushing the application area to the fascinating world of nanostructure plastic art! (see Fig. 2-13). In Fig. 2-12, the beam is scanned in digital mode. First a pillar is formed with beam in position 1. The beam is then moved within the diameter of the pillar and fixed there until the terrace formed has a thickness which exceeds the ion range a few tens of nm. This process is repeated to form 3D nanostructures. The key point is to adjust the beam scan speed and the vertical growth rate.
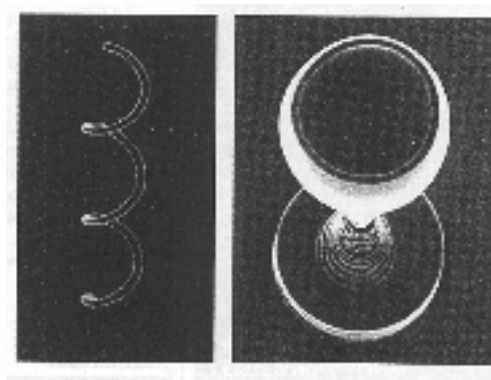
Figure 2-13: Examples of 3D structures fabricated by IBID: a spiral wire with 80 nm diameter and a micro wineglass with a diameter of 2.75 μm and a height of 12 μm (from [71])

2.2.2.4 Imaging possibilities

In electron columns different signals can be used to form the specimen image: the secondary electrons (SE), the backscattered electrons (BSE), the transmitted electrons or the induced specimen current. In ion columns imaging can be done also with the secondary ions signal. The typical imaging chain consists of an imaging signal detector (scintillator, multichannel plate, channeltron, semiconductor detector, isolated specimen holder, Faraday cup), an amplifier and the imaging monitor. The images can be recorded on conventional microscope plates, on high resolution video tape via TV camera system, on printers and plotters and the most modern way
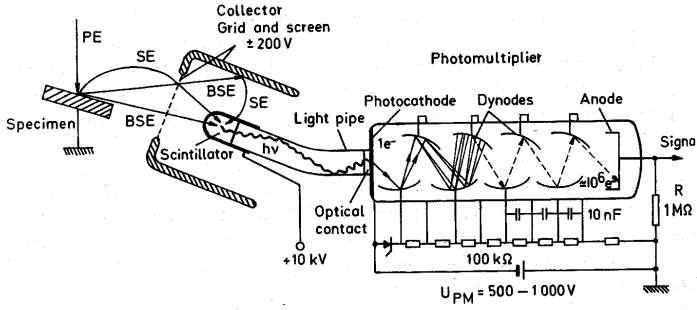
Figure 2-14: Scintillator-photomultiplier (E-T detector) for SE signal recording (from [85])

in an image file assisted by a computer and frame-grabber. The central criteria for the choice of detectors are the sensitivity, the noise, the electron detection capability and the lifetime.

An excellent and widely used detector for secondary electrons is the scintillator-photomultiplier combination, known as Everhart-Thornley (E-T) detector (see Fig. 2-14). The scintillators convert electrons to photons by cathodoluminiscence and can be made of plastic (NE102A), phosphor powder (P47) or the best and most modern single crystals of cerium activated yttrium aluminium garnet (YAG) [5, 92].

The quality of an image signal detector can be described by the factor r_n:

$$r_n = \frac{\left(\frac{S}{N}\right)_{in}}{\left(\frac{S}{N}\right)_{out}} > 1 \tag{2.2}$$

which is the measure of the increase in RMS noise amplification by the detector.

Alternatively the quality can be also described by the detector quantum efficiency (DQE), defined as:

$$DQE = \frac{\left(\frac{S}{N}\right)^2_{out}}{\left(\frac{S}{N}\right)^2_{in}} \tag{2.3}$$

For example the E-T construction with NE102A plastic scintillator has a factor $r_n = 2.5$ and for a phosphor powder P-47 scintillator $r_n=1.5$ [85].

The top view of a deposited structure is most frequently imaged by detecting the secondary or backscattered electrons in a SEM and less often in TEM by detecting the transmitted electrons. The profile and cross-sectional view of the deposited structures can be visualized both in TEM or SEM by tilting the specimen over 45 to 80 degrees or by using a scanning probe technique (AFM, STM) in case of small heights. In Fig. 2-15, Fig. 2-16 , Fig. ?? and Fig.2-18 typical imaging possibilities of structures obtained with EBID or IBID are shown.

In EBID the imaging tools are useful also to observe in-situ the growth, providing an
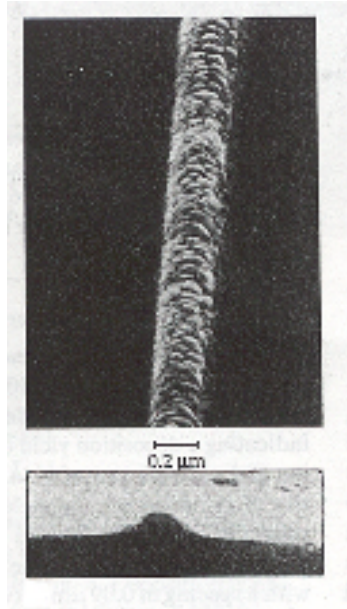
Figure 2-15: SEM image (top view and cross section) of a wire fabricated by IBID (from [9])
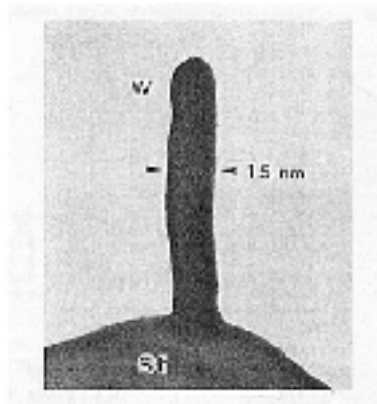
Figure 2-16: TEM micrograph of a tungsten rod fabricated by EBID on a Si particle (from [44])
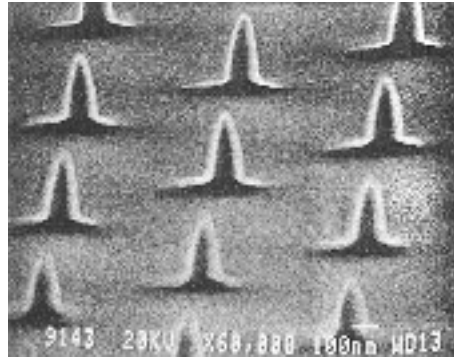
Figure 2-17: SEM tilted image of an array of Pt tips fabricated by EBID (from [59])
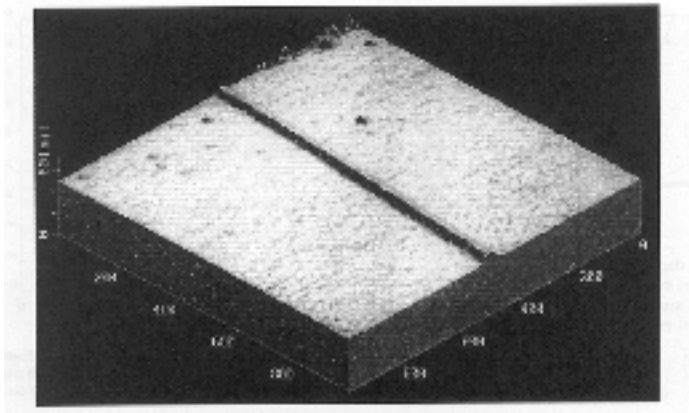
Figure 2-18: AFM image of a typical wire fabricated by EBID, where the image area is $1\mu m$ x $1~\mu m$ (from [57])
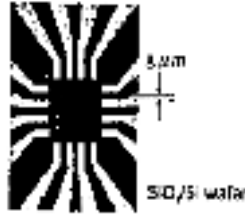
Figure 2-19: Prefabricated electrodes for resistivity measurement (from [79])

important advantage with respect to standard lithography. For example the secondary or Auger electrons signals can be used as indicator of film formation. A conventional AES system can be modified, by adding a gas system and a mass flow controller. Auger electrons are emitted and collected from the material when deposition starts, but the image resolution is rather poor ($1\mu m$) [68].

In-situ observation of deposition and growth has been performed also in a TEM [44, 68] using a real time TV monitor system. With a resolution of 0.23 nm at 120 keV sequential images could be obtained and recorded showing W atom rows in crystals followed by clusters colliding and coalescence in a continuous film.

The ultimate tool to study the fabrication resolution limits will not be a SEM because of its poor imaging resolution. Only TEM or scanning probe imaging (AFM, STM) will be able to image and analyze deposited structures of subnanometric size.

2.2.2.5 Specimens

The material

The substrate material used in EBID/IBID should have a minimum electrical conductivity to avoid charge-up and the resulting beam deflection. The substrates can be made of bulk material, suitable for use in SEM or STM or thin film, more suitable for use in TEM. The bulk specimens are usually silicon (Si) wafers with an oxide (SiO_2) layer of 100 nm - 300 nm grown on top, or semi insulating gallium-arsenide (GaAs) wafers. Often 100 nm thick gold electrodes are pre-evaporated on the substrate by conventional lithography methods in order to facilitate I-V resistivity measurements of the later deposited structures (see Fig.2-19).

The specimens used in TEMs are usually 3.05 mm diameter copper grids, blank or covered with 12-100 nm thin amorphous carbon or Si_3N_4 membranes [60, 38, 65]. Fine particles can be evaporated on the thin films as support for the deposition, like Ichihashi and Matsui who used 60 nm diameter Si particles covered by SiO_2 deposited on holey carbon film [44]. Also micromachined substrates can be used, like 200 x 100 μm^2 Si_3Ni_4 windows in a 3 mm diameter silicon plate [4]. The substrate can be also quartz glass plates in case of mask repair or fused quartz fibers when studying different incidence angles of the beam [116]. For beam induced etching, the substrates can be insulator material, SiO_2, Si_3N_4 or polyimide[115].

As already mentioned, the use of EBID/IBID is not restricted to planar geometries such that for example tip structures can also serve as substrate. By EBID the shape of scanning

probe tips and thus their imaging performance can be improved by growing a sharper supertip on top. Good results have been obtained by applying EBID on STM tungsten tips, AFM Pt-Ir tips, pyramidal Si_3N_4 tips or field emitter arrays made by conventional lithography and thermal oxidation sharpening.

Temperature

The substrates are kept usually at room temperature, but also cooling or heating during or after deposition have been experimented, following their implications in deposit growth and quality. For example, Koops [62] used a specimen stage which can be cooled or heated in the range from -40°C to 110 ° C, Scheuer [93] used EBID in the range -130°C to 60°C, both measuring the temperature with a thermocouple. The 0°C temperature represents the practical limit for cooling in order to avoid excessive hydrocarbon contamination and solid condensation of precursor vapours. Heating can be realized resistively with tantalum wire and cooling can be done with liquid nitrogen. The drift due to sample cooling with liquid nitrogen can be corrected by providing sufficient heat sinking to the SEM main chamber body. Thus the temperature can be kept stable within 1°C without drift in specimen position [65]. Another way to control the temperature is to use a Peltier element.

Treatment

The specimens may undergo preparation and treatment before being ready for the deposition. If in the case of contamination lithography, a dirty specimen is appreciated as extremely favorable for the carbon film formation, in the case of metal deposition, a clean specimen is the key to obtain high purity metal deposition characterized by a low resistivity. Different cleaning procedures have been developed during years. The classical way to clean a TEM thin carbon film is by ex-situ rinsing it in methanol for 18 hours [84] or degreasing and rinsing it in organic solvents (acetone, CCl_4) followed by in situ slow heating and cooling between 300 K and 1500 K [46] or annealing at 200°C for 1 h in ambient atmosphere [49].

The methods described above are wet cleaning methods. Because wet cleaning cannot assure highly conductive deposits with good reproducibility, dry cleaning methods are preferred, like ex-situ argon ion sputter cleaning (4 $\mu A/cm^2$ for 2 min) [93], or O_2 plasma cleaning (from 0.5 sec to 10 min) and annealing in vacuum at 300°C for 1h. The cleaning procedure can continue in the deposition chamber. After air exposure, O_2 is introduced in the EBID system and 200-400 V DC voltage [57, 33, 36] is applied (see Fig.2-20). Also in-situ dry cleaning can be performed by including in the same deposition UHV system an Ar^+ ion sputter cleaning facility [46, 70].

Electrical potential

The substrate is kept at ground potential during normal operation, except in the case when the induced specimen current has to be measured or a retarding bias potential has to be applied to the specimen.

2.2.2.6   Precursors and gas delivery systems

The precursor molecule has to contain atoms of the material to be deposited. In the case of beam induced etching, a reactive gas is needed. An essential but not sufficient condition for the deposition to happen is that the precursor vapours have to adsorb on the substrate. The chemical bonding of the precursor on the surface and the beam impact on this bond are criteria that make a precursor suitable for deposition.

The precursors commonly used in EBID were already known and synthesized in pyrolitic (CVD, MBE, MOCVD) or photolitic (LCVD) metal deposition techniques, like WF_6 for tungsten deposition and organometallic complexes ($Fe(CO)_5$, TMA and HFA) for iron, aluminum,
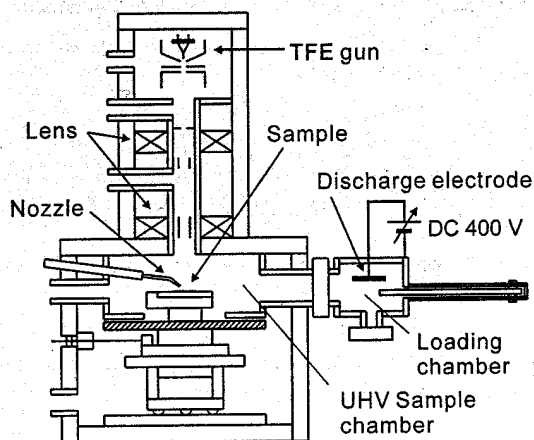
Figure 2-20: An UHV EB lithography system with a gas nozzle and plasma cleaning facilities (from [36])

respectively for copper deposition. For beam induced etching, gases from the RIE processes as Cl_2, I_2 , XeF_2 are used.

For contamination lithography, the residual gases in the microscope (H_2, O_2, CO, H_2O and hydrocarbons) offer usually a sufficient precursor source, but if necessary other hydrocarbon vapours can be introduced in the system, like styrene, benzene, toluene, liquid paraffin (a mixture of hydrocarbons from $C_{12}H_{26}$ to $C_{18}H_{38}$) or hexadecane $C_{16}H_{34}$ [108, 7, 8, 49].

An actual trend in EBID field is the search for new precursors. It has been observed that carbon contamination reduces the electrical properties of the deposit. Carbon impurities can come from the residual vacuum, a source which is difficult to avoid, but also from the composition of the precursor molecule, due to incomplete dissociation and chemisorption of carbon containing fragments. This effect can be diminished if low carbon content metal clusters [6] or carbon-free precursors are used. For example phosphines are metal bearing carbon-free precursors and are already experimented as alternatives to the widely used precursors [107].

The precursors can be liquid, solid or gaseous at room temperature and are usually kept in a small (ca 50 cc) reservoir. In Table 2.1 the vapour pressure of some precursors is given. In Table 2.2 the names of these precursors are summarized. Because all precursors used have a vapour pressure in the range of 10 - 400 mtorr at RT, which is higher than the operating pressure in the vacuum deposition chamber, typically 10^{-6} torr, the gas molecules will flow in the chamber down the pressure gradient. Important parameters for the EBID characterization are the gas flow rate (throughput) Q in the system, expressed in $torr \cdot liters/sec$ or Pa m^3/s in [SI] and the gas molecular flow on the substrate F, expressed in $molecules/sec/cm^2$ specimen area or in $molecules/\sec/m^2$ in [SI]. A necessary but not sufficient condition for the deposition is that the molecular flux has to be higher than the charged particle flux.

Depending on the approach used to protect the pressure-sensitive areas in the host column during the gas introduction, one can distinguish nowadays three types of experimental deposition systems for EBID study (see Fig. 2-22):
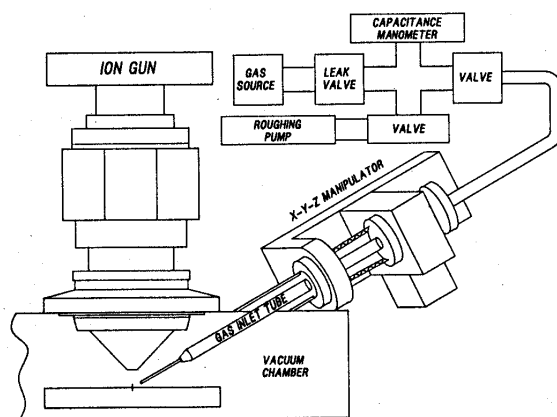
Figure 2-21: Schematic of a nozzle based gas delivery system in an IBID machine (from [32])

(A). A separate, differentially pumped subchamber, built around the substrate

(B). A miniature capillary gas feed nozzle

(C). An environmental electron beam deposition cell (E-EBID cell)

In the case of contamination lithography, a complicated gas inlet system is usually not necessary, because the precursor hydrocarbons will be attached on the surface anyway, due to previous immersion in the atmosphere or in a vacuum system with high partial pressure of hydrocarbons, or because of arrival from the residual vacuum of the lithography system. Other simple ways to create a hydrocarbon source are experimented, like using an adhesive tape as a stable source of monomers [117].

We will now describe these three experimental EBID systems.

Variant A: The subchamber [62, 65, 70]. The gas is introduced into the system through a metering needle valve. The subchamber can be differentially pumped through a 1 mm aperture, keeping an operating pressure in the subchamber of 10-100 mTorr. Because in this construction the collection angle of secondary and backscattered electrons is too small, a movable shutter can be used in place of the differential aperture. The shutter opens to let the beam through for high-resolution imaging and the EBID process can continue when the shutter is closed. The disadvantage of this variant is the small field of exposure and imaging. When the reservoir is a box attached to the specimen holder, the movement of the specimen is restricted. Even if the subchamber is built around the specimen, only the area under the shutter can be exposed (see Fig.2-5).

Variant B: The nozzle injector [51, 37, 15]. An advantage of the nozzle construction is that the gas is locally delivered in the beam irradiated specimen area, reducing the gas loading of the working chamber and thereby suppressing the pressure rise inside the optical column. Another advantage of this construction is that the beam can scan larger areas, creating larger imaging fields. The nozzle has to be brought in close proximity to the sample surface where the e-beam is incident, such that the line of sight intercepts the beam at the surface of the device (see Fig. 2-21).

Usually the angle between the nozzle and the substrate is 45 degrees. The nozzle position above the specimen can be fixed or adjusted manually or automatically by means of a XYZ

Depo mat.	Precursor molecular formula	Vap. press at RT	S	L	G	Reference
Au	$Me_2Au(hfac)$ $C_7H_7F_6O_2Au$	700 mtorr		x		[9, 18] [24, 23, 97]
	$Me_2Au(acac)$	8 mtorr				
	$Me_2Au(tfac)$	40 mtorr				[11, 22, 62, 65, 94]
	$AuClPF_3$		x			[107]
Al	$Al(CH_3)_3$			x		[45, 28]
Cu	$Cu(hfac)_2$		x			[113]
	$(C_5HF_6O_2)Cu(CH_3)$ $3SiCH = CH2)$	420 torr	x			[79]
Cr	$Cr(CO)_6$	10 torr		x		[70]
Fe	$Fe(CO)_5$	3 torr		x		[23, 63]
	$Fe(C_5H_5)_2$					[114]
Mo	$Mo(CO)_6$	78 mtorr	x			[112]
Os	$Os_3(CO)_{12}$					[93]
Ni	$Ni(CO)_4$	10 torr			x	[87, 109]
Pd	$Pd(OOCCH3)_2$					[89]
	$Pd(C_3H_5)(C_5H_5)$					[89]
Re	$Re_2(CO)_{10}$					[49]
Ru	$Ru_3(CO)_{12}$					[93]
Rh	$Rh(PF_3)_2Cl_2$	55 mtorr	x			[101, 67]
Pt	$(CH_3)_3(C_5H_5)Pt$ or $C_5H_5PtMe_3$ or $CpPtMe_3$	54 mtorr	x			[59, 43, 11, 22, 103, 66]
	$(CH_3C_5H_4)(CH_3)Pt$	54 mtorr	x			FEI FIB200,[104, 76, 83]
SiO_x	$Si(OCH_3)_4$	420 mtorr		x		[54]
SiO_2	$Si(C_2H_5O)_4$	1.5 torr				[64, 120]
Si	SiH_2Cl_2					[44, 68]
W	$W(CO)_6$	17 mtorr	x			[62, 100, 99, 81, 90, 38, 53, 73] Micrion FIB
	WF_6				x	[44, 33]
C	C_8H_8 or $C_6H_5CH = CH_2$	10-25 torr				[32, 15]
	$C_{12}H_{26}$ to $C_{18}H_{38}$			x		[8]
	$C_{16}H_{10}$					[118]

Table 2.1: Physical properties of EBID/IBID precursors (S - solid, L - liquid, G - gas)

Mat.	Precursor chemical formula	Name
Au	$(CH_3)_2Au(hfac)$ or $C_7H_7F_6O_2Au$	dimethyl gold hexafluoro acetylacetonate (DMG (hfac))
	$Me_2Au(acac)$	dimethyl gold acetylacetonate
	$Me_2Au(tfac)$	dimethyl gold trifluoroacetylacetonate
	$AuClPF_3$	gold trifluorophosphine chloride complex
Al	$Al(CH_3)_3$	trimethyl aluminium TMA
	$Al(C_4H_9)_3$	tri-isobutyl aluminium
Cu	$Cu(hfac)_2$	copper hexafluoroacetylacetonate
	$(C_5HF_6O_2)Cu(CH_3)$	hexafluoro acetyloacetonate copper vinyl-trimethyl-silane
	$3SiCH = CH2)$	or HFA-Cu-VTMS
Cr	$Cr(CO)_6$	chromium hexacarbonyl
Fe	$Fe(CO)_5$	iron pentacarbonyl
	$Fe(C_5H_5)_2$	ferrocene
Mo	$Mo(CO)_6$	molybdenum hexacarbonyl
Os	$Os_3(CO)_{12}$	osmium carbonyl
Pd	$Pd(OOCCH3)_2$	Pd-Ac palladium acetate
	$Pd(C_3H_5)(C_5H_5)$	paladium allylcyclopentadienyl
Re	$Re_2(CO)_{10}$	rhenium carbonyl
Ru	$Ru_3(CO)_{12}$	ruthenium carbonyl
Pt	$(CH_3)_3(C_5H_5)Pt$ or $C_5H_5PtMe_3$ or $CpPtMe_3$	cyclopentadienyl-trimethyl-platinum
	$(CH_3C_5H_4)(CH_3)Pt$	methylcyclopentadienyl-trimethyl platimum
SiO_x	$Si(OCH_3)_4$	tetramethoxysilane (TMS)
Si	SiH_2Cl_2	dichlorosilane
SiO_2	$Si(C_2H_5O)_4$	tetraethoxysilane (TEOS)
	$W(CO)_6$	tungsten hexacarbonyl
	WF_6	tungsten hexafluoride
	C_8H_8 or $C_6H_5CH = CH_2$	styrene
	$C_5H_8O_2$	methyl methacrylate (MMA)
	$C_{16}H_{34}$	hexadecane
	$C_{12}H_{26}$ to $C_{18}H_{38}$	liquid paraffin
	$C_{16}H_{10}$	pyrene

Table 2.2: The chemical formulae and corresponding names for EBID/IBID precursors
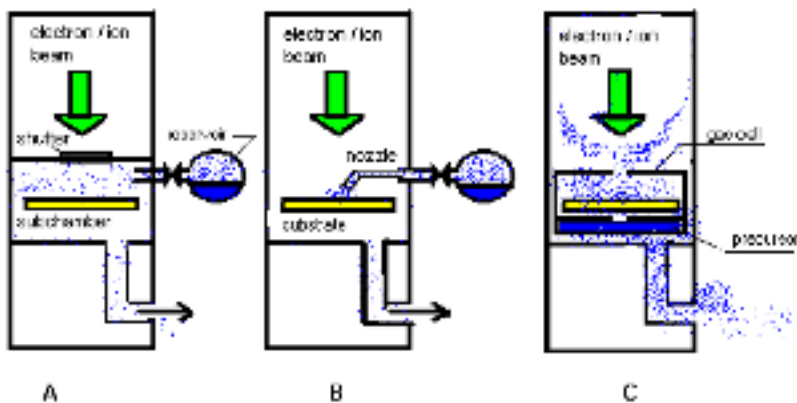
Figure 2-22: Different gas deposition system constructions. A- the differentially pumped sub-chamber; B - the capillary injection nozzle; C - the gas cell in an environmental SEM

translation stage. Examples of gas injectors systems (GIS) can be found in FEI focused ion beam tools like FIB200, FIB500 series and are produced and commercialized on small scale by for example Nawotec company [61, 43]. The positioning of the nozzle can be performed during SEM imaging with low magnification or under a video camera monitoring. Sometimes the precursor vapour is introduced in the system together with another carrier gas, for example O_2 [54].

The precursor molecular flow rate (throughput) in the system, Q can be controlled in three ways: with a variable leak valve, by choosing the dimensions and position of the nozzle, or by controlling the precursor reservoir temperature. The only restriction imposed on the molecular flow optimization is that the pressure in the working chamber, P may not exceed ca 1 x 10^{-5} torr. Usually the nozzle is a nonmagnetic steel or tantalum capillary with circular cross section of 0.2-5 mm diameter. Some authors tried to optimize the form of the nozzle section in order to maximize the molecular flow [51, 15]. For example, Kohlman calculated the effect of nozzle geometry on deposition parameters and found an optimal inner diameter at the end of the nozzle of $80\mu m$ with conically increasing diameter.

For example, a molecular flux on the specimen of 10^{18} $molecules/cm^2/s$ can be obtained with a nozzle of 0.8 mm inner diameter suspended at 0.2 mm above the substrate, with a vapour pressure of DMG precursor of 350 mtorr [9]. Typical nozzle parameters illustrated in Fig. 2-23 and the obtained molecular fluxes on the specimen are collected in Table 2.3.

The vapour molecular flow rate into the system, Q can be calculated as a function of the upstream pressure in the precursor reservoir P_{gas}, the nozzle length and diameter (L, d) and the pressure in the specimen chamber P [15] or it can be determined by solving the simple pumping speed relationship:

$$P = P_0 + \frac{Q}{S} \tag{2.4}$$

35
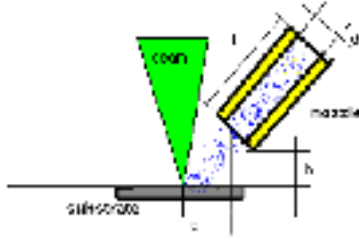
Figure 2-23: Illustration of nozzle construction parameters

Nozzle $d[mm]/$ $L[mm]$	Vertical $h[mm]$	Gas flow $[molec/cm^2/s]$	Precursor	Reference
0.8	0.2	10^{18}	DMG	[9]
0.254/13	1		C_8H_8	[15]
0.300	0.250/0.250	1.4×10^{16}	W(CO)$_6$	[38]
0.25/10	0.100	3×10^{19}	C_8H_8	[32]
3	5		WF$_6$	[44]
4	5		W(CO)$_6$	[50]
0.2	0.5		Si(OCH$_3$)$_4$	[54]
1.6	3		WF$_6$	[68]
0.080	0.05-0.250	10^{19}	W(CO)$_6$	[51]
0.7	0.4	8×10^{17}	C$_5$H$_5$Pt(CH$_3$)$_3$	[66]
0.5	1		W(CO)$_6$	[81]
0.2	0.2		Cl$_2$	[102]
0.260	4.2	8×10^{15}	WF$_6$	[36]

Table 2.3: Typical parameters for the gas feed nozzle

where P_0 is the base pressure in the deposition chamber measured before the gas introduction, S is the pumping speed for the gas in question and P is the pressure reading in the chamber after the gas flow is switched on and equilibrium is reached.

The pressure in the precursor reservoir P_{gas} can be sensed with a capacitance manometer. The pressure at the specimen cannot be measured exactly and usually it is sensed at some distance from the gas delivery point, by an ionization gauge. In some setups the pressure at the specimen can be measured more accurately, for example by replacing the sample holder with a stagnation tube connected to a capacitance manometer [9].

The first pressure tests can be done safely with N_2 introduction in place of the real precursor. The pumping speed S specified in the pumps manuals is given for water in case of cryogenic pumps and for N_2 in case of turbomolecular types. The correction for a specific precursor gas is done by:

$$S_{precursor} = S_{N_2} * \sqrt{\frac{M_{N_2}}{M_{precursor}}} \qquad (2.5)$$

where M is the molecular weight. A typical result of the N_2 test is shown in Fig. 2-24 for an EBL system modified to implement EBID. Note that in the shown situation the pressure in the gun and the stage mechanism chambers remains practically unchanged during the gas introduction in the specimen chamber.
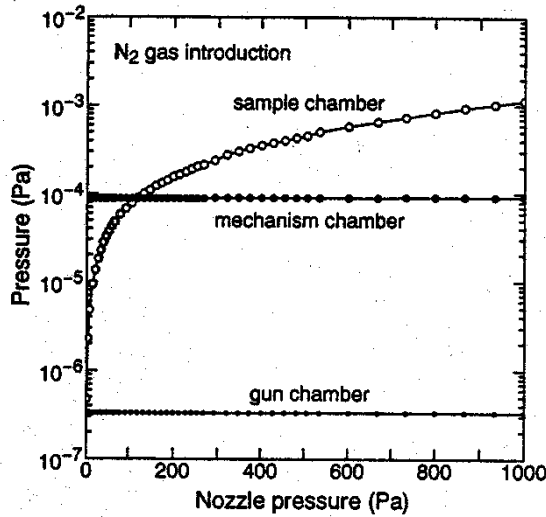
Figure 2-24: The pressure evolution in the deposition instrument as result of gas introduction (from [35])

The molecular flow can also be enhanced by resistively heating the precursor reservoir. A heat shield can be built around the reservoir in order to reduce the radiant heating of the

specimen [100, 93]. By varying the reservoir temperature, control over the vapour pressure is obtained and thus the influence of molecular flux on the deposition rate can be studied [51, 100, 113]. When considering the option of heating the gas delivery system, care should be taken to avoid condensation in colder places in the gas line. In order to avoid condensation, temperatures for the connection lines to the specimen chamber, the nozzle and the specimen have to be carefully maintained well above the temperature of the gas reservoir [78, 93]. It can also happen in some cases that the deposition yield does not depend strongly on precursor delivery pressure, like in the case of gold deposition from DMG by IBID [9]. In this case heating the gas delivery system would not be especially effective.

Variant C: The gas cell. [23]. Both gas delivery constructions with a subchamber (A) or with a nozzle (B) need modifications to the specimen chamber, which can be a technical inconvenience and a limitation in the normal functioning of the host microscope. To avoid these irreversible mechanical interventions, portable gas or wet cells should be designed. In order to study EBID, Folch [23] built a small 3.5 mm diameter cell, containing the liquid $Fe(CO)_5$ precursor and the specimen between two TEM apertures and the whole "sandwich" could be mounted on the specimen holder. The gas gets out through the apertures and eventually adsorbs on the specimen. The purpose was also to isolate the specimen from the residual vacuum, thus reducing the carbon contamination of the deposit. In order to avoid the vacuum constraints, an environmental SEM was used (1-3 torr pressure), but also a normal SEM has been previously used and the authors believe that the reactive gas cell can be used with precautions also in normal SEMs. Together with this experiment, a new concept of "environmental EBID" is introduced. More sophisticated and flexible gas cell constructions with variable apertures to control the gas flow will be necessary in the future.

2.2.2.7 Conclusion

EBID is most frequently studied in modified SEMs and EBL machines. Less often hosts like TEMs, STMs or dual beam instruments are encountered. IBID is used and studied in commercial or home-built FIB systems with lower optical resolution than the electron columns, but compensated by a higher reaction rate and more facilities necessary for IC surgery. The widest used gas delivery system at this moment is based on the nozzle injector, with perspectives towards environmental gas cells. The precursors commonly used are the organo-metallic compounds assimilated from the CVD technology. An actual trend is the search for new carbon free precursors.

2.2.3 Experimental results and theoretical models

To grow structures using direct electron or ion induced deposition is an encouraging step, but in most of the cases it turns out not to be sufficient. In some situations, the deposited structure has to be characterized. Its analysis is required, in order to evaluate the performance of the experiment and to present arguments in promoting or rejecting the chosen approach. In other situations, a theoretical model is welcome, that can explain the obtained experimental results. Both the analysis results, as well as the theoretical models create the environment necessary to understand EBID.

The analysis regards the electrical properties of deposited material, its microstructure, the chemical structure or the basic geometrical parameters such as thickness, growth rate and lateral size.

For each of these properties, our literature review will use the following scheme. First ideal values required by a high quality EBID are given. Then the methods and instruments used to measure the deposit properties are summarized. Relevant experimental results and numerical values encountered by different authors will be given. Also major theoretical models issued in order to explain and support these experimental results are described.

The EBID/IBID models operate with three basic entities: the substrate, the precursor vapors and the focused charged particle beam. It is a complicated triangle of interactions, precursor-beam-substrate, that governs the deposition process. The details of electron or ion beam induced deposition are still not completely understood. Firstly, the particle induced dissociation mechanism is complex and difficult to model because of the huge number of excitation channels possible even for small molecules. The presence of the substrate complicates the problem, because it creates new molecular dissociation paths and surface processes like diffusion, migration, desorption etc. The IBID modelling is even more complicated, because sputtering by ion beams occurs simultaneously with material deposition. It is difficult to identify the main causes of molecular dissociation among the electronic or vibrational excitations, the secondary electrons or the primary electrons. That is why no analytical solution for the modelling problem is possible without gross approximations. Models that partially work are built though, based on experimental observations.

In the conclusion we summarize some recommendations for a better quality beam induced deposition, where the experimental values would approach the ideal ones.

2.2.3.1   The electrical properties

Because EBID and IBID are expected to be mainly used for device manufacturing and wiring, it is necessary to produce deposits with low resistivity, as close as possible to the bulk metal values, which are for example for pure gold 2.2 $\mu\Omega cm$, for copper 2.05 $\mu\Omega cm$, for tungsten 5.5 $\mu\Omega cm$ and for platinum 10.6 $\mu\Omega cm$. For the deposition of insulator material, a resistivity value higher than 1 $M\Omega cm$ and a breakdown voltage higher than 10 V is required.

The electrical resistivity $\rho = RA/L$ can be determined by depositing lines or rectangles between pre-evaporated metal contacts (Au, W, Al or NiCr) (see Fig. 2-25) and by measuring their electrical resistance R, length L and cross-section area A. The area of the cross section can be determined by cleavage of the deposit. The resistance can be measured using a current voltage (I-V) method in two- or four-probes arrangement (Fig. 2-26). The two-probes arrangement is accurate enough when measuring resistances much larger than the resistance of an ohmic contact. But for lower resistances, less than 0.1 Ω, the voltage drop on the contacts cannot be neglected without considerable measurement errors. The four-probes arrangement is in this case recommended as a more accurate resistance measurement method.

More reliable results can be obtained if the film resistivity can be measured in-situ, by avoiding possible changes in conductance because of exposure to atmosphere [38].

In the following, a few resistivity results obtained by different authors using EBID and IBID are presented, sometimes followed by suggested explanations.

Gold, tungsten, copper, platinum or contamination lines have been deposited in order to study their electrical properties. The first effect observed in all cases is that the resistivity of deposited lines is higher than the bulk value. The resistivity of tungsten film deposited by IBID from W(CO)$_6$ is 600-800 $\mu\Omega cm$ [50] and 150-200 $\mu\Omega cm$ [99]. These values are still larger than the bulk tungsten value, but sufficient for IC repair. Also good STM images can be obtained with contamination grown tips [1]. It means that, without being a tragedy for some applications, the high resistivity is a drawback of the direct deposition method. For example,
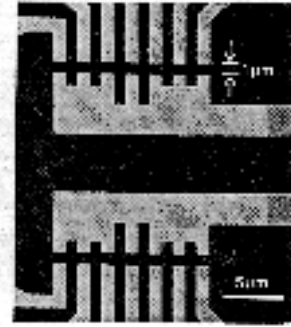
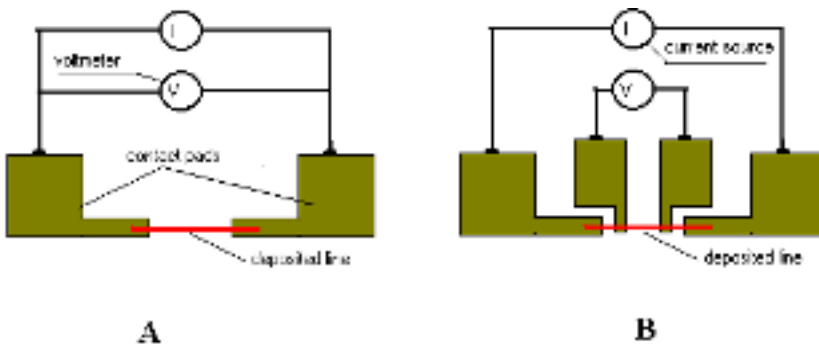Figure 2-25: Prefabricated contacts for resistance measurement (from [36])

Figure 2-26: Two or four probes arrangement schemes for resistance measurement

gold has been deposited by IBID from DMG with resistivities of 500-1500 $\mu\Omega cm$, also much higher than the bulk resistivity of pure gold. [9] . Koops [62, 60] used EBID to deposit tungsten from $W(CO)_6$. The tungsten deposits, bars of 2 μm length and 400 nm width, had a resistivity measured in four point measurement of 0.02 Ωcm, more than 4 orders of magnitude larger than bulk tungsten. Morimoto [76] measured the resistivity of Pt tips grown on SiO_2 wafers and he obtained 30 $\mu\Omega cm$, three times more than bulk platinum value. It is observed that the situation improves by modest substrate heating, when the obtained resistivity reaches the bulk values. Schössler and Koops [94] observed that by annealing the Pt containing resistors their resistivity reduces by 3 orders of magnitude and their value stabilizes.

Some authors observed that lower resistivity values could be obtained at higher exposure currents. Ochiai formulates slightly different the same dependence: a low resistivity can be obtained with a high current density [79]. Copper lines are deposited using EBID from HFA-Cu-VTMS in a ESEM and the lowest resistivity reported is 3.6 $\mu\Omega cm$, only two times larger than the bulk pure copper value. This result is explained by the very high current density exposure 1270 A/cm^2, created by a 1 nA beam focused in a 10 nm spot. Tao [104] used IBID to deposit platinum films and the resistivities were in the range of 70-700 $\mu\Omega cm$, decreasing with higher current densities. We think that it is a more correct formulation to relate the resistivity to the curent density. The reason for this dependence is not found yet.

The resistivity of the deposited lines depends also on the beam scanning conditions, i.e. the exposure dosis per pixel $[C/m^2]$, the dwell and loop times. The electrical properties of tungsten lines deposited from $W(CO)_6$ using EBID have been measured by Hoyle [39, 37]. The resistance was measured with the two-probe arrangement, depositing a line in the 10-20 μm gap between two gold contacts predeposited on semi-insulating GaAs substrate pads. The measurements show resistivities of 3000 $\mu\Omega cm$ obtained with a 5 kV electron beam, 1 nA probe current and fast scanning, while resistivities 40 times smaller could be obtained from slow scan conditions, proving that fast rastering is not suitable for low resistivity interconnects. Hiroshima and Komuro [33] used EBID in a 50 kV SEM to deposit tungsten from WF_6 and also studied the influence of scanning conditions on deposit resistivity, with the same conclusion as Hoyle, that slow scanning decreases the deposit resistivity. Conductive wires have been fabricated with a width of 10-20 nm with the lowest resistivity of 600 $\mu\Omega cm$. Another conclusion is that three times higher doses improve the conductivity up to five orders of magnitude.

Other experiments have shown that the electrical resistivity depends on the beam energy used during deposition, in the sense that at lower impact energies, lower resistivities are obtained. For example the decomposition of $W(CO)_6$ by 1 keV primary energy produces four times lower resistivity material than under a 20 keV beam. The lowest value, 600 $\mu\Omega cm$ is obtained for the impact energy of 0.25 keV, still two orders of magnitude larger than the bulk tungsten resistivity [39, 37].

An accepted explanation for the high resistivity of deposited materials blames the carbon impurities included during deposition. Because one of the sources of contamination seems to be the specimen itself, a condition to obtain a low resistivity deposit is to carefully treat and clean the sample. Experiments using FIBDD can provide much better results of Au, Cu and Al films with low resistivities 1.2 - 2.2 times larger than the bulk values, due to very low residual pressure. This result underlines also the importance of a clean ambient in obtaining low resistivities [77]. Folch [23] succeeded to reduce the carbon content by building a gas cell which includes both specimen and the liquid precursor $Fe(CO)_5$. The precursor is isolated by two TEM apertures, so that contaminant residual gases cannot easily reach and adsorb on the specimen. Another way to obtain pure deposits with low resistivity is to use carbon free precursors.
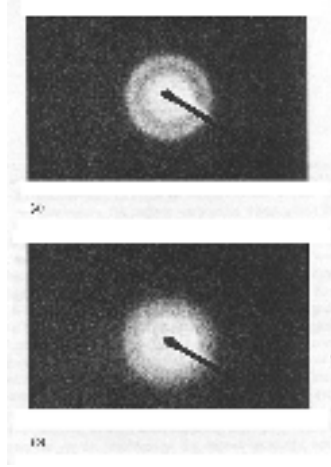
Figure 2-27: Transmission electron diffraction pattern of film deposited with a) a high dose 10000 C/m^2 and b) a low dose 5 C/m^2(from [38])

2.2.3.2   The morphological properties

The structure of the deposit may have an impact on the ultimate achievable fabrication resolution. For example, if the material is crystalline, the minimum obtainable feature size will be limited to the size of the nanocrystals.

The widest used techniques to determine the microstructure or morphology of the deposited material are high resolution electron microscopy (HREM) and the electron diffraction analysis in TEM. In order to be inspected in a TEM, the structures are deposited usually on a thin 3 mm diameter TEM carbon or Si$_3$N$_4$ membranes or they are grown as free-standing structures in open space, across holes in membranes or blank TEM meshes.

It is confirmed by TEM diffraction analysis that contamination growth usually deposits amorphous material [1]. The structures resulted from metal EBID can be amorphous or crystalline, depending on the exposure conditions. Hoyle [39, 37] studied EBID from $W(CO)_6$ in a TEM. Micrographs and diffraction patterns showed that the structure of 10 nm thick tungsten film is continuous and depends on the exposure dosis used. A low dose (5 C/m^2) gives amorphous structure (see Fig.2-27b)), while a higher dose (1000 C/m^2) deposits a polycrystalline structure, with crystals of less than 3 nm in diameter (see Fig.2-27 a)). The crystals are probably high temperature crystalline β-phase of tungsten carbide βWC_{1-x}. The continuous structure differs from that of films produced by IBID from the same W(CO)$_6$, which were reported to have discontinuous island structure for thickness up to 23 nm.

An in-situ observation of EBID can suggest a possible deposition mechanism. For example, Ichihashi [44] performed in-situ EBID observation from WF_6 and SiH_2Cl_2 in a TEM. This host microscope allowed to record successive electron micrographs of the deposit during the beam exposure, suggesting the following mechanism: First the adsorbed WF_6 dissociates under the beam impact in W and F$_2$. The deposition starts when clusters are formed, consisting of 3 nm β-W crystals. After a while, under beam irradiation, the clusters coalesce into a film. The same WF_6 adsorbed on fine Si particles on carbon film, deposits larger clusters α-W. Diffraction
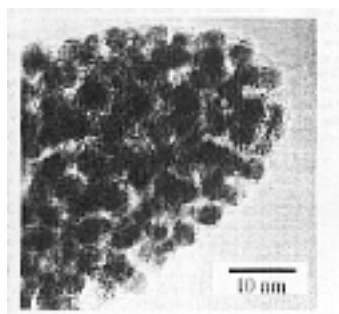
Figure 2-28: High resolution TEM micrograph of a tip grown by EBID that reveals the nanocrystallinity of material (from [96])

analysis shows that a Si layer formed from SiH_2Cl_2 is amorphous, probably because Cl atoms are destroying the crystallinity. In conclusion it is possible that other chlorine-free precursors like SiH_4 or Si_2H_6 would deposit crystalline Si.

From early stages, the TEM images in dark and bright field of deposited material by EBID and gold precursor showed small polycrystallites of Au of less than 5 nm in diameter [65]. Dubner [19] applied diffraction analysis on the results of IBID using DMG and also found that gold islands with 30 - 40 nm size are formed, randomly oriented in a carbon matrix.

Koops [60] used EBID to deposit gold from $Me_2Au(tfac)$ and $Me_2Au(acac)$ in a SEM, and also discovered a new class of nanocrystalline compound materials. The morphological information about this material is obtained by TEM at 100 - 400 kV and reveals metal or metal carbide crystallites of a few nanometers size, immersed in an amorphous carbonaceous matrix (see Fig. 2-28).

A more detailed analysis can be obtained by imaging the lattice planes of the deposited nanocrystallites. It has been found that the lattice planes of the crystallites have a lattice period of 0.233 nm, compared with 0.235 nm known from the literature for gold single crystals. The difference in structure obtained from the two different gold precursors is found to be negligible.

Diffraction patterns of deposit from $Me_2Au(tfac)$ show cubic fcc structure. The elementary lattice cell of the crystallites is 0.401 nm, while the base cell unit for gold is 0.408 nm. It results that the crystallites are mainly gold and the amorphous material in which they are embedded is carbon.

Koops also used EBID to deposit Pt from $CpPtMe_3$ and used the same two analysis methods, TEM and diffraction analysis. The lattice spacing is 0.231 nm for (111) and 0.196 nm for (200) planes. This is in good agreement with the platinum bulk values from literature. The diffraction analysis shows a face-centered cubic fcc structure of the elementary cell, with a lattice constant of 0.392 nm, corresponding to 0.3924 nm for bulk platinum. This agreement is the confirmation that the deposit contains Pt nanocrystals.

Interesting properties for field emission from EBID tips are concluded because the lattice distances are the same as the bulk material.

43
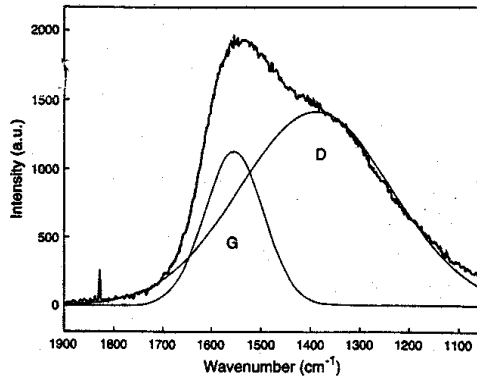
Raman spectra of FIB-CVD film

Figure 2-29: Raman spectra of a diamondlike amorphous carbon film deposited by IBID. The decomposed bands are shown in G - graphite and D diamond in solid lines (from [71])

2.2.3.3 The chemical structure analysis

Once the deposit is formed, it is also interesting to determine its chemical composition, to see how much metal it contains and to determine what causal relation exists between a certain composition and the conditions in which it has been deposited. A high quality deposition process has to create highly pure crystalline materials. The deposition from organometallic compounds has to create a high percentage of metal and a low percentage of carbon. The information about the composition can also offer some clues for a better understanding of step-by-step deposition mechanisms.

In order to detect different elements in the deposits composition, a series of spectroscopic methods are currently available, like Auger electron spectroscopy (AES), X-ray microanalysis (XMA), energy dispersive x-ray analysis (EDX), Raman spectroscopy (RS), secondary ion mass spectrometry (SIMS), X-ray photospectroscopy (XPS), etc. Because the spatial resolution of these microprobe analysis methods is about 1 μm, lower than the fabrication resolution in SEM and TEM, the analyzed deposited structures have to be large enough to be detected. For this purpose, rectangles have to be deposited instead of small dots or lines, and in case of small tips inspection, a wide band of tip material has to be mounted on a substrate and then analyzed.

Tips grown by contamination in a SEM or FIB, using as precursor the residual vacuum, have been analyzed by Auger spectroscopy showing carbon and oxygen, as expected from residual gases present in the microscope. The Raman spectroscopy revealed amorphous carbon a-C with sp^3 and sp^2 hybrids, corresponding to the bonding structure of diamond, respectively graphite (see Fig.2-29) [45, 71]. Castagne obtained a mass spectrum of carbon supertips grown in SEM from residual vacuum, which showed carbon, oxygen, and silicon atoms but also atomic hydrogen and complex carbon hydride molecules $^{12}C_2,^{12}CH,^{12}C_2H,^{13}C,^{12}C,^{13}C$, with no evidence of nitrogen or metal doping [12].

The deposits from tungsten precursors have been analyzed by Auger and X-ray analysis. The deposits using EBID and $W(CO)_6$ contained tungsten carbide and up to 75% tungsten but typically 55% W, 30% C and 15% O [38, 60, 49]. The deposits obtained by H_2^+ and Ar^+ ions

irradiation from the same precursor contained more tungsten, typically 75% W, 11% O and 14 % C, (see Fig.2-30). The disadvantage of IBID is the gallium implantation in the deposit. When Ga $^+$ ions were used, the deposit contained 70-75% tungsten, 10% carbon, 10 % gallium and 5-10% oxygen [100].
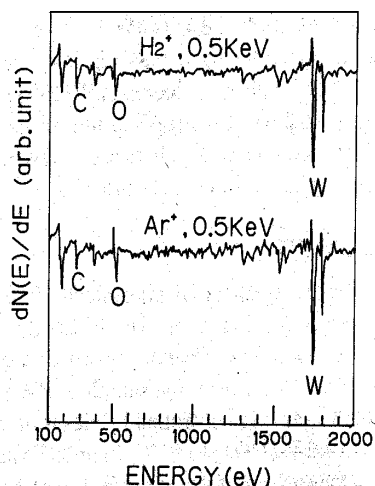
Figure 2-30: Auger spectra for films deposited by IBID with H_2^+ and Ar^+ ions (from [50])

These results can suggest a possible mechanism of electron beam deposition. For example, it is known from the organometallic chemistry that in the $W(CO)_6$ molecule, the bond energy between W atom and CO ligand is smaller than that between C and O atoms in the carbonyl group. Because the measured contents of C and O in deposits are equal, probably the C and O atoms come from the incomplete decomposition of the precursor and not from the ambient. The suggested decomposition products of $W(CO)_6$ are $W(CO)_{6-x}$ and $x(CO)$, (x = 1..6) which partially desorb from the surface.

The XPS data from the deposited and bulk tungsten are quite the same.

Different precursors containing the same metal can deposit different metal purity. For example a higher purity deposit is obtained from WF_6 than from $W(CO)_6$.

A trial to deposit Pt resulted in tips with 21.5 % Pt, 73 % C and 5.5 % O [76]. Pt films deposited by Ga$^+$ FIB are amorphous and their Auger analysis shows 46% Pt, 24% C, 28% Ga and 2% O [104].

Copper precursor HF-Cu-VMS used in EBID gives a copper contents of 10-20 %, with a percentage ratio in the deposit of Cu :C :O : Si : F = 1 :5 : 0.5 : 3 : <0.1. This ratio is different from the percentage ratio in the precursor, which is 1 :10:2:1:6. Comparing these results, it looks like C, O, and F content decrease, and Si percentage increases. The possible explanation could be that the SiO_2 substrate also decomposes under electron beam irradiation [79].

Kislov [49] using EBID followed by annealing from chromium and rhenium carbonyls, analyzed in diffraction mode the deposits and found that Cr rods contained some unidentified phases beside metal phase, but the rhenium deposits contained only one crystalline metal phase. In conclusion $Re(CO)_6$ has been promoted as an attractive precursor material for micro-engineering.

45

The deposits by EBID from gold precursors Me_2Au (tfac) have been analyzed by Auger, EDX and ion mass spectroscopy and showed 40% gold, 55% carbon, 1,5% oxygen and <5% rest [62].

It is observed that the gold content rises with the beam current as it can be seen in Fig. 2-31.
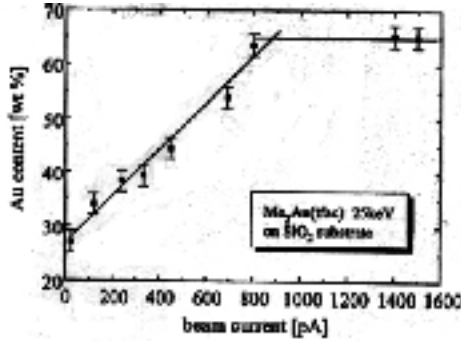
Figure 2-31: EDX analysis of material deposited by EBID from $Me_2Au(tfac)$ [from [60]]

Apparently the metal composition does not depend on the beam energy. Lee used EBID from $Me_2Au(tfac)$ by 30 keV electrons irradiation and obtained a content of 75% Au and 25% carbon. The film composition was similar for different beam energies : 2 keV, 5 keV and 30 keV [65].

2.2.3.4   The geometrical parameters

2.2.3.4.1   The thickness and growth rate   The growth rate or deposition rate is defined as the time gradient of thickness and it is usually expressed in EBID / IBID studies in nanometers per second. As a convention, the positive rate is adopted in case of net deposition and a negative rate is adopted for etching. Important for a deposition method to be qualified for industrial processes is a high throughput, expressed in wafers per hour. This requirement is translated in our case to a high deposition rate.

The thickness of deposited film can be measured in a SEM, by highly tilting the sample with more than 75 degrees [81, 62], by stylus profilometry [39, 62, 65, 70, 32, 50] or by scanning probe profilometry. Structures lower than 20 nm can be imaged by scanning probe techniques, like AFM [34, 56, 55, 111]. In case of etching, the depth is the equivalent of thickness and it can be measured with a diamond stylus moved over the sample surface [102].

Another way to measure the thickness of the deposit is by using the Auger signal from the deposited film. Matsui [68] gives a relation between the Auger signal intensity and the deposited film thickness. The normalized Auger intensity J, detected from a film in the case of applying a cylindrical mirror analyzer (CMA) as Auger electron detector is given by:

$$J = 1 - e^{-\frac{d}{0.75\lambda}} \tag{2.6}$$

where d is the deposited film thickness and λ is the electron mean escape depth. The deposited thickness d is proportional to the electron dose, which is proportional to the exposure time t if the current is maintained constant. Therefore the deposited film thickness d becomes:

$$d = Rt \tag{2.7}$$

where R is the EBID growth rate. Substituting, the relation becomes:

$$\ln(1 - J) = -\frac{R}{0.75\lambda}t \tag{2.8}$$

The values for the electron mean escape depth λ have been reported and empirical formulae have been issued. Therefore, the EBID growth rate R can be determined by measuring a relation between the normalized Auger intensity, J and the electron beam exposure time, t.

The relation between the growth rate and the deposition parameters has been experimentally and theoretically investigated by many authors.

Kohlmann calculated the deposition rate as a function of the current density of the primary beam with as variable parameter the gas flux on the surface (see Fig. 2-32).
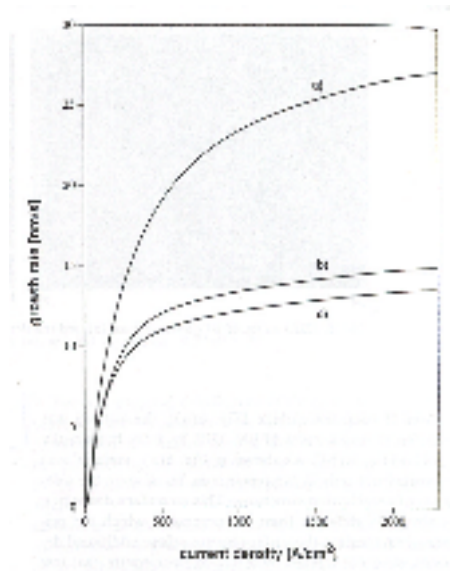
Figure 2-32: The calculated growth rate in EBID vs. current density for different gas fluxes; (a) 2 $\times 10^{17}$, (b) 1 $\times 10^{17}$,(c) 9×10^{16} cm^{-2}s^{-1}[from [52]]

The experimental results show that the deposit thickness is proportional to the irradiation time and the total dose. This is in agreement with the contamination observations, when the growth rate is proportional to the exposure time, provided the molecular supply is sufficient.

The growth rate increases with decreasing beam energy at a constant dose per scan, being 3 times higher at 2 kV than at 20 kV beam energy [38].

The growth rate for EBID can be about 1- 10 nm/s. Hubner [43] for example obtained 8.4 nm/s in SEM with Pt precursor. FIB give higher growth rates compared with EBID as large as 20 nm/s for small areas, as reported by Petzold for $W(CO)_6$ [81].

The deposition rate depends on the dwell and refresh times, and the curve shows a maximum. This dependences have been experimented by Petzold [81] (see Fig. 2-33 and Fig. 2-34) for IBID.
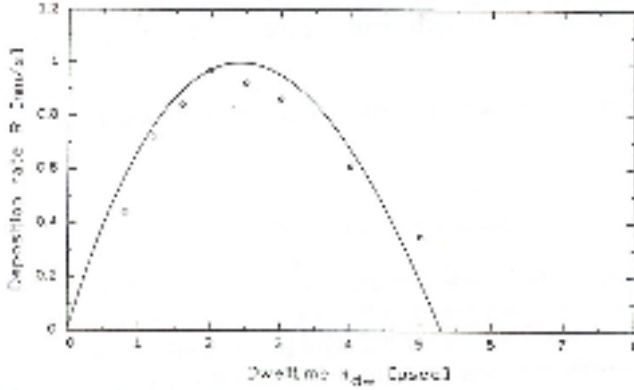
Figure 2-33: Deposition rate in IBID versus dwell time [from [81]]
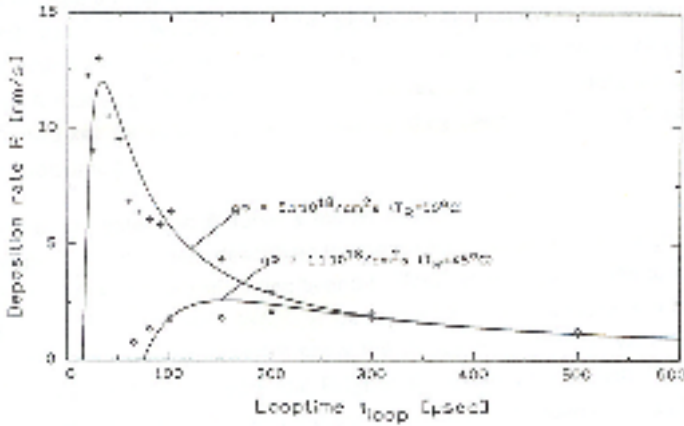
Figure 2-34: Deposition rate vs. loop time [from [81]]

The deposition efficiency or the deposition yield, defined as the number of deposited atoms per incident ion/electron, depends on the substrate, incident particle type and energy, as well

as the nozzle position. An example of high deposition efficiency of copper equals 2×10^{-2} atoms/electron [79], and tungsten deposition from $W(CO)_6$ could be obtained with an yield of 5×10^{-2} atoms/electron [62].

FIBD with 15 kV Ga^+ ions and gold precursor gives deposition yields of 4-5 atoms/ion, 1 atom/ion for Ar^+ ions at 0.75 kV and 8-16 atoms/ion with Si^+ ions at 50 keV [97]. IBID with 25 kV Ga^+ with $W(CO)_6$ has a deposition efficiency of 1-2 W atoms per incident ion .

The deposition yield is proportional to the precursor pressure around the specimen (see Fig.2-35). The dependence vs. the specimen temperature is also shown in Fig. 2-35. In ESEM, the condensation at 20°C increases the deposition yield about 20 times compared with 25 °C with a precursor pressure of 150 Pa.
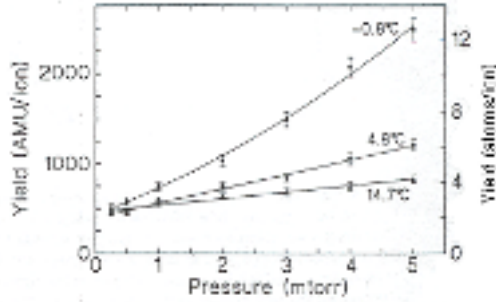
Figure 2-35: The deposition yield of IBID as function of DMG gas pressure and specimen temperature [from [18]]

Dubner published a list with ion beam induced deposition yields. For example from WF_6, 750 eV Ar^+ ions with a current density of 0.0004 A/cm^2 created an yield of 5 atoms/ion [17]. Blauner deposited gold using IBID on SiO_2 with a yield of 5.8 atoms/ion and a growth rate of 1.1 nm/sec. The current density was 180 $\mu A/cm^2$.

The theory of the growth rate is supported by a series of models, based on the following one, proposed by Scheuer.

Scheuer [93] proposes a phenomenological model of the growth process in a flood beam EBID system, supposing that only one gas monolayer is adsorbed on the surface and that only the molecules adsorbed in the beam irradiated area will decompose. Fig.2-36 illustrates the different processes on the surface. The adsorption rate of the precursor gas molecules on the substrate surface is given by the rate equation:

$$\frac{dN}{dt} = gF * \left(1 - \frac{N}{N_0}\right) - \frac{N}{\tau} - \sigma_{diss} N J \tag{2.9}$$

and the growth rate of the layer, R is given by:

$$R = V \sigma_{diss} N J \tag{2.10}$$
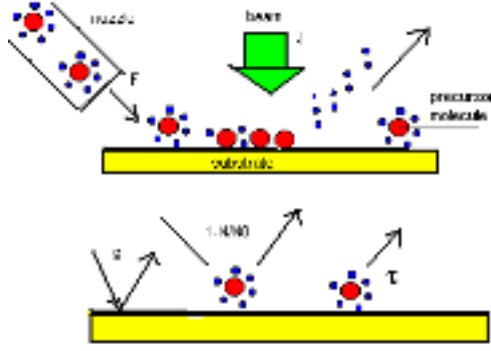
Figure 2-36: The illustration of surface processes in EBID modelling

where

N = the density of adsorbed molecules or the surface molecular coverage $[\#/cm^2]$

N_0 = the density of available adsorption sites in one monolayer $[\#/cm^2]$

g = the sticking coefficient of gas precursor on the target

F = the precursor molecular flux $[\#/cm^2/sec]$

τ = the mean life time of adsorption $[sec]$

σ_{diss} = molecular dissociation cross-section under electron impact $[cm^2]$

J = electron flux on the surface $[\#/cm^2/sec)]$

R = the layer growth rate $[cm/sec]$

V = the volume occupied by a dissociated molecule or its fragment $[cm^3]$

The first term in equation (2.9) governs the precursor adsorption on the surface, the second term represents the loss by spontaneous thermal desorption in the gas phase with the time constant τ and the third term corresponds to the electron induced dissociation rate of adsorbed molecules.

The steady state growth equation will be reached for $dN/dt = 0$, when the density of adsorbed molecules at equilibrium will be:

$$N = N_0 \frac{g\frac{F}{N_0}}{g\frac{F}{N_0} + \frac{1}{\tau} + \sigma_{diss}J} \tag{2.11}$$

and the growth rate in steady state R can be determined by :

$$R = VN_0 \frac{g\frac{F}{N_0}\sigma_{diss}J}{g\frac{F}{N_0} + \frac{1}{\tau} + \sigma_{diss}J} \tag{2.12}$$

From the equation (2.12) we can see that the growth rate is the result of a competition between two fluxes: the electron flux J and the molecular gas flux F, such that two situations are possible: the growth limited by the gas flux or the growth limited by the beam current.

We can see that the growth rate depends on the residence time of molecules on the substrate, τ. It confirms the experimental observations by Stewart in IBID showing that cooling the specimen increased the growth rate [100]. The maximum rate obtainable for any given electron flux is proportional to the current density on the surface:

$$R_{\max} = V N_0 \sigma_{diss} J \tag{2.13}$$

If the deposited mass can be measured, then based on the relation (2.9) other deposition or precursor parameters can be determined. Scheuer [93] measured the deposited material mass and thus the growth rate R and determined other unknown parameters, like the mean relaxation time for Os and Re carbonyls $\tau = 1.4 \pm 1$ sec and the deposition yield of $1/280$ atoms/electron.

Koops [62] uses the same model to optimize the EBID growth rate and gives a numerical example for $W(CO)_6$ precursor. For 20°C specimen temperature and a precursor pressure in the subchamber of 2 mtorr, the molecular flux is $F = 2.2 \times 10^{17}$ $molecules/cm^2/sec$. Some typical values are assumed, like the sticking coefficient g = 1, the dissociation cross section of $W(CO)_6$ of 2×10^{-17} cm^2 and the volume of a deposited tungsten carbide molecule $V = 7.3 \times 10^{-3}$ nm^3. In these conditions, the maximum growth rate from equation (2.12) is R = 82 nm/sec and it needs an electron flux of $J = 1.5 \times 10^{20}$ $electrons/sec$, i.e. a current density of 24 A/cm^2, which is a feasible value.

The model of Scheuer can be also used for IBID, if an extra term Ys is added, which takes into account the effect of sputtering of substrate atoms [19, 9]. The deposited material results then from a competition between the deposition and sputtering, and the net deposition yield Y_D, expressed in [atoms per incident ion] is:

$$Y_D = N\sigma_{diss} - Y_s \tag{2.14}$$

where
Y_s = the sputtering yield $[atoms/ion]$.

The first term in (2.14) depends on the gas pressure, substrate temperature and the gas-substrate interaction, the second term depends on the ions energy and mass and on the ion -substrate interaction.

Using the adsorbed density on equilibrium N from (2.11), we obtain an ion induced deposition yield in steady state conditions, Y_D:

$$Y_D = \frac{1}{\frac{1}{\sigma N_0} + \frac{1}{gF\sigma\tau} + \frac{J}{gF}} - Y_s \tag{2.15}$$

The deposition yield Y_D can be determined if the deposited material mass is measured, for example using a quartz crystal microbalance (QCM). The sputtering yield Y_s can be also measured. Using the model described above other ambiguous deposition parameters, like the molecular dissociation cross-section σ_{diss} can be determined. Dubner [18] determined this cross section for gold precursor DMG as equal to 2×10^{-13} cm^2 for IBID with 5 keV Ar^+ ions. In the same article it has been also measured that the deposition yield increases with increasing gas pressure and decreasing substrate temperature (see Fig. 2-35).

An earlier steady state model of IBID can be found in [88], where sputtering is neglected and the growth rate for IBID is calculated as a function of beam energy, gas pressure and current density.

Petzold [81] and Harriot [31] extended the Scheuer model for scanned beam FIBD systems and modelled the growth rate as a function of dwell time and refresh time.

Edinger [21] improves the Petzold model by considering a Gaussian beam current density distribution instead of a uniform one. The etching rate is expressed as function of the dwell and refresh time and the model is tested for gas assisted etching (GAE) of Si with Cl_2 and I_2.

Hoyle [39] developed the intermediate product model for EBID. He uses the Petzold model adapted for EBID and divides the precursor conversion process in two main stages, with two different products, having different carbon contents and resistivities. The first step is the dissociation of $W(CO)_6$ in an intermediate product with high resistivity and the second step is the conversion of this intermediate product into a final product, of low resistivity. From this model it results that a faster scan produces higher volume rates, but the resulting material has higher resistivity not suitable for the production of electrical interconnects. This conclusion coincides with the experimental observations of many authors (see 2.2.3.1). The two growth rates R_1 and R_2 are calculated as a function of the dwell and loop time. By fitting the model with the measured thickness of the deposit, a value for the sticking coefficient of $W(CO)_6$ of g = 0.32 and the electron induced dissociation cross section of $W(CO)_6$ molecules in the intermediate product is found $\sigma_1 = 2.2 \times 10^{-18} cm^2$ and $\sigma_2 = 1.5 \times 10^{-18} cm^2$.

2.2.3.4.2   The lateral size and the fabrication resolution.   Especially now, when the miniaturization process develops so rapidly, it is important to estimate the lateral size of the deposited structure, i.e. the resolution of the fabrication process. Without being a fast method or extremely high purity deposition method, EBID can gain credibility if it demonstrates a high fabrication resolution. Values that are considered promising at this moment are situated in the 1 nm-20 nm range, where other beam induced conventional lithography methods encounter difficulties.

The experimental resolution is usually described by the diameter of a singular dot, grown by a stationary focused electron probe or by the width of a singular line deposited by a scanned probe. For nanolithography application, the line width and the line spacing are the most important features. In conventional PMMA resist based electron lithography, the smallest center to center distance obtained is 30 nm and isolated features of 5 nm have been produced, although the smallest useful structures have been closer to 20 nm.

The lateral sizes in EBID are most frequently measured by high resolution electron microscopy imaging of the tilted specimen, SEM or TEM. If subnanometric structures will be ever deposited, the TEM might be preferred due to its much better imaging resolution, with the disadvantage that the target can be only very thin, less than 100 nm.

Another modality to measure the lateral size is to image the profile of a structure with an AFM. In order to eliminate ambiguities generated by the finite apex radius of the tip, it is necessary to deposit more sets of lines and average the profile data.

The lateral size of the deposited structures is in first approximation determined by the probe diameter. However, experiments have shown always structures larger than the diameter of the writing electron probe, and the multiple reasons of this broadening are not completely understood yet. One thing, however, is well established, i.e. the temporal evolution of the dot diameter in time. Initially the dot grows very fast and after a time of the order of minutes it reaches a saturation value (see Fig.2-37). The EBID fabrication resolution is thus not a constant

value. Most of the experimentally reported values are probably measured at the moment when the saturation stage of the growth has been reached.
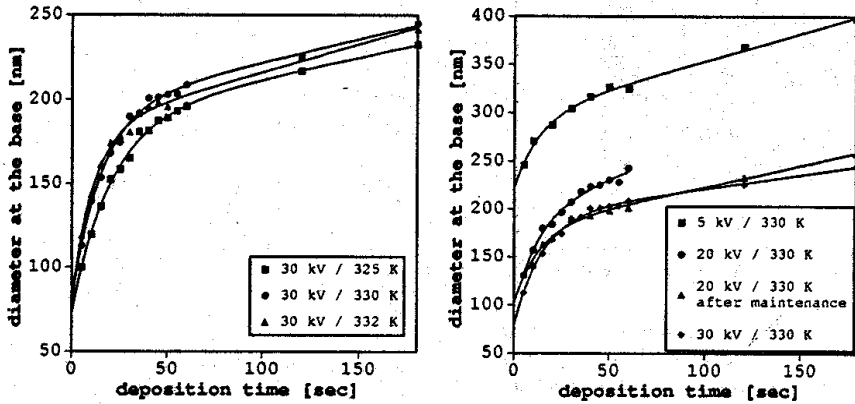
Figure 2-37: The dot diameter evolution in time (from [53])

The lateral fabrication size depends on the probe current, i.e. a lower current deposits narrower lines. Miura [74] used contamination growth in a 30 kV SEM and obtained high aspect ratio and narrow wires of 30 nm width for less than 40 pA current exposure, (see Fig.2-38). The information in this graphic is quite poor and ambiguous, because it is not clear the time that was necessary to grow these lines. The width grows in time until it reaches saturation and it is important to mention at what moment the measurement has been made.

Does the fabrication resolution depend on the beam energy? Experiments with different beam energy have been performed to observe its influence on the resolution. In depositing vertical tips with the same electron beam of 10 nm spot diameter, it is observed that by increasing the beam energy the width and cone apex radius of the grown tip decreases approximately with 10% at each 10 kV increment in beam voltage. It means that the tip shape is determined by forward scattered electrons at the apex of the deposited material. In conclusion better resolution can be obtained with higher beam voltage. Also experiments of Hubner [42] confirm that higher acceleration energies produce better lateral resolution.

The spacing depends on the so called proximity effect, which is low when the energy of electrons is low or when the specimen is thin and the electron energy very high. So there are two ways to obtain high resolution in EBID: to use it in a STEM with high beam energies and thin specimens or use it in STMs, by means of low energy electrons.

EBID and contamination growth have been investigated in STMs where it was possible to fabricate very small individual dots and narrow lines.

For example Uesugi used a STM with an electron beam size from the tip estimated as 0.4 nm and a negative biased tip. He obtained holes in graphite of 2.5 nm diameter and 0.7 nm depth in the center, using a bias voltage of -5 to -10 V in air. The probable reaction of the hole
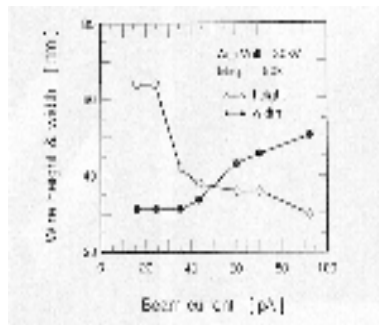
Figure 2-38: The dependence of the width of a carbonaceous wire on the electron beam current [From [74]]
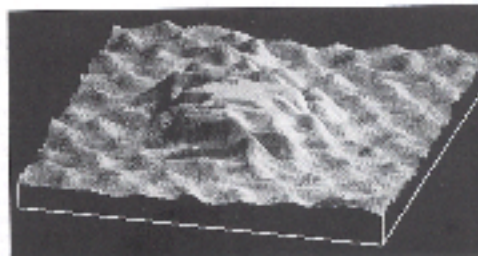
Figure 2-39: Contamination dot 0.8 nm diameter and 0.7 nm high, deposited in a STM (from [106])

drilling is the removal of carbon atoms from the target :

$$C(graphite) + O_2 \rightarrow CO_2$$
$$or\ C(graphite) + H_2O \rightarrow CO + H_2$$
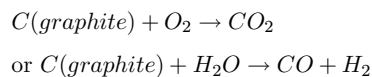
Organic molecules have been introduced in STM to produce carbon nanoscale structures [20]. Contamination deposition from acetone and hydrogen mixture produced an individual carbon dot of 0.8 nm in diameter and 0.7 nm in height, with a pulse of -4V of 50 μs applied to the tip (see Fig. 2-39).

Organometallic precursors have been used to deposit different metals in STM (W, Ni, Au, Rh). Wang used STM CVD with $Ni(CO)_4$ to fabricate 18 nm base wide (9 nm FWHM), 6 μm long and 4.5 nm high Ni nanowires on H-passivated silicon Si (111) surface [109]. The beam diameter is approximatively 10 nm, depending on the radius of curvature of the tip. The secondary electrons did not play an important role because the electron beam from the tip has not enough energy to excite them. It is an interesting observation for us, because it results that structures with the same diameter as the primary beam are obtained if no secondary electrons

54

are emitted to laterally enlarge the structure.

Szutnik [101] performed STM assisted CVD with $Rh(PF_3)_2Cl_2$ and very sharp optimized tips, with radii between 2 and 4 nm, making possible very small separation between adjacent deposited dots. Depending on the size of the tip and its shape, nanometer scale rhodium islands with separation down to 1.5 nm were obtained. In Fig. 2-40, 3 nm wide islands aligned with a separation of about 4 nm and 1.5 nm are shown.

Marchi [67] used STM assisted CVD with $Rh(PF_3)_2Cl_2$ to deposit Rh on gold coated mica substrates. The dot diameter has been measured as 3 nm and the spacing was 4 nm. The same experiment on a silicon surface could deposit a rhodium line, 17 nm wide and 5 nm high. The best resolution result of EBID in STM is obtained in deposition of magnetic material, where 5 nm FWHM and 2 nm high lines could be deposited from $Fe(C_5H_5)_2$ [80].

Surface oxidation induced by a SFM tip is also possible. The first report of tip induced oxidation of silicon was of a STM study by Dagata [14] Also oxidation induced by an AFM tip has been observed and GaAs oxide nanowires with 10 nm width could be fabricated [72]. There are important advantages in using AFM configuration rather than tunnelling based instruments, because the topographic viewing of the substrate does not induce exposure of the resist.

In conclusion low energy electrons deposition in STM can produce very small structures (1-10 nm), but they have also very small heights (1-10 nm). The diameter of the electron beam in STM is impossible to be measured accurately. STM images provide an idea of the topology of small structures, but it is not possible to discern their composition or crystalline phase.

Another conclusion is when EBID is induced by relatively large energy beams (thus excluding STM) the lateral size of the structures exceeds the primary beam diameter. Table 2.4 shows some experimental results where the ratio between the electron probe diameter and the obtained lateral size of the deposit can be appreciated. The table shows that not much progress has been done in improving the fabrication resolution. In 10 years the minimum feature size reduced by a factor of three and some authors are sceptic about the future.

Compared with the deposition rate and chemical quality studies, the spatial evolution during EBID is not enough investigated and the theoretical modelling is rather poor. There is a discrepance between the many experimental results and the theoretical explanations and models. This comes from the many approximations the present models accept.

One of the most flagrant mistakes is that the only player taken into account during the quantitative modelling of the deposition process has been the incident beam, either electrons or ions. But the situation is in reality more complicated, because the adsorbed molecules can be decomposed or vanish as result of more interactions, like:

- the direct impact of incident electrons/ ions

- the interaction with a sputtered ion or atom in the case of IBID

- the impact with the secondary electrons emitted upon primary particles impact.

- thermal spikes caused by the momentary temperature rise on the surface at the point of primary impact.

- surface diffusion and desorption induced by the beam irradiation.

The next degree of complexity in EBID/IBID modelling has to introduce the specimen mediation in the deposition process. At this moment, questions will appear like: "which factors are responsible for the growth (vertical and lateral) and to what degree?", "what are the limiting factors for vertical / lateral growth?", etc.
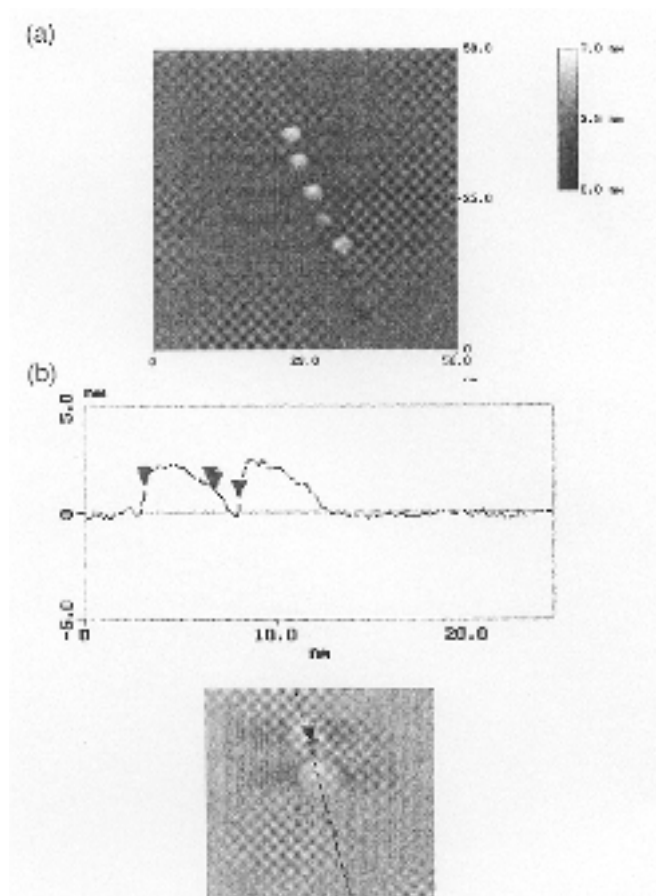
Figure 2-40: a) 3 nm rhodium islands separated by about 4 nm ; b) Rhodium islands separated by 1.5 nm deposited by STM CVD (from [101])

The specimen mediation modelling needs simulation of electron interactions with solid matter as well as of the electron interactions with the precursor molecules.

The modelling of electron impact with solid matter can be done by solving analytically the Boltzman transport equation or by Monte Carlo type methods.

Lee in 1989 obtained using EBID gold features of 30 nm width and 50 nm spacing, with a beam size smaller than 10 nm at 30 kV. Lines have been deposited both on thin Si_3N_4 membranes and thick bulk Si specimens and their widths were the same. It means that the lateral resolution is independent on the substrate thickness and the backscattered electrons do not play an important role in the resolution limitation [65]. Low energy electrons situated in the 0-20 eV range are expected to play a major role in the decomposition of adsorbed molecules via the processes of dissociative attachment and dipolar dissociation.

There have been a series of experiments reported that state the important role of secondary electrons in deposition. The strategy used by several authors is to measure the deposition rate for different incident energies, and compare it with the secondary electron yield dependence on the incident energy. Lipp [66] and Kunz [64] compared the deposition rate with the secondary emission yield and found that the curves are similar. Because the two curves are similar, the general conclusion drawn is that the chemical reactions induced by electron beam irradiation are mainly governed by the generated secondary electrons.

Deposit	Precursor	System	Beam energy and current	Probe diameter	Lateral resolution	Reference
Au	$Me_2Au(tfac)$	SEM	35keV/6 pA	2 nm	16-26 nm	[29]
Au	$Me_2Au(tfac)$	SEM	20keV/80 pA		20 nm	[60]
Pt	$(C_5H_5)Pt(CH_3)_3$	SEM	20keV/400 pA		20 nm	[60]
W	$W(CO)_6$	SEM	25keV/10 nA	150 nm	250 nm	[62]
W	$W(CO)_6$	STM	25V / 20 nA		25-30 nm	[73]
Au	$Me_2Au(tfac)$	SEM	25keV/1 nA	100 nm	200 nm	[62]
Au	$Me_2Au(tfac)$	SEM	30 keV / 50 pA	< 10 nm	30 nm	[65]
C	$C_{16}H_{34}$	SEM	30 keV	1 nm	10 nm	[8]
C	pump oil	SEM	35 keV / 6 pA	2 nm	8-15 nm	[29]
C	pump oil	SEM	15 keV / 100 pA	2 nm	20 -30 nm	[29]
C	AN	SEM	6 keV / 10 pA	8 nm	20 nm	[45]
Al	TMA	SEM	6 keV / 10 pA	8 nm	20 nm	[45]
C	styrene	SEM	50keV / 100 pA	5 nm	14 nm	[69]
Cu	HFA-Cu-VTMS	ESEM	30 keV / 600 pA	20 nm	100 nm	[79]
Fe	$Fe(CO)_5$	SEM	3 keV	100 nm	150 nm	[63]
Fe	$Fe(CO)_5$	SEM	1 keV/ 70 pA	300 nm	300 nm	[63]
Fe	$Fe(CO)_5$	STM	15 V / 50 pA		7 nm	[48]
Pt	$(C_5H_5)Pt(CH_3)_3$	SEM	30 keV / 70-100pA	3 nm	40 nm	[76]
Pt	$(C_5H_5)Pt(CH_3)_3$	DBI	30keV / 70-100pA	3 nm	40 nm	[103]
W	$W(CO)_6$	SEM	5 keV / 1 nA	400 nm		[39]
W	WF_6	SEM	50 KeV / 100 pA	3 nm	13 nm	[35, 33, 34]
W	WF_6	TEM	120 keV / 7 pA	3 nm	15 nm	[44]
W	WF_6	SEM	50 keV / 100 pA	3 nm	13-20 nm	[57, 55, 56]
Ni	$Ni(CO)_4$	STM	15 V		35 nm	[87]
Au	$Me_2Au(tfac)$	STM	6V / 300 nA		30 nm	[11]
C	acetone	STM	4V /	0.4 nm	0.8 nm	[106]
Rh	$[Rh(PF_3)_2Cl]_2$	STM	6V /		17 nm	[67]
Ni	$Ni(CO)_4$	STM	15 V/ 1-2nA	10 nm	18 nm	[109]
Fe	$Fe(C_2H_5)_2$	STM	10V/		5 nm	[80]

Table 2.4: Typical EBID experiments, showing the material deposited, the precursor and the description of the host system used. We tried to reveal the discrepancy between the size of the writer (electron beam) and the lateral size of the deposited structure.

2.2.3.5   Conclusions

At this moment, the resistivity of deposited materials (W, Au, Cu, Pt, Al, Fe) using both EBID and IBID is still 2-3 times larger than the values for the bulk metal. The materials grown by contamination lithography are conductive enough for scanning probe imaging. The resistivity obtained with IBID is lower than that from EBID. From experiments it resulted that high current densities, low impact energies, slow scanning and post annealing produce lower resistivities of the deposits. No explanations have been issued yet.

It is accepted that the conductivity is related to the carbon impurity content and to the packing between the nanocrystals. Clean ambient and precursor molecules devoid of carbon atoms should be important conditions required to obtain low resistivity films.

The result of contamination growth is amorphous carbon, a-C, with properties of diamond or graphite. Deposition from organometallic complexes grows metal nanocrystallites embedded in an amorphous carbonaceous matrix. The crystallite size is a few nanometers and it is influenced by the dwell time and the electron probe current. The lateral EBID fabrication resolution might be limited by the size of the nanocrystallites.

The growth rate increases linearly with the exposure dosis and the current density, with decrease of substrate temperature and the decrease of beam energy. Typical values for growth rates are 1-10 nm/sec for electron excitation and 10-20 nm/sec for ion excitation and a current density of 0.004 A/cm^2.

The average deposition yield for electron beams is 10^{-2} atoms/electron and for ions is 4-10 atoms/ion. Ion induced deposition yield can be 50-100 times larger than the electron induced yield.

The deposits from all currently used organometallic precursors contain C and O, and maximum 75% metal. The ratio of contents in the deposit is not always the same as the ratio in the precursor molecule structure suggesting that the substrate can also decompose under beam irradiation, or some content adheres better to the substrate than others.

The ratio between the metal contents and the rest of the elements in the deposit can say something about the decomposition paths. The step-by-step mechanism of decomposition is not known, but there are suppositions that the precursor does not always decompose totally to form pure metal atoms.

At present, the state-of-the-art in fabrication resolution using EBID looks as follows:

Carbon dots of 14 nm diameter have been deposited by contamination lithography in a 50 kV SEM with a 5 nm beam diameter [69].

Metal lines with 15-20 nm lateral size have been obtained on bulk substrates, with spot sizes of 2 nm in a 50 kV SEM [43, 33, 57].

15 nm diameter W rods have been grown on a Si fine particle on a thin membrane, with a 3 nm diameter electron beam in 120 keV TEM [68].

Individual dots with a diameter between 1 and 10 nm and 1 - 150 nm height and lines of 5 nm width and 2 nm height have been deposited by low energy electrons (5-10 V) in a STM [73, 80, 105].

The theoretical modelling of spatial evolution of EBID structures is not enough developed. We can say that despite the fact that some authors suspect the role of SE in deposition, no convincing quantitative arguments in a form of direct simulations or models free of fit-parameters have been issued yet.

2.2.4 Applications and achievements of electron and ion beam induced deposition methods

Most of the applications of EBID and IBID are found in mask and IC repair or in the nanofabrication of contacts and prototype devices. The restrictions of applications are caused by the high content of carbon in the deposits, the small exposed areas and the low reaction rates. Small beam diameters mean low current and long time necessary to deposit complicated, massive patterns.

We will describe the most valuable and interesting application areas (A-G), pointing out for each group the achieved performance, the encountered problems and the future predictions.

A Mask repair and mask fabrication

B IC modification and chip surgery

C STM, AFM, SFM supertips

D Field emission sources and field emitter arrays

E Electrical contacts for molecules

F Probing on small crystals

G 3D artifacts, nanostructures and devices

A1) Mask repair technique

Photo-mask repair

The generation of patterns used in semiconductor microcircuits by optical lithography relies upon the use of chromium-on-glass photomasks. One encounters two types of photomask defects: defects in the form of excess chromium (opaque defects) or absence of chromium (clear defects). The mask repair procedure has to be simple and fast and if possible in one step.

In the conventional chrome-glass photo-masks repair, the opaque defects can be removed by FIB in commercial tools or by laser zapping, i.e. a laser induced thermal vaporization. To repair submicron clear defects (pinholes), gas assisted IBID can be used, if some conditions are imposed on the process. For example, the deposited film has to be opaque, to adhere both to glass and metal surfaces, it has to be chemically and physically resistant to the mask cleaning procedures and the deposition has to be faster than sputtering induced by the ion beam. By studying the carbon deposition from a set of potential organic compound precursors (benzene, toluene, methylmetacrylate and styrene), all except styrene deposited thin and translucent and not continuous masks, making styrene the only suitable precursor for open mask defects repair by ion beam induced contamination growth [32].

Clear defects in silicon transmission masks can be repaired by contamination writing, using the so-called "darning method" by building bridges across the pinholes. These bridges will serve as support layer for ulterior gold deposition. The gold layer will fill the hole and the contamination layer will be removed later by O_2 plasma [7].

X-ray mask repair

X-ray lithography was a subject of much research and development interest because of its ability to produce patterns with critical dimensions below the 0.25 μm limit achievable with

optical and deep UV. The mask consists of a gold layer of 0.5 μm thickness on a 2 μm thick membrane of silicon or silicon nitride [82]. Compared with the photomask repair, which is now routinely done by means of laser systems or FIB, the repair of X-ray masks is significantly more critical because the small dimensions and higher aspect ratios.

Opaque defects can be repaired by FIB milling.

But repair of clear defects requires a very well localized deposition of high Z-material that offers a high X-ray opacity at the defect site. The deposited layer has to attenuate the X- rays by at least a factor of 8.

Focused beam deposition can be used for this purpose. The advantage of using a FIB is that both clear and opaque defects can be repaired. But the sputtering and gallium implantation in the mask are a problem. The use of EBID does not create this problem, but in order to improve the throughput in the repair of clear defects of X-ray masks using EBID the growth rate has to be maximized.

A2) Mask fabrication

EBID and contamination lithography have been occasionally and on a small scale used for mask fabrication in a RIE process. Using such a mask, made by contamination growth, Craighead [13] obtained arrays of 7 nm diameter silver and 10 nm diameter AuPd structures using a 2 nm probe.

Kohlmann von Platen fabricated by deposition of tungsten from $W(CO)_6$ a stable etching mask with a thickness of less than 200 nm. Hoyle used the same method to obtain a mask for CF_4 plasma etching of Si [38] and Koops for a high resolution mask for oxygen RIE of polyimide with a 57:1 selectivity [62].

B) IC modification and chip surgery

IBID is currently used in IC failure analysis and debugging because it can mill layers to reach a specified interface or discontinuity and deposit conductive metal films and wires to restore the damaged functionality. The resistivity of the material used in chip surgery has to be as low as possible.

C) Shape improvement for scanning probe microscopy tips

Scanning probe microscopes (STM, AFM) are profiling instruments that form images by scanning a sharp probe (tip) over the sample surface. The image is given in case of STMs by the current which flows between the surface and a small atomic cluster on the apex of the tip. In AFM, the image signal is given by the force between the cantilever tip and the target surface. The probe is one of the most crucial parts of the instrument, because the resulting topographic image is a convolution between the tip shape and the analyzed surface morphology.

In imaging with high, even atomic resolution of flat surfaces, almost any tip can be used, usually a conventional tip obtained by electropolishing of a metal Pt-Ir, gold, platinum or tungsten. But for imaging non-flat structures, with a high aspect ratio or very steep edges, deep grooves and depressions with vertical sidewalls, more rigorous requirements are imposed, not only to the tip but also on the whole tip geometry. The classical tip will give a deformed topographic image if its diameter is larger than the diameter of the groove/hole. The tip has to be thin, sharp, long, with low resistivity and still mechanically stable. The conventional electrochemically etched tips, with a 10-50 nm radius at the apex, cannot fulfill this requirement.

EBID can be used to add supertips to the commercial SPM tips improving their radius and aspect ratio. In Fig. 2-41 an example of a very high aspect ratio tip grown by EBID is shown. Since the grooves width in LSI fabrication is approaching 0.05 μm, tips with 50 nm diameter will be urgently needed for future topographic measurement of micro-patterns.
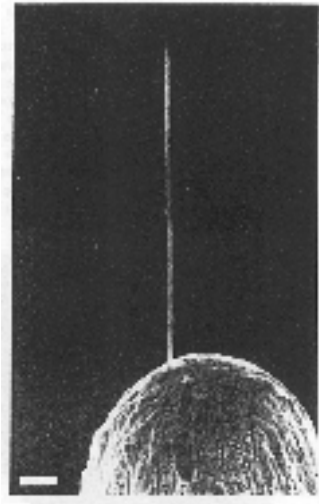
Figure 2-41: Tip with high aspect ratio fabricated by EBID. The scale marker indicates 1 μm (from [42])

C1) STM tips.

Akama [1] fabricated a long and straight microtip with submicron diameter on the top of a Pt-Ir STM tip by using contamination lithography. The tip is amorphous, containing C and O, smooth, with a diameter of 100 nm and uniform along the tip. The problem in growing tips is that the longer the tip grows, the more the beam is defocused. If this effect can be compensated, even smaller diameters can be realized. Succesfull STM experiments have been performed to test the improvement in the imaging quality of the new tip.

Using contamination lithography in a SEM, the shape of a conventional Pt-Ir STM tip has been improved [42]. With an electron beam diameter of 2-5 nm and a growth rate $0.1 - 1\mu m/minute$ a tip with a shank diameter below 200 nm is obtained. The radius of the tip was 10 nm independent of beam acceleration voltage. STM tunnelling experiments have shown enough conductivity of the deposited tip.

An interesting way to increase the STM imaging resolution by sharpening the existing tip can be performed in situ using EBID with organometallic Pd precursor and negative sample bias. A secondary much sharper tip is grown [89]

C2) AFM tips.

In order to investigate the morphology and roughness of surfaces, atomic force microscopy can be used. For surfaces with shallow relief or widely spaced features, pyramidal tips are appropriate, but for narrow and steep features more slender tips are needed. EBID is used to improve the shape of commercially available pyramidal Si_3N_4 tips by depositing carbon or gold supertips. The improved tips are mechanically stable and show no damage of the apex after a few scans, surviving days of continuous use [3, 29, 47].

Starting from a commercial pyramidal AFM tip with end radius of 50-100 nm and opening angle of 114 degrees, a contamination tip is fabricated in SEM spot mode with an end diameter of 30 nm and conical end of angle 10-20 degrees (see Fig.2-42). Because the carbon tips are
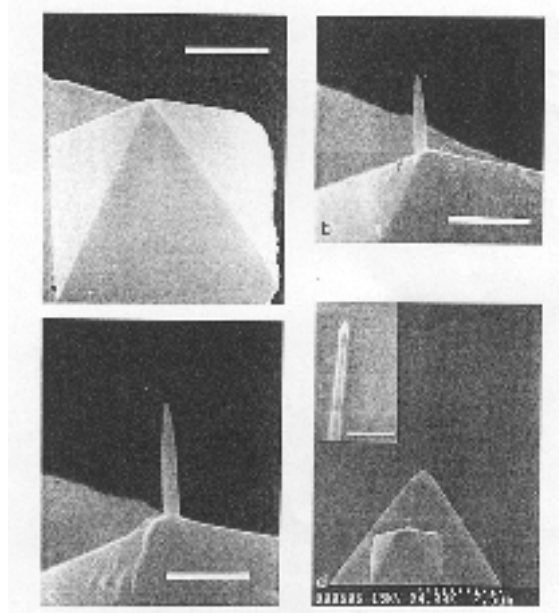
Figure 2-42: AFM supertips fabricated by EBID (from [47])

very durable, other tiny machine tools for milling samples on a small scale could be fabricated by the same method [47].

High resolution electron beam deposition is particulary suitable for the fabrication of AFM tips where different conventional lithography methods are difficult to implement. In AFM a tip with low spring constant is imposed for force detection sensitivity. The best tip achieved so far has a radius down to 15 nm , with shaft diameters of 100 nm and the length of 1000 nm. [42]

Miura [74] also uses contamination growth in SEM to improve the shape of an AFM tip. First on the Si_3N_4 tip a Pt-Pd alloy is deposited by rf-sputtering to make the surface electrically conductive. Then, a 1 μm long carbon conical structure is deposited on the top of a AFM tip, with a diameter of 40 nm. Improvements in planar resolution of AFM tip images is demonstrated.

Castagne [12] has grown carbon (diamond) supertips on the top of a silicon AFM probe in a 30kV SEM, with an electron spot size of 8 nm and a probe current of 100 pA. The tips are included in a photon scanning tunnelling microscopy (PSTM) experiment and used as near field converters in the infrared range of wavelengths.

D1) Field emission tips.

Koops deposited in 1994 by EBID an integrated structure consisting of a tip and an extractor anode on two Au islands and tested the field emission from this construction [60]. The current-voltage characteristic is given in a Fowler-Nordheim plot and it shows the presence of field emission. To stabilize the emission current, also a resistor could be deposited.

Later, Schössler and his colleagues [94] fabricated supertips with EBID with $MeAu(tfac)$ and $CpPtMe_3$ on top of an etched tungsten tip. Increased field enhancement factor has been

observed when nanocrystallites protruded from the tip itself. Current-voltage characteristics of these supertips were measured. The base tungsten tip was spot-welded to a hair pin or a carbon vice to elevate its temperature and a supertip was grown by EBID on its top. Field emission from supertips was measured in excess of 100 μA at 22 V extraction voltage. Emission has been observed on a phosphor screen situated in front of the tip and recorded by a CCD camera. Deposited supertips provided cold, single emission site field emitters with a brightness four times higher than that of conventional tips.

In 1998 the same authors [95] made a step further and fabricated a nanostructured integrated reliable high-brightness field emission electron source. EBID was used to fabricate the emitter, the resistor and the extractor. The deposited tip had a radius of 10 nm and a total height of 100 nm. A 200 kV TEM micrograph showed gold nanocrystals immersed in an amorphous carbon matrix. The protrusions were acting as supertips on which the simulation of emission showed an increased extracting field. The emission was tested in a field emission microscope in a hair pin construction. A total emission of up to $10\mu A$ has been observed for several hours. A comparison with the reduced brightness of a Philips ultrasharp Schottky W-Zr-O field emitter ($Br = 3 \times 10^5 A/cm^2 srV$) [26] shows that the deposited supertip has at least the same brightness. In conclusion the authors show that an integrated field emission source can be fabricated by combining conventional lithography and EBID from Au precursor. They even state that the deposited field emitter supertips using EBID exceed in brightness all conventional electron field emitters. In 1997 a microtriode with field emission for operation in air with a water Taylor cone has been built by Koops [58].

D2) Field emitter arrays (FEA)

FEA are one of the most important electron sources for vacuum microelectronics, for example for emissive flat panel displays (FPDs) with high intensity, fast response and wide viewing angle. One of the problems arising in FEA fabrication is that not all the tips have the same shape and thus inhomogeneities in the emission behavior occurs. FEA can be fabricated by EBID. The procedure to build a FEA is described as follows. First a 10 x 10 Si FEA array is fabricated by conventional methods (RIE and thermal oxidation sharpening) and introduced in the EBID chamber. Pt tips are deposited by EBID on the top of each Si tip from $C_5H_5Pt(CH_3)_3$ precursor. The beam diameter was 3 nm at 30 kV. The Pt columns are 1 μm high and have a 20 nm radius sharp tip. The field emission is tested after Pt deposition and a current of 10 μA per tip maximum is obtained with a stability of 20% over the operation time of 24h [76].

The combination EBID and FIB can be used to fabricate prototype FEA or to repair damaged emitters. FIB etching is used to fabricate the gate hole and EBID to deposit the Pt tip. Takai [103] uses a dual beam machine which combines focused EB and FIB to build a 10 x 10 FEA. The gate opening and an over-etched Si emitter are made by gas assisted etching (GAE) with 30kV Ga^+ ions and I_2 precursor. A sharp Pt tip is deposited by EBID in the gate opening with a 3 nm spot size at 30 kV(see Fig. 2-43). The Pt tips are 20 nm in radius and 1 μm long, containing 21.5% Pt, 73%C, 5.5% O, as analysed by Auger spectroscopy. The resistivity of deposited material is 30 $\mu\Omega cm$, 3 times higher than for the bulk Pt. The I-V characteristic is measured and field emission is demonstrated. In conclusion, the EBID combined with FIB etching can be a fast prototyping method for nanometer sized FEA. At this moment Ga^+ impurities are still a problem due to the leakage currents. The process has to be better controlled in the future.

E) Electrical contacts for molecules

Tiny electrical contacts are necessary in order to characterize the electron transport through a single molecular chain. There are two problems which occur when measuring the transport
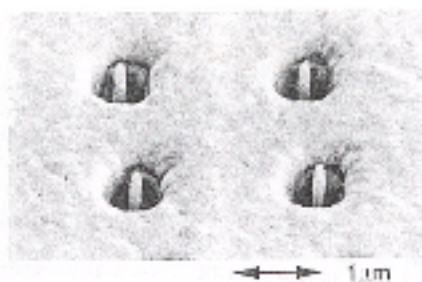
Figure 2-43: SEM view of a FEA after gate opening by FIB and Pt tip fabrication by EBID (from [103])

through single molecules. First of all, conducting electrodes have to be fabricated, separated by a distance smaller than the molecule's length. The molecules of interest are smaller than the resolution of conventional electron beam lithography; for example the conjugated olygomers are usually 5 nm in length. Secondly, a contact has to be established between the outside world electrodes and these molecules. An alternative to approaches based on scanning probe techniques could be EBID.

In this sense, Bezryadin [8] fabricated using contamination lithography in a SEM, two free-standing horizontal carbon nanowires of 5-20 nm in diameter, oriented towards each other with a gap in between of 3-5 nm (see Fig.2-44). This gap is small enough to trap a molecule between the electrodes by electrostatic trapping (ET). For example by applying a potential difference of 1 V between the electrodes, an electric field of 10^8 V/m is created, which can attract the polarized molecule in between. A thin metal layer is sputtered on top of the grown electrodes to improve their conductivity. ET has been also used for trapping of carbon nanotubes.

The most recent application of EBID for fabrication of electrical contacts to single molecules (MT-microtubules) is reported by Fritzsche in [27]. Microtubules are intercellular proteinaceous elements with essential functions in cell architecture and cellular transport with dimensions of micrometers (length) and nanometer (diameter) range. Some MT are adsorbed on an oxidized Si pad with gold pre-structured electrodes. A contamination line is deposited in situ between the existing gold electrodes and the MT biomolecule of interest. This line is used afterwards as etching mask and golden bridges between prestructured contacts and the molecule are obtained. SEM imaging in situ is used in order to choose the right orientation of the lines.

Our suggestion is that depositing directly a metal line should improve the situation. Nobody made metal nanowires to contact molecules yet, using EBID. Also in the case of MT experiments, a four wire resistance measurement scheme should bring an improvement. Using the two wires scheme, the authors measured not only the resistance of the trapped molecule, but also the resistance of the connecting gold electrodes.

F) Probing on small crystals

In the research of new materials, the measurement of their electric properties can become important. But when the sample is too small to directly attach probe electrodes and it is too frail to fabricate probe electrodes by metal deposition and photolithography, then beam induced deposition can be a unique technique to fabricate probe electrods patterns for such
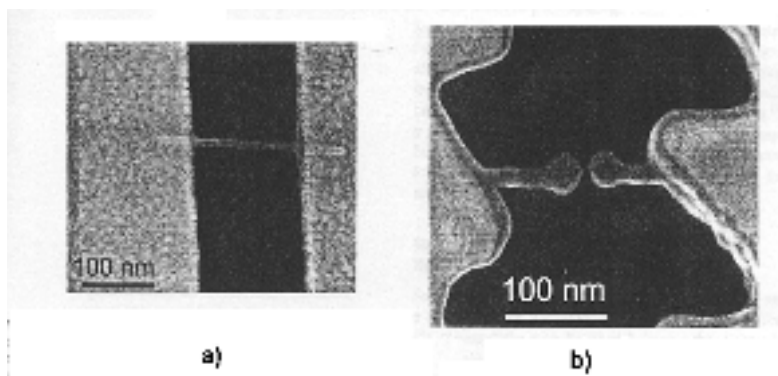
Figure 2-44: a) A free-standing carbon wire of about 10 nm grown by contamination lithography; b) Two free standing carbon nanowires grown towards each other by EBID and separated by about 4 nm (from [8])

small samples.

G) 3D artifacts, nanostructures and devices

EBID and IBID have occasionally been used to fabricate metal, dielectric and carbonaceous artifacts, as wires, sensors and transducers on nanometric scale (flow sensors), resistors in arch form, lens systems, Fresnel lenses, X-ray lenses as well as free-standing nanometric structures and bridge wires across a hole [60]. The deposited wires are very rigid and chemically inert to solvents and acids.

Dot arrays can be deposited in small deformed areas for the metrology of mechanical properties of micromechanically designed and fabricated parts. Diamond like carbon microsystem parts as microcoils, microdrills, and microbellows have been recently deposited by IBID from aromatic hydrocarbon and the application area can even extend towards microstructure plastic arts (for example a microwine glass with 2.75 μm external diameter and 12 μm height has been grown, see Fig. 2-13) [71].

Single electron transport (SET) devices for future integrated circuits such as high density memory and logic have attracted great interest. To realize device operation at high temperature, many attempts have been made to fabricate nanometer scale Coulomb islands using Si/SiO_2 and metal/insulator/metal (MIM) systems. In order to realize single electron devices operating at higher temperature, nanometer scale dot arrays and low resistivity deposits will be needed to keep low resistance even at high temperature.

Komuro [56, 55, 57] used EBID from WF_6 to fabricate single tunnel junctions for single electron devices. A single electron transistor composed of three EBID dots with 20 nm spacing connected to wires with a gate electrode exibited clear Coulomb oscillation at 230K.

Miura [75] used contamination growth in a SEM to deposit 40 nm diameter minute carbon dots. The dots were arranged in series between fine metal electrodes to form a device with multiple tunnel junctions. Single electron charging effects, such as the Coulomb blockade and the Coulomb staircase, were clearly observed at 9.4K.

2.2.4.1 Conclusions

Beam induced direct deposition can be applied with success in a few situations. Firstly, in rather rare occasions when structures are needed on non-planar substrates which cannot be created otherwise, like for example long tips. Secondly, in cases when a fast result on a small area is needed and the time needed for the resist based process would not be justified. Another appropriate situation is when a local micro repair is needed as soon as it is seen. Ions are better in this case than electrons due to their higher deposition rate.

The most exciting application is the deposition of nanometer size lines and spaces, with a higher resolution than other conventional lithography methods can at this moment. In this case the electrons are more favorable than the ions. Being resistless, EBID might be the key to break the resolution limit of 10 nm achieved in resist based lithography.

2.3 Conclusions

At the end of each section in this literature review some general conclusions have been presented, to be used by the interested reader. Here we present conclusions that will bring us to the main objective of this thesis.

The status of EBID at this moment can be summarized as follows:

1. EBID happens in the majority of cases in a more or less modified SEM. Less often it happens in a TEM, STM, dual beam instrument or EBL machines. The deposit analysis is made by SEM, TEM, AFM, Auger, EDX, profilometry.

2. People aim in their research for high deposition rate or high fabrication resolution or high quality: purity, resistivity, hardness, opacity.

3. The best EBID resolution results obtained in a SEM, with a 2-3 nm diameter beam, are linewidths of 15-20 nm at 50 kV [57, 43] on bulk silicon. In TEM 14 nm rods could be fabricated on Si fine particles [44]. In STM using a very low energy bean (5-10 eV), individual dots of 0.8 nm diameter and 0.7 nm height could be fabricated [106], and lines with a minimum width of 5 nm and 2 nm height [80].

By using ingenious tricks, small spaces can be created between EBID structures. For example spaces as small as 4 nm could be obtained by growing two wires towards each other [8]. It is intriguing that the sizes of EBID structures always exceed the beam diameter in SEM and TEM hosts.

4. The deposition process is not completely understood. It is obvious that up to now only simple theoretical models have been provided, especially for the deposition rate. The role of the secondary electrons is suspected, but a quantitative analysis is not done yet. There are still discrepancies between calculated and measured lateral sizes and thicknesses. People are happy if deposition occurs with the desired resolution and speed and few of them are interested in theoretical explanations. The electron induced dissociation cross sections for the specific precursor as a function of impact energy are practically unknown.

5. The application area of EBID is growing, extending to the life sciences. There is a growing interest and need for electrical contacts (2-5 nm) to single molecules and nanocrystals. Small dots less than 20 nm diameter are necessary for single electron devices to operate at room temperature.

Given this situation, a few challenges seem to be attractive for our research:

An experimental system has to be built, in order to study diferent EBID aspects.

A complete EBID model is very difficult to build. We can separate only one problem, the

EBID fabrication resolution. A complete theoretical evaluation of the EBID resolution should be a novelty longed for a long time by the experimentalists. Because the processes involved in EBID and specimen contamination are similar, the result of our study can be useful also for the contamination modelling in high resolution electron microscopy.

All the systems built up to now for the EBID study need modifications of the electron microscope ports, specimen holder or specimen area in order to create a gas atmosphere around the substrate. The idea to use an environmental cell, which will be portable and will require no interventions in the host system construction is a challenge and a novelty. Only Folch [23] made a simple aperture based sandwich used in ESEM. More sophisticated constructions of gas cells, with variable apertures for the gas flow control are still needed.

With a probe of 2 nm, visible structures of 15 nm have been deposited in SEM. An urgent need for smaller structures exists. We think that STEM offers a perfect environment for higher resolution EBID: a fine and stable focused probe (0.2 nm), beam focus and positioning control and a thin specimen. If we can show that with a 0.2 nm beam in a STEM smaller structures can be deposited, a major step forward is made. We will focus therefore our research on typical STEM conditions, thin specimens and high energy electron beams.

Bibliography

[1] AKAMA, Y., AND NISHIMURA, E. New scanning tunneling microscopy tip for measuring surface topology. *Journal of Vacuum Science and Technology A 8* (1990), 429.

[2] ALBRECHT, T., DOVEK, M., AND KIRK, M. Nanometer-scale hole formation on graphite using a scanning tunnelling microscope. *Applied Physics Letters 55* (1989), 1727.

[3] ANTOGNOZII, M., SENTIMENTI, A., AND VALDRE, U. Fabrication of nano-tips by carbon contamination in a SEM for use in scanning probe microscopy and field emission. *Microscopy, Microanalysis, Microstructures 8* (1997), 355.

[4] ARISTOV, V., KASUMOV, A., AND KISLOV, N. A new approach to fabrication of nanostructures. *Nanotechnology 6* (1995), 35.

[5] AUTRATA, R., AND ANS M. MULLER, R. H. An efficient single crystal BSE detector in SEM. *Scanning 14* (1992), 127.

[6] BEDSON, T., PALMER, R., AND WILCOXON, J. Electron beam lithography in passivated gold nanoclusters. *Microelectronic Engineering 57-58* (2001), 837.

[7] BEHRINGER, U. Repair techniques for silicon transmission masks used for submicron lithography. *Journal of Vacuum Science and Technology B 4* (1986), 94.

[8] BEZRYADIN, A., AND DEKKER, C. Nanofabrication of electrodes with sub-5 nm spacing for transport experiments on single molecules and metal clusters. *Journal of Vacuum Science and Technology B 15* (1997), 793.

[9] BLAUNER, P., AND RO, J. FIB of submicron gold structures. *Journal of Vacuum Science and Technology B 7, 4* (1989), 609.

[10] BROERS, A., AND MOLZEN, W. Electron-beam formation of 80 A metal structures. *Applied Physics Letters 29* (1976), 596.

[11] BRUCKL, H., KRETZ, J., KOOPS, H., AND REISS, G. Low energy electron beam decomposition of metalorganic precursor with a STM at ambient atmosphere. *Journal of Vacuum Science and Technology B 17* (1999), 1350.

[12] CASTAGNE, M., AND BENFEDDA, M. Near field optics behaviour of C supertips. *Ultramicroscopy 76* (1999), 187.

[13] CRAIGHEAD, H. G., AND MANKIEWICH, P. Ultra-small particle arrays produced by high resolution electron-beam lithography. *Journal of Applied Physics 53* (1982), 7187.

[14] DAGATA, J., SCHNEIR, J., HARARY, H., EVANS, C., POSTEK, M., AND BENETT, J. Modification of hydrogen passivated silicon by a scanning tunnelling microscope operating in air. *Applied Physics Letters 56* (1990), 2001.

[15] DAVIES, S., AND KHAMSEHPOUR. FIB machining and deposition for nanofabrication. *Vacuum 47* (1996), 455.

[16] DE JAGER, P. *Design of "the Fancier",an instrument for Fabrication and Analysis of Nanostructures Combining Ion and Electron Regulation.* PhD thesis, Delft University of Technology, 1997.

[17] DUBNER, A., AND SHEDD, G. Ion beam induced deposition of gold by focused and broad-beam sources. *JVSTB 5* (1987), 1434.

[18] DUBNER, A., AND WAGNER, A. Mechanism of ion beam induced deposition of gold. *Journal of Vacuum Science and Technology B 7* (1989), 1951.

[19] DUBNER, A., WAGNER, A., MELNGAILIS, J., AND THOMPSON, C. The role of the ion-solid intweractiomn in ion-beam-induced deposition of gold. *Journal of Applied Physics 70* (1991), 665.

[20] DUJARDIN, G., WALKUP, R., AND AVOURIS, P. Dissociation of individual molecules with electrons from the tip of a scanning tunelling microscope. *Science 255* (1992), 1232.

[21] EDINGER, K., AND KRAUS, T. Modeling of focused ion beam induced surface chemistry. *Journal of Vacuum Science and Technology B 18* (2000), 3190.

[22] FLOREANI, F., KOOPS, H., AND ELSASSER, W. Operation of high power field emitters fabricated with electron beam deposition and concept of a miniaturised free electron laser. *Microelectronic Engineering 57-58* (2001), 1009.

[23] FOLCH, A., AND SERVAT, J. High-vacuum versus "environmental" electron beam deposition. *Journal of Vacuum Science and Technology B 14* (1996), 2609.

[24] FOLCH, A., AND TEJADA, J. Electron beam deposition of gold nanostructures in a reactive environment. *Applied Physics Letters 66* (1995), 2080.

[25] FOURIE, J. A model for contamination phenomena in electron microscopy. In *VIth European congress on electron microscopy, Jerusalem* (1976), p. 396.

[26] FRANSEN, M., AND KRUIT, P. Characterization of ultrasharp field emitters by projection microscopy. *Applied Surface Science 94/95* (1996), 107.

[27] FRITZSCHE, W., AND KOHLER, K. Wiring of metallized microtubules by electron-beam induced structuring. *Nanotechnology 10* (1999), 331.

[28] GAMO, K., TAKAKURA, N., SAMOTO, N., SHIMIZU, R., AND NAMBA, S. Ion beam assisted deposition of metal organic films using focused ion beams. *Japanese Journal of Applied Physics 23* (1984), L293.

[29] GORTZ, W., AND KEMPF, B. Resolution enhanced SFM measurements for characterizing dry etching methods applied to Ti masked InP. *Journal of Vacuum Science and Technology B 13* (1995), 34.

[30] HARADA, V., TOMITA, T., WATABE, T., WATANABE, H., AND ETOH, T. Reduction of contamination in analytical electron microscopy. *Scanning Electron Microscopy II* (1979), 105.

[31] HARRIOT, L. Digital scan model for focused ion beam induced gas etching. *Journal of Vacuum Science and Technology B 11* (1993), 2012.

[32] HARRIOT, L., AND VASILE, M. FIB deposition of opaque carbon film. *Journal of Vacuum Science and Technology B 6* (1988), 18.

[33] HIROSHIMA, H., AND KOMURO, M. High growth rate for slow scanning in electron-beam-induced-deposition. *Japanese Journal of Applied Physics 36* (1997), 7686.

[34] HIROSHIMA, H., AND KOMURO, M. Fabrication of conductive wires by electron-beam-induced deposition. *Nanotechnology 9* (1998), 108.

[35] HIROSHIMA, H., OKAYAMA, S., AND KOMURO, M. Nanobeam process system: An ultrahigh vacuum electron beam lithography system with 3nm probe size. *Journal of Vacuum Science and Technology B 13* (1995), 2514.

[36] HIROSHIMA, H., SUZUKI, N., OGAWA, N., AND KOMURO, M. Conditions for fabrication of highly conductive wires by electron beam induced deposition. *Japanese Journal of Applied Physics 38* (1999), 7135.

[37] HOYLE, P., CLEAVER, J., AND AHMED. Ultralow-energy focused electron beam induced deposition. *Applied Physics Letters 64* (1994), 1448.

[38] HOYLE, P., CLEAVER, J., AND AHMED. Electron beam induced deposition from $W(CO)_6$ at 2 to 20 kev and its applications. *Journal of Vacuum Science and Technology B 14* (1996), 92.

[39] HOYLE, P., OGASAWARA, M., AND CLEAVER, J. Electrical resistance of electron beam induced deposits from tungsten hexacarbonyl. *Applied Physics Letters 62* (1993), 3043.

[40] HREN, J. Barriers to AEM: contamination and etching. In *Principles of analytical electron microscopy*, D. Joy, A. Romig, and J. Goldstein, Eds. Plenum, 1986, ch. 10, p. 353.

[41] HUBNER, B., JEDE, R., SPECHT, I., AND ZENGERLE, R. E-beam lithography by using a STEM with integrated laser interferometer stage. *Microelectronic Engineering 30* (1996), 41.

[42] HUBNER, B., AND KOOPS, H. Tips for scanning tunneling microscopy produced by EBID. *Ultramicroscopy 42-44* (1992), 1519.

[43] HUBNER, U., AND PLONTKE, R. On-line nanolithography using electron beam induced deposition technique. *Microelectronic Engineering 57-58* (2001), 953.

[44] ICHIHASHI, T., AND MATSUI, S. In situ observation on electron beam induced chemical vapor deposition by tem. *Journal of Vacuum Science and Technology B 6* (1988), 1869.

[45] ISHIBASHI, A., FUNATO, K., AND MORI, Y. Electron-beam-induced resist and aluminium formation. *Journal of Vacuum Science and Technology B 9* (1991), 169.

[46] JACKMAN, R., AND FOORD, J. Electron beam stimulated chemical vapor deposition of patterned tungsten films on si(100). *Applied Physics Letters 49* (1986), 196.

[47] KELLER, D., AND CHING, C. Imaging steep,high structures by scanning force microscopy with electron beam deposited tips. *Surface science 268* (1992), 333.

[48] KENT, A., SHAW, T., VON MOLNAR, S., AND AWSCHALOM, D. Growth of high aspect ratio nanometer scale magnets with cvd and stm. *Science 262* (1993), 1249.

[49] KISLOV, N., KHODOS, I., AND IVANOV, E. Electron-beam-induced fabrication of metal containing nanostructures. *Scanning 18* (1996), 115.

[50] KOH, Y., GAMO, K., AND NAMBA, S. Characteristics of W films formed by ion beam assisted deposition. *Journal of Vacuum Science and Technology B 9* (1991), 2648.

[51] KOHLMANN, K., THIEMANN, M., AND BRUNGER, W. E-beam induced X-ray mask repair with optimized gas nozzle geometry. *Microelectronic Engineering 13* (1991), 279.

[52] KOHLMANN-VON PLATEN, K., AND BUCHMANN, L. Electron beam induced tungsten deposition:growth rate enhancement and applications. *Journal of Vacuum Science and Technology B 10* (1992), 2690.

[53] KOHLMANN-VON PLATEN, K., AND CHLEBEK, J. Resolution limits in electron-beam induced tungsten deposition. *Journal of Vacuum Science and Technology B 11* (1993), 2219.

[54] KOMANO, H., OGAWA, Y., AND TAKIGAWA. Silicon oxide formation by FIB assisted deposition. *Japanese Journal of Applied Physics 28* (1989), 2372.

[55] KOMURO, M., AND HIROSHIMA, H. Fabrication and properties of dot array using electron-beam-induced deposition. *Microelectronic Engineering 35* (1997), 273.

[56] KOMURO, M., AND HIROSHIMA, H. Lateral junction produced by electron-beam - assisted-deposition. *Journal of Vacuum Science and Technology B 15* (1997), 2809.

[57] KOMURO, M., HIROSHIMA, H., AND TAKECHI, A. Miniature tunnel junction by electron-beam-induced deposition. *Nanotechnology 9* (1998), 104.

[58] KOOPS, H., DOBISZ, E., AND URBAN, J. Novel lithography and signal processing with water vapour ions. *Journal of Vacuum Science and Technology B 15* (1997), 1359.

[59] KOOPS, H., KAYA, A., AND WEBER, M. Fabricaton and characterization of platinum nanocrystal material grown by EBID. *Journal of Vacuum Science and Technology B 13* (1995), 2400.

[60] KOOPS, H., KRETZ, J., RUDOLPH, M., WEBER, M., DAHM, G., AND LEE, K. Characterization and application of materials grown by EBID. *Japanese Journal of Applied Physics 33* (1994), 7099.

[61] KOOPS, H., REINHARDT, A., KLABUNDE, F., KAYA, A., AND PLONTKE, R. Vapour supply manifold for additive nanolithography with electron beam induced deposition. *Microelectronic Engineering 57-58* (2001), 909.

[62] KOOPS, H., WEIEL, R., AND KERN, P. High-resolution electron-beam induced deposition. *Journal of Vacuum Science and Technology B 6* (1988), 477.

[63] KUNZ, R., ALLEN, T., AND MAYER, T. Selective area deposition of metals using low-energy electron beams. *Journal of Vacuum Science and Technology B 5* (1987).

[64] KUNZ, R., AND MAYER, T. Surface chemical reactions stimulated by low energy electron bombardment. *Mat. Res. Soc. Symp. Proc Materials Research Society 75* (1987).

[65] LEE, K., AND HATZAKIS, M. Direct electron-beam patterning for nanolithography. *Journal of Vacuum Science and Technology B 7* (1989), 1941.

[66] LIPP, S., FREY, L., AND LEHRER. A comparision of focused ion beam and electron beam induced deposition processes. *Microelectronics and reliability 36* (1996), 1779.

[67] MARCHI, F. Nanometer scale patterning by scanning tunnelling microscope assisted chemical vapour deposition. *Microelectronic engineering 50* (200), 2000.

[68] MATSUI, S., AND ICHIHASHI, T. Electron beam induced selective etching and deposition technology. *Journal of Vacuum Science and Technology B 7* (1989), 1182.

[69] MATSUI, S., ICHIHASHI, T., AND OCHIAI, Y. Technology developed through electron beam induced surface reaction. *Nanostructure Science and technology of mesoscopic structures* (1992), 335.

[70] MATSUI, S., AND MORI, K. New selective deposition technology by electron beam induced surface reaction. *Journal of Vacuum Science and Technology B 4* (1986), 299.

[71] MATSUI S., K. T. Three dimensional nanostructure fabrication by focused-ion-beam chemical vapor deposition. *Journal of Vacuum Science and Technology B 18*, 6 (2000), 3181.

[72] MATSUZAKI, Y., YAMADA, A., AND KONAGAI, M. Improvement of nanoscale patterning of heavily doped p-type gaas by afm based surface oxidation process. *Journal of Crystal Growth 209* (2000), 509.

[73] MCCORD, M., AND KERN, D. Direct deposition of 10 nm metallic features with the STM. *Journal of Vacuum Science and Technology B 6*, 6 (1988), 1877.

[74] MIURA, N., AND ISHII, H. Electron beam induced deposition of carbonaceous microstructures using SEM. *Applied surface science 113/114* (1997), 269.

[75] MIURA, N., AND NUMAGUCHI, T. Single-electron tunelling through amorphous carbon dots array. *Japanese Journal of Applied Physics 36* (1997), L1619.

[76] MORIMOTO, H., AND KISHIMOTO, T. Electron-beam -induced deposition of Pt for field emitter arrays. *Japanese Journal of Applied Physics 35* (1996), 6623.

[77] NAGAMACHI, S., AND UEDA, M. Focused ion beam direct deposition and its applications. *Journal of Vacuum Science and Technology B 16* (1998), 2515.

[78] NAMBU, Y., AND MORISHIGE, Y. High speed laser direct writing of tungsten conductors from W(CO)6. *Applied Physics Letters 56* (1995), 2581.

[79] OCHIAI, Y., AND FUJITA. Electron induced beam deposition of copper compound with low resistivity. *Journal of Vacuum Science and Technology B 14* (1996), 933.

[80] PAI, W., ZHANG, J., WENDELKEN, J., AND WARMACK, R. Magnetic nanostructures fabricated by scanning tunneling microscope-assisted chemical vapor deposition. *Journal of Vacuum Science and Technology B 15* (1997), 785.

[81] PETZOLD, H. Ion induced deposition for X-ray mask repair: rate optimization using time-dep. model. *Journal of Vacuum Science and Technology B 9* (1991), 2644.

[82] PREWET, P. Focused ion beams in microfabrication. *Review of Scientific Instruments 63* (1992), 2364.

[83] PURETZ, J., AND SWANSON, L. Focused ion beam depoistion of pt containing films. *Journal of Vacuum Science and Technology B 10* (1995), 2695.

[84] REIMER, L. Contribution to the contamination problem in transmission electron microscopy. *Ultramicroscopy 3* (1978), 169.

[85] REIMER, L. *Scanning electron microscopy.* Springer Verlag, Berlin Heidelberg New York, 1990.

[86] RISHTON, S. Measurement of the profile of finely focused beams in a SEM. *Journal of Physics E 17* (1984), 297.

[87] RUBEL, S., TROCHET, M., EHRICHS, E., SMITH, W., AND DE LOZANNE, A. Nanofabrication and rapid imaging with a scanning tunneling microscope. *Journal of Vacuum Science and Technology B 12* (1994), 1894.

[88] RUDENAUER, F., AND STEIGER. Localized ion beam induced deposition of al-containing layers. *Journal of Vacuum Science and Technology B 6* (1988), 1542.

[89] SAULYS, D., ERMAKOV, A., AND GARFUNKEL, E. Electron beam induced patterned deposition of allycyclopentadyenil palladium using stm. *Applied Physics 76* (1994), 7639.

[90] SAWARAGI, H., AND MIMURA, R. Performance of a combined focused ion and electron beam system. *Journal of Vacuum Science and Technology B 8* (1990), 1848.

[91] SAX, N. *Dangerous properties of industrial materials.* Van Nostrand Reinhold company New York, 1984.

[92] SCHAUER, P., AND AUTRATA, P. Electron-optical properties of a scintillation detector in SEM. *J. Microsc. Spectrosc. Electron. 4* (1979), 633.

[93] SCHEUER, V., AND KOOPS, H. Electron beam decomposition of carbonyls on silicon. *Microelectronic Engineering 5* (1986), 423.

[94] SCHOESSLER, C., KAYA, A., KRETZ, J., WEBER, M., AND KOOPS, H. Electrical and field emission properties of nanocrystalline materials fabricated by EBID. *Microelectronic Engineering 30* (1996), 471.

[95] SCHOESSLER, C., AND KOOPS, H. Nanostructured integrated electron source. *Journal of Vacuum Science and Technology B 16* (1998), 862.

[96] SCHOESSLER, C., AND URBAN, J. Conductive supertips for scanning probe applications. *Journal of Vacuum Science and Technology B 15* (1997), 1535.

[97] SHED, G., AND LEZEC, H. Focused ion beam induced deposition of gold. *Applied Physics Letters 49* (1986), 23.

[98] STARK, T., AND MAYER, T. Formation of complex features using electron-beam direct write decomposition of paladiunm acetate. *Journal of Vacuum Science and Technology B 10* (1992), 2685.

[99] STEWART, D., AND MORGAN, J. Focused ion beam induced deposition of tungsten on vertical sidewalls. *Journal of Vacuum Science and Technology B 9*, 5 (1991).

[100] STEWART, D., STERN, L., AND MORGAN, J. Focused ion beam induced deposition of metal for microcircuit modification. *SPIE Proceedings on Electron Beam, X-ray and ion beam technology 1089* (1989), 18.

[101] SZKUTNIK, P., PIEDNOIR, A., RONDA, A., MARCHI, F., TONNEAU, D., DALLAPORTA, H., AND HANBUCKEN, M. Scanning probes as a lithography tool for nanostructures. *Applied Surface Science 164* (2000), 169.

[102] TAKADO, N., AND YUICHI, I. Electron beam excited gaas maskless etching using Cl2 nozzle installed FIB/EB combined system. *SPIE Proceedings Multichamber and in-situ processing of electron. materials 1199* (1989), 134.

[103] TAKAI, M., AND KISHIMOTO, T. Fabrication of field emitter array using focused ion and electron beam induced deposition. *Microelectronic Engineering 41/42* (1998), 453.

[104] TAO, T., RO, S., AND MELNGAILIS, J. Focused ion beam induced deposition of platinum. *Journal of Vacuum Science and Technology B 8* (1990), 1826.

[105] UESUGI, K., AND YAO, T. Nanometer scale fabrication on graphite surface by scanning tunneling microscopy. *Ultramicroscopy 42-44* (1992), 1443.

[106] UESUGI, K., AND YAO, T. Nanometer scale fabrication on graphite surfaces by scanning tunneling microscopy. *Ultramicroscopy 42-44* (1992), 1443.

[107] UTKE, I., AND HOFFMAN, P. Focused electron beam induced deposition of gold. *Journal of Vacuum Science and Technology B 18* (2000), 3168.

[108] VASILE, M., AND HARRIOTT, L. FIB stimulated deposition of organic compounds. *Journal of Vacuum Science and Technology B 7* (1989), 1955.

[109] WANG, X., RUBEL, S., PURBACH, U., AND DE LOZANNE, A. Resistance of ni nanowires fabricated by STM-CVD. *Proceedings SPIE 3009* (1997), 2.

[110] WEBER, M. *Der Prozess der elektronstrahlinduzierten Deposition.* PhD thesis, Technische Hcheschule Darmstadt, 1997.

[111] WEBER, M., AND KOOPS, H. Scanning probe microscopy of deposits employed to image the current density distribution of electron beams. *Journal of Vacuum Science and Technology B 10* (1992), 3116.

[112] WEBER, M., KOOPS, H., ABD J. KRETZ, M. R., AND SCHMIDT, G. New compound quantum dots materials produced by EBID. *Journal of Vacuum Science and Technology B 13* (1995), 1364.

[113] WEBER, M., RUDOLPH, M., KRETZ, J., AND KOOPS, H. Electron-beam induced deposition for fabrication of vacuum field emiter devices. *Journal of Vacuum Science and Technology B 13* (1995), 461.

[114] WELIPITYA, D. Ultraviolet and electron radiation induced fragmentation of adsorbed ferrocene. *Journal of Applied Physics 79* (1996), 8730.

[115] WINKLER, D., AND ZIMMERMANN. E-beam probe station with integrated tool for electron beam induced etching. *Microelectronic Engineering 31* (1996), 141.

[116] XU, X., AND DEKLA, R. Focused ion beam induced deposition and ion milling as a function of angle of ion incidence. *Journal of Vacuum Science and Technology B 10*, 6 (1992), 2675.

[117] YAMAKI, M., AND MIWA, T. Efficient microtip fabrication with carbon coating and electron beam deposition for afm. *Journal of Vacuum Science and Technology B 10*, 6 (1992).

[118] YASAKA, A. Experimental study on the influence of liquid metal ion source energy districution on fib ind. depo. *Journal of Vacuum Science and Technology B 9*, 5 (1991).

[119] YAVAS, O. Field emitterr array fabricated using focussed ion and electron beam induced reaction. *Journal of Vacuum Science and Technology B 18*, 2 (2000), 976.

[120] YOUNG, R. Focused ion beam insulator deposition. *Journal of Vacuum Science and Technology B 13* (1995), 2576.

Chapter 3

The theory of EBID spatial resolution

3.1 The EBID spatial resolution - a general statement of the problem

An intriguing question in the field of electron beam induced deposition (EBID) is: what is the smallest structure that can be produced with this technique? Structures of 13-20 nm lateral size have been reported [69, 85, 51], but we know that electron beams with subnanometer size are nowadays available, so why are there no structures of subnanometer size produced until now? The typical answer found in literature explains this mainly with secondary electrons generated in the target and their range that exceeds the primary beam diameter. According to some authors the range of secondary electrons in the target limits the EBID minimum feature size to 15-20 nm [45, 51], but our feeling is that this broadening effect can be minimized.

Before beginning a discussion about fabrication resolution, we should first issue a definition for this important EBID characteristic. In measurements science, the resolution of a method is defined as the smallest value that can be obtained without errors. So let us assume that the finest electron beam is focused on a specimen and used to deposit dots by EBID method. Obviously the EBID fabrication resolution will be defined as a characteristic size of the smallest deposited dot, (see Fig. 3-1). Which size exactly should be considered here is still a controversial matter. Here we present different definitions as used in related fields, such as imaging in scanning electron microscopy, microanalysis in a transmission electron microscope or electron beam lithography.

One can define the EBID fabrication resolution as determined by the FWHM (full width at half maximum) of the radial density distribution [atoms/unit area] of the deposited dot (see Fig. 3-2 a). Another definition considers the FW50% of the integral of the radial distribution. This value, expressed in [atoms within a circle of radius r] is given by the diameter of the circle that contains 50% of deposited atoms, (see Fig. 3-2 b). In the particular case of a gaussian distribution of the dot spatial profile, these two definitions will coincide. In our research we will present both the FWHM and FW50% results.

A somewhat different definition is given in the practical assessment of the SEM imaging
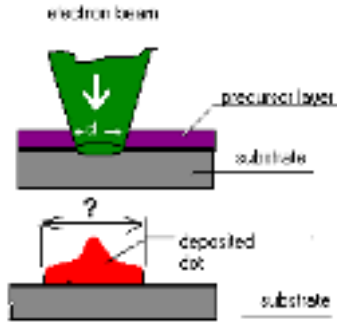
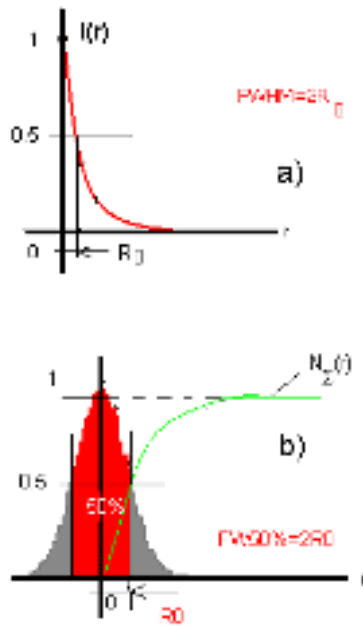Figure 3-1: Illustration for the definition of EBID fabrication resolution

Figure 3-2: Different possibilities to define the EBID fabrication resolution a) FWHM of the radial density distribution of the deposited dot $I(r)$ [atoms/unit area] ; b) FW50% of the normalized integral function of the deposited dot, $N_\Sigma(r)$ [atoms]

resolution, when not flat surfaces but fine heavy metal particles on light substrates are observed. The SEM *edge-to-edge resolution* is then defined as the minimum distance observable between two edges [25].

The definition of spatial resolution in TEM analysis is given by a relation between the beam spread in a thin film b, and the incident beam diameter d [137]. The beam diameter d is defined as the area where 90% of the electrons enter the specimen. The beam spread b has been subject of a lot of theoretical and experimental work. The single scattering model states that the beam spread in a thin film is given by [126]:

$$b = 7.21 \times 10^5 \frac{Z}{E_0} \left(\frac{\rho}{A}\right)^{1/2} t^{3/2} \text{ [cm]} \tag{3.1}$$

where t is the film thickness [cm], Z the atomic number, A the atomic weight and ρ the density [g/cm^3] of the target, and E_0 is the electron beam energy [keV]. This definition comprises 90% of the electrons emerging from the specimen. When the specimen has a more complicated geometry, Monte Carlo simulations can be used and the diameter of a disk at the exit surface of the specimen that contains 90% of the emerging electrons gives the beam spread. The spatial resolution is defined by adding b and d in quadrature:

$$R = \sqrt{b^2 + d^2} \tag{3.2}$$

This equation remained for a long time the standard definition. In the particular case of X-ray spatial resolution, based on the Gaussian model and experimental measurements, Michael [88] proposed that the definition of R be modified so as not to present the worse case but to define R midway through the foil, given by :

$$R = \frac{d + R_{\max}}{2} \tag{3.3}$$

where $R_{\max}$ is given by equation (3.2).

Another definition is given in the modeling of resist-based electron beam lithography. In this case, the fabrication resolution is given by the contour of the opening in the resist, made by the smallest electron beam after exposure and development, the so-called *dot exposure* or *beam-response* [40]. A simple resist solubility model is usually used, the threshold energy density model. Studying the energy deposited on the surface and comparing it to a threshold value gives the spatial fabrication resolution [43].

Identifying researchable problems

1. Let us draw a chart with the achievable EBID resolution, as shown in Fig. 3-3. The curve 1 shows the ideal situation, when the deposited dot sizes are equal to the diameter of the primary electron (PE) beam. The curve 2 contains some reported experimental data, showing the structure sizes plotted against the beam diameter used to deposit them. Regular sizes of 20-200 nm can be obtained with probe sizes between 2-100 nm. When analyzing this chart, the difference between curve 1 and curve 2 leads to a first question. What is the functional relation between the electron probe diameter and the deposited structure size? It is not a trivial
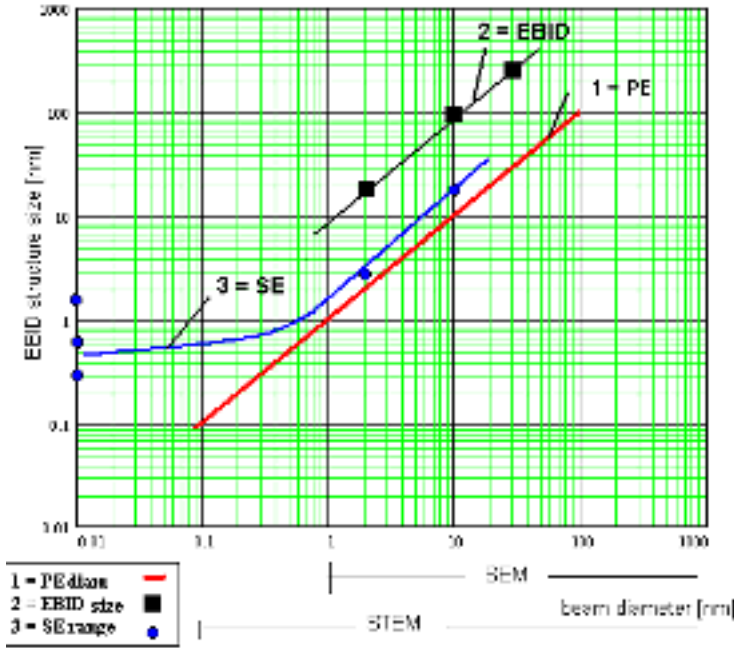
Figure 3-3: The achievable EBID resolution chart: Curve 1: an ideal situation: dot size = diameter of primary electrons beam (PE); Curve 2: experimental EBID feature sizes [67, 94, 51]; Curve 3: the calculated SE range on the target surface [25, 58, 56, 71].

problem, because the chart shows that this size is not directly given by the beam diameter. For example a 30 nm electron beam deposits a 250 nm diameter dot [67], a beam of 10 nm gives a dot of 100 nm diameter [94], 2 nm beam diameter gives a 20 nm diameter tip. [51]. It means that a theoretical model has to be built which takes into account more than only the incident electron beam parameters.

The current understanding of the EBID process often suggests that the main influence factor are the secondary electrons emitted at the target surface [51, 49, 77]. If we want to simply check this assumption, let us draw on the same chart the secondary electrons spatial range on the target surface, given by the curve 3. Actually we can only plot a cloud of secondary electron ranges due to the disagreement between different simulations [25, 58, 56, 71]. As we can see, taking into account the SE brings an improvement, curve 3 is closer to curve 1, but there is still a discrepancy. Our conclusion is that only the SE emitted from the target cannot explain the resolution currently achieved in EBID, given by curve 2. At this moment, the quantitative estimation of EBID resolution given by the beam, precursor and specimen parameters is a theoretical problem. A complete procedure of this kind that agrees with the experimental results has not been issued yet.

2. At this moment the left end of the EBID resolution curve 2 is given by the best reported experimental result: a linewidth of 13 nm, achieved in a SEM with an electron probe diameter of 2 nm [68]. Here the experimental results stop. Another question which is challenging our minds

is which way this curve will follow for smaller primary beams? Can this record be improved or have the fundamental resolution limits been reached? The theoretical modelling of EBID is a rather poorly explored field and this lack of fundamental results generated different and sometimes contradictory predictions of the ultimate resolution.

Some authors observed that in the particular case of tip growth, the fabrication resolution seems to be limited only by the primary beam diameter, so they promised higher resolution tips, provided a finer focused beam could be obtained [67, 50]. But this promise is valid as long as the beam diameter is larger than the secondary electrons range. It is possible that even if a finer primary beam will be achieved due to improvements of the electron optics, the emitted secondary electrons with their large spatial range will limit the size of ultimate EBID structure. This is the situation in SEM imaging. The same prediction has been given for PMMA conventional resist-based electron beam lithography. In that case, the ultimate fabrication resolution is fixed at about 10 nm [14] for beam energies from 20 keV to 120 keV.

If we succeed to solve the first challenge and develop an acceptable theoretical model of EBID, then we can contribute to the dispute concerning the future of the EBID resolution. The future evolution of the EBID curve 2 when the PE approaches and goes beyond 2 nm is still an open question. An important question, because nowadays the state-of-the-art transmission electron microscopes (STEM) can provide smaller probes than in SEMs, as small as 0.2 nm (e.g. the FEI Tecnai 20 series). Will the EBID resolution curve be limited the same way as the SEM imaging resolution or can it be forced to follow the primary beam size? The answer is not trivial because EBID differs from SEM, having two more active participants: the PE and the precursor. EBID is also a resist-less technique and these differences could be exploited to create a path to the higher fabrication resolution. This question generates two problems: the theoretical prediction and the experimental demonstration of EBID resolution limits.

Our first objective is:

The theoretical estimation of the deposited dot spatial profile for a given electron beam, precursor and target parameters.

Defining the strategy

The problem of predicting the deposited dot profile is similar to that of surface topography evolution during classical beam assisted lithography techniques (CVD, sputtering, etching). The surface profile simulators developed for this purpose are using, as mathematical background, string algorithms, level set methods or cellular automata [1, 7]. After a review of these methods, we conclude that whatever spatio-temporal technique we might choose, in order to predict the time evolution of the dot profile from initial moment T_0 to the final moment T_n, we need to know the deposition rate R(x) in any point on the surface, (see Fig. 3-4).

The deposition rate R(x) will be influenced by a number of factors that we will divide in two classes, depending on their accepted importance: the electrons and other factors (delocalization, surface migration of molecular fragments, surface plasmons, target temperature etc).

We will adopt the following strategy, summarized in Fig. 3-5. We will start with an assumption, noted A and we will calculate the profile of the smallest dot based on this assumption. The theoretically estimated size (T) will be compared with existing experimental data (E) and more factors will be introduced one by one, correcting the previous assumption until an agreement will be achieved within an acceptable accuracy $(E \approx T)$.

For example, we will start with the assumption that the main role in EBID is played by the electrons on the target and dot surface. Because we neglect the molecular fragments migration, the deposited dot will be formed in the precursor area damaged by electron radiation. If we suppose that electrons interact localized, i.e. only with adsorbed molecules situated on their
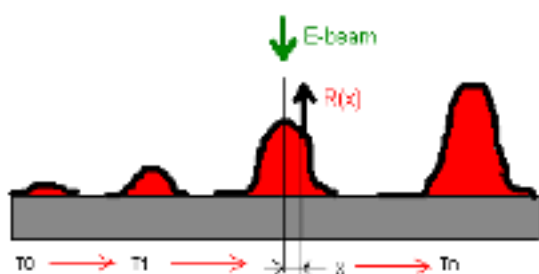
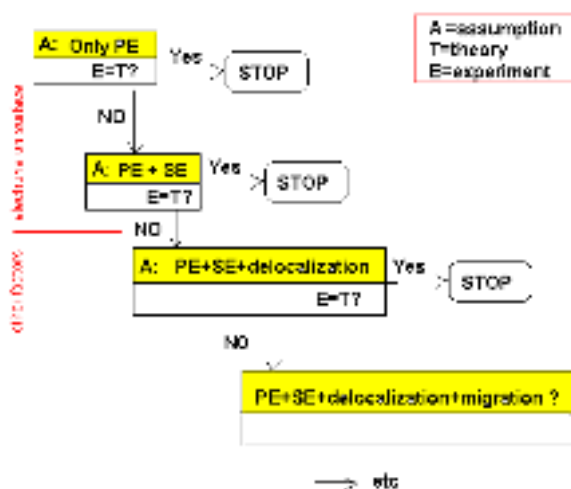Figure 3-4: The time evolution of the deposited dot boundary

Figure 3-5: The strategy adopted in solving the EBID resolution evaluation problem
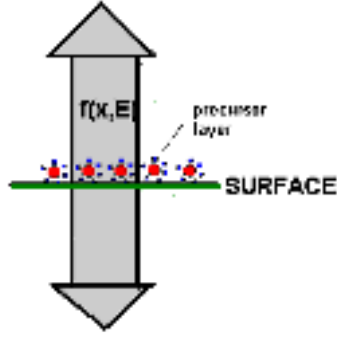
Figure 3-6: Illustration to the definition of deposition rate R(x)

trajectory and that the angle of incidence is not important then the damaged area will be given by the spatial distribution of the electrons on the surface, convolved with their "power" of dissociation.

The deposition rate R(x) under the action of an electron beam of energy E_0 at distance x from the beam central point of incidence can be expressed in molecules/unit area/sec and it is given by [75] :

$$R(x) = \int_0^{E_0} f(x, E)\sigma_{diss}(E)N\, dE \tag{3.4}$$

where

$f(x, E)$ = the flux of electrons passing through the surface as function of the position and energy [electrons/unit area/sec], see Fig. 3-6,

$\sigma_{diss}(E)$ = the electron-induced dissociation cross-section of the precursor molecule [unit area] as function of the incident electron energy,

and

N = the surface density of adsorbed precursor molecules [molecules/unit area].

The deposition rate can also be expressed in volume per unit area per second and it is given by [119]:

$$R(x) = \int_{\text{all energies}} f(x, E)\sigma_{diss}(E)NV\, dE \tag{3.5}$$

where

V = the volume occupied by a dissociated molecule.

83

As we can see from equations (4.1) and (3.5), in order to predict the deposited dot profile evolution, the following data will be necessary.

First, the total electron flux through the surface in the vicinity of the primary beam incidence point (spatial and energy distributions), $f(x, E)$. Because there is enough experimental evidence that not only primary electrons determine the structure size, both PE and SE surface distributions will be necessary.

Further, the electron-impact molecular dissociation cross-section as a function of the electron energy, $\sigma_{diss}(E)$ will be needed for the given precursor. In our case the precursor is an organometallic compound or a hydrocarbon complex. Unfortunately, there is only rather precarious information available about the electron impact dissociation cross-sections of different gases. More experimental data exist for electron impact ionization than dissociation, and usually for H_2, N_2, CO, CH_4, in general for gases abundantly present in the interstellar medium and planetary atmospheres. For some hydrocarbons (C_xH_y) the cross-sections have been measured or calculated. Recently collections of recommended data have been issued for gases used in plasma processing in microengineering. Some literature searching work will in this case be necessary.

The same type of modelling is found in resist based electron beam lithography. The contours developed in resist are controlled by two processes. On one side the electron scattering and the energy deposition in the resist film and on the other side the chemical etching and differential solubility of the irradiated film.

If the first results will show that the influence of electrons is not so strong that it can be solely held responsible for the broadening of the deposited structure, we will have to evaluate in detail the influences of other parameters on EBID resolution.

For example, we might have to consider the fact that a swift electron can interact with a target atom or a precursor molecule situated some distance away from its trajectory [89], (see Fig.3-7). The magnitude of this effect, known as delocalization of electron inelastic scattering, is still in dispute, but everybody agrees that it has to be considered, especially in the case of fine electron probes [61, 107]. The surface excitation problem in which an electron can excite a SE when it is still in vacuum, before entering the target needs also more research [27]. For this reason an extra analysis step will be introduced, estimating the eventual degradation of EBID resolution due to the delocalization of the electron inelastic scattering.
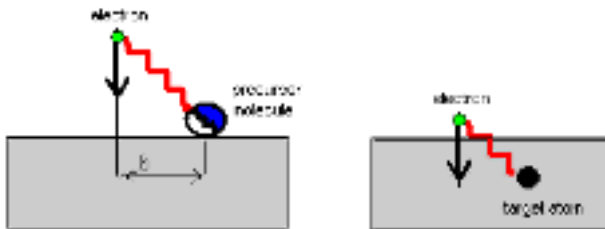

Figure 3-7: Illustration for the possible effects of the delocalization of electron inelastic scattering

Another deviation from the reality in our initial model is that migration of fragments created after electron-molecule impact is neglected. In reality, the ionized or dissociated fragments of

precursor molecule can get enough energy to hop on the surface before sticking definitely on a surface site and forming a deposit. An analysis of the influence of molecular fragment's migration on the surface might be necessary.

Depending on the result of these correction steps, one might take into consideration other influence parameters like surface plasmon decay, atoms clustering, electrons under the surface, charging effects, etc.

Conclusion

We will focus on the EBID fabrication resolution. We have localized an interesting problem - the theoretical estimation of EBID resolution and its fundamental limits. We have established a research strategy and based on this strategy, we can build an appropriate EBID model for the specimen- mediated electron beam interaction with the precursor (see Fig.3-8).

This objective will require an extended theoretical study in the following domains: A - the interactions between electrons and the adsorbed precursor molecules, B - the interactions between electrons and the solid matter and C - the interactions between the precursor and the substrate surface.

After building this model we can contribute to the dispute concerning the present and the future of the EBID resolution. In cases where not enough reliable experimental data is available to check our theory, we will have to perform such experiments ourselves.

Because the contamination and EBID phenomena are similar and contamination is a problem for high resolution surface analysis in electron microscopy, the results of this research will be useful for both direct electron beam deposition and electron microscopy.
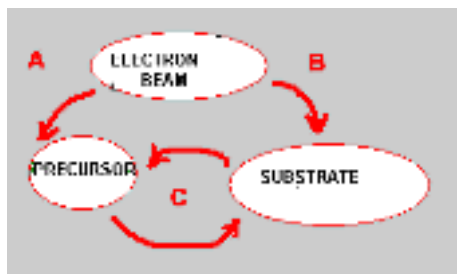

Figure 3-8: The EBID model based on the specimen mediated electron beam - precursor interactions

3.2 Relevant interactions between electrons and solid matter

A typical study of the electron-solid matter interaction starts with the incident electron beam, the so-called primary electrons (PE). The simplest representation of the primary electrons is the pin-point, zero-diameter, monoenergetic beam, usually incident normal to a solid target. It is not a realistic approximation, but it is a convenient simplification for the further study of the electrons scattering in the target. The primary electron current density distribution (or flux distribution) on the surface is a delta function in this case.

In reality the beam incident on the surface is two-dimensional and the current density distribution in the spot on the surface is usually modelled by a gaussian (or normal) function. The current density $I(r)$, expressed in electrons per unit area per unit time, is defined by the number of electrons striking the surface per second, at the radial distance r from the center of incidence:

$$I(r) = \frac{N_{total}}{0.38\pi d^2} \exp^{\frac{-r^2}{0.38 d^2}} \tag{3.6}$$

where

N_{total} = the total number of electrons crossing the surface per second,

r = the radial distance from the center [unit length]

d = the diameter of the beam distribution [unit length]

The diameter of the Gaussian beam distribution d, is usually defined as the diameter at half maximum (FWHM), which in the two-dimensional case is also the circle which contains half of the total current (FW50%). If we compare it with the gaussian beam standard deviation σ, then d = 1.67σ.

In Fig. 3-9 the surface flux of the primary incident electron beam in case of a gaussian beam of 2 nm diameter is plotted.
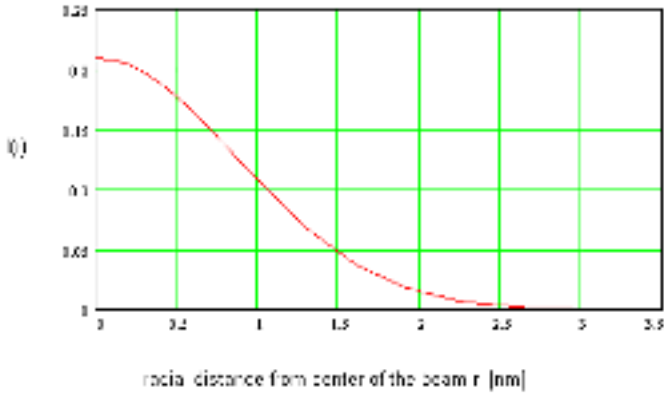

Figure 3-9: The normalized spatial distribution for a gaussian primary beam of diameter d = 2 nm.

When the primary electron beam hits a solid target covered with precursor molecules, a complex interaction scheme is generated, as shown in Fig. 3-10.

Let us analyze this typical EBID scheme and move "in the shoes" of the adsorbed precursor gas molecules. They can be dissociated by many species of electrons which happen to circulate in their proximity. Firstly, the incident primary electrons can interact with the adsorbed gas molecules and produce their dissociation. Further, it can be seen from the scheme that the primary electrons scattering through the target produce on their way secondary electrons which eventually emerge on the surface, labeled SE1 (zone 1). The primary beam also generates backscattered electrons (BSE), which in their turn can bounce further in the substrate and produce supplementary secondary electrons, labeled on the surface as SE2. This labeling of secondary electrons, used in [60], is of course artificial, taking as criteria their energy and exit position. From the scheme it is obvious that in addition to the PE (zone 2), the backscattered BSE and secondary electrons SE1 (zone 3) and SE2 (zone 4) can also induce decomposition of adsorbed precursor molecules, each species of electrons with a different cross- section and contribution to the deposited structure shape.
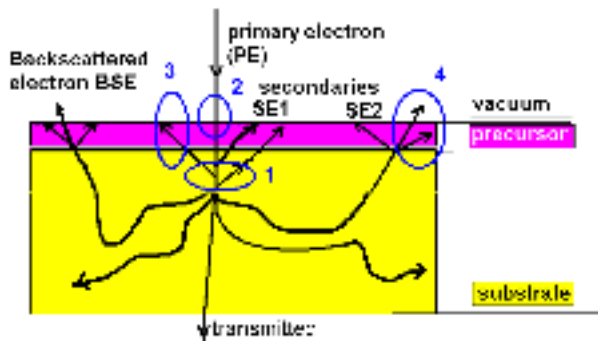

Figure 3-10: The typical EBID interaction electron-target-precursor interaction scheme.

3.3 Monte Carlo simulations for secondary electrons emission (MCSE)

The second usual suspect among the parameters that can influence the EBID resolution are the secondary electrons emitted from a target bombarded by the primary beam. Information about this secondary emission can be obtained by studying the electron scattering in the target. The problem of the electron-solid interaction should be ideally solved experimentally, by measuring the relevant physical quantities resulting from the primary beam bombardment. However, the interaction process remains partially unknown, due to the limitations of present experimental techniques. In this situation, simulations become the most powerful theoretical method, as an idealized replacement for an experiment.

The subject of secondary electron emission has been treated extensively in the past, mostly supporting the development in the scanning electron microscopy.

Three elements are necessary to simulate the secondary electrons: their generation, their transport and their escape from the target. Theories of secondary emission caused by electron bombardment have been given for many years using different methods. These theories can be divided in four levels of approximation. The first uses a simple empirical equation for SE emission and uses adjustable parameters for each material. A second one assumes an analytical model for the geometry of electron diffusion and yields the spatial or energy distribution of SE emission. For example Chung and Everhart [19] used a simple exponential decay law and quantum theory in order to obtain the energy distribution of SE. The third approach solves analytically or numerically the Boltzmann transport equation [5, 138, 24, 109, 112, 113] The fourth uses probability distributions to express each phenomenon in the production and propagation of SE and obtains by MC simulations the electron's trajectory in three dimensions [70]. After calculation of a large number of trajectories, the results are summed to obtain various physical quantities of SE. The theories become progressively more general in going from first to fourth.

Our main interest goes to the MC type of simulations, because they are lately very widely used and can be performed computerized using relatively simple mathematics..

Monte Carlo (MC) electron trajectory simulation techniques have been earlier studied by Koshikawa and Shimizu (1974), and constantly improved by Joy, Ding, Shimizu, Reimer, Murata, Kotera, Hovington, Ziegler etc. The method has been applied with success to electron probe microanalysis, electron spectroscopy, scanning electron microscopy and electron/ion beam lithography. The existing MC programs are of a half-commercial type, their use being restricted to a certain research group or institute. Usually authors publish their results in a graphical form and only partial descriptions of the MC procedures are given. A very elementary book about MC methods in general is [127]. A mathematical discussion on MC methods is given by James in [53]. A primer for the MC method applied in electron microscopy is the book of Joy [62] and a description of the procedures and useful formulae for MC in electron-probe microanalysis is given by Scott and Love [120], and by Henoc and Maurice in [44]. A review of MC methods used for secondary emission can be found in [122]. A very detailed description of a MC program for low energy electrons is given by [47, 48], supplying the information and the source codes also on the website *http://casino.gme.usherb.ca.casino.* Another series of MC programs have been written for high energy (100 keV - 1MeV) electron scattering in accelerators [132, 64]. They use the same models as in electron probe microanalysis but corrected for relativistic velocities. Some of these programs are for public use, like ETRAN, ITN, etc.

In this section we will present the widest used simulation technique for secondary electron emission, the Monte Carlo method. Some existing MC programs will be described, together with some of their results relevant for the EBID case. Some theoretical models and typical calculation procedures are given for a physicist interested in secondary electron emission and doing his own programming. The description of a typical MCSE program can be divided in two parts. The first one treats the data transfer between the computer program and its user. The second part is more programmer-oriented and treats the MC procedures and the physical background of the electron-target interaction.

3.3.1   The input data for a MCSE program

The typical electron-solid matter program considers a pin-point (zero-diameter) electron beam incident on a target situated in vacuum, as illustrated in Fig. 3-11. The necessary input data is usually: the energy of the primary electron beam E, the angle of incidence θ, the target thickness h and the material of the target, the number of simulated trajectories and the required
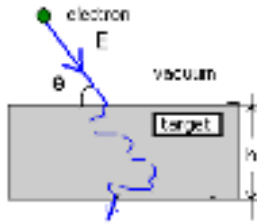
calculation accuracy.

Figure 3-11: The typical input parameters for a MCSE program

The quantitative modelling of the electron-solid interactions using MC techniques is only possible if there is sufficient experimental data on which to base the model and against which to test its predictions. The accuracy of the method depends among others on how accurate we know these parameters. That is the reason why, transparent for the user but of great importance for the programmer, adjacent information sources are needed, like data bases with target properties, dielectric functions, scattering or ionization cross sections, energy loss spectra, secondary electron yields, electron stopping powers, mean ionization potentials, etc. There have been efforts to build these kind of data bases. For example a typical data base for electron solid interactions is described by Joy [63]. There is still a need for more detailed and comprehensive sets of relevant data presented to the researcher in an accurate and convenient form.

The targets are bulk materials (typically 200-500 nm), usually metals like copper, aluminium, silver, gold or materials from semiconductor IC industry (silicon, silicon oxide, PMMA resist). In electron lithography the target is multilayered, a substrate of Si of different thicknesses and a typically 100 nm thick resist layer.

The primary beam energies are specific to SEM applications, typically 5-30 kV. For lower primary energies a new generation of MC programs is in progress [74, 73, 47, 48].

3.3.2   The output data of a MCSE program

While the MCSE program is running, a graphical display of PE and SE electron trajectories in the target is very often provided. This display has the disadvantage that it slows down the computation but it can be very useful as test for the programmer and as a visual tool for the user to estimate for example the electron interaction volume. The display can be made in the target cross section, projected in a plane parallel to the incident beam initial trajectory (YZ), or by showing the emission sites on the surface, clustered around the beam incidence point (XY). Some examples of both types of this direct visual assessment displays are given in Fig. 3-12. In modern programs the screen displays with electron trajectories can be saved in bitmap image files.

If the MC procedure considers a pin-point infinitesimal electron beam (PE) normal incident on the target, then the emerging secondary electrons (SE) will have a symmetric radial distribution around the incidence position. The target surface in the XY plane is then divided in concentric circles centered around the incidence point, having a distance dr between them. The
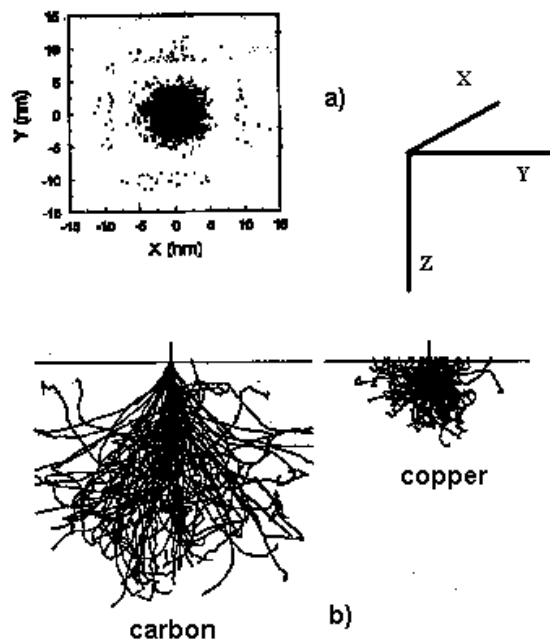
Figure 3-12: Examples of typical MCSE graphical display a) The emission sites on the target surface XY plane [from [76]]; b) The SE trajectories in the target YZ plane [from [59]]; The primary electrons are incident along the Z axis.
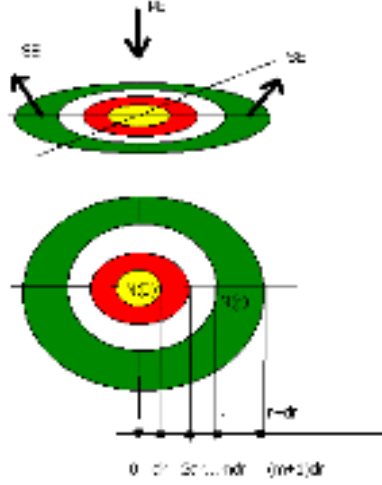
Figure 3-13: The geometry used by MC methods

direct results from MC simulation are the number of SE emitted from a ring between the circle of radius r and the next circle of radius $r + dr$, expressed in number of secondary electrons emitted per primary incident electron (see Fig.3-13). Let us denote this number by N(r) where r = 0, dr, 2dr, 3dr, ... mdr, m∈ N. We will try to make clear the format in which this data can be processed and graphically presented. Different plots are usually shown in articles, not always very clearly specifying what type of results they represent, making a comparison difficult or even impossible:

The radial distribution of outgoing secondary electron current, N(r)

N(r) represents the number of SE emitted in a ring between $[r, r + dr]$ per incident primary electron, which is the direct result from MC simulation. Here r is the distance of emergence of the secondary electrons with respect to the entrance point of the primary beam. If determined by numerical Monte Carlo simulations, $N(r)$ is a discrete function. Sometimes N(r) is plotted normalized.

The radial intensity distribution of the secondary electrons, I(r)

The radial intensity distribution of SE on the surface, $I(r)$, is the most frequently shown result of MCSE simulations, sometimes under the simple name of spatial distribution. It represents the number of SE emitted per unit area from a surface ring $[r, r + dr]$ situated at a distance r from the incidence point. It is expressed in [electrons/unit area/ incident primary electron] and it is defined by :
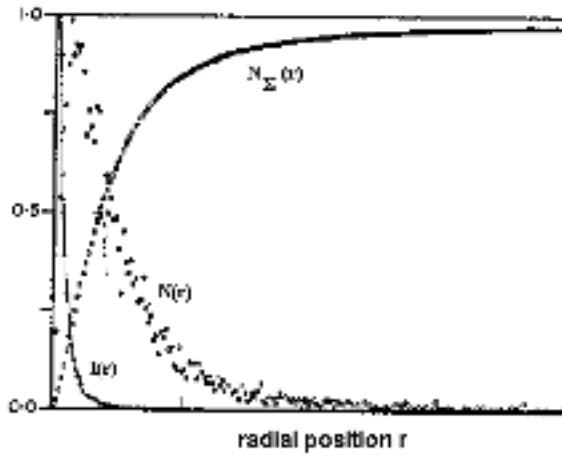
$$I(r) = \frac{N(r)}{A(r)} \tag{3.7}$$

91

Figure 3-14: Example of cumulated distributions for SE spatial distributions on the target surface; N(r) = the normalized radial distribution of outgoing SE current; I(r) = the normalized radial intensity distribution of SE; $N_\Sigma(r)$ = the normalized SE current from a circle of radius r (from [25])

where $A(r)$ is the area of the ring between a circle of radius r and a circle of radius $r + dr$:

$$A(r) = \pi(2r + dr)dr \approx 2\pi r dr \tag{3.8}$$

$$I(r) = \frac{N(r)}{\pi(2r + dr)dr} \approx \frac{N(r)}{2\pi r dr} \tag{3.9}$$

If analytically determined, I(r) is continuous and has a singularity in r=0.

The SE current emitted inside a circle of radius r, $N_\Sigma(r)$

$$N_\Sigma(r) = \sum_0^r N(r') \tag{3.10}$$

is the number of SE emitted from within a circle of radius r per incident primary electron, expressed in number of SE per unit length per incident primary electron. The curve $N_\Sigma(r)$ is asymptotic to the total number of emitted SE, equal to the SE yield or $N_\Sigma(\infty)$. The curve can be also plotted normalized and it is then asymptotic to 1.

92

The lateral distribution of SE on the surface, D(x).

The lateral distribution shows the number of SE emitted from a unit length, obtained by integration of the radial distribution I(r) in one direction parallel to the surface. For example if this direction is x, then the lateral distribution on the surface D(x) expressed in [electrons/unit length/incident primary electron] is:

$$D(x) = \int\limits_{-\infty}^{\infty} I(\sqrt{x^2 + y^2})dx \qquad (3.11)$$

If the SE radial distribution I(r) is a Gaussian function, it does not change by integration and the lateral distribution is the same as the radial intensity distribution.

An example of cumulated radial distributions of SE spatial distributions is shown in Fig. 3-14.

3.4 The MCSE programmer's guide

3.4.1 The MCSE basic procedure

We will move now in the shoes of the programmer of a MCSE simulation and we will present the typical information necessary to complete this kind of program. The programmer has to know how to write a typical MC program and he needs some theoretical models for secondary electron emission. After reading this chapter, a beginner will be able to understand the language used by MC authors in their articles.

Passing through the target, the electron will lose energy by excitation of plasmons, phonons, X-rays, secondary electrons etc., and will suffer a series of deflections as a result of close encounters with atomic nuclei. In Monte Carlo programs these processes are usually treated entirely independent. Monte Carlo simulation programs consider that the electron can suffer two possible types of scattering events: elastic and inelastic and between two processes the electron moves linearly, see Fig. 3-15.

An elastic scattering is assumed to produce only an electron deviation from its trajectory and no energy loss. An inelastic scattering happens as a result of electron interaction with the electrons from the target atoms and deviates the electron producing an energy loss. This energy loss can result in the generation of one or more so-called internal secondary electrons. These electrons will scatter in the target and eventually will be emitted from the surface, being registered as secondary electrons and contribute to the results of the MC simulation.

A typical MCSE procedure consists of tracing the electron between two successive scattering events. Before each collision, an electron is defined by its energy, position, and direction given by the cosines of angles with the axes of a three-dimensional coordinate system.

The essential problem of a MCSE program is to calculate the energy and direction of travel for each electron after it suffered a collision, based on the previous values. In this way, the path of the electron can be traced until it emerges from the sample or until it has lost so much energy that no other secondary particles can be generated.

Let us start, like the majority of MCSE programs do, with a primary electron normal incident on a target. First the program needs some input parameters, like the energy of the electron E_p, the thickness and material of the target and the number of simulated trajectories.
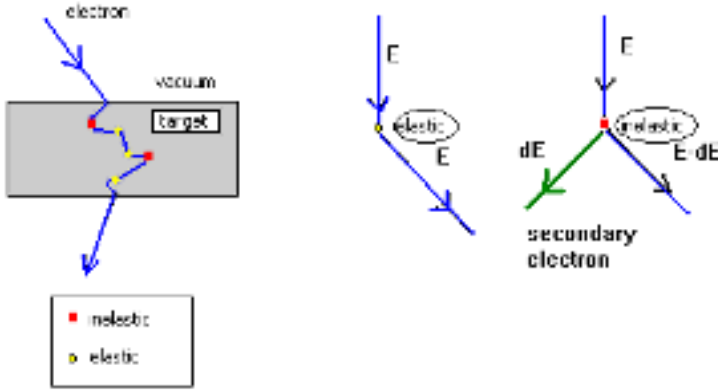
Figure 3-15: Typical electron scattering events in the target

The influence of the surface barrier is the same as the light refraction at the interface of two media. The primary electron penetrating the surface from vacuum modifies its energy E_p to:

$$E = E_p + U_0 = E_P + E_F + W \tag{3.12}$$

where E_p is the energy measured from the vacuum level and E is its energy measured from the bottom of the conduction band. U_0 is the inner potential and is equal to the sum of the Fermi energy E_F and the target work function W.

The usual MC procedure traces the primary electron step by step between two scattering events, until it reaches a target boundary or lost all its energy. We can consider that the path between the events is short, so that the electron moves linearly without losing energy and only one event takes place at a time. This is the so called single scattering model.

The geometry widely used in simulating the electron trajectory in the solid is shown in the Fig. 3-16.

The XYZ coordinate system is attached to the specimen and it is chosen such that the Z axis is normal to the specimen surface and directed towards the specimen, X axis parallel with the tilt axis of the specimen holder and X-Y the plane of the untilted sample [59]. After each event a coordinate system X'Y'Z' connected with the electron is generated from XYZ by rotation with angles θ and ϕ. The following scattering angles wil be then defined with respect to the X'Y'Z' system.

Let's consider the scattering event 1, (see Fig. 3-16). The previous event is 0 and the next scattering event will be noted with 2. Each electron before a scattering event 1 is characterized by an energy E, a position (X_1, Y_1, Z_1) and a direction given by the direction cosines of the trajectory segment 0-1 with respect to the XYZ axes $(cx_{01}, cy_{01}, cz_{01})$.

First we have to decide which kind of scattering event is 1 : elastic or inelastic. Secondly, after the scattering event 1 happens, some calculation steps are necessary.
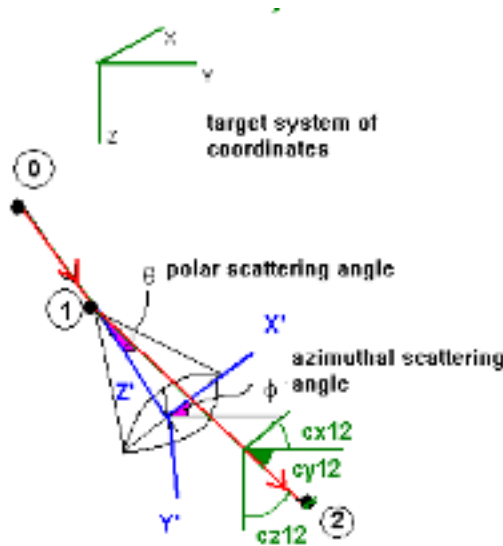
Figure 3-16: Typical geometry used to simulate the electron scattering in the target

If event 1 was elastic, we need the PE new direction, given by its scattering angles (polar θ and azimuthal ϕ). Also the new direction cosines cx_{12},cy_{12},cz_{12} can be calculated using the set of relations (3.13)-(3.19).

$$cx_{12} = cx_{01}\cos(\theta) + V_1 V_3 + cy_{01} V_2 V_4 \qquad (3.13)$$

$$cy_{12} = cy_{01}\cos(\theta) + V_4(cz_{01} V_1 - cx_{01} V_2) \qquad (3.14)$$

$$cz_{12} = cz_{01}\cos(\theta) + V_2 V_4 - cy_{01} V_1 V_4 \qquad (3.15)$$

$$V1 = AM\sin(\theta) \qquad (3.16)$$

$$V2 = AN \cdot AM \cdot \sin(\theta) \qquad (3.17)$$

$$V3 = \cos(\phi), V4 = \sin(\phi) \qquad (3.18)$$

$$AN = -\frac{cx_{01}}{cz_{01}}, AM = \frac{1}{\sqrt{1 + AN^2}} \qquad (3.19)$$

If event 1 was inelastic, a secondary electron is also generated. The energy and scattering angles for both electrons have to be determined. The new direction cosines can be calculated for both electrons using (3.13)-(3.19). The energy, position and direction data for the new secondary electron is stored in memory. The simulation of the PE continues with a new step until the next event 2.

The new electron position given by $x2, y2, z2$ is calculated using (3.20)-(3.22).

95

$$X_2 = X_1 + step \cdot cx_{12} \tag{3.20}$$

$$Y_2 = Y_1 + step \cdot cy_{12} \tag{3.21}$$

$$Z_2 = Z_1 + step \cdot cz_{12} \tag{3.22}$$

This sequence is repeated until the PE reaches a specimen boundary, escapes on the surface or its energy drops below the lower limit of the chosen energy window.

When the PE simulation is finished, the information about the stored secondary electrons is recalled and the trajectories are simulated in the same way as for PE. This time the transport of each generated secondary electron is simulated until it exits on the surface or comes to rest within the sample.

The essential problem is to determine after each scattering event the step length to the next event, related to the mean free paths for both elastic and inelastic scattering, the energy loss and the scattering angles. For all these quantities the theoretical models give us the scattering cross sections f(x), but we need an algorithm which can sample these parameters in conjunction with these cross sections.

It can be demonstrated in statistics theory that random numbers x which are distributed according to a certain function f(x) can be obtained from a uniform random number R between zero and unity, according to the equality :

$$R = \frac{\int\limits_{x_{min}}^{x} f(x)dx}{\int\limits_{x_{min}}^{x_{max}} f(x)dx} \tag{3.23}$$

Using this relation, and knowing the cross sections f(x) we can sample using a uniform random number R, for each scattering parameter x we need.

If the cross sections f(x) have a simple form, then analytical formulae relating x to R can be obtained.

In more difficult cases, when no analytical solutions exist, only numerical integration can solve the problem. In this case look-up tables have to be generated which will allow to pick a value x when a uniform random number R is generated. This approach needs a lot of memory, but it has the advantage of shorter computing time, because no on-line calculations are needed.

3.4.2 Theoretical models for electron scattering simulation

After an electron enters a solid target, a complicated cascade multiplication of electrons is generated. Because usually the secondary generation is simulated with a classical binary collision approximation, where only one secondary electron is generated after each inelastic scattering event, the cascade process can be simulated by the programmer with a binary tree data structure (Fig. 3-17).

Solving the full cascade collisions tree generated in the target is a titanic work, both for the computer and for the programmer. If we think that the distance between two events can be
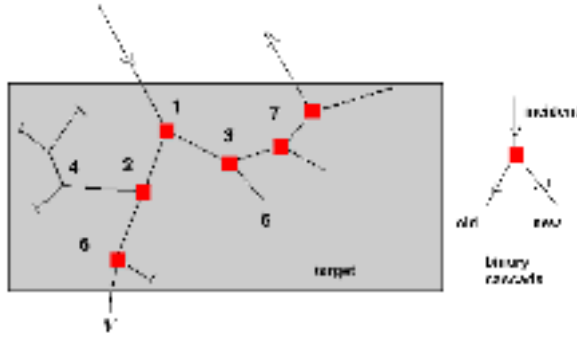
Figure 3-17: Electron trajectories in the target can be simulated by a binary tree data structure.

0.1-1 nm, and the specimens can be 1000 nm thick, we can imagine how many levels in the tree we have to follow only to simulate one electron trajectory.

Further, only a representation obtained from a large number of computed trajectories is a good approximation to experimental reality. The relative error of a MC simulation varies as $\sqrt{N}$, where N is the number of trajectories computed. Because a large number of trajectories needs to be calculated, the method becomes time consuming and to avoid this, different approximations were used in the past. Until recently, the computing time and memory capacity have been until recently an impediment against the simulation of the full interaction scheme. Nowadays, high speed computers, supercomputers and high memory capacities facilitate a fast progress towards the implementation of more complete models in MC simulations.

The computing time is not the only problem. Even if we have enough time, it is unknown how exactly the electron scatters in the target. Monte Carlo simulations of electron transport in a solid solves this problem by a stochastic description of the scattering process. The techniques use random numbers as a means of predicting the magnitude of various events (scattering angles, loss of energy by the electron) as well as to select between different scattering options. As the present state-of-the-art, it is particulary important to pay close attention to these simplifications which are often introduced in the model in order to reduce the complication of calculations or by neglecting the unknown distributions.

Approximative models for MCSE have been generated as time savers and as replacement for the unknown scattering phenomena. It has to be understood that there is not one single Monte Carlo approach, but a large number of models which differ by more or less arbitrary simplifications of the real process. The development of Monte Carlo modelling of electron solid interactions is a history of improvement to the approximations adopted to describe the elastic and inelastic scattering. A compromise has to be found between the accuracy needed and the time available.

A safe start for a MC programmer is to build simple programs using rough approximations, progressively introducing more realistic models, until the accuracy satisfies the application requirements. Various approximations have been issued to simplify the MCSE simulations. In the following section we will present some of these approaches organized according to the flow chart shown in Fig.3-18.
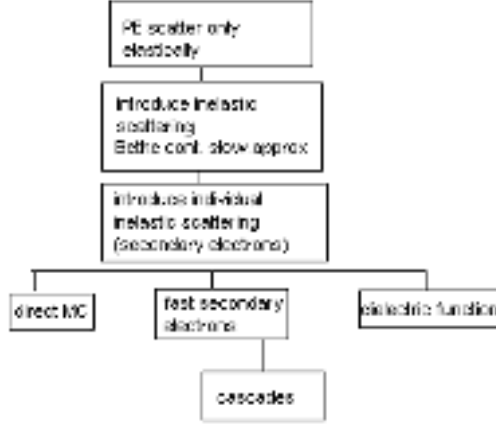
97

Figure 3-18: The flow chart for SE theoretical models

3.4.2.1 The elastic scattering

A very simple approximation considers that PE scatter in the target only elastically. The electron trajectory is a chain of liniar segments between two elastic events (see Fig.3-19).

The first unknown is the elastic mean free path, as function of the energy of the electron λ_{el}. After each elastic scattering event we will also need to determine the future direction of electron movement, given by the elastic collision scattering angles: polar angle θ and azimuthal angle ϕ. To determine these parameters we have two options, given by the Rutherford and Mott cross sections.

The Rutherford total cross section, corrected for relativistic effects and screening of the nucleus by inner shell electrons is for an electron of energy E, scattering through an angle θ is [62, 93]:

$$\sigma_{el} = 5.21 \times 10^{-21} \frac{Z^2}{E^2} \left(\frac{E + mc^2}{E + 2mc^2} \right)^2 \frac{4\pi}{\alpha(1 + \alpha)} [\text{cm}^2] \qquad (3.24)$$

where

E = the electron energy [keV]

θ = the polar scattering angle

α = the screening parameter.

mc^2 = the rest energy of the primary electron = 511 keV.

The screening parameter α takes into account the diminution of the net charge of the atom because of the effect of the atomic electrons and can be calculated using the relation [44]:
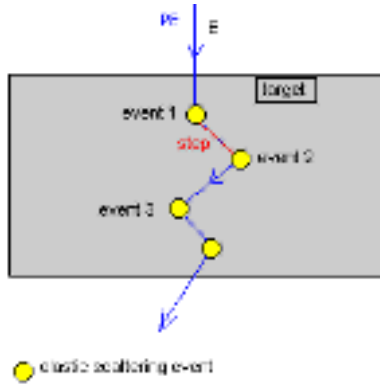
98

Figure 3-19: The primary electrons scatter only elasticaly

$$\alpha = \frac{3.4 \times 10^{-3} Z^{2/3}}{E} \qquad (3.25)$$

where Z is the atomic number of the target material and E is the electron energy in keV.
The polar scattering angle for a particular elastic collision can be found using relation [44] :

$$\cos(\theta) = 1 - \frac{2\alpha R}{1 + \alpha - R} \qquad (3.26)$$

where R is a random number uniformly distributed between 0 and 1.

The azimuthal angle ϕ can be assumed to be uniformly distributed because scattering in the radially symmetric field of the atom exhibits cylindrical symmetry:

$$\phi = 2\pi R \qquad (3.27)$$

where R is another uniform random number between 0 and 1.

The elastic mean free path between two elastic events can then be calculated as:

$$\lambda_{el} = \frac{A}{N_A \rho \sigma_{el}} [\text{cm}] \qquad (3.28)$$

where
A = atomic weight of the target [g/mole],
N_A = Avogadro number = $6.0221367 \times 10^{23}\,\text{mol}^{-1}$
ρ = the target's density [g/cm^3]

99

The step between two elastic events can be expressed as a function of a random number:

$$step = -\lambda_{el} \ln(R) \tag{3.29}$$

Since it has been found that the use of the Mott cross section is more satisfactory in the case of low energy electrons than the Rutherford cross section [123] the employment of the Mott cross section in the keV and sub-keV energy regions is now popular.

The relativistic representation of the Mott differential elastic cross section is expressed as:

$$\left(\frac{d\sigma_{el}}{d\Omega} \right)_{Mott} = |f(\theta)|^2 + |g(\theta)|^2 \tag{3.30}$$

where the element of solid angle $d\Omega = 2\pi \sin\theta d\theta$, and θ is the scattering angle. The total Mott relativistic screened elastic cross-section can be found by integrating eq. (3.30) over the range $0\theta\pi$. The f (θ) and g (θ) are the scattering amplitudes obtained from the partial wave expansion solution of Pauli-Dirac's equation instead of the Schrödinger equation used by Bethe. The partial wave method PWM can be used to calculate f and g. There is no analytical solution to this problem, but tabulated values with Mott coefficients are available for a few materials on request from the authors [21, 108]. But the data set for tabulated Mott cross-sections is large and computations tend to be slow, due to the need to interpolate between data points.

Browning and Gauvin [15, 38] proposed empirical equations for the total elastic cross section as substitute to tabulated Mott cross sections. The proposed form is very similar to the Rutherford screened cross section except for some correction coefficients (λ, β).

$$\sigma_{el}^{Mott} = 5.21 \times 10^{-21} \frac{Z^2}{E^2} \left(\frac{E + mc^2}{E + 2mc^2} \right)^2 \frac{4\pi\lambda(1 - e^{-\beta\sqrt{E}})}{\alpha(1 + \alpha)} \ [\text{cm}^2] \tag{3.31}$$

Usually graphics showing the ratio $\eta(\theta) = (\sigma_{el})^{Mott}/(\sigma_{el})^{Ruth}$ between the two types of elastic cross sections are given for each scattering angle θ. An example from [11] is shown in Fig. 3-20.

Conclusion

The Rutherford formula has been widely used because of its simplicity and usefulness. It results from the Coulomb screened potential treated by means of the first Born approximation. The theory is useful for SE spatial profiles for light element targets and high accelerating voltages, beyond several keV, but less effective for SE energy distribution and heavy element targets, particulary in the low energy region, where the Born theory breaks down. In these situations the Mott cross sections should be used.

3.4.2.2 The electron inelastic scattering.

In reality, the electron loses energy via inelastic scattering through interaction with the electrons of the target atoms. A widely used model that takes in consideration these interactions is the
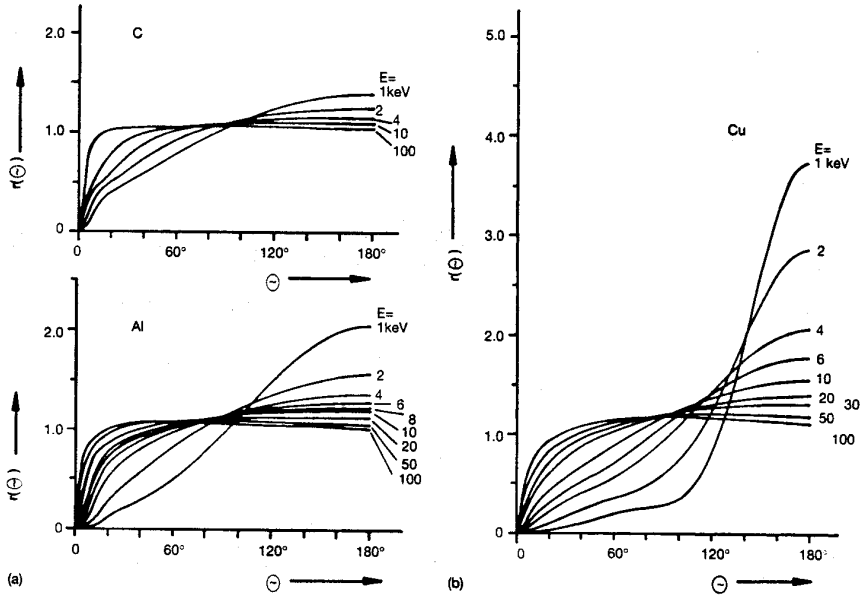
Figure 3-20: The curves $\eta(\theta) = (\sigma_{el})^{Mott}/(\sigma_{el})^{Ruth}$ for different materials and energies (from [11])
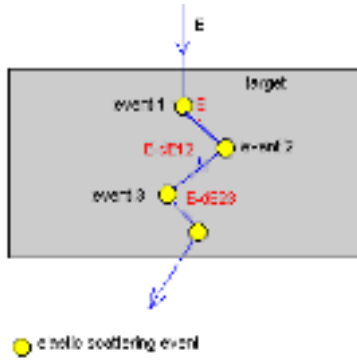
Figure 3-21: Illustration for the continuous slowing down approximation (CSDA)

so-called continuous slowing down approximation (CSDA). It assumes that the electron is losing continuously energy, slowing down as it travels through the target. In this way the effect of all individual inelastic scattering that happens between two elastic events is simulated.

The stopping power, defined as the rate at which the energy of the electron is lost, can be expressed very accurately in case of high energies (>10 kV) using the Bethe equation [122]:

$$\frac{dE}{ds} = -\frac{2\pi e^4 N_A Z \rho}{EA} \ln\left(\frac{1.166E}{J}\right) \ [\text{kV/cm}] \tag{3.32}$$

where
s = the electron path length [cm]
E = the energy of the incident electron [kV]
J = mean ionization potential of the target material [kV]
ρ = the density of the target material
A = the atomic weight of the target material (g/mol)
N_A= Avogadro number
Z = the atomic number of the target
e = the electron charge

The mean ionization potential of the target material J can be found analytically using the empirical formula [59, 80, 71]:

$$J = 9.76Z + 58.5Z^{-0.19} \tag{3.33}$$

where Z is the atomic number of the target material.

Rao-Sahib and Wittry [105] proposed a relation that uses the Bethe equation for energies E > 6.338 J and an extrapolation for energies lower than the mean ionization potential, E < 6.338 J :

$$\frac{dE}{ds} = -\frac{2\pi e^4 NZ}{1.26(JE)^{1/2}} \tag{3.34}$$

A semi-empirical stopping power for electron energies above 50 eV was recently proposed by Joy and Luo and very widely used by MC programmers. Luo and Joy modified the Bethe formula and corrected it for energies lower than the ionization potential as follows [80]:

$$\frac{dE}{ds} = -78500\rho\frac{Z}{AE}\ln\left(\frac{1.166(E+kJ)}{J}\right) \;\; [kV/cm] \tag{3.35}$$

where s = the path length along the trajectory [cm]

and k = a variable whose value depends on the material. k is always close to, but less than unity. For example k= 0.851 for Au, 0.852 for Ag, 0.83 for Cu, and 0.851 for Al. [80]

The energy lost by the electron between two elastic events situated at distance *step* is then:

$$\Delta E = step\frac{dE}{ds} \tag{3.36}$$

Evidently the Bethe continuous slowing down approximation lacks physical background. But nevertheless Monte Carlo simulations based on the conventional model which uses the Rutherford differential cross section for elastic scattering and the Bethe equation (CSDA) for inelastic scattering, have been successfully used to solve difficult problems in electron beam lithography and electron beam microanalysis [46]. But when the primary energies become several kV or lower, the model cannot be used anymore. The lower the electron energy, the lower the accuracy of the Bethe approach.

At low electron energies the stopping power can be computed from the imaginary part of the dielectric function obtained either by electron energy loss spectrum (EELS) measurement or optical measurement of the refractive index.

The generation of secondary electrons

Until now we could get an idea about the scattering of PE in the target but we don't know anything about the secondary electrons. The next model uses a stricter theory, that replaces the global energy loss between two elastic events, based on the CSDA, with individual inelastic scattering events. As result of these inelastic collisions, the so-called internal secondary electrons can be generated. These secondary electrons can scatter in the target and eventually emerge on the target top surface registered by the MC program as secondary electrons (Fig 3-22). Conventionally the true secondary electrons are those with energies between 0 and 50 eV at the surface.

In this model, PE can suffer two types of possible events: elastic or inelastic scattering. The PE trajectory in the target is a chain of linear segments between two successive interactions.

The length of the linear segments, i.e. the step between the events is Poisson distributed and can be sampled using a uniform random number:
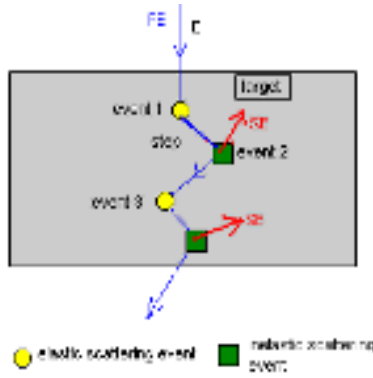
Figure 3-22: Introducing the secondary electron generation

$$step = -\lambda_T \ln(R) \qquad (3.37)$$

where λ_T is the total mean free path which is related to the corresponding elastic (λ_{el}) and inelastic (λ_{inel}) mean free paths through [122]:

$$\frac{1}{\lambda_T} = \frac{1}{\lambda_{el}} + \frac{1}{\lambda_{inel}} \qquad (3.38)$$

The interaction sampling, i.e. the type of event (elastic/inelastic) will be also determined using a random number as follows. If R is a random number between 0 and 1, the interaction will be elastic if $R < \frac{\lambda_T}{\lambda_{el}}$, and inelastic otherwise.

A new unknown appeared, the inelastic mean free path, λ_{inel}. Because it can play a crucial role in the spatial results of the simulation, we will give special attention to this parameter.

The inelastic mean free path (IMFP).

$\lambda_{inel}(E)$ is the inelastic (electron-electron) mean free path (IMFP) of the electron of energy E in the solid, i.e. the distance it can travel between two inelastic collisions. This quantity depends also on the material and can be calculated or measured but is still a subject of discussion. Some authors take in their MC programs an average value for this parameter, as for example 0.5 nm for Cu targets, [70]. But in reality, IMFP varies with the electron energy and a few analytical expressions are given. The ideal situation for MCSE would be a universal predictive formula valid for a large number of materials and energies.

Early calculations of electron IMFP were based on the "jellium model" for a solid. The only parameter in this model was the valence electron density, often expressed in terms of r_s, the average interelectron spacing. For example in the beginning of SE emission studies, Chung [19] used such a relation, proposed by Quinn and Kanter, valid for metallic targets:

$$\lambda(E) = \frac{14.7(Ep\beta)^{3/2}E(E - E_F)^{-2}}{(m^*)^{1/2}(\tan^{-1}(1/\beta)^{1/2} + \beta^{1/2}/(1+\beta)} \quad [\text{Å}] \tag{3.39}$$

where

E = the electron energy [eV] ,

E_F = the Fermi energy of the target material [eV],

$\beta = (4/9\pi)^{1/3}$,

$r_s = (3/4\pi na_0^3)^{1/3}$ = radius of the volume element per electron, measured in units of the first Bohr radius,

m* = the effective mass of the electron, measured in units of the free electron mass

a_0 = the first Bohr radius 0.529 Å.

Later, Seah and Dench published a compilation of electron IMFP values measured for a lot of solid targets. Based on this collection of data, they also proposed some still very widely used empiric formulae, valid for electron energies between 1 and 10000 eV. According to Seah and Dench, the inelastic mean free path for elements is [121]:

$$\lambda_{inel}(E) = a_0 \left(\frac{538}{(E - E_F)^2} + 0.41(a_0(E - E_F))^{1/2} \right) \quad [\text{nm}] \tag{3.40}$$

for anorganic compounds:

$$\lambda_{inel}(E) = a_0 \left(\frac{2170}{(E - E_F)^2} + 0.72(a_0(E - E_F))^{1/2} \right) \quad [\text{nm}] \tag{3.41}$$

for organic compounds:

$$\lambda_{inel}(E) = \frac{10^6}{\rho} \left(\frac{49}{(E - E_F)^2} + 0.11(E - E_F)^{1/2} \right) \quad [\text{nm}] \tag{3.42}$$

where

$a_0 = 10^7 \left(\frac{A_{mol}}{n_A \rho N_A} \right)^{1/3}$ = the average thickness of a monolayer [nm]

E = the energy of the electron with respect to the bottom of the conduction band [eV]

E_F = the Fermi energy of the target material

ρ = the target density [g/cm^3]

A_{mol} = the molar mass [g/mol]

n_A = the number of atoms in a compound molecule

$N_A = 6.0221367 \times 10^{23} \, \text{mol}^{-1}$ = the Avogadro number

In Fig. 3-23 we have plotted the IMFP for a carbon target ($E_F = 20 \ eV$), using the Seah and Dench formula (3.40), where E is the electron energy with respect to the bottom of the conduction band.

The IMFP can also be indirectly calculated from the measured EELS or the experimentaly obtained dielectric function. The results usually agree with the empirical Seah and Dench formula.
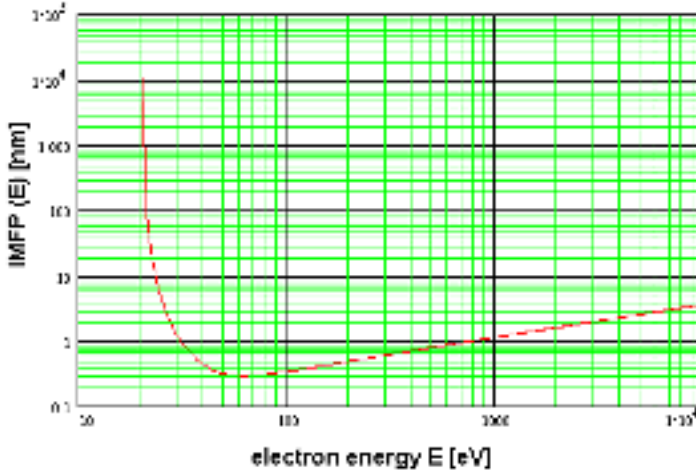
Figure 3-23: The inelastic mean free path (IMFP) of electrons in a carbon target, plotted as a function of electron energy E, measured from the bottom of the conduction band

The theoretical treatment of SE emission is based on the conception of a three stage mechanism consisting of the generation, transport and escape in the vacuum.

3.4.2.3 The SE generation

Secondary electrons are generated as result of electron inelastic scattering in the target. Inelastic scattering produces excitation of atomic electrons in the jellium and an energy loss of the incident electron. The secondary electrons can be created as result of different electron-induced processes in the target, artificially divided in single electron excitations (valence or conduction electrons, core electrons) and collective plasma excitations (decay of a volume or surface plasmon), each process happening with a specific cross-section. Usually it is assumed that each inelastic scattering generates a secondary electron and the energy of the SE is the energy lost by the PE. Thus, in each inelastic scattering two electrons are involved: the primary electron PE and the secondary electron generated SE.

To implement this model in a Monte Carlo simulation, we need, (see Fig. 3-24):

-for the primary electron: its energy after scattering $E_{PE} = E - \Delta E$ and its scattering angles $(\theta, \phi)_{PE}$

-for the secondary electron: its initial energy $E_{SE} = \Delta E$ and initial direction $(\theta, \phi)_{SE}$

We wil present different approaches to solve this problem.

3.4.2.3.1 The direct model The direct method treats artificially each type of excitation individually and defines a cross section for each type of excitation. The total cross section is then the sum of the partial cross sections based on an observation by Ritchie [110], who found that the stopping power described by Bethe's equation is the summation of stopping powers for each excitation mechanism. The direct method can be applied for high energy incident
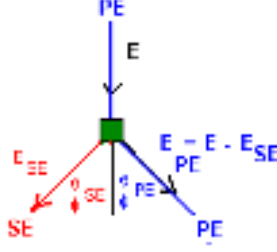
Figure 3-24: The secondary electron is generated in an inelastic scattering event

electrons.

For metal targets, the main SE generation mechanism is the excitation of conduction electrons. Most existing simulations consider only the SE generated by this excitation process. More detailed models consider also the other generation mechanisms, like ionization of inner-shell (core) electrons, the plasmon decay, etc. with corresponding cross-sections. The type of particular excitation is sampled using again a uniform number R.

For metals bombarded by electrons, Streitwolf [130] gives the differential cross-section for conduction electron excitation $d\sigma_{inel}/d(E_{SE})$ [46, 5, 124]:

$$\frac{d\sigma_c(E_{SE})}{d(E_{SE})} = \frac{e^4 N \pi}{E(E_{SE} - E_F)^2} \tag{3.43}$$

where N is the Avogadro number and E_F the Fermi energy.

The total energy loss cross section $\sigma_c(E_{SE})$ can be obtained by integrating the Streitwolf differential cross section between the lower limit $E_F + W$ and the upper energy limit Ep, by using a random number R, between 0 and 1 and the inversion formula (3.23). The obtained relation samples the energy of the secondary electron with the random number R [70, 71] :

$$E_{SE}(R) = \frac{RE_F - A(E_F + W)}{R - A} \tag{3.44}$$

$$A = \frac{E_P - E_F}{E_P - E_F - W} \tag{3.45}$$

This relation is ready to use in Monte Carlo simulation programming. This kind of relation is what the programmer needs and sometimes it takes a lot of work to obtain them starting from the theoretical expression of the differential inelastic scattering cross section $d\sigma_{inel}/d(E_{SE})$. In this formula all the energies are calculated from the bottom of conduction band. In Fig. 3-25 we plotted the excitation function for SE as a function of a uniform random number R between 0 and 1, for different incident electron energies, as given by the Streitwolf formula (3.44) and (3.45), with all energies calculated from the Fermi energy level.
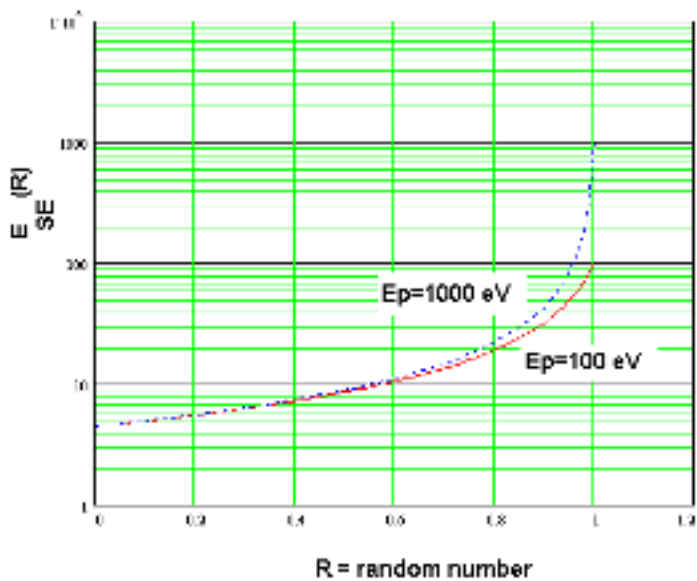
Figure 3-25: The secondary electrons excitation function as a function of a random number R between 0 and 1, $E_{SE} = f(R)$ plotted for different incident electron energies 100 eV and 1000 eV. The enrgies are given with respect to the Fermi energy level.
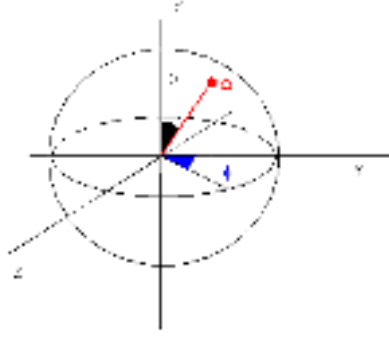
Figure 3-26: A random direction in space

If the energy of the secondary electron at generation equal to the energy lost by the primary electron is known, the next question is how are the two electrons oriented in space? The simplest approximation, the isotropic approximation, assumes that after each inelastic event no deviation occurs to the high energy electrons (PE) and that the low energy electrons (SE) are generated isotropically. It means that after an inelastic event the PE does not change its direction $(\theta_{PE}0, \phi_{PE}0$), an approximation valid especially for high energy electrons incident on thin films. Also the SE are isotropically generated, i.e. all the directions of motion of an excited internal SE are equally probable, which is a reasonable aproximation for electrons below 100 eV.

The electron direction can be specified by a unit vector from the origin whose endpoint lies on the surface of the unit sphere. The words "all directions are equally probable" mean that the endpoint Ω is a random point uniformly distributed on the surface of the sphere, see Fig. 3-26.

In the spherical coordinates (θ, ϕ) on the sphere, we have for the polar scattering angle of the secondary electron:

$$\cos(\theta_{SE}) = 2R_1 - 1 \tag{3.46}$$

and the azimuthal angle of SE is :

$$\phi = 2\pi R_2 \tag{3.47}$$

where R_1 and R_2 are two different random numbers between 0 and 1.

More accurate results can be obtained if the classical binary collision approximation is used, that results from the energy and moment conservation. The azimuthal angle is again assumed isotropic.

For the incident electron, we have:

$$\sin(\theta_{PE}) \quad = \quad \sqrt{\frac{\Delta E}{E}} \tag{3.48}$$

$$\phi_{PE} \quad = \quad 2\pi R \tag{3.49}$$

where ΔE is the energy lost by the incident electron.

For the secondary electron SE the scattering angles can be calculated as follows::

$$\sin(\theta_{SE}) \quad = \quad \cos(\theta_{PE}) \tag{3.50}$$

$$\phi_{SE} \quad = \quad \pi + \phi_{PE} \tag{3.51}$$

3.4.2.3.2   The fast secondary electron (FSE) model   The isotropic approximation holds for so called slow internal SE with energies lower than 100 eV. Slow electrons are ejected from the conduction or valence bands of the atoms in the specimen. But sometimes high energy electrons can be generated, receiving a large fraction of beam energy, up to E/2. These high energy electrons are named fast secondary electrons (FSE). The FSE model starts from the free-electron model and the Coulomb interaction between the incident electron and the free electrons of the target atoms. In this approach, the generation process is not isotropic, as previously assumed, but predominantly at relatively high angles to the beam direction [56].

The fast secondary electrons (FSE) will broaden the spatial distribution of SE obtained in the isotropic approximation and thus degrade the spatial resolution in microanalysis in electron microscopy and in electron beam lithography [91]. Joy used this model and obtained results situated in the middle of the range of numerical values spanned by other formulations and gives thus a good estimation of SE spatial distribution.

The differential cross section per electron for the FSE excitation proces is :

$$\frac{d\sigma}{d(E_{SE})} = \frac{\pi e^4}{E^2}\left(\frac{1}{\varepsilon^2} + \frac{1}{(1-\varepsilon)^2}\right) \tag{3.52}$$

where E is the primary electron energy and $E_{SE} = \varepsilon E$ is the energy of the SE generated .

Integrating equation(3.52) between 0.001 E and 0.5 E, the energy of the FSE can be sampled by using a random number R between 0 and 1 according to the relation [62]:

$$E_{SE} = \varepsilon E = \frac{1}{1000 - 998R}E \tag{3.53}$$

where all energies are measured from the bottom of the vacuum level.

In order to compare different approaches, in Fig. 3-27 we plot the energy excitation function for the fast secondary electrons given by (3.53), where all the energies are calculated from the Fermi energy level..
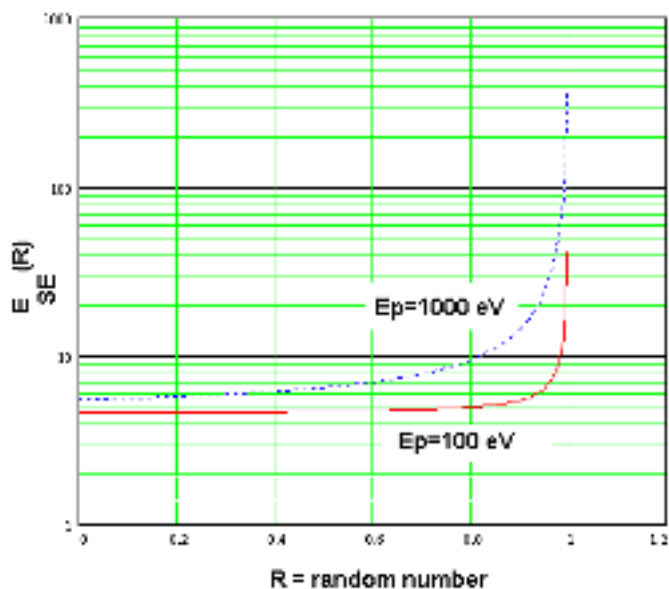
Figure 3-27: The energy of the fast secondary electrons $E_{SE}(R)$ as a function of a random number R between 0 and 1, for two different primary beam energies. The energies are given with respect to the Fermi energy level.

Knowing the FSE energy, from the conservation of energy and momentum the scattering angles for PE and SE can be obtained, the same way as in the binary collision approximation.

The polar scattering angle of the primary electron after the collision is:

$$\sin^2(\theta_{PE}) = \frac{2(1-\varepsilon)}{2+\tau\varepsilon} \tag{3.54}$$

where $\tau = E/mc^2$.

The polar scattering angle of the fast secondary electron after its generation is:

$$\sin^2(\theta_{SE}) = \frac{2\varepsilon}{2+\tau-\tau\varepsilon} \tag{3.55}$$

3.4.2.3.3   The dielectric function model   Up to now, all the models for SE generation needed fitting coefficients to get the correct secondary electron yields. Therefore a unified treatment of electron inelastic scattering and SE generation is quite necessary. The best approach should be based on the dielectric function which characterizes an excitation process specific to the sample. Bethe stopping power theory is not necessary anymore if the dielectric approach is used.

The dielectric function $\varepsilon(\omega, q)$ describes a dielectric response of a material to an external perturbation such as an electromagnetic wave or an incident electron. It is an attractive approach because it uses a measurable feature of the target material and thus it includes almost all excitation mechanisms (valence electron excitations, conduction, plasmons, but not core ionizations).

Ding showed that if the cascades of secondary electrons are included, very good results can be obtained. The dielectric function is very useful for MC simulations of electron inelastic scattering, the best simulation for SEM application. Ding presented a very good model based on dielectric theory [27, 26]. Secondary electron yields which agree with experiments are thus obtained.

The theoretical formulation of inelastic scattering of an incident electron in a solid has been well established in terms of the dielectric function in which the differential cross section for inelastic scattering is given by [26]:

$$\frac{d\lambda_{inel}^{-1}}{d(\Delta E)dq} = \frac{1}{\pi a_0 E} \, \mathrm{Im}\left(\frac{-1}{\varepsilon(\omega, q)}\right) \frac{1}{q} \tag{3.56}$$

where q is the momentum transfer from an incident electron of energy E to the solid, causing an energy loss of $\Delta E = \hbar\omega$, a_0 is the first Bohr radius and $\mathrm{Im}\left(\frac{-1}{\varepsilon(\omega,q)}\right)$ is the energy loss function (ELF).

The energy loss function completely determines the probability of an inelastic scattering event, the energy loss distribution and the scattering angle distribution necessary for MC simulation. The ELF can be obtained from optical measurements or from electron energy loss spectroscopy (EELS).

Optical data has been compiled for a number of materials giving the optical constants n

and k, where n and k are the real and imaginary part of the refractive index. The optical ELF corresponding to q=0 can then be determined as:

$$\varepsilon(\omega, 0) = (n + ik)^2 \tag{3.57}$$

From the optical dielectric function $\varepsilon(\omega, 0)$ a dispersion relation is needed to obtain $\varepsilon(\omega, q)$. For example Penn [98] suggests the bulk plasmon pole approximation: $\omega_q = \omega_p + \frac{\hbar q^2}{2m}$.

Then the ELF for other $q \neq 0$ is given by:

$$\mathrm{Im}\left(\frac{-1}{\varepsilon(\omega, q)}\right) = \frac{\omega - \hbar q^2/2m}{\omega}\mathrm{Im}\left(\frac{-1}{\varepsilon(\omega - \hbar q^2/2m, 0)}\right) \tag{3.58}$$

The energy of SE as well as its scattering angle can be sampled by integrating (3.56) and using random numbers. At this moment there is no analytical inversion formula which can be applied for all materials and this is a disadvantage compared with Streitwolf or FSE formulae. Numerical integration of the inelastic cross section is needed for each material and it involves time consuming procedures. An inversion algorithm which builds look up tables seems to be the only alternative [31, 74, 73, 26].

As an example we used the dielectric model [26] to calculate the energy of SE as a function of a random number R, for a Cu target. We started with the optical dielectric function $\varepsilon(\omega, 0)$ where $n(\omega)$ and $k(\omega)$ have been taken from a handbook of optical data [96]. A bulk plasmon pole approximation dispersion relation has been used to obtain the extrapolated dielectric function $\varepsilon(\omega, q)$ for $q \neq 0$. The inelastic cross section has been numerically integrated. In Fig. 3-28 we plot the dependence of the SE energy of the random number R between 0 and 1, for two incident beam energies, as given by the dielectric function approach. All the energies are calculated with respect to the Fermi energy level.

If we compare this result with the other two models exposed earlier, specific for slow and fast electrons respectively, we notice that in dielectric function approach, the SE have a chance to receive all energies ranging from W up to the energy of the primary electron, making this model the most realistic one and free of approximations. As expected though, most of the SE however have energies between 0 and 50 eV.

A disadvantage of this approach is that it can be used only for materials of known dielectric constant. It can be used only for so called free electron materials but it is hardly applicable to heavy and noble materials. But recent rapid progress in synchrotron radiation facilities enables the provision of databases of optical dielectric constants $\varepsilon(0, \omega)$ for a wide range of materials.

Even the dielectric function approach is complicated, because close to the surface, surface plasmons can be generated, so the dielectric function should be a function of the depth in the material. Pijper and Kruit [99] showed that surface plasmons play a significant role in SE emission.

3.4.2.4 The SE transport towards the surface

Now that we know the energy of the generated SE and its initial direction, we will follow its transport in the target.

The straight line approximation model (SLA) is a very simple transport model, proposed
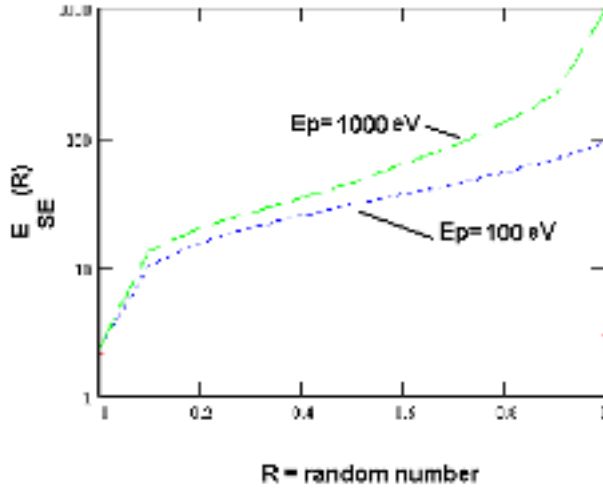
Figure 3-28: The SE energy as a function of a random numbrer R between 0 and 1 for different incident beam energies (100 eV and 1000 eV), as given by the dielectric model. All energies are given with respect to the Fermi energy level.

by Chung and Everhart [19]. It considers that after generation, SE moves straight linearly to the surface. It is assumed that scattering in the electron gas in the solid produces immediate absorbtion, so that a scattered SE is absorbed and not counted anymore. This assumption is realistic for low energy SE. As the energy of the excited electron increases, the assumption becomes more approximative.

In the SLA, the adsorbtion effect of the target via scattering by the lattice and energy losses in collisions with conduction electrons is quantified by $p(E, z_0)$ the probability that a SE of energy E, generated at depth z_0, moving in a direction θ, will reach the surface unscattered (see Fig. 4-7).

$$p(E, z_0) = e^{-\frac{z_0}{\lambda_{inel}(E)\cos(\theta)}} \tag{3.59}$$

This is the so-called exponential decay: A compromise approach can be used to improve this approximation, if we consider that SE scatter only elastically until the surface is reached, ressembling a diffusion-like transport (see Fig. 3-30).

In reality the exponential decay is the statistical result of a cascade process The straight line approximation can be improved using a more complete model, which takes into account the cascades produced by the internal SE on their way to the surface. In this way we are getting closer to the complete scheme proposed in the beginning of this chapter. In fact the scattering of excited SE does not produce adsorbtion of all these SE. SE generate cascade multiplications (see Fig.3-31) . These cascades become important for low energy internal SE < 100 eV. A classical cascade model has been proposed by Koshikawa and Shimizu in [70] and was later
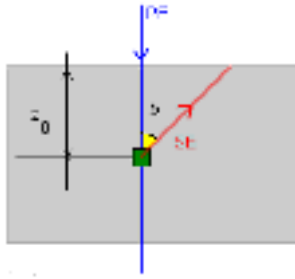
114

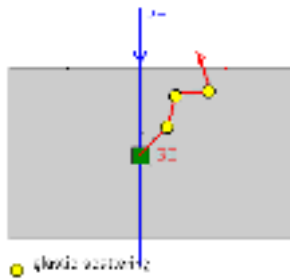Figure 3-29: In SLA the SE propagates linearly towards the surface

Figure 3-30: The SE scatter elastically on their way to the surface
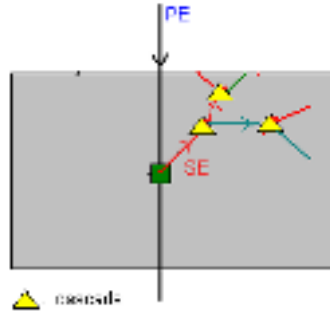
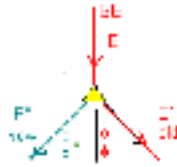Figure 3-31: Introducing the cascade multiplication of SE in the target

Figure 3-32: Illustration of a cascade multiplication

used by almost all authors. This model is based on the classical binary collision approximation. It assumes that the scattered SE suffers an inelastic collision with the target atom and thus 2 secondary electrons are generated: the old one, with energy E' and the new one, with energy E".

According to this model, that neglects the binding energy of the atomic electron, the energy of the incident electron after collision is:

$$E' = E\cos^2(\theta')$$ (3.60)

where θ' is the old electron scattering angle (see Fig. 3-32). On the other hand, assuming spherical symmetric scattering in the center of mass system, Wolff showed in [138] that the average electron energy after scattering E' is related to the electron energy before scattering E as follows:

$$E' = E\sqrt{R}$$ (3.61)

where R is a uniform random number.

The energy loss is then

$$\Delta E = E - E' = E(1 - \sqrt{R}) \tag{3.62}$$

From here we can determine the scattering angle of the old electron:

$$\theta' = \arccos\left(\sqrt{\frac{E'}{E}}\right) = \arcsin\left(\sqrt{\frac{\Delta E}{E}}\right) \tag{3.63}$$

The energy of the new electron is $E" = \Delta E + E_F$ and the scattering angle of the new electron is then :

$$\theta" = \arcsin\left(\sqrt{\frac{E'}{E}}\right) = \arccos\left(\sqrt{\frac{\Delta E}{E}}\right) \tag{3.64}$$

3.4.2.5 The SE escape in vacuum

Once arrived under the surface, in order to escape in vacuum, the SE has to overcome the surface barrier, i.e:

$$E > E_F + W \tag{3.65}$$

where E_F is the Fermi energy and W is the work function of the target material. Therefore, the approaching angle to surface has to be lower than a critical value, in order to not to be reflected back into the specimen.

The probability for a SE with energy E at the surface to be transmitted in the vacuum is [81, 80]:

$$T(E) = 1 - \sqrt{\frac{E_F + W}{E}} = 1 - \sqrt{\frac{U_0}{E}} \tag{3.66}$$

where the inner potential U_0 is the sum of the Fermi energy and work function. For metals most of the excited electrons cannot be emitted since they have energies lower than the work function. For large gap insulators nearly all excited electrons can be emitted into vacuum since they have energies higher than the vacuum level in accordance with the energy band theory.

The surface barrier is important to obtain the correct absolute SE yield. According to their calculations for SE < 50 eV the average T(E) = 0.1 and the reflection coefficient at the metal vacuum interface is about 0.9.

The energy of SE is considered relative to the bottom of the conduction band. The energy of PE is calculated with respect to the vacuum level. Each time a SE escapes into the vacuum its energy is reduced with E_F+W.

3.5 A compilation of secondary emission data relevant for EBID resolution

One of our main objectives is to theoretically estimate the role of secondary electrons in the EBID spatial resolution. An orientation step should consider a review of results already obtained for secondary emission. During years, a lot of theoretical work has been done in order to simulate the secondary emission from a target bombarded with an electron beam. From this enormous sea of information we need to extract some systematic results, which can serve as reliable reference and guidance in our future work.

What exactly can we learn from our predecessors? The results relevant to us will concern the spatial resolution, the energy and the angular distributions of SE. A compilation of the results concerning the resolution in SEM imaging, resist-based EB lithography and EBID will be presented. When necessary we will present also results obtained using other methods than Monte Carlo e.g. the analytical approaches. We will try to build a unitary opinion, to conciliate results from different authors and in conclusion take as reliable the most frequently encountered result.

3.5.1 Results from the SEM imaging analysis

The theoretical estimation of the imaging resolution in a SEM can be defined by referring to a certain SE spatial distribution. We consider it very important to specify relative to which profile it is defined.

The most popular way to define the SEM spatial resolution is by using the FWHM of SE radial distribution I(r) obtained as response to the primary beam. In case this beam is zero dimensional, the delta function response will define the ultimate SEM resolution.

The drawback of this definition is that for the zero diameter beam used in Monte Carlo simulations the width of I(r) peak depends on the choice of the step dr used. [71]. But for a gaussian distributed two dimensional beam, the convolution between the delta response and the beam profile will get a more realistic distribution and then FWHM can be better defined. For example Kotera presents the MC results convolved with a gaussian beam of 0.1 nm diameter [71], Allen & Kunz do the same with a beam of 100 nm [3, 75] .

In cases when the profile I(r) is very narrow in the center and has wide tails, the peak contains only a small percentage of the total number of emitted SE. In this case an other approach becomes more realistic, which defines the resolution by the FW50% of the integral of radial intensity distribution i.e. the diameter of the circle which contains 50% of emitted SE . This definition is in our opinion more suitable also for material deposition characterisation.

To determine the FW50% we will need the normalized integral function of radial density distribution, i.e. the number of SE emitted inside a circle of radius r, $N_\Sigma(r)$.

Many authors observed that for the SE emission FW50% is usually larger than the FWHM. For example 3-4 nm instead of 0.8 nm for Au targets [25].

When scanning along a line, a common situation in SEM imaging, the lateral distribution is more important due to its emphasis on the change of information along a special direction and its relation to the practical contrast. Some authors consider that the lateral distribution of SE on the surface determines in practice the ultimate resolving power of the SEM. The FWHM of the lateral distribution is larger than that of the radial distribution. For example 0.423 nm instead of 0.157 nm for Cu targets [71].

Wells, using an analytical approach, concluded a long time ago, that the half of FWHM of

I(r) for a zero-diameter beam is of the order of the average electron inelastic mean free path (IMFP) in the target material [136]. Using MC calculations, Shimizu and Murata pointed out that the ultimate resolution of SEM was restricted by IMFP. The results of a simple diffusion calculation [30] and another MC simulation for SE in cascade processes [70] agreed with this observation. Koshikawa & Shimizu obtained a value of 1 nm for FWHM of SE lateral distribution for Cu targets. Shimizu [125] calculated using a very simple model the lateral distributions for Cu and Al. The conclusion was that BSE have low contribution in lateral distribution. The FWHM of lateral distribution of SE is almost completely determined by the yield due to PE and it depends on the IMFP of the target material. The values of IMFP as given by Seah & Dench [121] and calculated and tabulated by Powell [100, 101, 103, 102, 104] vary between 0.5 nm and 2 nm for metals and are several times larger for insulating materials.

From optical design a minimum probe size in SEM has been predicted as 0.6 nm. Taking into account this probe size, a common feeling can be that the ultimate resolution of SEM is 1-2 nm. But experimentally it has been shown that an edge-to-edge resolution of 0.8 nm can be obtained [25]. Ding showed that the edge-to-edge resolution can extend beyond the ultimate resolution of 1-2 nm by image processing and improvement of the signal to noise ratio in the edge image. Ding simulated the scattering of 10 keV and 30 keV electrons incident on a 10 nm Au substrate on the edge of the specimen. The curves I(r) and $N_\Sigma(r)$ are similar to the simple calculation made earlier by Everhart [30]. The FWHM of I(r) gives an estimation of resolution of 0.8 nm. But because only 8% of the SE current is contained in this FWHM peak, a more reasonable radial resolution is recommended, the FW50%, estimated to 3.4 nm for 30 keV and 4.4 nm for 10 keV electrons. The FWHM of the lateral distribution is 2.2 nm .

Joy [56, 57] implemented the FSE model with no tertiary electrons considered. The calculated FWHM of the FSE spatial distribution (not clear whether radial or lateral) is around 2-3 nm for Cu and C targets bombarded by a 20-30 keV pin point electron beam. His general conclusion is that the spatial extend of FSE is around 2-3 nm for a 20 kV electron beam irradiating a metal target.

Kotera [71, 72] used a hybrid model, which divides the internal secondary electrons in fast and slow, according to their initial energy. The cascades are treated only for slow electrons (<100 eV). He neglects the plasmons and the Auger electrons. The fast electrons >100 eV are treated with the single scattering model and the slow secondary electrons < 100 eV are treated including their cascades. The treatment of cascades and the calculation of IMFP are done following the model of Koshikawa and Shimizu. Later, Kotera [82] also includes the plasmons and Auger electron excitation mechanisms. The lateral and radial distribution for Cu and Al are presented separated in 2-5 nm region and in 0-0.5 nm region. For example for a 10 kV and 0.1 nm diameter primary beam in Cu target, the FWHM of SE radial distribution is 0.157 nm. The FWHM of the SE lateral distribution is larger, 0.423 nm for 10 kV for Cu. We think that the result is so small compared with the results of Joy because the cascades of secondary electrons have been included. Luo&Joy [80] also considered the SE cascades and the core electrons excitations, but to our knowledge did not present the spatial distributions anymore, so we cannot compare with the case when the cascades were neglected.

The conclusion is that when the multiplication cascades are also included, a sharper SE spatial distributions is obtained. This is a result which encourages us.

Another conclusion is the importance of the target surface barrier. The SE yield can be 10 times lower when the transmission through the surface barrier is considered.

3.5.2   Results from resist-based electron beam lithography (EBL)

Murata applied MC simulations in order to determine the resolution in PMMA resist based EBL [91]. In this kind of applications, the spatial distribution of energy dissipation in the resist is the most important quantity. The slow electrons are not so important, because they cannot travel too far from the incidence point. Interesting are the fast electrons with keV energy and their effect on the spatial resolution of energy deposition in the polymer film, because FSE travel almost perpendicular to the PE path. The secondary electrons they generate can create a spatial spread of the resist exposed area. The contribution of secondary electrons to the energy deposition will be dominant on the surface.

Joy [55] also calculated the role of FSE in the resist exposure. The resolution limits in lithography are given by the adsorbed energy profiles in the PMMA resist, where a threshold model is used. The values predicted by MC simulations for the linewidth are in excellent agreement with the results of Broers [13] and show that a fundamental limit exists to this type of lithography. It is determined by the inelastic scattering of electrons in the substrate and the sensitivity of resist to exposure with low energy electrons.

Samoto& Shimizu [115] developed MC simulations of secondary emission for the theoretical study of ultimate resolution in electron beam lithography. The energy dissipation profiles in PMMA resist have been calculated. Their calculations showed that the blurring due to SE at the surface of PMMA resist on Si substrate is of the order of 10 nm for a 20 keV electron beam.

3.5.3   Results from EBID studies

Very few attempts to use Monte Carlo simulation for the secondary electron emission in EBID study have been undertaken up to this moment. Allen and Kunz used an approach very similar to the one we want to follow. Their application is the selective deposition of iron from $Fe(CO)_5$ precursor using a low energy electron beam. They have written a MC simulation for the secondary emission on the target surface in case of low energy primary beam, from 250 eV to 2 keV. They used the elastical Mott cross section for the low energy electrons and the Streitwolf excitation function for the treatment of the electron inelastic scattering. The cascades of secondary electrons are modelled with the classical binary collision approximation. They calculated the BSE and SE yield per unit area and the secondary flux as a function of the radial distance. They also applied these simulations for deposition, but didn't really finish the analysis and didn't couple the MC results to the dissociation cross section of the iron pentacarbonyl precursor. Their conclusion was: "We do not know precisely the energy dependence of nucleation cross-section, so this exercise is not warranted at the moment".

For a different purpose but also in the EBID study Weber [135] performed Monte Carlo simulations of electron scattering in tip structures grown by EBID to investigate if electron induced tip heating can explain the growth. He used the Rutherford cross section for the elastic scattering and the dielectric function approach for IMFP determination, but the isotropic approximation for the calculation of angles in inelastic scattering.

3.6 Relevant interactions between electrons and a gaseous precursor

3.6.1 Introduction

An important step in the understanding of EBID is to develop an appreciation of the electronic structure and bonding of the precursor molecules and a knowledge of the principles of electron beam induced surface chemistry of these molecules. Beside being a central problem in the understanding of EBID, the electron - gas interaction is also important for other fields, like astrophysics, plasma assisted microtechnology, environmental SEM, etc. Electron impact phenomena play a major role in two naturally occurring atmospheric phenomena: the secondary emission in the earth ionosphere and the auroral emissions in earth polar atmosphere. Here is where abundant information can be found.

During the EBID process, the precursor molecules adsorbed on the target are exposed to a "shower" of electrons: the monoenergetic primary electrons (PE), with high energies (40-200kV) and secondary electrons (SE) emerging from the surface, with a whole spectrum of energies peaking at low values (2-5 eV). These electrons can stimulate in the adsorbed molecular layer many processes as: molecular excitation, dissociation, ionization and also surface processes as desorption, adsorption, migration. Our attention is focused only on the interactions between electrons and gas molecules that might be interesting for the EBID spatial resolution.

The data we expect to obtain in the end of this section is: the electron impact dissociation cross-section versus the electron kinetic energy, necessary for the estimation of SE and PE role in deposition. The electron energy loss during the interaction with gas molecules is also necessary for the estimation of the localization of the energy transfer.

Because the behavior under electron irradiation is quantitatively different for each molecular species, and because the existing experimental data is so vast and diverse, we will focus gradually on precursors relevant for EBID, following the path: gases in general→organometallic complexes→metal carbonyls→tungsten hexacarbonyl. A first example of electron impact data available in literature will be given for the hydrogen molecule H_2. The molecule is of reduced relevance for EBID, but it is the simplest and the most frequently studied molecule, with an almost complete data set available. Because of the similarities between the EBID process and the specimen contamination in electron microscopy practice, a special attention will be given to hydrocarbon complexes C_xH_y which are easy to find in the microscope vacuum systems. Further some information about organometallic precursors is given.

3.6.2 The electronic structure and energy states of atoms and molecules

Although the atoms are composed of three types of subatomic particles - protons, neutrons and electrons, the chemical behaviour of the atom is governed only by the behaviour of the electrons.

In the case of a one-electron atom or the so-called hydrogen-like atom, the Schrödinger wave equation for the electron is:

$$H\Psi = E\Psi \tag{3.67}$$

where H = the hamiltonian operator and E = the energy of the electron.

Symbol	Name	Possible values	Description
n	principal	1, 2, 3,...	describes size and energy of orbitals
l	azymuthal	0,1,2...(n-1)	describes the shape of orbitals
	momentum		
m_l	magnetic	$0,\pm 1,\pm 2,\pm l$	describes the orientation of the orbital
m_s	spin	$\frac{1}{2}$, - $\frac{1}{2}$	describes the spin of electron in the orbital

Table 3.1: The quantum numbers of electron in the hydrogen like atom

The solution of the equation is the wave function Ψ, and its characteristics are essential for an understanding of the chemical bonding. The characteristics of wave function Ψ are:

1. It describes the probable location of electrons; it is not capable to predict exactly where an electron is at a given place and time.

2. For any atom there are more solutions to the wave equation. Each solution (wave function) describes the motion of an electron in an orbital of the atom.

3. Ψ is a mathematical description of a region of space (an atomic orbital) that can be ocupied by up to two electrons.

4. the square of the wave function, Ψ^2, evaluated for a given set of coordinates (x,y,z) is a direct measure of the probability density of the electron in that point (the probability that an electron will be at that point).

5. the mathematical expression of Ψ incorporates quantum numbers which are related to the size, energy and shape of atomic orbitals (see Table 3.1).

An electron bonded in an atom has the states noted by s, p, d, f according to this angular momentum number l, as follows: l = 0 →s (ground state), l = 1 →p , l = 2 →d, l = 3→ f.

The first symbols stand for *sharp, principal, diffused, fundamental* refferring to the order of appearance in the spectrum.

In a many-electron atom, the Schrödinger equation can be set up but it can not be evaluated exactly. In a first approximation, each electron should be assigned a set of quantum numbers. But there is a fairly strong interaction between these electrons so that this assumption is not realistic. The interactions are not easy to describe, but the behaviour of real atoms can be approximated with a situation called L-S or Russell-Saunders coupling scheme. The L-S coupling scheme uses two quantum numers: L, the total orbital angular momentum of all the electrons, and S, the total spin angular momentum of all the electrons. Two electrons can interact by coupling their angular momenta l and their spins s, giving the total L and S for the configuration.

Because of electron-electron repulsion in many-electron atoms, it is possible that one electronic configuration (L, S) results in several atomic energy states, or terms.

The most convenient classification of atomic energy states is in terms of L, S and J, where J is defined as the total angular momentum and it can take all values J = L+S, L+S-1, |L-S|, in total 2S+1 different values. In this way, one electron configuration (L,S) can give 2S+1 different energy states (terms). The value 2S+1 is called multiplicity of the term. Each energy state can be assigned a term symbol:

^{multiplicity}**state**$_J$ or $^{2S+1}$**state**$_{L+S,L+S-1,L+S-2}$

The atomic states notation employs capital letters S, P, D, corresponding to the total electronic orbital angular momentum quantum number L :

L = 0 1 2 3 4 5 6

    S P D F G H I

The notation agrees with the corresponding lower case letters that are used to designate the quantum number l, the angular momentum of electrons in individual orbitals.

Molecules are formed when more atoms are bonded together. Even for a diatomic molecule the Schrödinger equation cannot be solved analytically. To overcome this difficulty, the Born-Oppenheim approximation is usually used. The nuclei are considered static and the equation is solved only for the electrons. Different arrangements of the nuclei may be adopted and the calculations repeated. Thus an approximate solution of the wave equation for a molecule can be obtained by solving the wave equation for the electrons alone, with the nuclei held in a fixed configuration. The set of solutions allows to build the molecular potential energy curve for a diatomic molecule. The Born-Oppenheim approximation is reliable for ground electronic states but becomes less reliable for excited states.

The electronic structure and binding in molecules can be calculated by the molecular quantum mechanics, that tries to solve the Schrödinger equation for the electrons in a molecule. All the techniques applied in solving this equation make heavy use of computers. There are two main approaches to the solutions of this equation. In *ab initio* calculations, a model is chosen for the electron wavefunction and the calculations are made only based on fundamental constants and atomic numbers of nuclei. The model tries to predict the properties of atomic and molecular systems. Examples of ab initio methods are the self consistent field method (SCF), the density functional theory (DFT), the Moller-Plesset perturbation theory (MPPT), self consistent field $X\alpha$-Dirac-scattered-wave molecular orbital method (DSW). For large molecules accurate ab initio calculations are computationally expensive and *semi empirical* methods have been developed in an attempt to treat a larger number of chemical species. A semiempirical method makes use of a simplified form for the hamiltonian as well as adjustable parameters with values obtained from experimental data. Examples of semiempirical methods are the Huckel molecular orbital theory (HMO), Pariser-Parr-Pole method (PPP). In both cases it is a chalenging task to compute chemically accurate energies, that is energies calculated within about 0.01 eV of the exact values [9].

Sophisticated software packages have been developed over the past three decades to perform electronic structure calculations using the existing ab initio and semiempirical methods. These packages are widely available and are becoming increasingly easy to use. Some of the packages are commercially available like Gaussian [32, 37], GAMESS, CADPAC, MOPAC, others are used in only a research group like ADF, the Amsterdam density functional program.

3.6.3   Electron beam induced molecular degradation

3.6.3.1   The mechanisms of electron induced molecular degradation

An energetic electron passing through a volume with gas molecules loses most of its energy through excitations and ionizations of these molecules.

The interaction between an electron e$^-$ and the molecule AB can generate one of the following molecular reactions:

Excitation (electronic, vibrational, rotational):

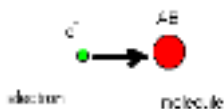$$e^- + AB \rightarrow (AB)^* + e^-$$
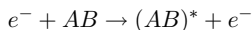
Dissociative electron attachment (DEA) :

Figure 3-33: An electron incident on a molecule AB

$$e^- + AB \rightarrow (AB)^- \rightarrow A + B^- + e^-$$

Dissociation in neutrals :

$$e^- + AB \rightarrow A + B + e^-$$

Dipolar dissociation (DD):

$$e^- + AB \rightarrow A^+ + B^- + e^-$$

Ionization:

$$e^- + AB \rightarrow (AB)^+ + e^-$$

Dissociative ionization (DI):

$$e^- + AB \rightarrow A + B^+ + 2e^-$$
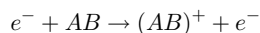
The dissociative recombination :

$$(AB)^+ + e^- \rightarrow A + B$$
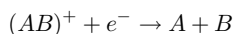
One of the most frequent mechanisms for the electron-impact dissociation is the electronic excitation of the molecule to a repulsive molecular state. However, in the region very close to the dissociation threshold, these states are hardly accessible. In this case the resonance mechanism involving the formation of the negative-ion state may be more important. The excited states can decay and result in dissociation of neutrals. If the energy of the electron is greater than a critical value, some molecules in the gas target will be ionized. As the energy of the electron beam increases, the abundance and variety of ionized species will increase. Some of the ionized molecules will dissociate if the electron energy is sufficiently large. The ionization can

occur via several channels: single ionization, double ionization, multiple ionization, dissociative ionization, ion pair formation. For us it is relevant that ionized molecules can later dissociate, through the so-called dissociative ionization. Another process that can cause a dissociation is when an already ionized molecule captures an electron and dissociates via recombination.

In conclusion there are a lot of channels (pathways) possible for a molecule to dissociate under electron impact. The more complicated the molecule is, the more channels are possible.

The main mechanisms for the molecular dissociation under electron impact are:

Dipolar dissociation (DD)

This is a non-resonant process. It occurs above a threshold energy and corresponds to the inelastic electron scattering process resulting in a molecular excitation followed by dissociation to both positive and negative ions.

Dissociative ionization (DI)

DI involves dissociation via an ionized species. The dependence of the probability of this process versus electron kinetic energy does not have a maximum.

Dissociative electron attachment: (DEA)

DEA is a resonant process that involves the formation of a negative ion due to electron capture and occurs when the excited state is dissociative in a particular vibrational coordinate. DEA process is known to result from the transfer of an electron to an antibonding σ^* orbital of the adsorbate molecule, i.e. an electron transfer between the substrate and the adsorbate. The DEA mechanism can be explained by the resonance theory [129]. First an electron attaches itself to the parent molecule and forms a temporarily molecular negative ion. Then this state either decays to the parent state (auto-ionization) or it dissociates into a stable negative ion and a neutral.

Within the energy range of secondary electrons (0-20 eV) dissociative electron attachment (DEA) and dipolar dissociation (DD) are believed to be the major processes leading to molecular dissociation. For higher impact energies, dipolar dissociation and dissociative ionization mechanisms play the most important role.

3.6.3.2 The electron energy loss in the electron interaction with gas molecules

Let us suppose that an electron collides with an atom and excites it to an excited state, discrete or continuum at an excitation energy E, measured from the ground state. The kinetic energy of the electron will be reduced with ΔE, which may be called the energy loss for the incident electron or the energy transfer for the target atom.

The theoretical treatments of electron inelastic scattering with atoms and molecules can be conveniently classified into two kinds: those dealing with fast electrons and those dealing with slow ones. The criterion used in this classification is the mean orbital velocity of the electrons of target atom, situated in the shell taking part in the interaction. The primary electrons in EBID can be considered as fast electrons and the secondary electrons can be considered as slow electrons.

The fast electrons

Fast incident electrons have velocities higher than the velocities of bounded target electrons. Their influence upon the target can be considered as a sudden and small external perturbation. The Bethe theory provides the general framework for discussing the inelastic scattering of fast electrons. The theory has been conceived for free atoms, but it can be applied also for solids. The Bethe theory uses the Born approximation. Inokuti gives a very detailed discussion of the Bethe theory [52].
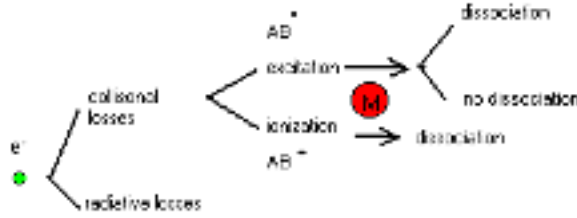
Figure 3-34: Different pathways for an electron to lose energy in an interaction with a gas molecule

For fast incident electrons, the electron energy loss due to the target ionization and excitation, represents the so called collisional losses and can be modelled using the continuous slowing down approximation (CSDA) and the Bethe stopping power. The relativistic Bethe stopping power is defined as the energy loss of the projectile per unit distance travelled [66] :

$$-\left(\frac{dE}{dx}\right)_c = \frac{2\pi e^4 NZ}{mv^2}\left[\ln\frac{mvE}{2I^2(1-\beta^2)} - \left[2\sqrt{1-\beta^2}-1+\beta^2\right]\ln 2 + (1-\beta) + \frac{1}{8}(1-\sqrt{1-\beta^2})^2\right]$$

where v = the velocity of the primary electron

m = the rest mass of electron

e = the electronic charge

I = the mean ionization or excitation potential of the absorber target

N, Z = the atomic density and the atomic number of the target atoms

$\beta = v/c$.

The electrons differ from other heavy charged particles in that the energy may be lost by radiative processes as well as by Coulomb interactions. These radiative losses take the form of "bremsstrahlung" . The linear specific energy loss through this radiative process is [66]:

$$-\left(\frac{dE}{dx}\right)_r = \frac{NEZ(Z+1)e^4}{137m^2c^4}\left(4\ln\frac{2E}{mc^2} - \frac{4}{3}\right)$$

The radiative losses are most important for high electron energies and absorber materials of large atomic number. The ratio between the radiative and collisional losses is EZ / 700, where E is the electron energy in MeV. We see that radiative losses are only a small part of the collisional losses.

The total linear stopping power of the electron is then the sum of its collisional and radiative

losses:

$$\frac{dE}{dx} = \left(\frac{dE}{dx}\right)_c + \left(\frac{dE}{dx}\right)_r$$

The most important nontrivial quantity in the Bethe stopping power formula is the mean excitation potential, I. It summarizes the properties of the target in terms of energies and oscillator strength of transitions. Its direct evaluation requires the knowledge of ground and excited states atomic wave functions. Such direct calculations are feasible only for a few atoms for low Z. In case of hydrogen, I = 15 eV. Usually I is an experimentally determined parameter for each material. Ahlen gives a table with I for a lot of elements [2].

$$\ln I = \sum_n f_n \ln E_n$$

where f_n is the oscillator strength of a transition from the ground state to a state of energy E_n.

For compound targets, the Bragg-Kleeman rule can be used (with sometimes 10%-20% error) which assumes that the stopping power per atom is additive.

The generalized oscillator strength f_n, or GOS, is the central notion of the Bethe theory and is a function of both the energy transfer and the momentum transfer. The calculation of the generalized oscillator strength for many electron atoms is obstructed by the lack of sufficiently accurate wave functions. The oscillator strength for molecules has been calculated only in a few cases like H_2 and other diatomic molecules like N_2 ,O_2 ,CO.

Another way to obtain the energy loss spectrum for the high energy primary beam is from photochemistry, using the photoabsorbtion spectrum because at such high energies, only optically allowed transitions are possible, where the dipole approximation can be used. High energy electrons are ideal photon sources or pseudophotons.

The total loss in inelastic scattering (the collisional losses) can be also experimentally measured by EELS.

The slow electrons

In the case of slow electrons incident on a molecule, the relative and absolute magnitude of each interaction process is different than those for the equivalent reactions produced by the fast primary electrons. The Bethe approximation is not valid anymore. It was valid only when the speed of the electron is much greater than that of the electrons bound in the absorbing medium. The combined system of incoming electron and target system has to be considered now. The molecular orbitals are strongly perturbed by the slow electrons and forbidden transitions are favoured, and fenomena such as electron resonances happen. This phenomenon can lead to vibrational and electronic excitation and dissociative attachment. Most energy losses by secondary electrons result in vibrational excitation when their energy lies within the range of resonance. The impact of low energy electrons with gas molecules have been extensively treated by Sanche in [116, 117, 118].

The experimental determination of the energy loss spectrum for the slow electrons incident on molecular targets is much more difficult. The only solutions are theoretical calculations. In case of He, the Bethe approximation is valid only for electron energies higher than 500 eV. The energy loss in helium for slow electrons has been calculated by Dayashankar for energies from 50 eV up to 10 keV as the sum of ionization and excitation energy losses [22, 23].

At low energies under the dissociation threshold, only the dissociative attachment and elastic

scattering are allowed. The secondary electrons yield a considerable amount of their energy by exciting phonon modes and vibrational levels of individual molecules of the irradiated solid. DA and DI are the major processes leading to dissociation.

In some cases the secondary electrons do not play an important role in molecular dissociative attachment like in the case of cyclopropyl on Cu. The peak is at 10 eV above the SE maximum energy [84].

The fate of the energy lost by the incident electron

The formulae presented until now can be used to determine the total energy lost by an electron during its inelastic scattering on a target molecule, ΔE_{total}. But how is this energy divided in the molecule? Which energy fraction is lost by the electron for the dissociation of the molecule? This is a difficult problem. The solution starts from the fact that the total electron energy loss is a sum of the energy loss for molecular ionization and the energy loss for molecular excitation. A fraction of both losses results eventually in molecular dissociation.

$$\Delta E_{total} = \Delta E_{ioniz} + \Delta E_{excitation}$$

The electron energy loss for ionization ΔE_{ioniz} is a quantity that can be obtained directly from a coincidence measurement between the electron energy loss spectrum EELS and all ions produced.

The electron energy loss for molecular ionization can be also indirectly deduced from the photoelectron spectrum HeI or $HeII$. In the photoelectron spectrum experiment, a photon of E=21.2 eV is incident on the molecule and the electron resulting from the molecular ionization is collected. The measured photoelectron spectrum is the probability $P(E_{He}, E_n)$ that the emitted electron has an energy E_{He}. The probability for the electron to lose an energy E in this molecular ionization is determined by [86].

$$P(E, E_n) = P(E_{He}, E_n) \left/ \left[\int_{E_0}^{E_n - E_0} P(E_{He,E_n}) dE \right] \right.$$

Another method to determine the energy lost for ionization is by using the photoionization cross-section of the gas molecule $\sigma_i(E_n)$, a known quantity for many molecules.:

$$P(E_n) = \left(\frac{\sigma_i(E_n)}{E_n} \right) \left/ \left[\int_{I_P}^{E_{max}} \left(\frac{\sigma_i(E_n)}{E_n} \right) dE_n \right] \right.$$

where E_n is the energy of the incident photon, and I_P the ionization potential.

In conclusion there are enough ways to determine the electron energy loss for molecular ionization. The energy lost for excitation $\Delta E_{excitation}$ can be determined then as the difference between the total electron energy lost and the energy lost for ionization.

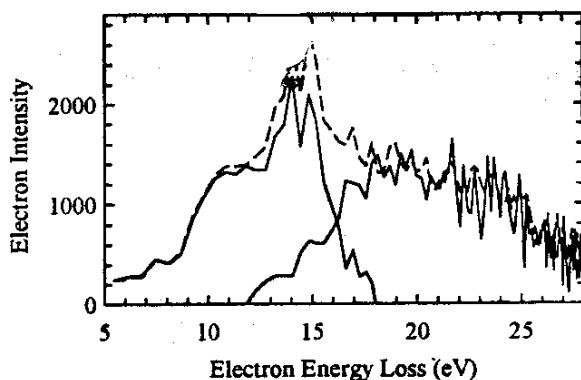$$\Delta E_{excitation} = \Delta E_{total} - \Delta E_{ioniz}$$

Figure 3-35: The total inelastic energy loss, the energy loss for ionization and their difference responsible for the excitation. 33 eV electron impact with N_2 molecule [from [87]] The dotted curve is the total inelastic scattering, the solid curve on th eright is the ion coincidence data. The solid curve on the left is the difference between the former two curves and represents the contribution from the sum of netral dissociation and excitation.

In Fig.3-35 the three curves are shown for the impact of an 33 eV electron on a N_2 molecule [87].

The energy losses in the excitation of molecular vibration and rotation are relatively small compared with the energy lost to electronic transitions. For the low energy secondary electrons, most energy loss goes to vibrational excitation when the energy lies within the range of resonance.

The energy loss for dissociation is much more difficult to estimate or measure.

Cross-sections for electron induced molecular degradation

The results of electron collision experiments are usually expressed in terms of quantities called cross-sections. They can be defined as a transition probability per unit time per unit target scatterer and per unit flux of the incident particles with respect to the target. Total cross sections have the dimensions of an area. Since in atomic units (a.u.) the unit of length is the first Bohr radius $a_0 = 5.29$ x 10^{-11} m, it is convenient to express the atomic cross sections in units of $\pi a_0^2 = 2.80$ x 10^{-21} m^2. Another unit is also frequently used, the barn. 1 barn $= 10^{-24}$ cm^2. A typical ionization crossection dependence of electron energy is shown in Fig. 3-36.

The cross sections for electron impact excitation of molecular states $\sigma_{excitation}$.

The electrons are very effective in molecular vibrational excitation, especially at low energies via a resonant mechanism. The largest cross-section is for the electronic excitations associated with optically allowed transitions at intermediate energies. The value of the excitation cross-section increases gradually with the impact energy from the threshold to about 10 times the threshold energy and then slowly decrease at high energies. At low impact energies (within a few eV of threshold) the forbidden transitions dominate the energy loss spectra and represent an important cross section. The cross section for spin forbidden processes rise steeply near
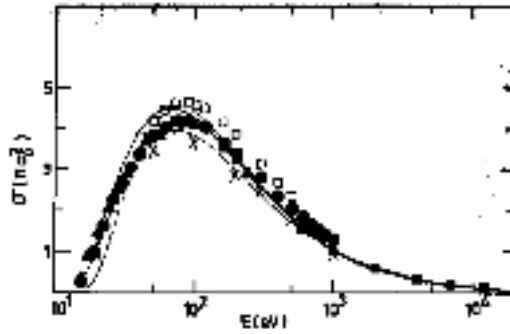
129

Figure 3-36: Example of ionization cross section of methane during electron impact energy range from 10eV to 20keV.

the threshold, reach their maximum within a few eV from threshold and decrease sharply with increasing energy. Summarized sources of experimental data are given in [133]. Most experimental work is done on the N_2 molecule. The motivation was the very important role $e^- - N_2$ process plays in a variety of atmospheric phenomena and the fact that the molecule is easy to handle experimentally. With exception of the N_2 molecule, only fragmentary data exists for electron impact excitation of molecules.

Theoretical models for electronic excitation by electrons are difficult to develop. The difficulty comes from computational problems associated with the accurate representation of many electron electronic and nuclear force fields experienced by the incident and the scattered electron. The Born-Oppenheimer approximations are better for high energy electrons. More theoretical work has been done for H_2 molecule because of its simple electronic structure. Very little theoretical work has been done for the excitation of other molecules than H_2 and N_2 and it is summarized in [133].

The cross sections for electron-impact molecular ionization σ_{ioniz}

The electron impact ionization cross-sections are needed in applications such as modelling of fusion plasmas in tokamaks, modelling of radiation effects for material and medical research, in astrophysics research and atomic molecular and plasma physics. These cross-sections are quantitatively better known than the dissociation cross sections. Because of the great need for reasonable estimates of ionization cross sections and the present scarcity of accurate data, a number of empirical formulae for the ionization cross-sections have been published. The general goal of an empirical formula is to have a few parameters and to be easily implemented in a computer model. During past years, many formulae have been given for the ionization cross-sections of the most popular molecular species. A set of such formulae can be found in [140].

For fast electron collisions, the ionization cross-section formula consists of two different factors: one involving the properties of the incoming electron and the other dealing with the properties of the target molecule, i.e. the generalized oscillator strength. This picture is used by the Born approximation and a general formula is given in [52].

130

$$\sigma_{ioniz} = \frac{4\pi a_0^2 R}{E} M_i^2 \ln\left(\frac{4c_i E}{R}\right)$$

where M_i^2 and c_i are constants related to the oscillator strength f.

For slow collisions the combined system of incoming electron plus target molecule has to be considered.

Other formulas (empirical semiempirical, classical and semiclassical quantum mechanical) and summarized data sources can be found in [83]

We consider as most interesting a model free from adjustable parameters for calculation of the electron impact ionization cross-section of atoms and molecules given by Kim in [65]. This model uses the binary encounter Bethe BEB model. This model provides reliable electron impact ionization crossections using very simple input data for the ground state, all of which can be obtained from standard molecular wave function codes. The model predicts the total ionization cross section as the sum of ionization cross section for ejecting one electron form each of the molecular orbitals. The formula is valid from the first ionization threshold to several keV incident electron energies. The BEB model is a simpler version of the binary encounter dipole model (BED) for the electron impact ionization of atoms and molecules. The BED model combines the binary encounter theory with the Bethe theory. At high energies the two theories coincide.

According to the binary encounter Bethe BEB model, the total ionization cross section per molecular orbital is :

$$\sigma_{ioniz}(E) = \frac{S}{t+u+1}\left[\frac{\ln t}{2}\left(1-\frac{1}{t^2}\right) + 1 - \frac{1}{t} - \frac{\ln t}{t+1}\right] \tag{3.68}$$

where $t = E/B, u = U/B$, and

$$S = \frac{4\pi a_0^2 N R^2}{B^2}$$

$a_0 = 0.529177249 \times 10^{-10}$ m,

$R = 13.61 eV$,

N = the occupation number of the orbital ,

U = the kinetic energy of the orbital in the initial state, usually ground state of the target,

B = the electron binding energy .

U can be calculated by any molecular wave function software package. Kim gives the U,N, B values for 11 atmospheric molecules determined by using the GAMESS package.

The term associated with the first logarithm function represents the distant collisions at large impact parameter, dominated by the dipole interactions and the rest of the terms on the right hand side represent the close collisions at small impact parameters. The summation over all orbitals gives the total ionization cross-section.

In Fig. 3-37 we plot the cross section for ionization of methane $\sigma_{ioniz}(E)$ as calculated by using eq. (3.68).

.

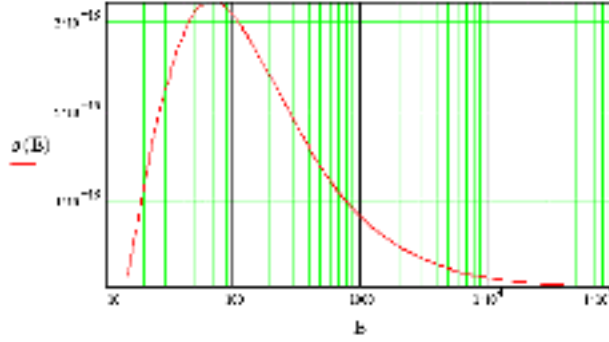**The cross sections for electron-induced molecular dissociation σ_{diss}**

Figure 3-37: The electron impact ionization $\sigma_{ioniz}(E)$ [cm^2] cross-section for CH$_4$ calculated using formula 3.68. The electron energy E is in eV.

Dissociative processes play a major role in the physics and chemistry of planetary and cometary atmospheres and in many industrial applications which use gaseous discharges or laser systems. A comprehensive set of accurate cross section values is of great importance. Nearly complete cross-section sets for major diatomic molecules and polyatomic molecules of planetary and cometary importance (H$_2$, D$_2$,O$_2$, N$_2$,NO, CO,CO$_2$,NH$_3$) have been measured .

The dissociation mechanisms depend on the impact energy and in general all the curves have the same shape, starting with a threshold followed by a maximum in 10-100 eV range and a decay at high impact energies. But sometimes the curve can have another form.

The general dependence of the dissociation cross section on incident electron energy can be written as [41]:

$$\sigma_{diss}(E) \approx (K/E)\ln(E/B)$$

where K and B are some constants.

Different formulae have been constructed in last years to facilitate the numerical calculations of dissociation cross sections for O$_2$ and N$_2$. For example in [141] the following formula is given.

$$\sigma_{diss}(E) = \frac{4\pi a_0^2 R^2 f[1 - (W/E)^\alpha]^\beta}{EW} \ln\left(\frac{4EC}{W} + e\right)$$

were a$_0$ the Bohr radius, R the Rydberg energy, W a parameter that influences the low energy shape of the cross section and it is usually close to the energy loss W$_j$ associated with an excitation of the j state, f is the optical oscillator strength, C is a factor determined from the high energy behaviour of the cross section, e is the base of natural logarithm, α and β are adjustable parameters.

¨**The dissociative electron attachment $\sigma_{\mathbf{DEA}}$ and the dissociative ionization $\sigma_{\mathbf{DI}}$ cross sections**

Rigorous theoretical calculations of DI cross sections are not possible, except perhaps for
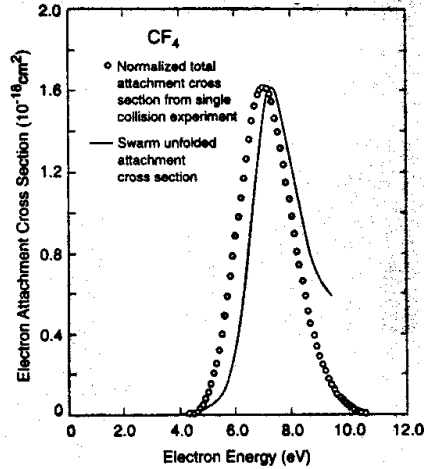
132

Figure 3-38: Dissociative electron attachment cross-section for CF$_4$ [from [18]]

molecular hydrogen H$_2$. Experimentally more information is available. Parikh [97] developed a theoretical model to calculate DI cross sections for diatomic molecules using the binary encounter model. For DI the threshold behaviour is not too different from a dependence x^y, where y=1.0÷1.127 [97]. The magnitude of the DEA cross-sections might be unknown, but the general form is peaked over a very narrow energy region, as it can be seen in the Fig.3-38 for CF$_4$.

3.6.4 Electron-molecular impact data available from literature

In our EBID study we are searching for electron impact data for possible gas precursors as organometalic molecules or hydrocarbons. The data we need to know as accurately as possible is the dissociation cross section versus the electron energy $\sigma_{diss}(E)$ and the electron energy loss invested in the molecular dissociation EEL$_{diss}$ (E). Our conclusion after an extensive literature search is that there is only precarious information available about the electron impact properties of the gases we need. Nearly complete experimental and theoretical data exist only for H$_2$, N$_2$, CO, CH$_4$, in general for the gases abundantly present in the interstellar medium and planetary atmospheres and for some hydrocarbons (C_xH_y). Recently collections of recommended electron impact data have been issued for the gases used in plasma processing in microengineering (CF$_4$). We will give as a first example the most simple and extensively studied molecule, hydrogen H$_2$ for which most data exists. Further we collected in a systematic manner all the information on electron impact we could find for some precursors used in EBID (hydrocarbons and organometallic complexes $M_x(CO)_y$).

3.6.4.1 The hydrogen molecule H$_2$ under electron impact

A good example of quantitative description of electron induced molecular dissociation is difficult to find because the information is far from complete for most of the gas molecules. Maybe the
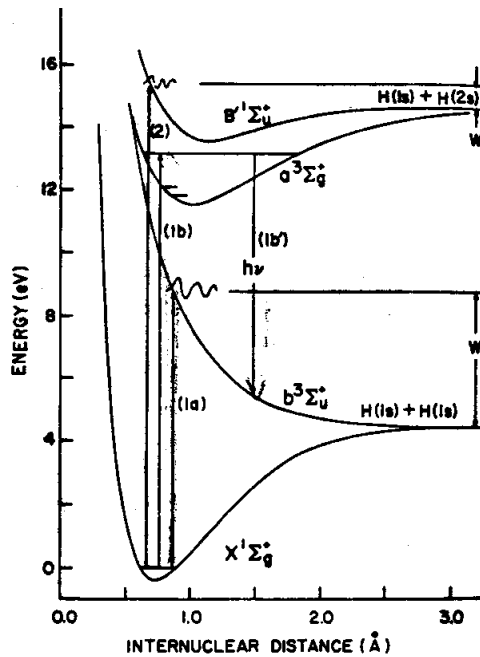
133

Figure 3-39: Potential energy curves of the H$_2$ molecule illustrating different mechanisms of dissociation under electron impact (from [20]).

best example is the case of the hydrogen molecule, the most simple gas molecule found in the nature. Even for such a simple molecule more than one dissociation path is possible, as it can be seen from the potential energy diagram in Fig. 3-39.

Consider that the H$_2$ molecule is initially in the ground state $X^1\Sigma_g^+$. Under electron impact, the molecule can be dissociated via two processes with different products:

$$H_2 \rightarrow H_2^* \rightarrow H(1s) + H(1s) \quad (1)$$
$$H_2 \rightarrow H_2^* \rightarrow H(1s) + H(2s) \quad (2)$$
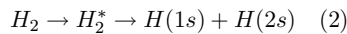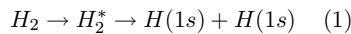
The excited state H$_2^*$ in the process (1) can result via a direct excitation to the repulsive state $b^3\Sigma_u^+$ (1a) but also via a excitation to a higher state (1b) followed by a cascade deexcitation to the same repulsive state (1b') . The excited state in the process (2) may be any of the four states $B'^1\Sigma_u^+$,$E^1\Sigma_g^+$, $e^3\Sigma_u^+$, $a^3\Sigma_g^+$, all of which are bound states. Dissociation results from excitation only to continuum levels of these states above the dissociation limit.

The electron-impact excitation cross section (dissociative and non dissociative)

Despite being the simplest dissociation process, only a few theoretical calculations of high energy electron impact dissociative excitation cross sections from the ground state have been
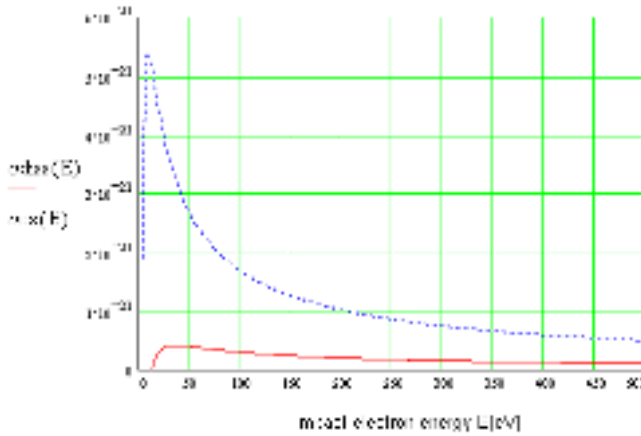
Figure 3-40: The electron impact excitation and dissociation cross-sections for the hydrogen molecule [m^2]

done until the present moment. Chung made the first steps with an ab-initio calculation of dissociation cross section of H$_2$ under electron impact [20].

Since then, efforts are still made to determine more accurately the electron impact dissociation cross section for the H$_2$ molecule. At electron energies higher than 100 eV, the contribution due to the excitation via state $B'^1\Sigma_u^+$ accounts for more than 95% of the total dissociation. Liu gives a very accurately deduced formula for the dissociation cross-section only for excitations to the state $B'^1\Sigma_u^+$ process (2) resulting in the production of H (1s) and H (2s). The potential energy curves for both ground and excited states have been calculated using the Le Roy method. [78].

The formula is valid for very high projectile energies, since it used the Born-Bethe approximation. Thus, the dissociation in neutrals from the excited states cross-section is:

$$\sigma_d = \frac{4\pi a_0^2}{E(R_y)}[0.0317\ln(E(R_y)+0.0006)] \ [m^2]$$

where E is the energy of incident electron in Rydberg units (R$_y$=13.61eV) , a$_0$ is the Bohr radius (a0 = 5.29 x 10^{-11} m).

The excitation cross section (dissociative and nondissociative) is:

$$\sigma_{ex} = \frac{4\pi a_0^2}{E(R_y)}[0.1054\ln(E(R_y)+0.1461)]$$

We calculated using these formulae the electron-impact excitation and dissociation cross section for the H$_2$ molecule versus the electron energy and we show the both curves in Fig. 3-40.

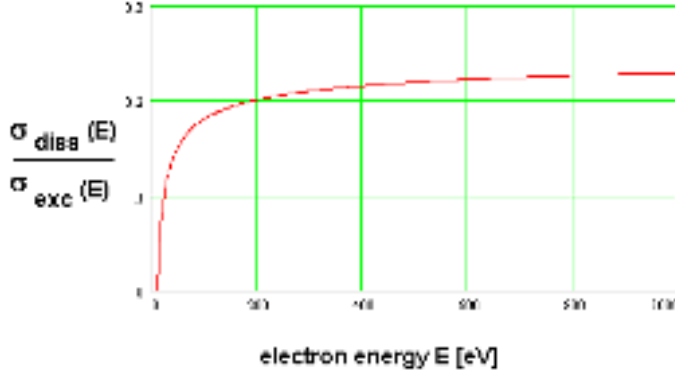$$\frac{\sigma_{diss}(E)}{\sigma_{exc}(E)}$$

electron energy E [eV]

Figure 3-41: The ratio betwen the electron impact dissociation and total excitation cross sections for the hydrogen molecule.

The dissociation in neutrals resulted from excited states cross- section represents cca 20% of the total excitation (dissociative and nondissociative) cross section (see Fig. 3-41).

The energy loss spectra of H_2 in coincidence with the dissociation process (1) is measured by Odagiri [95].

The electron impact ionization cross section

An empirical formula for the ionization of the H_2 molecule by a fast particle of velocity v is given by [131]:

$$\sigma_{ioniz} = \frac{4\pi}{v^2} 0.58 \ln \frac{v^2}{0.046}$$

The binary encounter model developed by Kim [**?**] gives the electron impact ionization cross-section for H_2 shown in Fig. 3-42.

The ionization cross section for high impact energies is calculated by Saksena for electrons with 100 keV to 3 MeV kinetic energy [114] shown in Fig. 3-43.

The resonant dissociation

The process (1) is considered to be a direct scattering process, pictured schematically as :

$$e^- + H_2(X^1\Sigma_g^+, v = 0) \rightarrow e^- + H_2(b^3\Sigma_g^+)$$
$$\rightarrow e^- + H(1s) + H(1s)$$
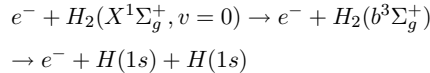
The threshold energy for this process is approximately 8 eV and the cross section is of order of 10^{-17} cm^2. Significant cross sections for dissociation at lower impact energies are not observed experimentally under normal laboratory conditions. A new effect is observed due to
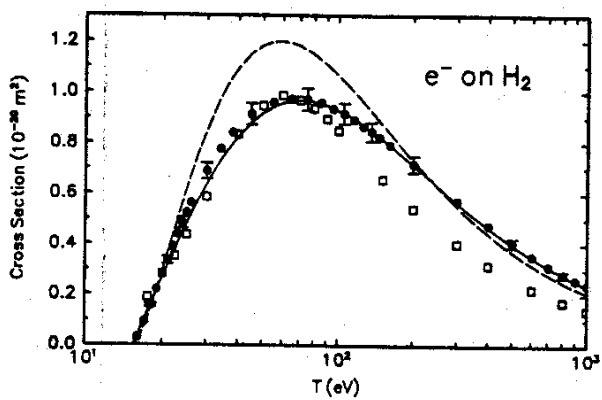
Figure 3-42: Electron impact ionization cross section for H_2 molecule (from [?])
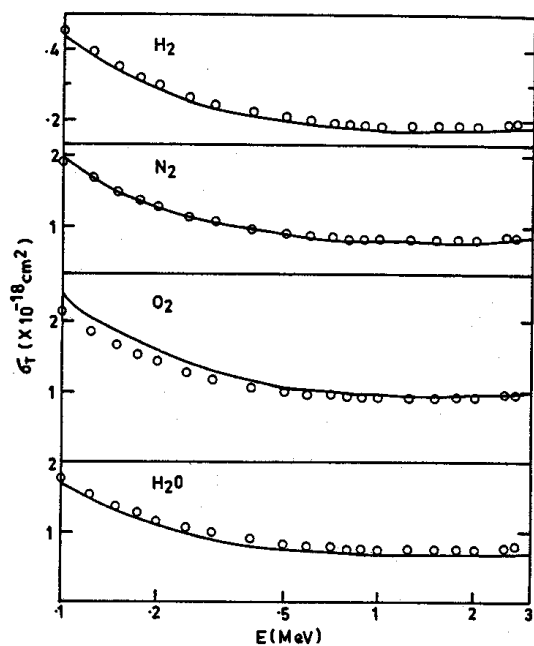

Figure 3-43: Electron impact ionization cross section for H_2 and high energy electrons [from [114]]

resonant scattering, i.e. an enhancement of dissociation caused by trapping of an electron in a temporary anion states of H_2^-. More dissociation resonant channels are opened due to the temporary excitation of two lowest lying resonant anion states of H_2^-.: $X^2\Sigma_u^+, B^2\Sigma_g^+$

3.6.4.2 The hydrocarbon complexes C_xH_y under electron impact

We collected information about the electron impact induced degradation of hydrocarbon organic molecules, of importance for the study of contamination in electron microscopy. Usually the absolute total dissociation cross sections are virtually unknown. Experimentally by detecting the fragments, partial dissociation cross sections can be measured. The difficulty consists in measuring the number of neutral fragments created in electron-molecule collision. Using the experimental data and eventually scaling algorithms, extensions to other similar gases can be theoretically obtained.

The electron impact induced molecular dissociation of hydrocarbons plays an important role not only in our contamination growth study but also in plasma, atmospheric, interstellar and radiation chemistry. Recently cross section sets for different gases necessary in industrial applications have been published. A very systematic and complete set of electron impact data can be found in[18], a review article for the CF_4 molecule. Carbon tetrafluoride CF_4 is one of the most widely used component of feed gas used in plasma assisted material processing applications. CF_4 is unfortunately also a green house gas with a high potential of global warming. To assess the behaviour of this gas in the atmosphere and in many applications especially in semiconductor industry it is necessary to have accurate basic information on its fundamental properties and reactions. The authors assess and synthesize the available information on the cross sections and rate coefficients for collisional interactions of CF_4 with electrons. We can follow the same division to arrange the data we found about other precursors of interest.

For the case of hydrocarbons, we consider useful the general empiric formulae proposed by Alman in [4] for the electron impact ionization and dissociation cross sections of 16 hydrocarbon molecules. Based on the experimental electron impact data for simple hydrocarbons , a general formula is presented that allows extensions to heavier hydrocarbons .

The electron impact ionization cross section $\sigma_{ioniz}(E)$ versus the electron kinetic energy E is:

$$\sigma_{ioniz}(E) = \begin{cases} 0, E < E_{th} \\ \sigma_{\max}\left(1 - \frac{(E_{\max}-E)^2}{(E_{\max}-E_{th})^2}\right), E_{th} < E < E_{\max} \\ \sigma_{\max} \times e^{-\frac{E-E_{\max}}{\lambda}}, E E_{\max} \end{cases} \qquad (3.69)$$

where E_{th} is the threshold energy for ionization, E_{max} is the energy where the cross-section is peaked, $\sigma_{\max}$ is the maximum value achieved by the cross section, and λ is a constant hat determines the rate of decay of the cross section beyond E_{max}. $E_{\max}$ does not vary too much from molecule to molecule and a value of $E_{\max}$ between 70 eV and 90 eV is considered reasonable.

A relation for $E_{\max}$ is given for each hydrocarbon, using the number of H and C atoms in the molecule:

$$E_{\max} = (7.71eV)C + (1.31eV)H + 67.0 \quad [eV]$$

138

The maximum cross section σ_{max} shows a more definite dependence on the C and H number in molecule.The fit relationship is :

$$\sigma_{\max} = (2.36C + 0.413H - 0.631) \times 10^{-16} \quad [\text{cm}^2]$$

The decay constant λ increases with the number of C and H atoms in the molecule. The recommended approximative fit relation is:

$$\lambda = (-64.3739eV)C + (35.3963eV)H + 668.358 \quad [eV]$$

Altman gives in [4] tables with values for E_{th} , E_{max} and λ for a series of hydrocarbons.

In the case of electron impact dissociation the measured data is available only for CH_y family. This information is used to make an extension to heavier hydrocarbons.For the electron impact dissociation, the shape of the curve is the same as that for electron impact ionization.The same functional form can be used to describe the cross section curve in terms of four parameters E_{th}, E_{max}, σ_{max} and λ.

$$\sigma_{diss}(E) = \begin{cases} 0, E < E_{th} \\ \sigma_{\max}\left(1 - \frac{(E_{\max}-E)^2}{(E_{\max}-E_{th})^2}\right), E_{th} < E < E_{\max} \\ \sigma_{\max} \times e^{-\frac{E-E_{\max}}{\lambda}}, E \geq E_{\max} \end{cases} \tag{3.70}$$

where E_{th} is the threshold energy for dissociation and is always $\approx 10eV$, $E_{\max}$ is the energy at which the maximum of the cross section σ_{max} is achieved. Finally λ is a constant that determines the rate of decay of the cross section beyond E_{max}.

The same graph shape as for methane is obtained,but the graph is scaled up or down with different values of σ_{max}. The maximum is 80% of the ionization cross-section maximum.

$$\sigma_{\max} = (1.89C + 0.330H - 0.505) \times 10^{-16} cm^2$$

The rest of the scaling formulae remain the same as in the case of ionization under electron impact.

We need to know what kind of hydrocarbons are usually found in electron microscopy producing contamination. In the vacuum system of an electron microscope the following hydrocarbon molecules can be found: C_2H_5, C_3H_7, C_4H_5 [139]. For some of these hydrocarbons we applied the scaling laws and obtained some curves for the ionization and dissociation cross sections as function of the electron energy. For example we made the calculations for the electron impact dissociation and ionization cross-section for C_2H_5 and we show the curves in Fig.. 3-44. We mention that these cross sections are valid for the C_2H_5 molecule in the gas phase.
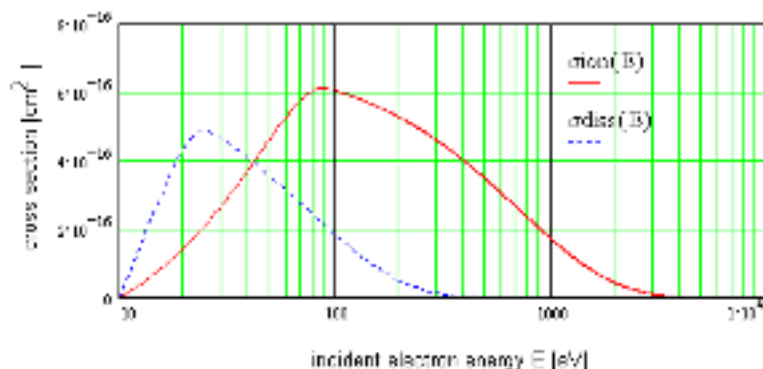
Figure 3-44: The electron impact ionization and dissociation cross sections versus electron energy for C_2H_5
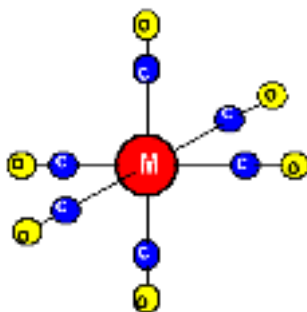

Figure 3-45: The geometry of transition metal hexacarbonyl molecule $M(CO)_6$

3.6.4.3   Organometallic compounds under electron impact

Because the main application of EBID is expected to be in the IC industry, where conductive material deposition is required, a basic condition for the chosen precursor molecule is to bear metal atoms. This is the reason why molecule species widely used in EBID are the organometallic complexes. Metallic complexes in general are molecules containing metal atoms and ligands. If the molecule contains a carbon-metal bond it is called organometallic compound. Depending on the ligand, the molecule has specific names as carbonyl if the ligand is CO. An examination of the interactions between metal orbitals and orbitals of the ligand can provide valuable insight in how organometallic molecules form and react. A few books have been published on the organometallic chemistry and photochemistry [79, 39, 128].

The commonly known carbonyls of transition metals are six coordinate octahedral complexes $M(CO)_6$, where M = Cr, Mo, W (see Fig. 3.2). This geometry is confirmed by X-ray and electron diffraction studies. These studies also confirmed the linearity of M-C-O chain.

The electronic structure and geometry of hexacarbonyls $M(CO)_6$ have been measured or calculated using software packages by many authors. The measurements on electronic structure

	W(CO)$_6$	Mo(CO)$_6$	Cr(CO)$_6$	Fe(CO)$_5$	Ni(CO)$_4$
Nr. of terminally bonded CO	6	6	6	5	4
Terminal distance M-C [Å]	2.049-2.07	2.06	1.92	1.83	1.82
Terminal distance C-O [Å]	1.16	1.156-1.164	1.17	1.15	1.15
Terminal M-C-O angle [deg]	180	180	180		

Table 3.2: The geometry of metal hexacarbonyl molecules

have been performed by electron and X-ray diffraction in [12, 10]. Calculations have been made using DSW method by [8], with DFT and MP in Gaussian package [54] and DFT with relativistic corrections has been used by Rosa in [111]. The electron impact dissociation cross sections are practically unknown.

3.7   Relevant surface processes

3.7.1   Adsorption

Molecules in the gas strike the surface from an arbitrary direction. Some of them are reflected back in the gas by elastic collisions. Others undergo inelastic collisions binding to the surface for a period of time. The molecules encounter an attractive potential that ultimately will bind them to the surface under proper circumstances and trap them in a potential barrier. This phenomenon is named adsorption.

The time the molecules stay on the surface depends on factors as: the type of surface and molecule, the temperature of the surface, etc. Once the molecule is bonded to the surface, its mobility across the surface depends on interaction of the adsorbed molecule with the surface and the interaction with other adsorbed molecules. The resultant adsorbed layer, the density of which depends on the pressure is usually treated as a monolayer. Even at high pressures the adsorbed material may be no more than a few atomic monolayers.

Adsorption is likely to occur if the incident atom or molecule has a kinetic energy that is smaller than the well depth of the attractive surface potential. An atom with higher kinetic energy may be first trapped in the surface potential and then slide along the surface before desorbing again into the gas phase, since it has enough kinetic energy left to escape.

Adsorption is always an exothermic process. The heat (energy) of adsorption ΔH_{ads} has a positive sign. The residence time τ of an adsorbed atom is given by:

$$\tau = \tau_0 \exp\left(\frac{\Delta H_{ads}}{RT}\right) \tag{3.71}$$

where τ_0 is correlated with the surface atom vibration times of the order of 10^{-13} to 10^{-12} s, T is the temperature, R is the gas constant. It is customary to divide adsorption in two classes namely physical adsorption and chemisorption. Physical adsorption equilibrium is very rapidly attained and is reversible. We can call the adsorbate-surface interaction weak if it leads to heats of adsorption of less than 110 kcal/mole. Then the adsorbate-adsorbate and adsorbate-surface interactions are of the same order of magnitude. If the residence time is several vibration periods it becomes reasonable to consider that adsorption occurs.

Adsorbed atoms and molecules achieve their equilibrium surface concentrations through a

transport process along the surface called surface diffusion.

3.7.2 The surface diffusion of precuror molecules

The surface diffusion role in specimen contamination under electron bombardment has been emphasized by Hart, Muller, Wall, Reimer, Amman in [42, 90, 92, 134, 6, 106]. A simple proof that the surface diffusion plays a role in contamination is the deposition of a dot inside and outside a labyrinth frame. The height of the dot, so the amount of contamination decreases with the number of frame walls [6].

The crucial parameters are the concentration of precursor molecules n and the diffusion constant D.

Let us consider a pulsed electron beam irradiation of a substrate and a delay time between two successive exposures. Because during one exposure the molecules are continuously cross-linked, the concentration of molecules on the surface is out of equilibrium, with a minimum in the irradiated area. To regain the equilibrium concentration, the hydrocarbons have to be transported from outside into the irradiated area, down the concentration gradient.

The molecules can arrive in the vicinity of the irradiation area by two mechanisms: from the specimen surface by diffusion or from the vacuum. If we assume that the vacuum is good enough, then only the surface diffusion is important. A finite time is needed for the molecules to reach the interaction place and replenish the irradiated area, τ_{fill} . This time is dictated by the mechanism of contaminant molecule transport on the surface. The structure cross-sectional profile depends on the relation between the replenishment time τ_{fill} and the delay time between two electron exposures, τ_d. If the delay time between two successive exposures τ_d is shorter than the time necessary for the molecules to travel from the source to the place of electron impact, then the zone is complete depleted of molecules and crater type of dots are grown (see Fig. 3-46) [6]. If the delay time is large enough, then the growth is proportional to the exposure. The peak height in the center of the irradiated area decreases when delay time is shorter. This simple model has been proven experimentally.

The concentration of mobile hydrocarbon molecules at the moment t at the distance x from the center of the radiated area can be described by the following diffusion equation:

$$\frac{\partial n(x,t)}{\partial t} = D_s \nabla^2 n(x,t) \tag{3.72}$$

where $n(x,t)$ is the surface density of the mobile hydrocarbon and D_s is the diffusion constant. Given the distribution after a particular exposure n(x,t=0) the distribution at the start of the second exposure can be determined by solving the equation (3.72).

For a dot geometry some appropriate initial conditions are:

$$n(r, t = 0) = \begin{cases} n_r & \text{if } 0 < r < d \\ n_0 & \text{if } r > d \end{cases} \tag{3.73}$$

The time dependence of the density in the center of the beam can be for example calculated as the solution of the diffusion equation (3.72) assuming initial conditions (3.73):
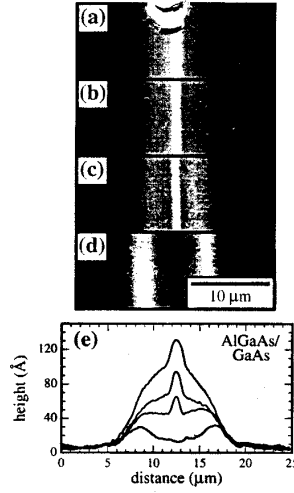
Figure 3-46: AFM images and cross sectional profiles of electron beam written contamination lines using with various delay times a)-d) decreasing delay time, e) cross sectional profile of the lines a-d (from [6])

$$n(r = 0, t = \tau_d) = n_r + (n_0 - n_r) \exp(\frac{-d^2}{4D_s\tau_d}) \tag{3.74}$$

where $2d$ is the effective size of the exposed circular region and polar coordinates $x = (r, \theta)$ have been used. The solution can be plotted as a function of the dimensionless delay time $\frac{4D\tau_d}{d^2}$ (see Fig.3-47).

By comparing this curve with an experimental curve obtained by examining contamination dots grown with different delay times, Amman obtained a value of 3 s for the diffusion time parameter $d^2/4D$ for a beam at 40 keV and a current of 100 nA on a GaAs substrate.

Muller considers that surface diffusion of molecules towards the irradiated area is the main mechanism of contamination. He calculates the contamination rate dependence of the beam diameter and current density and explains the crater formations [90, 92].

The steady state rate of transport of molecules diffusing from a source of radius r_e to a sink of radius r_0 can be determined as (see Fig. 3-48):

$$\frac{dn}{dt} = \frac{2\pi D_s n_0}{ln(\frac{r_e}{r_0})} \tag{3.75}$$

where dn/dt is the number of molecules reaching r_0 per unit time.

If the beam current is not sufficient to immediately cross-link the molecule when it reaches the periphery r_0 then the contamination rate will decrease. Hart introduced a correction factor
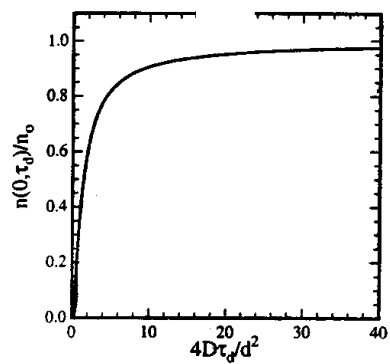
Figure 3-47: Normalized carbon surface density plotted as a function of the dimensionless delay time for the dot geometry (from [6])
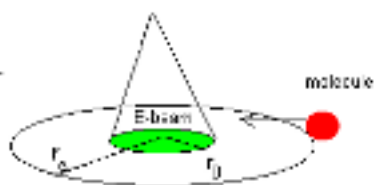

Figure 3-48: A hydrocarbon molecule diffuses from a source of radius r_e to a sink of radius r_0

to take this into account [42]:

$$\frac{dn}{dt} = \frac{2\pi D_s n_0}{(1 + \frac{1}{D\sigma})ln(\frac{r_e}{r_0})} \tag{3.76}$$

where D is the exposure dose, in electrons per unit area and σ the cross section for formation of a cross link. Multiplying this expression by the volume of a molecule v and we note that $vn_0 = h_0$, the effective thickness of the diffusing layer, we obtain :

$$\frac{dV}{dt} = v\frac{dn}{dt} = \frac{2\pi D_s h_0}{(1 + \frac{1}{D\sigma})ln(\frac{r_e}{r_0})} \tag{3.77}$$

where $\frac{dV}{dt}$ is the volume of contaminant deposited per unit time.

From the equation (3.77) we notice that for high dose ($D\sigma >> 1$)the number of molecules deposited per unit time is almost independent on the beam size. For low doses ($D\sigma << 1$)the amount of contamination obtained by the integral of eq. (3.77) is proportional with the dose. When $D\sigma = 1$ the contamination rate is 50% of maximum rate.

The interpretation of r_0 is not really the half diameter of the beam due to the larger volume of interaction for inelastic scattering in the substrate of approx. 20 Å. For small beams we should replace r_0 with $\sqrt{r_0^2 + (20\text{Å})^2}$. For larger beams the contamination may not be deposited uniformly over the beam cross section.

The magnitude of this effect can be estimated using the Einstein equation:

$$<x^2> = 4D_s t \tag{3.78}$$

where x is the mean distance travelled by a molecule in the time t.

The diffusion coefficient D_s depends on the temperature according to the relation:

$$D_s = D_{s0}exp\frac{-E_s}{kT} \tag{3.79}$$

where E_s is the activation energy and D_{s0} the diffusion coefficient at 0 ° C. The activation energy has been measured by Wall [134], and it is found to be 0.97 eV compared with 0.6 eV measured by Hart [42].

3.7.3 The electric field on the surface

When a specimen is bombarded by an electron beam in SEM, TEM or other microprobe analysis technique, the specimen charges electrically because secondary electrons are emitted. Depending on the acceleration energy which controls the SE yield, the material becomes positively or negatively charged. These excess charges (positive or negative) are accumulated in the specimen. If the specimen has a conductive path to a sink or reservoir, the excess charges will be always neutralized and the specimen will remain at its initial potential. However if this
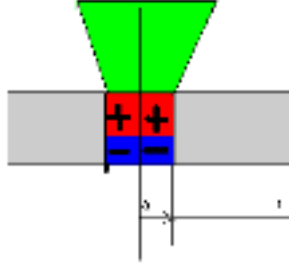
Figure 3-49: Illustration for the charging effect of an insulator bombarded by an electron beam of radius a.

path does not exist, these charges in excess will accumulate and will cause the potential on the specimen to change. The difference between metals and dielectrics is that the dielectric does not have sufficient conduction electrons to quickly restore the neutrality of the specimen. The electrical field can be a danger if the specimen is isolated in the specimen holder or if the specimen is an insulator.

The charging of the specimen gives rise to an electrical field that can produce a breakdown in the insulator, electrostatic deflection of the beam or of low energy SE. In SEM the charging is observed by bright zones charged negatively and dark zone charged positively. Maybe the most spectacular effect is the mobile ion migration in glass materials (Na^+,Cl^-, etc).

We are interested to see if the electrical field created on the substrate surface can produce the migration of ionized molecular fragments away from the irradiated area. If they will get fixed at some distance from the irradiated area, then this electrical field migth attack negatively the EBID spatial resolution.

Cazeaux gives analytical formulas for the radial field intensity E_r and potential V_r on a dielectric surface irradiated by a focused electron beam for different specimen geometries [16, 17].

The general relations for the radial field intensity are:

$$E_r(r) = \frac{\rho d}{2\varepsilon}\frac{2a}{\pi}\left[J_1\left(\frac{r}{a}\right) - J_2\left(\frac{r}{a}\right)\right], r < a \tag{3.80}$$

$$= \frac{\rho d}{2\pi}\frac{2}{\pi}\left[J_1\left(\frac{a}{r}\right) - J_2\left(\frac{a}{r}\right)\right], r > a \tag{3.81}$$

where $J_1(k)$ and $J_2(k)$ are the elliptic integrals :

$$J_1(k) = \int_0^{\frac{\pi}{2}} \frac{d\psi}{(1 - k^2\sin^2\psi)^{1/2}}$$

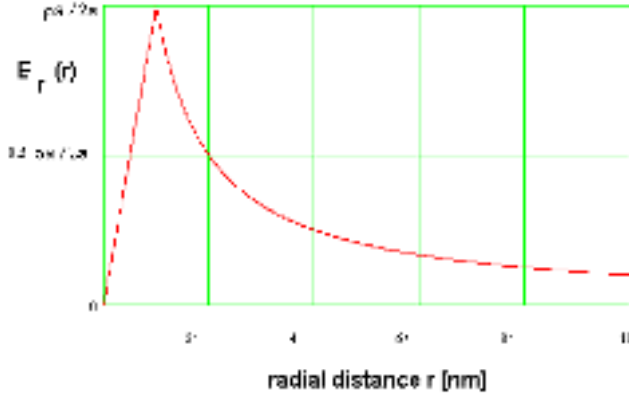$$J_2(k) = \int_0^{\frac{\pi}{2}} (1 - k^2\sin^2\psi)^{1/2}d\psi$$

146

Figure 3-50: The typical electrical field intensity distribution on a surface irradiated with an electron beam of radius a = 1 nm

For a thin film in vacuum, the relations are (see Fig.3-49):

$$E_r(r) = \frac{q}{2\pi\varepsilon d}\frac{1}{r}, r > a \tag{3.82}$$

$$= \frac{qr}{2\pi\varepsilon da^2}, 0 < r < a \tag{3.83}$$

where

d = thickness of the film [m]
a = radius of the beam
$\varepsilon = \varepsilon_r\varepsilon_0$
ε_0= the permittivity of vacuum = $8.854187817 \times 10^{-12}\,\mathrm{F\,m^{-1}}$
q= the accumulated charge in the target [C]

If the film is thin, then the negative charge is zero, because all the electrons are transmitted.
The electrical potential V_r at a radial distance r from the center of the beam on the surface, with the condition $V_r(r_0) = 0$ is

$$V_r(r) = \frac{q}{2\pi\varepsilon d}\ln\left(\frac{r_0}{r}\right), a < r < r_0 \tag{3.84}$$

$$= \frac{q}{4\pi\varepsilon d}\left[1 - \frac{r^2}{a^2} + 2\ln\frac{r_0}{a}\right], 0 < r \le a \tag{3.85}$$

The electrostatic approach is a different way to explain the crater shaped contamination marks and has been proposed by Fourie [33, 35, 36]. Here the local positive charge of the irradiated area enhances the diffusion of polarisable molecules.

A positive potential is constantly created under and near the electron irradiated area due to escaping secondary electrons. The field intensity is in the range of 10^9 V/m, for example 0.1V/Å for a SiO film irradiated with 10^{-11} A beam of 1 μm diameter [34].

The electrical field around the illuminated region can exercise a drift force on the molecules, influencing the local concentrations. The adsorbed hydrocarbon molecules diffusion towards the illuminated region is different for field present or field absent situations.

When a specimen is irradiated with a focused primary electron beam, secondary electrons are emitted from the target, leaving a net positive charge. For a conductor foil the charge will be neutralized by conduction of electrons from the grid bar. An insulator is different because there are less conduction electrons. For an insulator or a conductor foil covered with a insulator layer (like contamination), the charge will accumulate until a steady-state condition (produced charge vs. flux of electron from the grid bar) will be reached.

The hydrocarbon molecules can become polarized in a strong electric field according to their polarisability α. If the field is inhomogeneous, a drift force will act on the molecular dipole.

The drift force on polarised molecules in the electric field is given by:

$$F = \alpha E_r \frac{dE_r}{dr} \tag{3.86}$$

where α is the polarisability of the molecule.

In Fig. 3-50 we plotted a typical electrical field intensity distribution on a surface irradiated with a beam of radius a = 1 nm. We used the equations given by Cazeux (3.82). We see that for distances r > a, molecules will be attracted towards the illuminated region and for r < a, they will be deflected in the opposite direction. So at the perimeter of the beam the concentration of molecules will increase.

The idea of Fourie, supported by Cazeaux, but criticized by Reimer [106], is that this electrical field enhances the molecules diffusion to the periphery of the radiated area, explaining the rings formed for defocused beam. In microbiology the fact that an electrical field can induce migration of polarizable cells is known as diaphoresis.

3.8   Conclusions

At this moment a theoretical model for EBID resolution that agrees with experimental results have not been issued yet. The theoretically estimation of EBID resolution needs the following practical steps. First the role of the secondary electrons in EBID has to be theoretically evaluated. For this purpose, Monte Carlo methods can be used to simulate the secondary electron emission and the deposited profile evolution.

A compilation of MC results shows that the radial distribution of secondary electrons on the surface has a typical minimum FWHM of 0.1 - 2 nm and the radial distribution has a FWHM of 0.5 - 2 nm for metal targets. In the Table 3.3 some relevant SE spatial data determined using MC simulations by different authors is summarized.

The spatial distribution of SE is not a final result for us, but it gives an estimation of the maximum extend of SE influence in EBID. The results are only interesting in conjunction with the spatial extend of the SE energies in the exit point. The same conclusion was obtained in the resist based EBL case. "For further discussion on the effect of SE to the ultimate resolution in EBL, the MC calculations combined with a development model are needed" [115]

In the past, numerous (say N) Monte Carlo simulation programs for SE emission have been already generated. So an obvious question is why should we produce another simulation program (N+1) instead of using the existing accumulated tools?

1. The first feeling is that there is not a unanimous opinion about the spatial distribution of SE. The results are quite different so we can talk only about a range of scattered results.

2. The existing programs are written for SEM applications. Therefore they accept as input only electron energies up to 30 kV. We can extend it to TEM applications for 100-200 kV with relativistic corrections.

3. For the same reason, the specimens are usually bulk, 1-1000 μm thick, which require a long calculation time for each simulated trajectory. Although a lot of programs have been written, they all used a lot of simplifications in modelling in order to save time. We can restrict the program to thin foil targets 10-50 nm and afford more complex theoretical models.

4. The MC simulations for SEM use provide the secondary electrons as a global signal for image formation. The output data is given as spatial profile, which is good for us, but the energy is presented as a cumulated spectrum. The data is not classified by position and energy. We need secondary electrons energy spectra in each position on the surface, to couple it to the dissociation cross sections of different precursors. In resist EBL modelling only the threshold model of resist solubility is used. But the real dissociation cross section for a gas precursor is far from a step function.

5. The absolute SE yield calculation is still a challenging task. All simulation methods used until a few years ago needed an empirical fit parameter to scale the yield curve for each element. For us the SE yield is very important if we want to compare PE vs. SE role in dissociation. Only the dielectric function approach can calculate this yield [27, 29]. This attractive approach in MC simulations is relatively new, it can be used only recently since optical data and measured EELS data become accessible and fast computers are provided. It is an attractive approach.

6. Our own program will give us flexibility and all the advantages of an accessible source code. For example, a more complex computer simulation customized for EBID can be built. It should have more modules - the MC simulation of electrons trajectories, a profile simulator to trace on-line the boundary evolution of a deposited dot, a module for migration influences, etc.

The spatial distribution of SE obtained by Monte Carlo simulations has to be further combined with the electron-impact dissociation cross section, specific for the given precursor. An

| Radial distribution [nm] | | Lateral distribution [nm] | | Substrate | Beam energy [keV] | Beam diameter [nm] | Ref. |
FW50%	FWHM	FW50%	FWHM				
4.4	0.8	2.3	2.2	Au 10nm	10	0	[28]
3.4	0.8	2	2.2	Au 10nm	30	0	[28]
			3	Al 5nm	20	0	[57]
			3	C	30	0	[57]
	0.125		0.491	Cu	1	0.1	[71]
	0.157		0.423	Cu	10	0.1	[71]
	0.1			Al	1	0	[82]
			1	Cu	1	0	[70]

Table 3.3: The spatial distribution of secondary electrons on the target surface. Typical results reported by different MC simulations authors.

accurate expression for this cross section is hard to find for most of the gases. Practically such a complex analysis has never been made. If we succeed, this will bring an improvement to the existing results. Other effects, even less investigated than the secondary electrons, but that might affect the EBID resolution have to be quantified, as well, like the delocalization of electron inelastic scattering, electron beam induced fragments migration and electric field induced molecular displacement.

Bibliography

[1] ADALSSTEINSSON, D., AND SETHIAN, J. A level set approach to a unified model for etching, deposition, and lithography. *Journal of computational physics A 120* (1995), 128.

[2] AHLEN, S. Theoretical and experimnetal aspects of the energy loss of relativistic heavily ionizing particles. *Reviews of Modern Physics 52* (1980), 121.

[3] ALLEN, T., AND MAYER, T. Monte Carlo calculations of low energy electron emission from surfaces. *Journal of Vacuum Science and Technology B 6* (1988), 2057.

[4] ALMAN, D., RUZIC, D., AND BROOKS, J. A hydrocarbon reaction model for low temperature hydrogen plasma and an application to the Joint European Torus. *Physics of Plasmas 7* (2000), 1421.

[5] AMELIO, G. Theory for the energy distribution of secondary electrons. *Journal of Vacuum Science and Technology 7* (1970), 593.

[6] AMMAN, M., SLEIGHT, J., LOMBARDI, D., WELSER, R., AND DESHPANDE, M. Atomic force microscopy study of electron beam written contamination structures. *Journal of Vacuum Science and Technology B 14* (1996), 54.

[7] A.R.NEUREUTHER. Applications of line-edge profile simulation to thin film deposition processes. *IEEE Trans. on El. Devices ED-27* (1980), 1449.

[8] ARRATIA-PEREZ, R., AND YANG, C. Bonding in metal carbonyls. *J. Chem. Phys. 83* (1985), 4005.

[9] ATKINS, P., AND FRIEDMAN, R. *Molecular Quantum Mechanics*. Oxford University Press, Oxford, 1997.

[10] BEACH, N., AND GRAY, H. Electronic structures of metal hexacarbonyls. *J. Am. Chem. Soc 90*, 21 (1968), 5713.

[11] BONGELIER, R., GOLLA, U., KASSENS, M., REIMER, L., SCHINDLER, B., SENKEL, R., AND SPRANK, M. Electron specimen interactions in low voltage scanning electron microscopy. *Scanning 15* (1992), 1.

[12] BROCKWAY, L., EWENS, R., AND LISTER, M. W. An electron diffraction investigation of the hexacarbonyls of chromium, molybdenum and tungsten. *Trans. Faraday Society 34* (1938), 1350.

[13] BROERS, A. Resolution limits for electron beam lithography. *IBM Journal of research and development 32* (1988), 49.

[14] BROERS, A. N., AND HOOLE, A. Electron beam lithography-resolution limits. *Microelectronic Engineering 32* (1996), 131.

[15] BROWNING, R., LI, T., CHUI, B., YE, J., PEASE, R., CZYZEWSKI, Z., AND JOY, D. Empirical forms for the electron-atom elastic scattering cross sections from 0 to 30 keV. *Journal of Applied Physics 76* (1994), 2016.

[16] CAZEAUX, J. Some considerations on the electric field induced insulators electron bombardment. *Journal of Applied Physics 59* (1986), 1418.

[17] CAZEAUX, J. Correlations between ionization radiation damage and charging effects in transmission electron microscopy. *Ultramicroscopy 60* (1995), 411.

[18] CHRISTOPHOROU, L., OLTHOFF, J., AND RAO, M. Electron interactions with CF4. *J. Phys. Chem. Ref. Data 25* (1996), 1341.

[19] CHUNG, M., AND EVERHART, T. Simple calculations of energy distribution of low energy secondary electrons emitted from metals under electron bombardment. *Journal of Applied Physics 45* (1974), 707.

[20] CHUNG, S., LIN, C., AND LEE, E. Dissociation of the hydrogen molecule by electron impact. *Physical Review A 12* (1975), 1340.

[21] CZYZEWSKI, Z., McCALLUM, D., ROMIG, A., AND JOY, D. Calculations of Mott scattering cross section. *Journal of Applied Physics 68* (1990), 3066.

[22] DAYASHANKAR. Construction of energy loss function for low energy electrons in helium. *Physica C 81* (1976), 409.

[23] DAYASHANKAR. Electron energy deposition in helium. *Physica C 85* (1977), 219.

[24] DEVOOGD, J., DUBUS, A., AND DEHAES, J. Improved diffusion model for low energy electron transport in solids. *Physical Review B 36* (1987), 5093.

[25] DING, Z., AND SHIMIZU, R. Theoretical study of the ultimate resolutiom of SEM. *Journal of Microscopy 154* (1989), 1989.

[26] DING, Z., AND SHIMIZU, R. A Monte Carlo modelling of electron interaction with solids including cascade secondary electron production. *Scanning 18* (1996), 92.

[27] DING, Z., AND SHIMIZU, R. Monte Carlo simulation study of secondary electron emission and surface excitation. *Inst. Phys. Conf. 165* (2000), 279.

[28] DING, Z., SHIMIZU, R., SEKINE, T., AND SAKAI, Y. Theoretical and experimental studies of N(E) spectra in Auger Electron spectroscopy. *Applied Surface Science 33/34* (1988), 99.

[29] DING, Z., AND TANG, X. Monte Carlo study of secondary electron emission. *Journal of Applied Physics 89* (2001), 718.

[30] EVERHART, T., AND CHUNG, M. Normalized spatial emission distribution of secondary electrons. *Journal of Applied Physics 43* (1972), 3707.

[31] FITTING, H., HINKFOTH, C., GLAEFEKE, AND KUHR, J. C. Electron scattering in the keV and sub-keV range. *Phys. Status Solidi A 126* (1991), 85.

[32] FORESMAN, J., AND FRISCH, A. *Exploring chemistry with electronic structure methods.* Gaussian Inc, Pittsburgh, 1995-96.

[33] FOURIE, J. The controlling parameter in contamination of specimens in electron microscopy. *Optik 44* (1975), 111.

[34] FOURIE, J. High contamination rates from strongly adsorbed hydrocarbon molecules and a suggested solution. *Optik 52* (1978), 91.

[35] FOURIE, J. A theory of surface origination contamination and a method for its elimination. *Scanning Electron Microscopy II* (1979), 87.

[36] FOURIE, J. Electric effects in contamination and electron beam etching. *Scanning Electron Microscopy I* (1981), 127.

[37] FRISCH, A., AND FRISCH, M. *Gaussian98 user's reference.* Gaussian Inc, Pittsburgh, 1998.

[38] GAUVIN, R., AND DROUIN, D. A formula to compute total elastic Mott cross sections. *Scanning 15* (1993), 140.

[39] GEOFFROY, G. *Organometallic photochemistry.* Academic Press, New York, 1979.

[40] GREENICH, J. S., AND VAN DUZER, T. Model for exposure of electron sensitive resists. *Journal of Vacuum Science and Technology 10* (1973), 1056.

[41] HALL, J., HANSMA, P., AND PARIKH, M. Electron beam damage of chemisorbed surface species: a tunnelling spectroscopy study. *Surface science 65* (1977), 552.

[42] HART, R., KASSNER, T., AND MAURIN, J. The contamination of surfaces during high-energy electron irradiation. *Philosophical Magazine* (1969), 453.

[43] HAWRYLUK, R., HAWRYLUK, A., AND SMITH, H. Energy dissipation in a thin polymer film by electron beam scattering. *Journal of Applied Physics 45* (1974), 2551.

[44] HENOC, J., AND MAURICE, F. A flexible and complete Monte Carlo procedure for the study of the choice of parameters. In *Electron Probe Quantitation*, K. Heinrich and D.E.Newburry, Eds. Plenum Press, 1991, p. 105.

[45] HIROSHIMA, H., AND KOMURO, M. High growth rate for slow scanning in electron-beam-induced-deposition. *Japanese Journal of Applied Physics 36* (1997), 7686.

[46] HO, Y., Z.TAN, X.WANG, AND CHEN, J. A theory and Monte Carlo calculation on low energy electron scattering. *Scanning microscopy 5* (1991), 945.

[47] HOVINGTON, P., DROUIN, D., AND GAUVIN, R. CASINO:A new Monte Carlo Code in C language for electron beam interaction- I:Description of the program. *Scanning 19* (1997), 1–14.

[48] HOVINGTON, P., DROUIN, D., GAUVIN, R., JOY, D., AND EVANS, N. CASINO:A new Monte Carlo Code in C language for electron beam interaction-III:Stopping power at low energies. *Scanning 19* (1997), 29–35.

[49] HOYLE, P., CLEAVER, J., AND AHMED. Electron beam induced deposition from $W(CO)_6$ at 2 to 20 kev and its applications. *Journal of Vacuum Science and Technology B 14* (1996), 92.

[50] HUBNER, B., AND KOOPS, H. Tips for scanning tunneling microscopy produced by EBID. *Ultramicroscopy 42-44* (1992), 1519.

[51] HUBNER, U., AND PLONTKE, R. On-line nanolithography using electron beam induced deposition technique. *Microelectronic Engineering 57-58* (2001), 953.

[52] INOKUTI, M. Inelastic collisions of fast charged particles with atoms and molecules-the Bethe theory revisited. *Reviews of Modern Physics 43* (1971), 297.

[53] JAMES, F. Monte Carlo theory and practice. *Rep. Prog. Phys. 43* (1980), 73.

[54] JONAS, V., AND THIEL, W. Theoretical study of the vibrational spectra of transition metals carbonyls $M(CO)_6$. *J. Chem. Phys 102*, 21 (1995), 8474.

[55] JOY, D. The spatial resolution limit of electron lithography. *Microelectronic Engineering 1* (1983), 103.

[56] JOY, D. Beam interactions, contrast and resolution in the SEM. *Journal of Microscopy 136* (1984), 241.

[57] JOY, D. Monte Carlo studies of high resolution imaging. In *Microbeam analysis* (1984), A. Romig and J. Goldstein, Eds., San Francisco press, p. 81.

[58] JOY, D. Resolution in low voltage scanning electron microscopy. *Journal of Microscopy 140* (1985), 283.

[59] JOY, D. An introduction to Monte Carlo simulations. *Int. Phys. Conf. Ser. 1* (1988), 23.

[60] JOY, D. The theory and practice of high-resolution scanning electron microscopy. *Ultramicroscopy 37* (1991), 216.

[61] JOY, D. High-resolution scanning electron microscopy. *Ultramiscopy 47* (1992), 80.

[62] JOY, D. *Monte Carlo Modeling for electron microscopy and microanalysis.* Oxford university press, New York, 1994.

[63] JOY, D. A database for electron-solid interactions. *Scanning 17* (1995), 270.

[64] KIJIMA, T., KOTERA, M., SUGA, H., AND NAKASE, Y. Monte Carlo alculations on the passage of electrons through thin films irradiated by 300 kev electrons. *IEICE trans. Electron E78-C* (1995), 557.

[65] KIM, Y., HWANG, W., WEINBERG, N., ALI, M., AND RUDD, M. Electron-impact ionization cross section on atmospheric molecules. *J. Chem. Phys. 106* (1997), 1026.

[66] KNOLL, G. *Radiation detection and measurement.* John Wiley and Sons, New York, 1979.

[67] KOHLMANN-VON PLATEN, K., AND CHLEBEK, J. Resolution limits in electron-beam induced tungsten deposition. *Journal of Vacuum Science and Technology B 11* (1993), 2219.

[68] Komuro, M., and Hiroshima, H. Fabrication and properties of dot array using electron-beam-induced deposition. *Microelectronic Engineering 35* (1997), 273.

[69] Komuro, M., Hiroshima, H., and Takechi, A. Miniature tunnel junction by electron-beam-induced deposition. *Nanotechnology 9* (1998), 104.

[70] Koshikawa, T., and Shimizu, R. A Monte Carlo calculation of low energy secondary electron emission from metals. *Journal of Physics D 7* (1974), 1303.

[71] Kotera, M. A Monte Carlo simulation of primary and secondary electron trajectories in a specimen. *Journal of Applied Physics 65* (1989), 3991.

[72] Kotera, M., Kishida, T., and Suga, H. A simulation of secondary electron trajectories in solids. *Scanning microscopy 3* (1989), 993.

[73] Kuhr, J., and Fitting, H. Monte Carlo simulation of low energy electron scattering in solids. *Phys. Stat. Solidi. a 172* (1999), 433.

[74] Kuhr, J. C., and Fitting, H. Monte Carlo simulation of electron emission from solids. *Journal of Electron spectroscopy and related phenomena 105* (1999), 257.

[75] Kunz, R., Allen, T., and Mayer, T. Selective area deposition of metals using low energy electron beams. *Journal of Vacuum Science and Technology B 5* (1987), 1427.

[76] Li, H., Ding, Z., and Ziquin, W. Multifractal behaviour on the distribution of secondary electron emission sites on solid surface. *Physical Review B 51* (1995), 51.

[77] Lipp, S., Frey, L., and Lehrer. A comparision of focused ion beam and electron beam induced deposition processes. *Microelectronics and reliability 36* (1996), 1779.

[78] Liu, J., and Hagstrom, S. Dissociative cross sections of H_2 by electron impact. *Physical Review A 50* (1994), 3181.

[79] Lukehart, C. *Fundamental transition metal organometallic chemistry.* Brooks/Cole Publishing Company, Monterey, 1985.

[80] Luo, S., and Joy, D. Monte Carlo calculations of secondary electron emission. *Scanning microscopy supplement 4* (1990), 127.

[81] Luo, S., Yongsheng, Z., and Ziqin, W. A Monte Carlo calculation of secondary electrons emitted from Au, Ag and Cu. *Journal of Microscopy 148* (1987), 289.

[82] M. Kotera, R. I., Fujiwara, T., Suga, H., and Witry, D. A simulation of electrons in metals. *Japanese Journal of Applied Physics 29* (1990), 2277.

[83] Mark, T. Ionization of molecules by electron impact. In *Electron-molecule interactions and their applications*, L. Christophorou, Ed. Academic Press, 1984, p. 251.

[84] Martel, R., and McBreen, P. Dissociative resonance activation of cyclopropane monolayers on copper: evidence for ch and cc bond scission. *J. Chem Phys. 107* (1997), 8619.

[85] Matsui, S., and Ichihashi, T. Electron beam induced selective etching and deposition technology. *Journal of Vacuum Science and Technology B 7* (1989), 1182.

155

[86] MEISELS, G., CHEN, C., GIESSNER, B., AND EMMEL, R. Energy deposition functions in mass spectroscopy. *The journal of chemical physics 56* (1972), 793.

[87] MI, L., AND BONHAM, R. Electron-ion coincidence measurements: the neutral dissociation cross section for CF_4. *J. Chem. Phys 108* (1998), 1910.

[88] MICHAEL, J., WILLIAMS, D., KLEIN, C., AND AYER, R. The measurement and calculation of the X-ray spatial-resolution obtained in the analytical electron microscope. *Journal of microscopy 160* (1990), 41.

[89] MULLER, D., AND J.SILCOX. Delocalization in inelastic scattering. *Ultramicroscopy 59* (1995), 195–213.

[90] MÜLLER, K. Elektronen mikroschreiber mit geschwindigkeitsgesteuerter strahlfurung. II. *Optik 33* (1971), 296.

[91] MURATA, K. Monte Carlo simulation of fast secondary electron production in electron beam resists. *Journal of Applied Physics 52* (1981), 4396.

[92] MÜULLER, K. Elektronen mikroschreiber mit geschwindigkeitsgesteuerter strahlfurung. I. *Optik 33* (1971), 331.

[93] NEWBURY, D. Electron beam specimen interactions in the analytical electron microscope. In *Principles of analytical electron microscopy*. Plenum Press New York, 1986.

[94] OCHIAI, Y., AND FUJITA. Electron induced beam deposition of copper compound with low resistivity. *Journal of Vacuum Science and Technology B 14* (1996), 933.

[95] ODAGIRI, T., UEMURA, N., KOYAMA, K., AND UKSAI, M. Electron energy loss study of superexcited nydrogen molecules with the coincidence detection of the neutral dissociation. *J. Phys. B: At. Mol. Opt. Phys. 28* (1995), L465.

[96] PALIK, E. *Handbook of optical constants of solids*. Academic Press, San Diego, 1998.

[97] PARIKH, M. Calculation of dissociative ionization cross section of diatomic molecules. *Physical Review A 12* (1975), 1872.

[98] PENN, D. Electron mean free path calculations using a model dielectric function. *Physical Review B 35* (1987), 482.

[99] PIJPER, F., AND KRUIT, P. Detection of energy selected secondary electrons in coincidence with energy loss events in thin carbon foils. *Physical Review B 44* (1991), 9192.

[100] POWELL, C. Inelastic mean free paths and attenuation lengths of low energy electron in solids. *Scanning electron microscopy IV* (1984), 1649.

[101] POWELL, C. Cross sections for inelastic electron scattering in solids. *Ultramicroscopy 28* (1989), 24.

[102] POWELL, C., AND JABLONSKI, A. Consistency of calculated and measured electron elastic mean free paths. *Journal of Vacuum Science and Technology A 17* (1999), 1122.

[103] POWELL, C., AND JABLONSKI, A. Evaluation of calculated and measured electron inelastic mean free paths near solid surfaces. *J.Phys. Chem Ref. Data 28* (1999), 19.

[104] POWELL, C., AND JABLONSKI, A. Evaluation of electron inelastic mean free paths for selected elements and compounds. *Surface and interface analysis 29* (2000), 108.

[105] RAO-SAHIB, T., AND WITTRY, D. X-ray continuum from thick element targets for 10-50 keV electrons. *Journal of Applied Physics 45* (1974), 5060.

[106] REIMER, L. Contribution to the contamination problem in transmission electron microscopy. *Ultramicroscopy 3* (1978), 169.

[107] REIMER, L. *Scanning electron microscopy*. Springer Verlag, Berlin Heidelberg New York, 1990.

[108] REIMER, L., AND LODDING, B. Theory of secondary electron emission ii. *Scanning 6* (1984), 128.

[109] REZ, P. A transport equation theory of beam spreading in the lectron microscope. *Ultramicroscopy 12* (1983), 29.

[110] RITCHIE, R., GARBER, F., NAKAI, M., AND BIRKHOFF, R. *Advances in Radiation Biology 3* (1969), 1.

[111] ROSA, A., BAERENDS, E., VAN GISBEREN, S., VAN LENTHE, E., GROENEVELD, J., AND SNIJDERS, J. Electronic spectra of $M(CO)_6$ revisited by a relativistic DDFT approach. *J. Am. Chem. Soc 121* (1999), 10356.

[112] ROSLER, M. Theory of secondary electron emission i. *Phys. Stat. Sol.b 104* (1981), 161.

[113] ROSLER, M. Theory of secondary electron emission ii. *Phys. Stat. Sol.b 104* (1981), 575.

[114] SAKSENA, V., KUSHWAHA, M., AND KHARE, S. Electron impact ionisation of molecules at high energies. *Int. J. of Mass Spectrometry and Ion processes 171* (1997), L1.

[115] SAMOTO, N., AND SHIMIZU, R. Theoretical study of the ultimate resolution in electron beam lithography by Monte Carlo simulation, including secondary electron generation: Energy dissipation profile in PMMA. *Journal of Applied Physics 54* (1983), 3855.

[116] SANCHE, L. Investigation of ultra fast events in radiation chemistry with low energy electrons. *Radiat. Phys. Chem 34* (1989), 15.

[117] SANCHE, L. Low energy electron scattering from molecules on surface. *J. Phys B 23* (1990), 1597.

[118] SANCHE, L. Les electrons secondaires en chimie et biologie sous rayonnement. *J. Chim. Phys 94* (1997), 216.

[119] SCHEUER, V., AND KOOPS, H. Electron beam decomposition of carbonyls on silicon. *Microelectronic Engineering 5* (1986), 423.

[120] SCOTT, V., LOVE, G., AND REED, S. B. *Quantitative electron-probe microanalysis*. Ellis Horwood, New York, 1995.

[121] SEAH, M., AND DENCH, W. Quantitative electron spectroscopy. *Surface and interface analysis 1* (1979), 2.

[122] Shimizu, R., and Ding, Z. Monte Carlo modelling of electron-solid interactions. *Rep. Prog. Phys.* (1992), 487.

[123] Shimizu, R., and Ichimura, S. Direct Monte Carlo simulation of scattering processes. *Surface science 133* (1983), 250.

[124] Shimizu, R., and Ichimura, S. Direct Monte Carlo simulation of scattering processes. *Surface science 133* (1983), 250.

[125] Shimizu, R., and Murata, K. Monte Carlo calculations of electron sample interactions in the scanning electron microscope. *Journal of Applied Physics 42* (1971), 387.

[126] S.J.B.Reed. The single-scattering model and spatial resolution in X-ray analysis in thin foils. *Ultramicroscopy 7* (1982), 405.

[127] Sobol, I. *A primer for Monte Carlo Method*. CRC Press, Boca Raton, 1994.

[128] Spessard, G. *Organometallic chemistry*. Prentice Hall, Upper Saddle River, 1997.

[129] Sristava, S. Present status of the measured dissociation attachment cross sections. *American Institute of Physics* (1987), 69.

[130] Streitwolf, H. Zur theorie der sekundarelektronenemission von metallen. *Annalen der Physik 3* (1959), 183.

[131] Tilnin, I. Energy and angular distributions of secondary electrons induced by fast charged particles in the near surface layer of solid molecular hudrogen. *Phys. Chem. Mech. Surfaces 4* (1986), 1350.

[132] T.Kijima, and Nakase, Y. Monte Carlo calculations of the behaviour of 300 keV electrons from accelerators. *Radiation Measurements 26* (1996), 159.

[133] Trajmar, S. Excitation of molecules by electron impact. In *Electron-molecule interactions and their applications*, L. Christophorou, Ed. Academic Press, Orlando, 1984, p. 155.

[134] Wall, J. Contamination in the STEM at ultra high vacuum. *Scanning Electron Microscopy I* (1980), 99.

[135] Weber, M. Scattering of non-relativistic electrons in tip structures. *Journal of Applied Physics 27* (1994), 1363.

[136] Wells, O. *Scanning eletron microscopy*. McGraw Hill, New York, 1974.

[137] Williams, D., and Carter, B. *Transmission electron microscopy*. Plenum press, 1996.

[138] Wolf, P. Theory of secondary electron cascade in metals. *Physical review 95* (1954), 56.

[139] Yoshimura, N., Hirano, H., and Etoh, T. Mechanism of contamination build-up induced by fine electron probe irradiation. *Vacuum 33* (1983), 391.

[140] Younger, S., and Mark, T. Semi-empirical and semi-classical approximations for electron ionization. In *Electron impact ionization*, T. Mark and G. Dunn, Eds. Springer Verlag, Wien, New York, 1985, p. 24.

[141] Zipf, E. Dissociation of molecules by electron impact. In *Electron-molecule interactions and their applications*, L. Christophorou, Ed. Academic Press, Orlando, 1984, p. 335.

Chapter 4

The role of secondary electrons in EBID

4.1 Introduction

The spatial resolution of EBID is determined by many factors, like the electron transport to the surface, the parameters of the precursor gas, the target and its environment, various surface processes, delocalization effects, etc. Most EBID models take into consideration only the parameters of the primary electron (PE) beam [21]. However, there is abundant experimental evidence that the lateral size of dots and lines, fabricated by EBID with high energy electrons, considerably exceeds the diameter of the electron beam writing tool [22, 16, 15, 14]. From the EBID literature survey we noticed that many authors consider that this lateral broadening is mainly caused by the low energy secondary electrons (SE), emitted from the substrate as a result of the primary electron beam irradiation. This assumption is based on the fact that the electron-impact molecular dissociation, the main process in EBID, has cross-sections peaked at low kinetic energies. EBID performed in a STM also indicates that dissociation is induced by these primary low energy electrons. The diameter of the structures grown in STM are similar to the beam diameter and this might be explained with the absence of secondary electrons. However, a complete theoretical model that explains the lateral broadening based on the role of secondary electrons, offering results in agreement with experiments, has not been issued yet.

Our objective in this chapter is to fill this gap and quantify the role of the secondary electrons in EBID spatial resolution. Our model uses Monte Carlo methods for the simulation of electron scattering in the solid and for the prediction of the deposit growth under the influence of secondary electrons. We will present the results of these simulations which are well in agreement with experimental observations.

The model

Let us consider a typical EBID process, in which a finely focused electron beam is kept stationary on a target covered by precursor molecules. After a short time, a conical structure starts to grow on the target, localized in the electron irradiated area. This process is also well-known from the contamination growth in electron microscopes.

The diameter of the cone, measured at its base or at half maximum height, grows steeply and after some time reaches a saturation value, which always exceeds the diameter of the electron
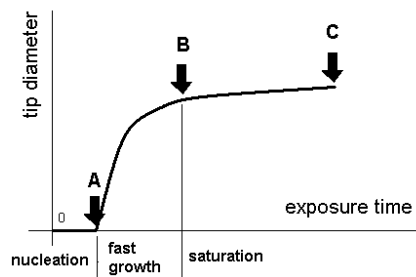
Figure 4-1: A typical curve showing the evolution of the cone diameter

probe at the target. Typically encountered values range from 20 to 500 nm for beam diameters of 2 -10 nm on both thin and bulk specimens.

The exact time behaviour of the diameter is hard to give, as it depends on many parameters like the settings of the electron optics, the partial pressure of the precursor gas, the surface diffusion of the precursor molecules, the cleanliness of the specimen, etc. But qualitatively the diameter vs. time curve will be as sketched in Fig. 4-1, in which the following regimes can be distinguished: the nucleation stage (marked 0-A in Fig. 4-1) when no significant growth is observed, an intermediate regime (A-B) characterized by a fast growth of the structure diameter, and the saturation regime (B-C) where the diameter attains a more or less constant value.

We will model this behaviour by assuming that it is the result of exclusively the secondary electrons emitted as result of primary beam bombardment. The model we propose describes the growth process as follows.

After some time following the start of the electron beam exposure, the nucleation is completed (point A in Fig. 4-1). The primary electrons hit the flat substrate surface and generate secondary electrons in the substrate, which are partly emitted from the flat substrate, from an area larger than the beam diameter. Both types of electrons, PE and SE, will dissociate the adsorbed molecules and a dot will start to be deposited, its diameter being determined by the exit area of SE on the target surface (Fig. 4-2 a).
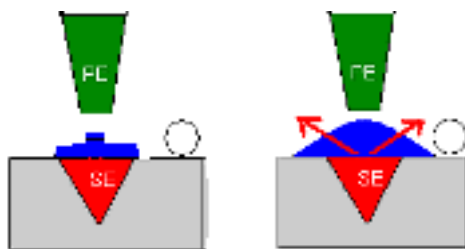
Figure 4-2: Illustration on the role of the secondary electrons (SE) at different growth moments: a) in the beginning, b) after a tip structure has grown

162

Although this scenario has been brought up by many authors as an explanation for the growth of structures broader than the primary beam size, we will show from Monte Carlo simulations that experimentally observed structure sizes cannot be explained this way at all. Therefore we extended this model by including the electron scattering in the freshly grown structure. While the tip-like structure grows in vertical direction, the PE entering the apex of the tip may scatter in the tip, generating SE that can exit the tip from its side walls. These secondary electrons will dissociate the precursor molecules adsorbed on the tip flanks and thus will contribute to an extra lateral broadening (Fig. 4-2 b). Saturation will occur when the secondary electrons will not be able to exit the side flanks anymore. This moment will be determined by the escape depth, i.e. the inelastic mean free path, of the secondary electrons in the deposit (5 -15 nm) [20].

The next step is to develop a model based on this scenario. The problem is thus reduced to the prediction of the spatial profile of a cone grown by the secondary electrons between the moments A and B. We will first give the general procedure followed in order to solve this problem.

The dissociation rate produced by secondary electrons will be given by:

$$R_{SE}(x) = \int\limits_0^{E_P} f_{SE}(x,E)\sigma_{diss}(E)N\,dE \quad [\text{atoms/Å}^2/\text{s}] \qquad (4.1)$$

Some authors tried to extend the fabrication resolution analysis by including the role of secondary electrons [8, 2, 11, 6]. They all started with a Monte Carlo simulation or an analytical approach and determined the SE spatial and energy distributions on the target surface, $f_{SE}(x,E)$. But they encountered difficulties at the dissociation cross section $\sigma_{diss}(E)$ which is in general unknown for the precursors used in EBID process. The authors reactions in front of this challenge were different. Some authors used a simplified model like Dubner did for IBID [8], Joy did for resist EBL [11] and de Jager did for the ion beam induced chemistry - the so-called threshold model. Others took in consideration another available dissociation cross section of a known gas, CO for example and made a simple speculation about the real $W(CO)_6$ precursor [17]. Some authors stopped and did not finish the exercise, like Allen & Kunz [2].

We will use the same general procedure but we will improve the models of these authors by including a more accurate dissociation cross section for a specific precursor.

For the simulation of electron scattering in solid targets and secondary electron emission we will use Monte Carlo methods. The Monte Carlo simulations will give us the energy distribution of secondary electrons and a spatial distribution for a zero diameter primary beam. This result will be convolved with a primary beam gaussian distribution and will give the SE spatial and energy distribution on the surface f_{SE} (x,E). This distribution will be used in conjunction with the precursor electron impact properties. The result will be the molecular dissociation rate $R(x)$ due to secondary electrons emitted on the flat target surface.

The EBID fabrication resolution can be defined as the FWHM of the radial intensity distribution of the dissociated molecules $I_{diss}(r)$ or as the FW50% of its integral function $N_{diss\,tot}$ (r), i.e. the radius of the circle that contains 50% of the dissociated molecules.

According to our model, the spatial profile of the deposited cone is determined by the secondary electrons generated and propagating in two different materials. Initially by the SE emitted from the flat substrate (Fig. 4-2 a) and later by the SE emitted from the side flanks of the deposited tip (Fig. 4-2 b). If we define the EBID resolution as the smallest lateral

structure size that can be deposited, then the ultimate resolution will be determined only by the SE emitted on the flat target surface and it is obtained at point A in Fig. 4-1. This will be achieved only for very small primary beam diameter and very fast after the start of growth. A more realistic lateral resolution, which can be routinely achieved, will be obtained at point B in Fig. 4-1 and it is determined by the SE emitted from the more complicated shape of the grown tip.

In the following sections we will investigate the role the secondary electrons play at these two moments in EBID.

4.2 The secondary electrons on a flat target surface

4.2.1 A Monte Carlo simulation program for secondary electron emission

In the past many Monte Carlo programs have been written in order to simulate the secondary electron emission from targets irradiated with electron or ion beams. In most of the cases these programs have been applied in the image analysis in SEMs or studies of proximity effects in resist-based EBL.

Following the arguments and the programmers' guide presented in Chapter 3, we have developed a new 3D Monte Carlo simulation program for secondary electron emission under electron bombardment of flat surfaces. The simulation is customized for high-spatial resolution EBID performed in a STEM, i.e. thin films targets (1 - 100 nm) and high electron kinetic energies (10-200 keV) necessary to practically obtain a finely focused probe. The secondary electron emission output data is organized in a more complex way than in a classical MCSE simulation used for SEM imaging analysis. Thus, the secondary electrons ejected on the surface are classified not only by their exit radial position with respect to the beam incident point, but also by their energy. This additional information is necessary because the results have to be further coupled to a dissociation cross-section dependence on electron energy.

Our MC program, named SEEBID, is designed as an interactive Windows NT application, developed in the programming environment Delphi 5.0. The Windows based programming environment allows practically unlimited memory sizes, facilitating a high resolution for the position and energy results, as well as a good calculation accuracy, offered by a large number of simulated trajectories. The user can interactively introduce as input data the energy of primary electrons E_p [keV], the specimen thickness [Å] and the number of simulated PE trajectories PE_{max}. In Fig. 4-3 is shown the screen capture of the SEEBID main page.

The general scheme of the program follows the electron scattering in the target, according to the flow chart presented in Fig. 4-4.

When a programmer wants to treat the elastic and inelastic scattering of the electrons in the target, he has to make choices. We presented in Chapter 3 different existing theoretical approaches, some of them very simple and widely used, some of them more accurate, but only recently possible to implement, due to the amazing progress in the computing hardware.

We decided to treat the elastic scattering with the Rutherford formulae, because they are simple. In the high energy ranges of the PE this theory will hold very well. For the elastic scattering of the secondary electrons, the Mott cross-section would hold better, but we leave it as a future exercise.

For the simulation of electron inelastic scattering, the options are very diverse. We took as task to realize a comparative analysis of three different approaches in case of EBID. We will compare three models, with different degrees of complexity and computational demands: the
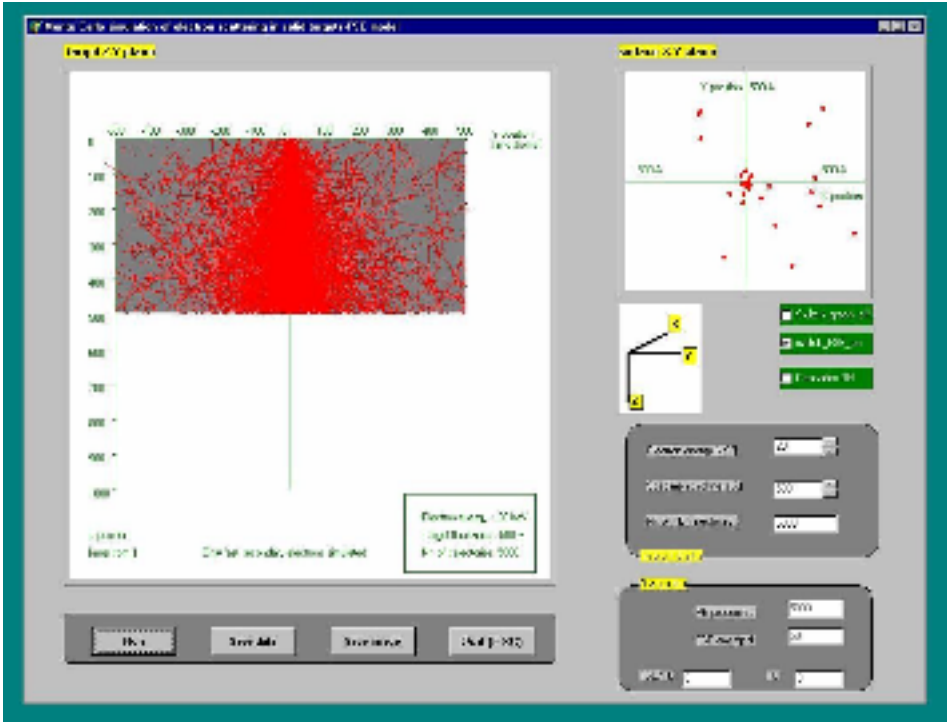
Figure 4-3: The main page of SEEBID program. The secondary electron trajectories in a 500 Å thick Cu target are shown in Y-Z plane and their exit sites on the top surface are marked in X-Y plane .
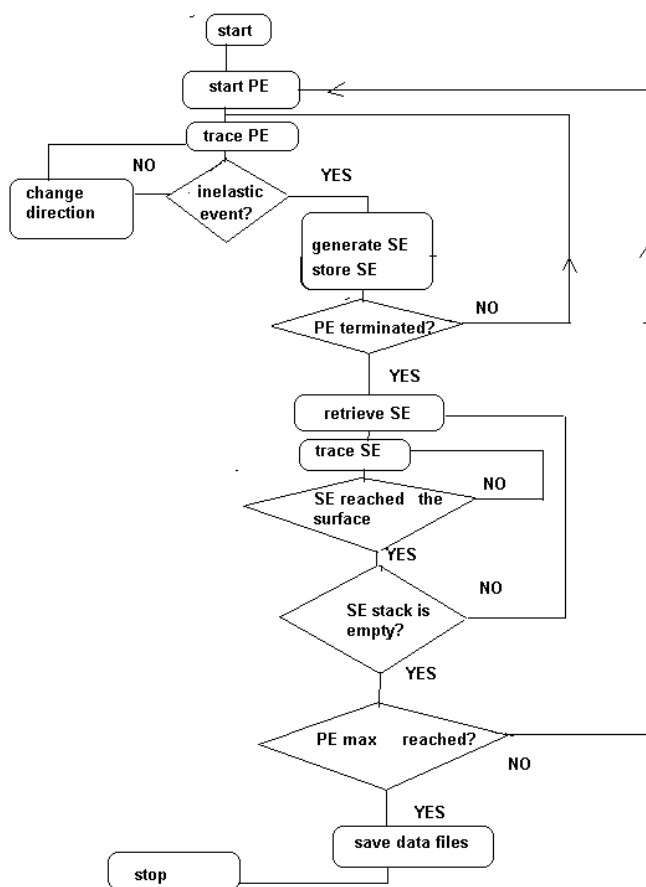
Figure 4-4: The general flow chart for the MC program for SE emission simulation
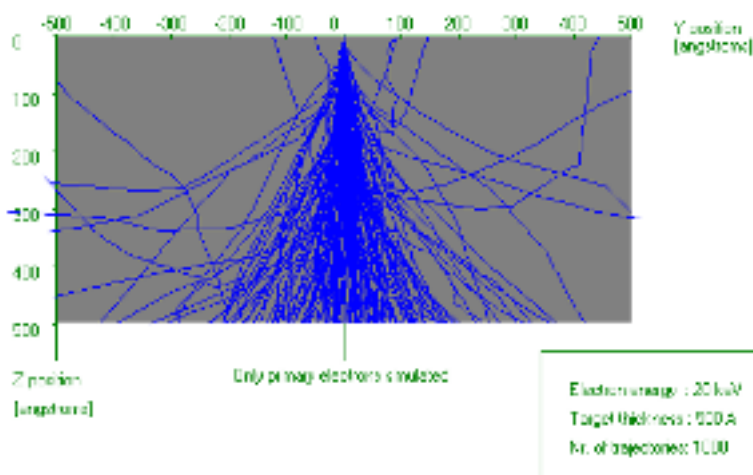
166

Figure 4-5: The graphical display of SEEBID for a 500 Å thick Cu target irradiated by a 20 keV beam. 1000 PE trajectories are shown.

straight line approximation SLA [5, 9, 18], the fast secondary electrons FSE model with no tertiary electrons [13, 19] and the fast secondary electrons model with the cascades included.

The simulations run in the 3D coordinate system of the microscope (XYZ). The Z axis is normal to the target surface, the Y axis is parallel with the tilt axis of the specimen holder. Two types of graphical displays are produced during the program running: the electron trajectories in the plane Y-Z and the emission sites distribution on the target surface in the plane X-Y.

The user can select the complexity of the information displayed on the screen. The selection offers the primary electron and /or the secondary electron trajectories display with or without the secondary electron cascades. An example of only the PE trajectories, displayed in Y-Z plane in a Cu target is shown in Fig. 4-5. In Fig. 4-3, the trajectories of SE are displayed in the Y-Z plane, and their exit sites on the target surface are marked by circles in the X-Y plane. Both displays Y-Z and X-Y can be saved at the end of the simulation as bitmap images on the disk.

On the main page the values of two counters are displayed during program running: the counter for the simulated trajectory number and the counter for the emitted secondary electrons.

The numerical output of the SEEBID program is the zero-diameter primary beam response and is organized in two matrices noted $N[r]$, one-dimensional, counting the number of SE emitted on the top surface from a ring $[r, r + dr]$, centered around the beam incidence point, and $NE[r, E]$, two-dimensional, counting the number of electrons of energy E emitted in each ring $[r, r + dr]$. All this data is written in ASCII files on the disk and can be off line processed by using an appropriate scientific engineering package (Mathcad or Maple) in order to obtain the secondary electrons spatial and energy distributions on the target surface.

Some results from our simulation program, showing the spatial and energy distribution of
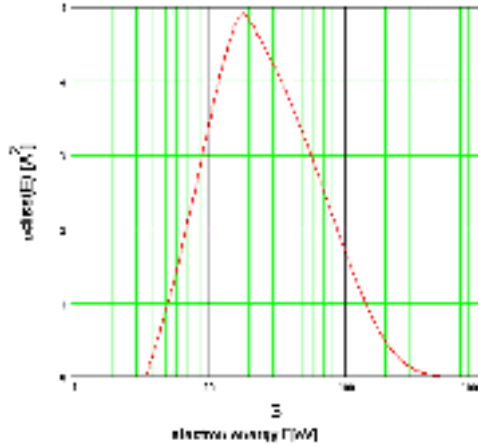
Figure 4-6: The dissociation cross-section for C_2H_5 adsorbed on the target surface $\sigma_{diss}(E)$ [Å^2]

the secondary electrons for thin Cu targets are presented in the following paragraphs.

4.2.2   The EBID spatial resolution determined by the SE on the flat surface

We consider as an example a 100 Å thin copper target, covered with C_2H_5 hydrocarbon precursor molecules and irradiated by an electron beam accelerated at 20 keV. We have chosen for a copper target because it has been widely used in existing Monte Carlo simulations and a lot of results are at this moment available for comparison. As precursor we have chosen for a hydrocarbon molecule, because for these type of molecules, the electron impact dissociation cross-section is better known than for any other organometallic complex. In this way we actually simulate the electron beam induced contamination growth, a particular case of EBID. We will calculate the rate of dissociation produced by the SE emitted from the target surface, i.e. the profile of the dot at the very beginning of the deposition, when the SE exit surface is flat.

We use our MC simulation program SEEBID to get information about the SE emitted on the flat target surface. The relevant result of this simulation is the spatial dependent energy distribution of SE on the flat target surface, $f_{SE}(r, E)$ for a zero-diameter electron beam, resulting directly from $NE[r, E]$. This distribution has to be combined with the electron impact dissociation cross-section dependence on the electron energy, σ_{diss} (E) given for a hydrocarbon precursor. The final result will be the SE induced dissociation rate $R_{SE}(x)$, calculated in atoms/Å^2/sec, at each point situated at a radial distance x from the beam incidence point, using formula (4.1). If we assume that each molecule is fixed to the surface immediately in the same place where it dissociates, and that the PE enter always the substrate at level z=0, then the FW50% of the obtained profile $R_{SE}(x)$ will give the EBID resolution in the very beginning (point A on the curve in Fig. 4-1).

The electron impact dissociation cross-section for the hydrocarbon molecule C_2H_5, $\sigma_{diss}(E)$ [Å^2] is plotted versus the electron energy in Fig.4-6. This curve has been obtained by adapting a similar curve valid for the precursor in gas phase.

168
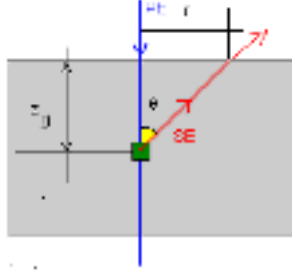
Figure 4-7: Illustration for the straight line approximation (SLA) model.

The data for this precursor in the gas phase, taken from [3] had a dissociation threshold at an electron energy of 10 eV. We adapted this data for the case of an adsorbed molecule, knowing from STM literature that the threshold for the dissociation of adsorbed hydrocarbon molecules is about 3.5 eV. The cross-section we obtain this way is shifted towards lower energies, so that the threshold becomes 3.5 eV.

In the following sections we will solve this exercise by applying different degrees of approximation in the MCSE simulation of electron scattering in the target. Three models will be used in the order of their complexity and compared afterwards, regarding the compromise between the accuracy of their results and the computational time they offer.

4.2.2.1   The slow electrons and the straight line approximation (SLA)

A simple model is a trade-off. It offers a fast way to get the right feeling, but it has to accept rough approximations. We start with a simple model that combines different approximations used currently in the SE studies from Chung, Koshikawa & Shimizu and Joy [5, 18, 12].

In the first place, we can neglect the energy loss of the primary electron during its passage through the target. The target is thin, so according to the discussion from chapter 3, this approximation holds for high enough energies.

We consider that the SE are generated at random depths z_0, ranging between $Z_{min} = 0$ and $Z_{max} = 100$ Å, according to the algorithm used by Koshikawa [18] for a similar situation (see Fig. 4-7).

We restrict ourselves to the SE generated by conduction electron excitations, where the excitation function (energy distribution) is given by the Streitwolf eq. (3.44) and (3.45). The initial polar angle θ of the SE, made with the normal to the target surface, is considered uniform randomly distributed in space, thus assuming an isotropic SE generation. This assumption holds especially for slow secondary electrons. The azimuthal angle φ is randomly distributed on a circle.

After generation, the SE are transported linearly unscattered to the surface. This approximation, that neglects the SE angular deflection and considers each scattered electron like absorbed, is known as the straight-line-approximation (SLA), a term used by Dwyer&Matthew in [9] and Joy in [12], or exponential attenuation. In this model, the probability that an electron

with energy E, generated at depth z will reach the surface unscattered, is:

$$p1(E, z) = e^{-\frac{z}{\lambda_{inel}(E) \cos(\theta)}} \qquad (4.2)$$

For the inelastic mean free path (IMFP) of the SE, $\lambda_{inel}(E)$, we used the empirical formula given by Seah and Dench [23].

Each time a SE reaches the target top surface, the radial electron counter is incremented with the product of the SE probability $p1(E, z)$ to reach the surface and the probability $p2(E)$ of SE to escape the surface barrier:

$$p2(E_{SE}) = 1 - \sqrt{\frac{E_F + W}{E_{SE}}} \qquad (4.3)$$

Each time a SE escapes into the vacuum, its energy is reduced with the surface barrier energy $(E_F + W)$ and the two dimensional array containing the SE energy information correlated with its exit position is incremented in the same way.

We implemented the SLA model in our MC program. As an example we show a copy of the screen during the program running. 1000 SE trajectories in a 800 Å thick copper target, bombarded by a 20 keV electron beam, are shown in Fig. 4-8. The direct results of MCSE noted $N(r)$, are further processed in the Mathcad package to determine the radial intensity distribution $I(r)$ and the integral function of the outgoing SE current $N_{tot}(r)$.

In Fig. 4-9 are shown the normalized plots of the SE outgoing current N(r), the SE intensity distribution I(r) and its integral function, i.e. the total number of SE emitted within a circle of radius r, $N_{tot}(r)$. For this example we simulated 50 000 000 primary electron trajectories.

The normalized SE energy spectra at different radial distances from the point of primary beam incidence are plotted in Fig. 4-10. We observe that the electrons that exit closer to the beam center have a broader energy peak, containing also higher energy values.

Combining these results with a gaussian primary beam distribution and with the dissociation cross-section for a hydrocarbon molecule, we can obtain the spatial profile of the structure initially deposited on the target surface. In Fig. 4-11 and Fig. 4-12 are plotted the density distribution of the dot initially deposited by SE, $I_{diss}(r)$ and its integral function, showing the number of molecules dissociated within a circle of radius r, $N_{diss\,tot}(r)$, for two situations: a beam with 20 Å diameter and a beam with 2 Å diameter.

We conclude that according to the SLA model, the following spatial results have been obtained for the secondary electron emission:

For a zero-diameter, 20 keV primary beam, normal incident on a 100 Å copper target, the FW50% of the outgoing SE current on the surface, defined as the diameter of the area from where 50% SE are emitted, is FW50% = 5 Å.

The spatial extent of the single dot initially deposited by the SE on the flat surface has the following values. For a 2 Å beam diameter, 50% of the molecules dissociated by SE are contained in a circle with diameter equal to 2.3 Å. For a 20 Å beam diameter, 50% of the molecules dissociated by SE are found within a circle of diameter 21 Å.

It is interesting to compare the profile of SE on the surface and the profile of the dot they deposit. This comparison should give an indication on the influence of the dissociation cross-section dependence on the electron energy. Our results show that for a broad beam, for example 20 Å diameter, there is almost no difference between the profile of SE on the surface and the
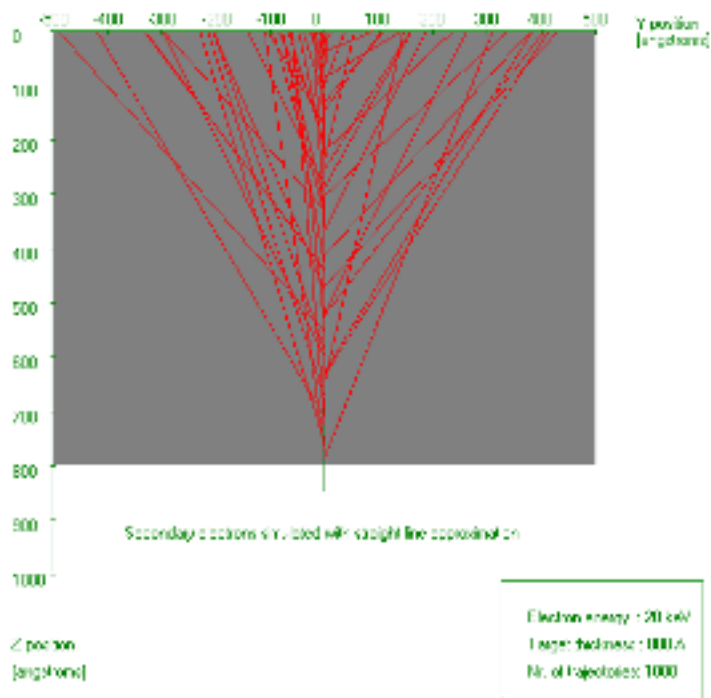
Figure 4-8: Graphical display from SEEBID program during the SE simulation using the SLA model. 1000 SE trajectories are shown in a 800 Å Cu target, bombarded by a zero diameter, 20 keV electron beam.
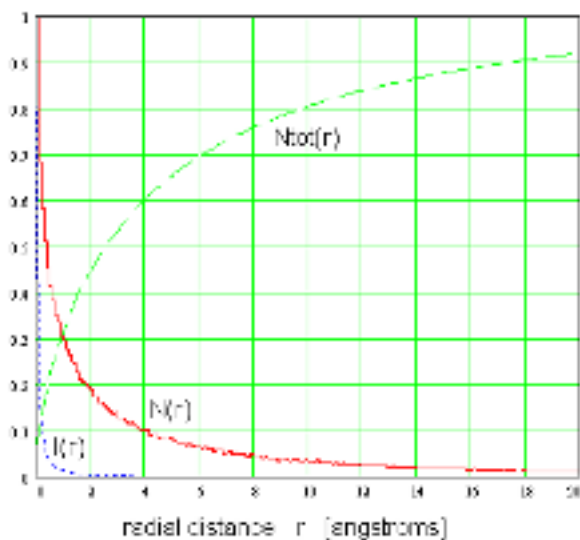
Figure 4-9: Cumulated plot of SE normalized spatial distribution on the surface, according to the SLA model (20 keV beam on a 100 Å Cu target). N(r) = total outgoing SE current, I(r) = SE intensity distribution on the surface, Ntot(r)=number of SE emitted within a circle of radius r.
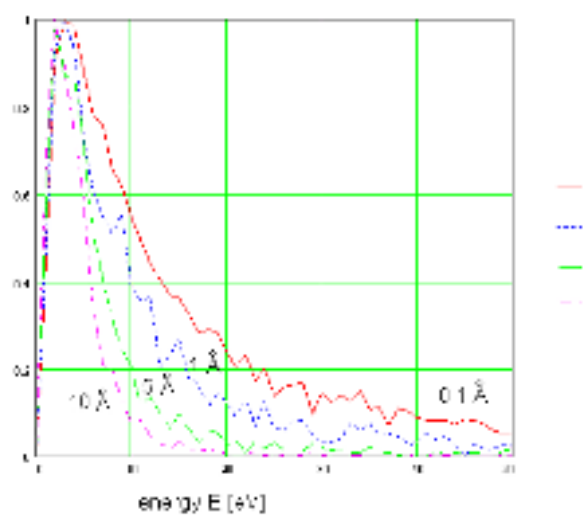
Figure 4-10: The normalized SE energy spectra at different radial distances from the center of beam incidence.
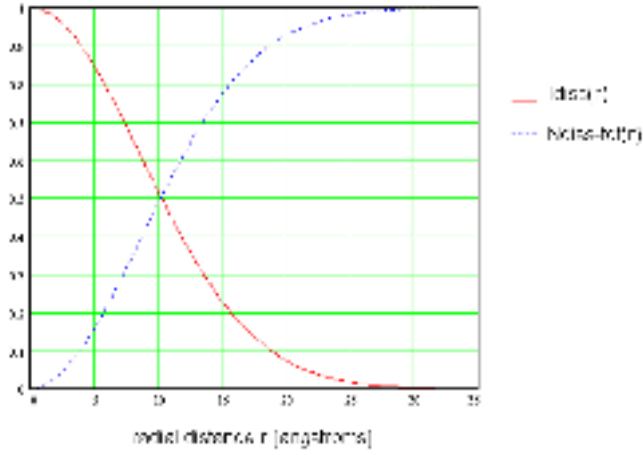
Figure 4-11: Spatial distribution of dissociated molecules by the SE emitted by a 20 Å diameter electron beam. I_{diss}(r)=normalized density distribution of the deposited atoms [atoms/Å^2]; $N_{diss\ tot}(r)$ =number of deposited atoms within a circle of radius r. The beam energy is 20 keV and the target is 100 Å Cu.
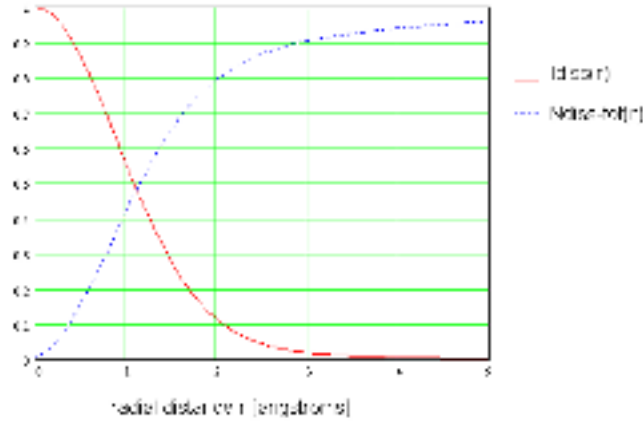
Figure 4-12: Spatial distribution of dissociated molecules by the SE emitted by a 2 Å diameter electron beam. I_{diss}(r)=normalized density distribution of the deposited atoms [atoms/Å^2]; $N_{diss\ tot}(r)$ =number of deposited atoms within a circle of radius r. The beam energy is 20 keV and the target is 100 Å Cu.

profile of the molecules they dissociated. In the case of a narrower beam, for example 2 Å, the FW50% of the dissociated profile is ca. 25 % smaller than the FW50% of the SE profile, 2.3 Å instead of 3.1 Å.

4.2.2.2 The fast secondary electron (FSE) model

Fast secondary electrons (FSE) are secondary electrons with energies up to E/2. A few authors have been preoccupied with the role FSE might play in resolution limitations in SEM imaging, microanalysis and EB lithography. Because they start, when generated, almost normal to the PE direction, they are thought to determine the limit of SEM imaging resolution [19]. Joy calculated the accumulated energy on the surface due to FSE, but did not classify them by energy and position[13], Gauvin simulated their role in X-ray generation [10]. According to Murata these FSE establish the lateral resolution limit in electron beam lithography [19]. We are concerned with the role FSE might play in EBID spatial resolution.

We implemented the FSE model in our SEEBID simulation program. The program displays the electron scattering picture during simulations. In Fig. 4-13 some FSE trajectories are shown. In this example, a 200 keV zero-diameter electron beam is normal incident along the Z axis on a 800 Å thick Cu target.
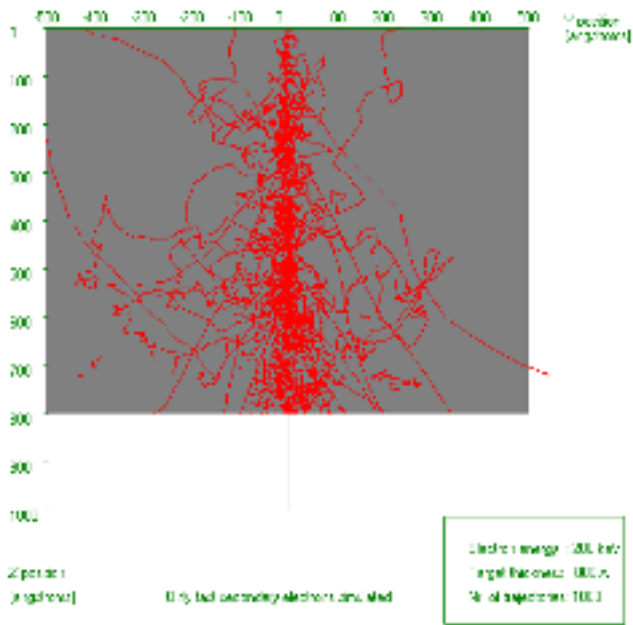
Figure 4-13: Graphical display from the SEEBID simulation program, showing the trajectories of FSE generated in a 800 Å Cu target by a zero diameter electron beam accelerated at 200 keV.

175
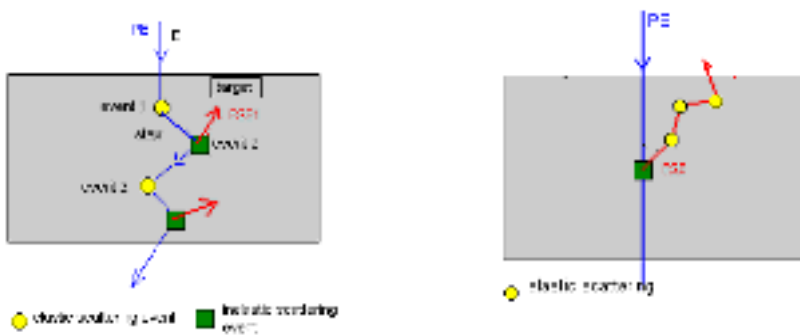
Figure 4-14: Illustration for the FSE model. a) the FSE generation b) the FSE propagation towards the surface.

We will describe the model we used in this simulation, adapted from the articles mentioned above. During the passage through the target, the PE is scattered elastically and inelastically. The step between two events depends on the elastic and inelastic mean free path of the electron. The elastic scattering of PE is treated with the Rutherford screened cross-section. The inelastic scattering is treated according to the FSE model exposed in Chapter 3. Each inelastic scattering generates a fast secondary electron (see Fig. 4-14 a). After each inelastic scattering event, the energy and scattering angles for both parent primary electron and the new FSE are calculated. During the simulation of each primary electron trajectory, all the information about the FSE it generates is stored in memory in order to be used later.

When the PE trajectory simulation is terminated, because it reached a boundary of the specimen or it lost its energy, the FSE are extracted from the memory and followed in the target until they leave the specimen or are thermalized. For the simulation of FSE scattering in the target, the conventional model Rutherford-Bethe is used. The elastic scattering of FSE is modeled using the screened Rutherford cross section and the inelastic scattering of the FSE is modeled using the CSDA approximation (Fig.4-14 b). The electron inelastic mean free path is given by Seah and Dench's empirical formula. The tracing of FSE stops if the electron exits the surface or its energy falls below $E_F + W$. In this approach no tertiary electrons are considered, in order to gain time.

Numerical results

We consider the same example, a 20 keV primary beam normal incident on 100 Å thin Cu target. Three situations will be analysed: The zero-diameter electron beam, the 20 Å diameter beam (a typical situation in SEM) and the 2 Å diameter beam (the smallest probe size in a modern STEM). The MC program will give the zero-diameter beam response. The other two cases will be obtained by convolving the MC results with primary beam gaussian current density distributions. The number of primary trajectories simulated was 50 000 000. The spatial distribution of the exit sites of FSE on the top surface of the target is shown in Fig. 4-15.

The cumulative results for the FSE spatial distributions on the target surface for a zero-diameter primary electron beam are shown in Fig.4-16.

For a zero diameter beam, 50% of FSE are emitted from a circle of diameter 28 Å.

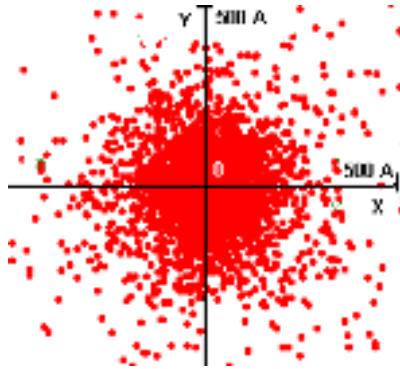For 20 Å diameter gaussian primary beam, the area from where 50% of FSE are emitted

Figure 4-15: The spatial distribution of the FSE exit sites on the top surface of the target, marked in X-Y plane. The primary beam is zero dimensional, accelerated at 20 keV and the target is 100 Å thick Cu.
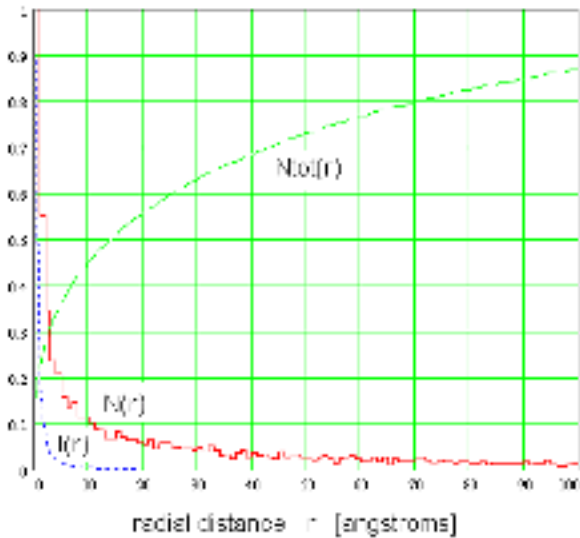

Figure 4-16: Cimulated plot of the spatial FSE distributions. The beam is zero diameter, accelerated at 20 keV, the target is 100 Å thick Cu. N(r) = total outgoing SE current, I(r) = SE intensity distribution on the surface, Ntot(r)=number of SE emitted within a circle of radius r.
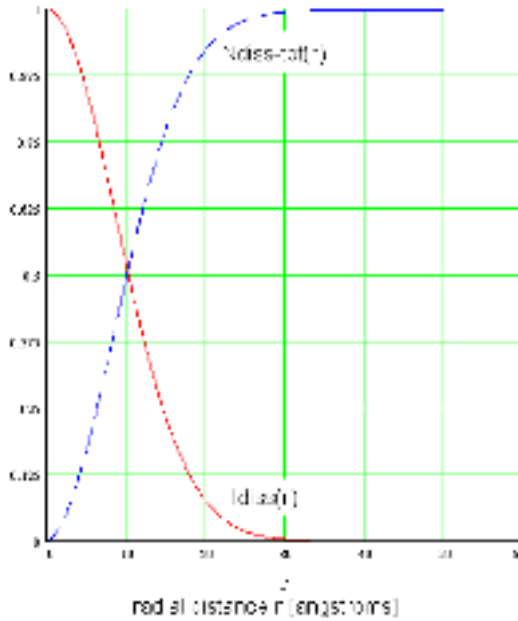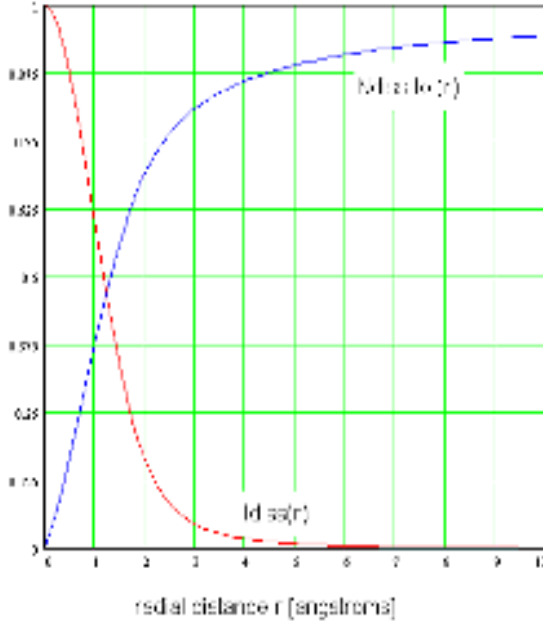
Figure 4-17: The normalized plots of radial intensity distribution I $_{diss}(r)$ [atoms/Å^2] and its integral function N$_{diss-tot}(r)$ [atoms] for a single dot deposited by FSE on the top surface of the target. The beam diameter is 20 Å, the beam energy 20 keV, the Cu target is 100 Å thick.

has a diameter of 24 Å.

For 2 Å diameter gaussian beam, the area containing 50% of FSE emitted on the top surface of the target has a diameter of (FW50%) 23 Å. Until here, these results agree quite well with other simulations of FSE [7, 12].

The profile of the dot deposited by the FSE emitted on the flat target surface is obtained by combining the spatial and energetical FSE data with the dissociation cross-section of C_2H_5 molecule. In Fig. 4-17 the normalized radial intensity distribution $I_{diss}(r)$ [atoms /A^2] and the number of deposited atoms contained in a circle of radius r , N$_{diss-tot}(r)$ [atoms] for a 20 Å diameter beam are shown. In Fig.4-18 the same curves are plotted for a 2 Å beam. Our results show that FSE have a larger influence on the spatial evolution of the dot grown by finely focused beams. For 2 Å beam diameter the FW50% of the dot is 2.8 Å. For 20 Å beam diameter the dot FW50% is practically unchanged, equal to the primary beam diameter.

4.2.2.3 Including the cascades of secondary electrons.

We concluded from the MC literature that taking into account the cascade multiplication of the generated FSE improves the spatial resolution on the target surface. The present FSE model can be improved if the cascades are also included and higher order electrons are generated. We used the classical binary collision scattering model for the treatment of the FSE cascades.

Figure 4-18: The normalized plots of radial intensity distribution I $_{diss}(r)$ [atoms/Å^2] and its integral function N$_{diss-tot}(r)$ [atoms] for a single dot deposited by FSE on the top surface of the target The beam diameter is 2 Å, the beam energy 20 keV, the Cu target is 100 Å thick.
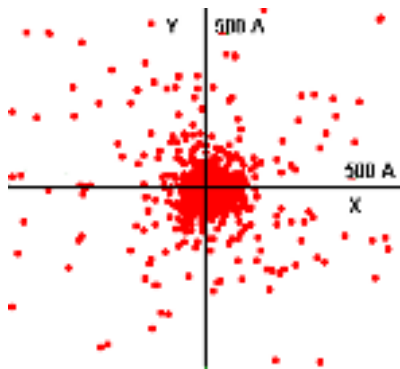
Figure 4-19: The spatial distribution of FSE exit sites on the top surface of the target when cascades are included

The higher order generation electrons are stored in memory and when the FSE trajectory is terminated they are extracted and followed during their scattering in the target. New electrons will be generated and the process continues until the memory store is empty. In this way we simulate the complete binary interaction tree presented in the beginning of Chapter 3. We implemented the cascade model in our Monte Carlo simulation SEEBID. The distribution of the emission sites on the surface in the X-Y plane is shown in Fig. 4-19. We see that the FSE are emitted more clustered around the beam center, a fact that agrees with the expectations. We calculated the profile of the dot deposited by the secondary electrons emitted on the surface in this case. THis profile was almost identical to the one obtained when no cascades were included. Our conclusion is that even if the spatial distribution of FSE on the surface becomes sharper, the influence of the cascades introduction on the dot spatial extend is neglijible.

4.2.3 Conclusions

The role of secondary electrons in EBID spatial resolution has been estimated by combining the results of our MCSE simulation with an accurate dissociation cross-section for a specific hydrocarbon precursor. The studied case was a 20 keV primary beam normally incident on a 100 Å Cu target, on which a hydrocarbon gas is adsorbed (C_2H_5). We considered two cases: a beam diameter of 20 Å, an exponent of a typical modern SEM performance, often reported by EBID users and a beam diameter of 2 Å, representing the state-of-art in a STEM, never used for EBID yet.

We used three theoretical models for the secondary electron simulation: the straight line approximation (SLA), valid more for slow secondary electrons, generated from conduction electron excitation, the fast secondary electron model (FSE), suitable more for faster electrons with energies up to half of the primary electron energy and the fast secondary electron model with cascades included. Our conclusion is that, at least for a thin target (< 100 Å) the three models give similar results. According to our calculations, the FW50% (the area containing 50% of the deposited atoms) for a single dot made only by secondary electrons emitted on the target surface is similar to the beam diameter if the beam diameter is 20 Å and it is enlarged to 2.8 Å when the beam diameter is 2 Å. Even if we don't have yet experimental results for the 2

Å to compare with our theoretical prediction, we can conclude that this result does not agree with the values reported from EBID practice with a 20 Å diameter beam. The best EBID experimental results with a 20 Å beam in SEM showed 150 Å diameter tips.

There is still a discrepance between these experimental values and our calculations. This can mean two things: that SE are not the only important influence in EBID or that the experimentally measured results we use for comparision are always taken at the point B and not at A on the curve from Fig. 4-1. So the discrepance might be not between different influences on EBID resolution, but between different moments A and B of the time action of the same influence parameter: the secondary electrons.

We investigate the latter option and we simulate further, according to our model, the tip growth towards the point B. If the results we obtain in B and the cross -sectional shapes of the tip will agree with the experimental results, then we will have proven that SE play the main role in the shapes and sizes in EBID.

4.3 The role of secondary electrons scattered in the tip structure

4.3.1 Introduction

At the very beginning of the deposition process after the nucleation started, the secondary electrons (SE) emitted from the flat target will govern the spatial extent of the structure. We estimated in the previous chapter the size of these SE exit area on the target surface and we obtained a FWHM of around 1 nm for a pin point incident beam. This value is still smaller then the experimentaly measured saturation value. We will try to prove that broadening happens because of the SE generated in the freshly grown tip structure and emited from its side flanks. For this purpose, a Monte Carlo profile simulator has been written, that evaluates the border of the tip structure each time a new PE is simulated, as determined by the secondary electrons.

4.3.2 Description of a 2D profile simulator for EBID

The methods to simulate the profile evolution during deposition or etching processes fall under two categories: geometric methods or cellular automata methods (CA). In the geometric method the substrate is treated as a continuous entity. To this group belong the string and set level methods [1, 4]. The cellular automata method represents the target by a large number of cells that reside in the substrate.

Using the CA method, we have built a simulator for the spatial evolution of a dot grown by EBID in the spot mode of an electron microscope. The simulator is written as a Windows application in the Delphi programming environment.

We consider a simplified case, in which a carbon contamination dot is grown by a zero diameter beam on a thin carbon foil covered by C_2H_5 hydrocarbon molecules, in order to avoid complicated interface effects. This situation is practically possible to experience, at high acceleration voltage (100-300kV) in a modern high-resolution STEM. In this way the simulation results can be easily checked when necessary against the experiments.

All the space of interest is represented with an array of discrete square cells with lateral size of 0.5 nm (Fig. 4-20). This value is an average between a precursor molecule size and a deposited atom diameter. The simulated space is 801 cells long in the Y direction and 151 cells

wide in the X direction. The origin of the coordinate system coincides with the impact point of the beam. The substrate together with the already deposited structure form one object (OBJ), permanently covered by a border of one monolayer of gas molecules. This is an ideal situation, when the diffusion time necessary for a gas molecule to reach the irradiated area from the sink is considered zero.

Each discrete cell in the mesh is described by its occupational state. The occupational flag can assert three states, codified as: 0 if it is empty, 1 if it is occupied by a molecule which might be dissociated and create a deposited atom (border), and 2 if it is occupied.
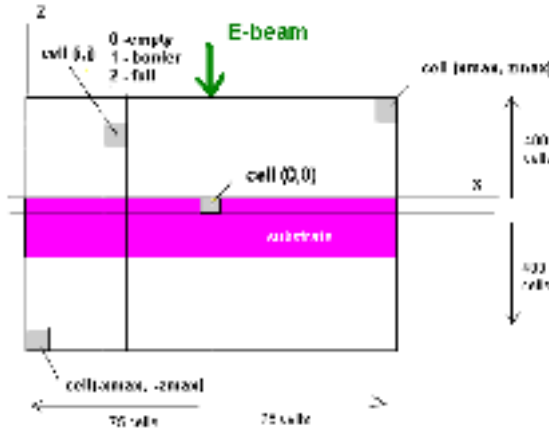
Figure 4-20: The simulated space divided in discrete cells.

We use the Monte Carlo method to simulate the SE generated in the solid object OBJ, on the trajectory of the primary electron. The flow chart of the program can be followed in Fig. 4-24.

The primary beam enters the object OBJ in the center of the deposit and scatters inside, generating secondary electrons during inelastic scattering. It moves linearly between two inelastic scattering events (see Fig. 4-21). The step between inelastic scattering events can be sampled using a uniform random number R, the same way as in the previous paragraph.

The interaction sampling, i.e. the type of event (elastic/inelastic) will be also determined using a random number as follows. If R is a uniform random number, the interaction will be elastic if $R < \frac{\lambda_r}{\lambda_{el}}$, and inelastic otherwise. We neglect the elastic scattering, due to high energy and thin substrate.

We assume that SE are generated isotropically in space. A 3D simulation is time consuming and for this reason, often 2D simulations are preferred.

In the 2D simulation we will observe only the SE emitted on a narrow band situated in the X-Y plane, shaded in Fig. 4-22. We will build a shape grown by these SE seen as a one cell thick wall, parallel with the X-Z plane. The result will be a cross section of the 3D dot grown in reality. The SE emerged on the narrow band are uniformly generated on a one cell thick ring. The polar scattering angle θ of the SE is :
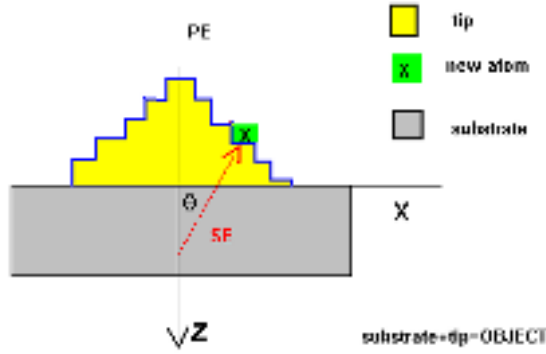
182

Figure 4-21: The geometry used in growth simulation. PE = primary electrons, SE= secondary electron.

$$\theta = \frac{1}{2}\pi - 2\pi R \qquad (4.4)$$

where R is a random number between 0 and 1.

The energy of the SE, E_{SE} is given by the excitation function of conduction electrons given by Streitwolf formula.

After its generation, at depth z, the SE propagates linearly in the given direction. With small steps it is checked if the cell it crosses on its way is full (2), in the border (1) or empty (0). The propagation continues as long as the encountered cells are full and until SE hits a border cell. (see Fig.4-21). When SE reaches the surface, its energy E_{SE} is corrected with the exponential probability $P_1(z)$ that it will reach the surface and the probability to escape in vacuum, $P_2(E_{SE})$ and finally reduced with the surface barrier. The reason for these corrections can be found in Chapter 3.

$$E_{SE} = (E_{SE} - W - E_F)P1(z)P2(E_{SE})$$
$$P1(z) = e^{-\frac{path}{\lambda_{inel}(E_{SE})}} ; P2(E_{SE}) = 1 - \sqrt{\frac{E_F + W}{E_{SE}}} \qquad (4.5)$$

The secondary electron energy will be combined with the dissociation cross-section of the C_2H_5 precursor, given in the previous paragraph.

The probability that the emerging SE will dissociate the molecule on the border is equal to the dissociation cross-section divided by the area seen by SE:

$$P_{diss}(E_{SE}) = \frac{\sigma_{diss}(E_{SE})[\text{Å}^2]}{5 \times 5[\text{Å}^2]} \qquad (4.6)$$

183
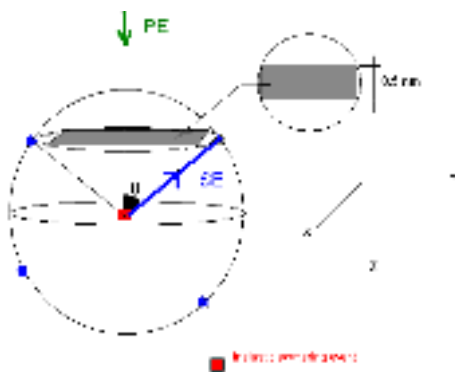
Figure 4-22: The 3D - 2D transformation

Using another random number, we decide according to this probability if the molecule situated in the exit cell will be dissociated or not. A dissociated molecule is translated in our program to a "shot" cell. When a cell (X,Z)) is shot, its state changes to "occupied", by switching its occupancy flag to 2 and its neighbours with the coordinates (X,Z+1), (X,Z-1), (X+1,Z), (X-1,Z) are included in the border (see Fig. 4-23).
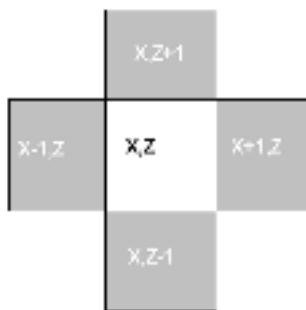

Figure 4-23: The neighbours of the shot cell.

A cell needs to have at least one side in common with a filled cell in order to be declared candidate to deposition and be included in the border.

When the simulation of one PE is terminated, the border of OBJ is adjusted and the entrance point of the beam is set in the top of the grown tip. If the foil is thin the tip grown on its bottom side l is also shown and is also part of OBJ.

The simulation process can continue according to the flow chart in Fig. 4-24, where only one time quantum equivalent with the effect of one primary electron is shown.

The cross sectional shapes are at regular exposure intervals saved in bitmap files in order to be later processed.
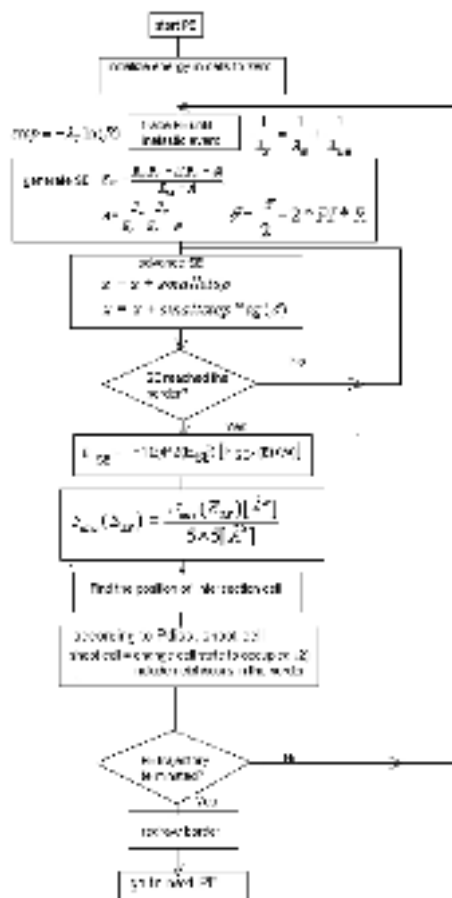
Figure 4-24: The flow chart of the 2D rofile simulator programming

In Fig. 4-25 is presented the time evolution of the shape of a tip grown by the secondary electrons generated by a primary 20 keV primary beam incident on a 10 nm thick carbon target. Each 200000 PE a profile is plotted. If we consider that the probe current was 5 pA, the time step between two profiles is estimated as 6 ms. The last profile shown is grown in 39 ms, giving a vertical growth rate of ca. 1.6 nm / ms. We observe that the shapes obtained by simulations agree with the experimentally observed. We notice that the base diameter of the tip tends to stabilize at 15-20 nm, a value also noticed in our experiments.
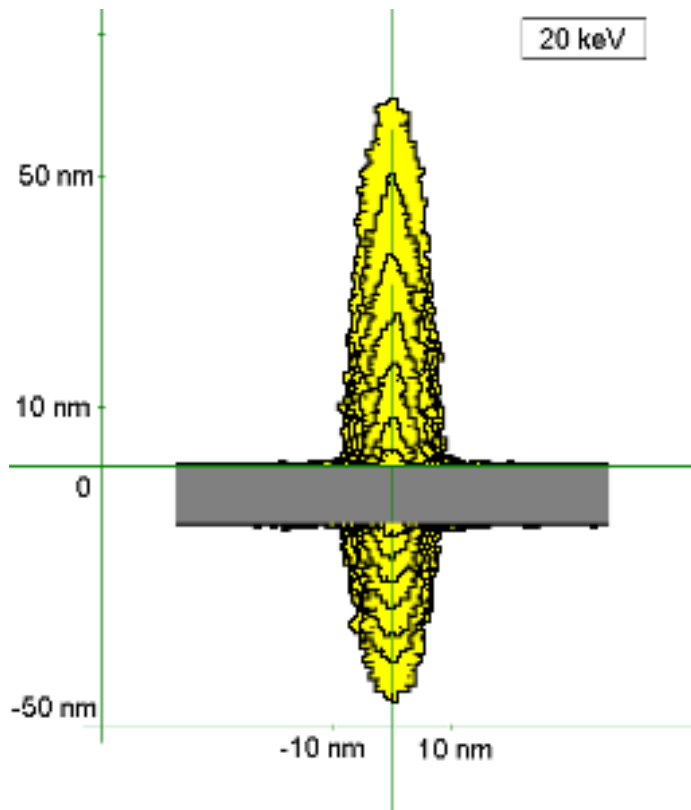
Figure 4-25: A sequence of profile of a single tip deposited by SE generated by a zero diameter 20 keV beam incident on a 10 nm carbon target.

In Fig. 4-26 a series of tips grown from the beginning until a height of 150 nm is simulated. We observe that the diameter at the base of the tips tends to saturate at a value of 15-20 nm, a situation confirmed also experimentally. We can also observe that according to our simulations, if the exposure time is very low, then structures with 2 nm lateral size should be possible to fabricate.
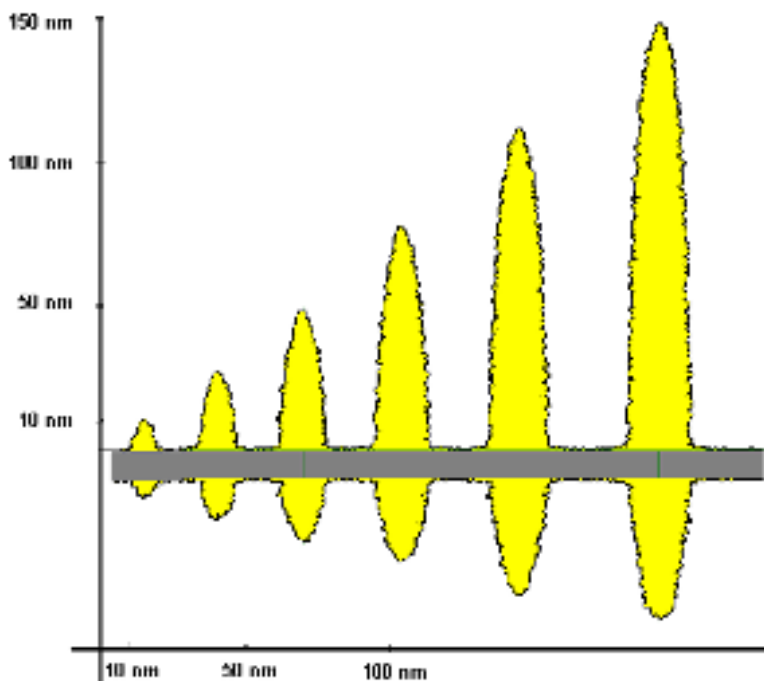
Figure 4-26: A sequence of tips deposited in the same conditions by a 20 keV zero diameter beam. It is obvious that the diameter at base tends to saturate. Each 400 000 PE a profile has been plotted.

187

4.4   Conclusion

A model was presented to explain the shape and the lateral size of tips, experimentally grown using EBID in spot mode of an electron microscope. The model confirms the major role played by the secondary electrons emitted under electron beam irradiation. The secondary electrons emitted from the substrate surface play a key role in the very beginning of the growth process and establish the 'theoretical' ultimate EBID resolution at around 2 nm. To build such small structures is quite a challenge because they are also very thin, making the visualization difficult and ambiguous in a SEM or a STEM system.

What happens after the very beginning has for the first time been succesfully modeled by taking into account the electron scattering in the grown structure. This leads to a broadening of the structures caused by secondary electrons generated in the deposit dissociating adsorbed molecules on the side flanks of the deposit. This broadening is in agreement with experimental observations. Visible tips with heights > 50 nm, have already diameters of 10 - 20 nm even for a zero-diameter primary beam.

Because of similarities between EBID and specimen contamination in electron microscopes, the proposed model can be also very useful for high-resolution electron microscopy.

Bibliography

[1] ADALSSTEINSSON, D., AND SETHIAN, J. A level set approach to a unified model for etching, deposition, and lithography. *Journal of computational physics A 120* (1995), 128.

[2] ALLEN, T., AND MAYER, T. Monte Carlo calculations of low energy electron emission from surfaces. *Journal of Vacuum Science and Technology B 6* (1988), 2057.

[3] ALMAN, D., RUZIC, D., AND BROOKS, J. A hydrocarbon reaction model for low temperature hydrogen plasma and an application to the Joint European Torus. *Physics of Plasmas 7* (2000), 1421.

[4] A.R.NEUREUTHER. Applications of line-edge profile simulation to thin film deposition processes. *IEEE Trans. on El. Devices ED-27* (1980), 1449.

[5] CHUNG, M., AND EVERHART, T. Simple calculations of energy distribution of low energy secondary electrons emitted from metals under electron bombardment. *Journal of Applied Physics 45* (1974), 707.

[6] DE JAGER, P. *Design of "the Fancier",an instrument for Fabrication and Analysis of Nanostructures Combining Ion and Electron Regulation*. PhD thesis, Delft University of Technology, 1997.

[7] DING, Z., AND SHIMIZU, R. Theoretical study of the ultimate resolutiom of SEM. *Journal of Microscopy 154* (1989), 1989.

[8] DUBNER, A., AND WAGNER, A. Mechanism of ion beam induced deposition of gold. *Journal of Vacuum Science and Technology B 7* (1989), 1951.

[9] DWYER, V., AND MATTHEW, J. A comparison of electron transport in AES/PES with neutron transport theory. *Surface science 152/153* (1985), 884.

[10] GAUVIN, R., AND LÉSPERANCE, G. A Monte Carlo to simulate the effect of fast secondary electrons on k_{AB} factors and spatial resolution in the tem. *Journal of Microscopy 168* (1992), 153.

[11] JOY, D. The spatial resolution limit of electron lithography. *Microelectronic Engineering 1* (1983), 103.

[12] JOY, D. *Monte Carlo Modeling for electron microscopy and microanalysis*. Oxford university press, New York, 1994.

[13] JOY, D., NEWBURRY, D., AND MYKLEBUST, R. The role of fast secondary electrons in degrading spatial resolution in the analytical electron microscope. *Journal of Microscopy 128* (1982), RP1.

[14] KOHLMANN-VON PLATEN, K., AND CHLEBEK, J. Resolution limits in electron-beam induced tungsten deposition. *Journal of Vacuum Science and Technology B 11* (1993), 2219.

[15] KOMURO, M., AND HIROSHIMA, H. Fabrication and properties of dot array using electron-beam-induced deposition. *Microelectronic Engineering 35* (1997), 273.

[16] KOMURO, M., AND HIROSHIMA, H. Lateral junction produced by electron-beam -assisted-deposition. *Journal of Vacuum Science and Technology B 15* (1997), 2809.

[17] KOOPS, H., KAYA, A., AND WEBER, M. Fabricaton and characterization of platinum nanocrystal material grown by EBID. *Journal of Vacuum Science and Technology B 13* (1995), 2400.

[18] KOSHIKAWA, T., AND SHIMIZU, R. A Monte Carlo calculation of low energy secondary electron emission from metals. *Journal of Physics D 7* (1974), 1303.

[19] MURATA, K. Monte Carlo simulation of fast secondary electron production in electron beam resists. *Journal of Applied Physics 52* (1981), 4396.

[20] REIMER, L. *Scanning electron microscopy.* Springer Verlag, Berlin Heidelberg New York, 1990.

[21] SCHEUER, V., AND KOOPS, H. Electron beam decomposition of carbonyls on silicon. *Microelectronic Engineering 5* (1986), 423.

[22] SCHIFFMANN, K. Investigation of fabrication parameters for the electron beam induced deposition of contamination tips used in atomic force microscopy. *Nanotechnology 4* (1993), 163.

[23] SEAH, M., AND DENCH, W. Quantitative electron spectroscopy. *Surface and interface analysis 1* (1979), 2.

Chapter 5

Delocalization effects in EBID

5.1 The delocalization of electron inelastic scattering - a general formulation of the problem

The electron inelastic scattering in matter is a delocalized process, in a degree inversely proportional to the electron energy loss. As a result, all processes initiated by this energy loss, especially when the energy loss is small, like the secondary electrons generation or the gas molecules degradation, are also delocalized. A loss of resolution in inelastic dark field images due to inelastic scattering delocalization has been observed experimentally in a high resolution STEM [23, 9]. A quantitative comparison with theoretical results is difficult, because the weakness of the signals involved, uncertainties in the specimen shape and in the electron probe positioning. However subnanometric resolution plasmon maps can be occasionaly achieved and recent measurement of the delocalization of the EELS signal by Muller and Silcox [30], obtained a localization as good as 0.5 nm.

Difficulties in the theoretical modeling of delocalization are imposed by the unknown elements in electron scattering in a solid or a gas. At this moment only very simple models have been used to quantify the delocalization effects, mainly in the studies of SEM or STEM imaging resolution. The results of different approaches differ sometimes drastically, leading to pessimistic as well as optimistic predictions. For example the delocalization of the secondary electron generation is expected to be as large as 0.05-70 nm [25, 26, 35] but "in practice the degree of localization will fall somewhere between these extremes"[25].

This predicted range approaches, in the order of magnitude, the smallest electron beam diameter obtainable nowadays in a STEM, around 0.2 nm. That is why it is feared that the delocalization of electron inelastic scattering imposes a fundamental resolution limit on any analysis technique performed in an electron microscope, as well as any electron beam induced fabrication process in general and EBID in particular. One of the few attempts to study the localization of energy transfer in electron beam lithography between electrons and PMMA resist has been done recently by Han and Cerrina [19]. They calculated that the range of interaction between a 1 keV electron and the PMMA molecules is of the order of 2.0 nm from the electron trajectory. In this chapter we make a first step to quantify the role the electron inelastic scattering delocalization plays in EBID resolution. This type of analysis has not been done yet, according to our knowledge.
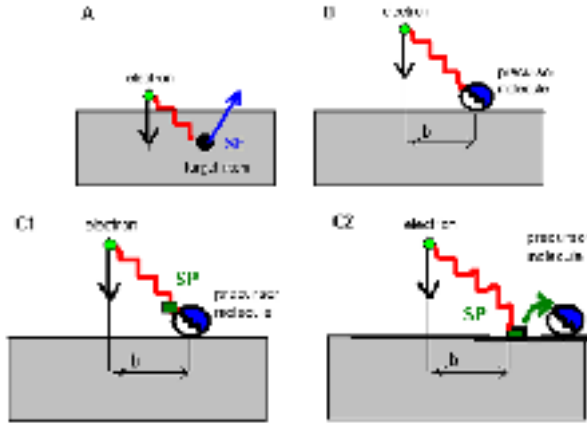
Figure 5-1: Illustration of different effects that delocalization of inelastic scattering can have in EBID A) the secondary electron generation is delocalized; B) electron induced precursor dissociation is delocalized; C) molecular dissociation can be induced by surface plasmons (SP) whose generation is a delocalized phenomenon: C1) a SP on the gas molecule and C2) a SP on the target surface interacting with a molecule.

First we identify the important EBID events that could be affected by the delocalization of electron inelastic scattering (see Fig.5-1):

A. Because the inelastic scattering in the solid substrate is delocalized, it can happen that a secondary electron is generated away from the incident electron path, so that its exit point on the surface is not exactly where it is expected from the Monte Carlo simulations described in Chapter 4 (Fig.5-1 A). The effect will be a broadening of the spatial profile of secondary electrons on the target surface.

B. Because the energy transfer between the electron and the precursor molecules is also delocalized, it can happen that a molecule adsorbed on the surface at a certain distance away from the electron trajectory will be excited and eventually dissociate (fig. 5-1 B). The effect will be a deposited dot profile larger than the one given by the secondary electrons only.

We will try to quantify the impact of the electron scattering delocalization on the spatial resolution of EBID, studying the cases A and B. Both cases A and B are single electron excitation proceses. Because an opinion exists that the precursor molecules can be dissociated as result of collective excitations, like surface plasmon (SP) decay, another useful result would be also the estimation of delocalization of surface plasmons generated by an electron in EBID. Two cases will be analysed : the generation of a surface plasmon directly on the precursor molecule (Fig. 5-1 C1) and the generation of a SP on the flat substrate surface, which can transfer its energy to an adsorbed precursor molecule (Fig. 5-1 C2). Both events can lead to molecular dissociation.

5.2 Approaches for quantitative estimation of electron inelastic scattering delocalization

Let's consider the case of an electron with energy E, that interacts with an atom or molecule, losing some energy, ΔE. The electron can excite also atoms situated away from its trajectory, at a certain distance b, called impact parameter. It is said in this case that the interaction is delocalized.
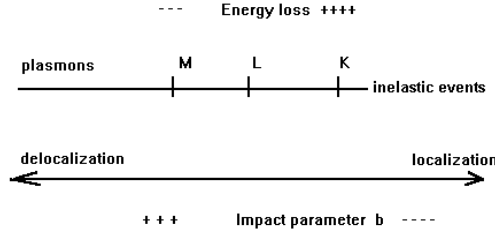

Figure 5-2: The delocalization degree is inversely proportional with the electron energy loss

The delocalization degree depends inversely proportional on the incident electron energy loss (see Fig. 5-2) and can be described by the impact parameter b.

During past years, several approaches have been formulated in order to evaluate the degree of delocalization. Their complexity grows from an almost straightforward one, the classical model, to a semiclassical one and it ends with a very complicated quantum mechanical approach. We will describe only the first two models, because we do not expect to use the quantum mechanical model. According to Ritchie, the electrons with energies between 10 keV and 100 keV behave as classical point charge particles, and quantum corrections are negligible [36].

5.2.1 The classical model 1

The classical model treats the electron as a point charge with the energy E, passing next to an atom A and losing some energy ΔE. The impact parameter b, known also as the Bohr cut-off radius, is defined as the radius of a sphere inside which the electron must pass for the interaction to really happen (see Fig.5-3) [17].

The magnitude of the impact parameter can be straightforwardly estimated from the wave nature of the electron and the Heisenberg uncertainty principle $\Delta x \Delta p \approx \hbar$ where Δx represents the impact parameter b and $\Delta p = \hbar \Delta q$, where Δq is the momentum change. If the momentum change is small, then the electron can for instance pass a distance away from an atom and still ionize it. The minimum momentum transfer for an energy loss ΔE is given for a zero scattering angle by $\Delta q_{\min} = \frac{\Delta E}{\hbar v}$. The maximum impact parameter is given then by:

$$b_{\max} = \frac{\hbar v}{\Delta E} \text{ [SI units]} \tag{5.1}$$

where $\hbar$ is the Planck constant, v is the velocity of the incident electron and ΔE is the energy lost by the incident electron.
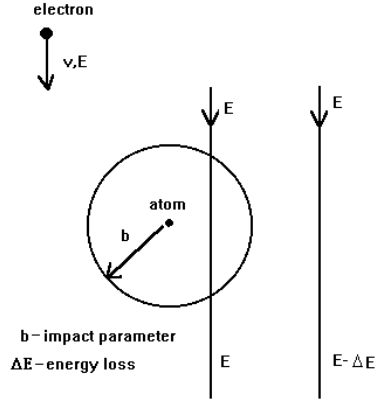
Figure 5-3: . The interaction between an electron and an atom can happen only within the impact parameter b.

The same result can be obtained from another formulation of the Heisenberg undetermination principle, $\Delta E \Delta t \simeq \hbar$ where the accuracy of energy measurement ΔE is connected with the time interval Δt required for this measurement [9, 17]. Taking the interaction and measurement time equal to b/v, where b is again the impact parameter, we obtain:

$$b_{\max} = v\Delta t = \frac{\hbar v}{\Delta E} \qquad (5.2)$$

The energy of the electron can be expressed as :

$$E = \frac{hc}{\lambda} = \frac{hv}{\lambda\beta} \qquad (5.3)$$

where $\beta = v/c$, λ is the wave length of the incident electron and c is the light velocity.

By substituting the electron velocity in (5.1) another expression can be obtained for the impact parameter:

$$b_{\max} = \frac{\hbar}{\Delta E}\frac{E\lambda}{h}\beta = \frac{\lambda E}{2\pi\Delta E}\beta \qquad (5.4)$$

By denoting with $\theta = \frac{\Delta E}{2E}$ the characteristic scattering semi-angle for an energy loss ΔE, the radius of interaction sphere is :

$$b_{\max} = \frac{\lambda}{4\pi\theta_E}\beta \qquad (5.5)$$

194
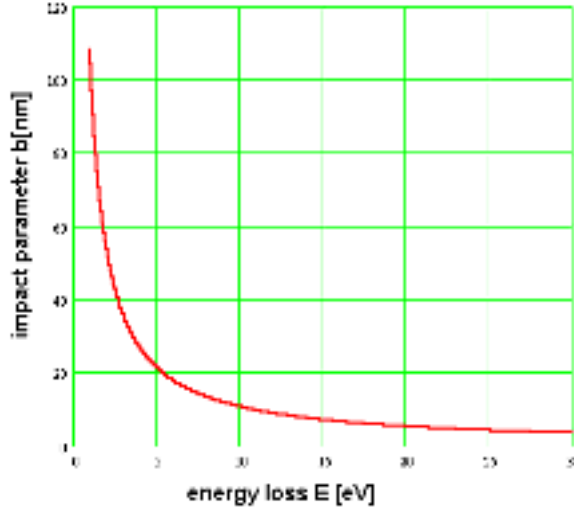
Figure 5-4: The classical dependence $b_{\mathrm{max}}(\Delta E)$ for a 100 keV electron

The diameter of localization given by the diameter of the interaction sphere will be then :

$$d = 2b_{\mathrm{max}} = \frac{\lambda}{2\pi\theta_E}\beta \qquad (5.6)$$

Some authors [24, 7, 25, 8] obtained a formula similar to (5.1) by using the Heisenberg principle with h in place of $\hbar$. In this case, the radius of the interaction sphere is:

$$b_{max} = \frac{hv}{\Delta E} = \lambda\beta\frac{E}{\Delta E} = \frac{\lambda}{2\theta_{\mathrm{E}}}\beta \qquad (5.7)$$

and the diameter of localization in this approach is given by:

$$d = 2b_{\mathrm{max}} = \frac{\lambda}{\theta_E}\beta \qquad (5.8)$$

As an example, we can use the equation 5.1 to estimate that a swift electron with 100 keV energy, having a velocity v = 0.55 c, can lose ΔE =5 eV energy within an impact parameter of 20 nm, and can lose ΔE= 25 eV within a localization radius of b = 4.31 nm. In Fig. 5-4 the classical dependence of the impact parameter is plotted as function of the electron energy according to formula (5.1).

Pennycook gives an expression for the ionization impact parameter as function of the electron energy loss, considered equal to the ionization energy E_i [33] :

195

$$b_{rms} = \frac{\hbar v}{E_i} \left(\ln \frac{4E}{E_i} \right)^{-1/2} \tag{5.9}$$

5.2.2 The classical model 2

In this approach the energy loss when passing through the matter is modelled by the Coulomb interaction between the incident swift electron and an electron in the target atom. From classical electrodynamics, the energy lost by a swift electron with a velocity v in interaction with the atom electron is: [24, p.619]

$$\Delta E(b) = \frac{e^4}{mv^2} \left(\frac{1}{b} \right)^2 \text{ (in cgs system)} \tag{5.10}$$

This expression is valid if we consider the electron in the target atom as free. For very distant collisions the result of this approach is in error, because of binding of electrons. The energy transfer to a harmonically bound charge is then:

$$\Delta E(b) = \frac{2e^4}{mv^2} \left(\frac{1}{b^2} \right) \left[\xi^2 K_1^2(\xi) + \frac{1}{\gamma^2} \xi^2 K_0^2(\xi) \right] \tag{5.11}$$

where $\xi = \frac{\omega_0 b}{\gamma v}$, ω_0 is the characteristic frequency of the binding and $\hbar\omega_0$ the ionization potential of the atom. $K_0(x)$ and $K_1(x)$ are the modified Bessel functions of second kind.

5.2.3 The semiclassical approach

If the classical model was correct, then a dissociation process, which needs an energy loss of 5 eV, could give EBID features, limited in resolution by the delocalization process to 20 nm. This is not really the situation we observed experimentally in a high resolution STEM. This is a reason to continue the study with a model better than the classical one.

Semiclassical models treat the incident electron as a classical point charge with a well defined straight linear trajectory and constant velocity. The interaction with the target is treated quantum mechanically. The classical relation between the impact parameter and the energy loss $\Delta E(b)$ is not correct anymore, because in quantum mechanics only a certain probability of interaction makes sense. A new quantity is thus introduced, P(b,E) given by the probability for a swift electron to lose a discrete energy E in an interaction with a target atom situated at a distance b. For a large number of collisions the average energy loss at b will be P(b,E)E quantum mechanically and $\Delta E(b)$ classically. The two values have to be equal for regions where the electron can be treated as a classical particle. Because this model is valid for distances larger than the atomic radius, where a linear trajectory can be assumed, and because the electron as a point charge causes the function P(b,E) to diverge in the origin, a cut-off radius of a_0 has to be introduced.

The origin of coordinates is considered in the center of mass of the target atom, its nucleus. The nearest approach at the impact parameter b is at the moment t=0 (see Fig.5-5). For simplicity a hydrogen-like atom is considered, with only one electron. The impact vector $\bar{b}$ and
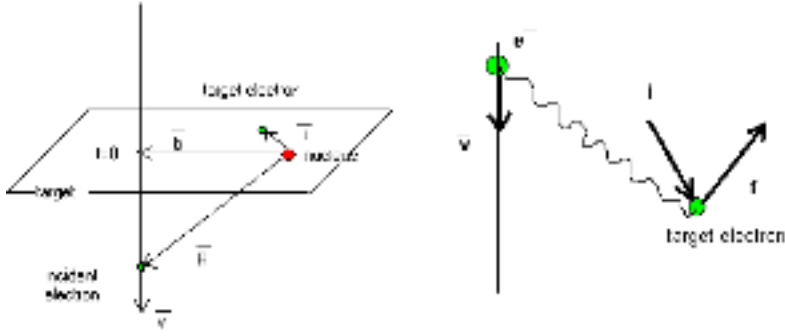
Figure 5-5: The Feynman diagram of electron-medium interaction

velocity vector $\overline{v}$ are mutually perpendicular vectors. The trajectory of the incident electron can be expressed as:

$$\overline{R(t)} = \overline{b} + \overline{v} \cdot t \tag{5.12}$$

where $\overline{R}$ is the coordinate vector of the incident electron.

The hamiltonian characterizing the interaction between the fast electron and the target atom is given by [36]:

$$V(t) = \frac{e^2}{\left|\overline{b} + \overline{v}t - \overline{r}\right|} \tag{5.13}$$

where $\overline{r}$ is the coordinate vector of the electron in the excited atom.

The atom is considered in its ground state until the moment t = 0, when the swift electron field is suddenly "switched on". During the interaction, the incident electron loses an energy E, by transferring it to the target atom, situated at a distance b. The result of this energy transfer is that the atom makes a transition from its initial ground state (i) to a final higher energy state (f) (see Fig. 5-5) . Each state of the target atom is described by a wave function φ_i and φ_f respectively. The calculation of these wave functions is a very difficult and time consuming, even sometimes impossible operation. For this reason, usually only hydrogen atom like wave functions are used.

Time dependent perturbation theory gives the probability that the atom experiences a transition $i \rightarrow f$ under the influence of the Coulomb field of a classical point electron, travelling with a constant velocity v along a path specified by the impact parameter b [36]:

$$P_{i \rightarrow f} = \frac{1}{i\hbar^2} \left| \int_{-\infty}^{\infty} \langle \varphi_i | V(t) | \varphi_f \rangle \exp^{\frac{i(E_f - E_i)t}{\hbar}} dt \right|^2$$

197

where the energy transfer necessary for the transition is $E = \hbar\omega = E_f - E_i$.

The dimensions of the target atoms and molecules are small. Because the origin of $\overline{r}$ is in the center of the atom, the exponentials $e^{i\omega t} = e^{i\overline{k}\overline{r}}$ can be expanded as a power series, since this series will converge very rapidly. $e^{i\overline{k}\overline{r}} = 1 + \overline{k}\overline{r} - i\left(\overline{k}\overline{r}\right)^2 + \ldots$

The classical analog of this expansion of the exponential is a multipole expansion of the charges that interact with the radiation field. The transitions that are due to the first term of the expansion are called electric dipole transitions, and the transition due to the second term are known as magnetic dipole and electric quadrupole transitions. [18]

Very widely used is the so-called dipolar approximation, that takes into account only the electric dipole transitions. The dipole moment operator is defined as $e\overline{r}$. The matrix element of the electric dipole moment operator between the target states i and f is responsible for the electric dipole transitions between the two states i and f and known as the transition moment between the two states [28].

Time-dependent perturbation theory in dipolar approximation gives the probability that the atom electron will be excited from the ground state i to the state f :[6]

$$P_{(i \to f)} = \frac{1}{\pi^2 b_{max}^2} \left(\frac{\lambda_0}{a_0}\right)^2 \left[(\overline{r}_{fi} \cdot \overline{e_v})^2 K_0^2(b/b_{max}) + (\overline{r}_{fi} \cdot \overline{e_b})^2 K_1^2(b/b_{max})\right] \quad (5.14)$$

where

$\lambda_0 = h/mv$ is the nonrelativistic de Broglie wave length of the incoming electron

$a_0 = $ the Bohr radius

$\overline{e_v}, \overline{e_b} = $ the unit vectors of $\overline{v}$ and $\overline{b}$ directions

$\overline{r_{fi}} = \langle \varphi_f | \overline{r} | \varphi_i \rangle = $ the dipole matrix element of target electron coordinate operator $\overline{r}$

$K_0(x)$ and $K_1(x) = $ the modified Bessel functions of the second kind

$b_{max} = v\hbar/E_{fi} = $ the Bohr cut-off parameter

The unknown quantities in this expression are the dipole matrix elements $\overline{r_{fi}}$, that are difficult to calculate. Using the approximation suggested by Fano [15] and Hameka [18, p.115] we can consider that the atoms in the target are randomly oriented in the coordinate system related to the electron microscope with respect to the radiation wave In this approximation, the components of the dipole matrix elements are equal to one another and can be expressed in terms of the oscillator strength f_{fi}, according to the relation:

$$(r_{fi})_v^2 = (r_{fi})_b^2 = \frac{\hbar^2}{2mE_{fi}} f_{fi} \quad (5.15)$$

Replacing these dipole matrix elements in (5.14) we obtain the transition probability:

$$P(b, E_{fi})_{(i \to f)} = \frac{1}{\pi^2 b_{max}^2} \left(\frac{\lambda_0}{a_0}\right)^2 \frac{\hbar^2}{2mE_{fi}} f_{fi} \left[K_0^2(b/b_{max}) + K_1^2(b/b_{max})\right] \quad (5.16)$$

where f_{fi} is the oscillator strength for the transition between initial and final states $i \to f$, a property of the target material that quantifies its response to an electromagnetic perturbation.

In order to plot the transition probability P(b,E) we can simplify its expression by taking f_{fi} = 1, an assumption valid for a bound electron that oscillates harmonically in three dimensions

[5]. In STEM calculations the oscillator strength is often modelled simply as unity up to a cut-off angle, and zero for larger collection angles [33].

In Fig. 5-6 we present two curves for P(b,E) for different energy losses E = 25 eV and E =100 eV for a 100keV electron, assuming that the oscillator strength is equal to unity.

In reality, the oscillator strength is a function of both the energy loss E and the momentum transfer q, $f(E,q)$, and it is known as the generalized oscillator strength (GOS). The theoretical calculation of the GOS for many electron atoms is obstructed by the lack of sufficiently accurate wave functions. For q = 0, the GOS is reduced to the optical dielectric oscillator strength valid for photon induced excitations. In the case of electron beam induced excitations, f $\simeq 1$ for the allowed dipole transitions (q=0) and f $\ll 1$ for forbidden transitions (q $\neq$ 0) [5].

All target materials have the same form for the probability of excitation P(b,E) curve, the difference being established only by the oscillator strength f_{fi}.

If we analyze the curves in Fig. 5-6, two variation regimes can be distinguished, separated by the Bohr cut-off parameter $b_{max} = v\hbar/E_{fi}$. In the first region, (b<b_{max}) and $P(b,E)1/b^2$ and in the second region (b>b_{max}) and $P(b,E)e^{(-2b/bmax)}$ [30].

The undetermination that occurs in the origin of the P(b,E) plot can be eliminated if b is replaced with $\sqrt{b_{\min}^2 + b^2}$, where $b_{\min} = \frac{1}{q\theta_c(E)}$, $q = \sqrt{2mE_P}/\hbar$ and $\theta_c = \sqrt{E/E_P}$ where E_P is the kinetic energy of the incident electron . This idea has been suggested by Muller and it is found also in Jackson's classical electrodynamics [24].

A plot of P(b,E) after this correction, showing the two distiguishable regions, is presented in Fig. 5-7 We can see that the impact parameter looks already a lot smaller than in the classical approach for the same energy loss.

5.3 The delocalization of secondary electron generation

5.3.1 Introduction

Our results from Chapter 4 have shown that the secondary electrons are the main tool used by the primary electron beam to dissociate precursor molecules.

Secondary electrons (SE) are generated as a result of primary electrons (PE) inelastic scattering in the irradiated material. Normally the simulations of secondary emission, as well as our estimation of secondary electrons spatial extent in EBID obtained in Chapter 4 assumed that their generation occurred exclusively where the inelastic scattering took place. However, because the energy transfer in an inelastic scattering is not perfectly localized, a non-zero probability exists for a SE to be generated away from the PE scattering center. The ultimate spatial resolution of a SE image formed by scanning a subnanometer probe across a surface is limited by the delocalization of the generation process. The FWHM of the SE localization profile for a 100 keV zero diameter electron beam is estimated from the measurements to be 2 nm. [10]. Even if the necessity for quantitative evaluation of this delocalization effect in high-resolution SEM imaging has been signaled by some authors, [25, 35], no convincing response has been issued yet and the different results do not agree with each other.

One of the frequent mistakes leading to pessimistic estimations in evaluating the SE delocalization is the use of the classical expression (5.1) with the energy of SE after it escaped in vacuum, with respect to E_F + W (around 4 eV), which is lower than the energy lost by the primary electron at the moment of internal SE generation (around 25 eV) [25].

Our goal is to quantify the role of delocalization of SE generation phenomenon in EBID. This problem is reduced to the estimation of the probability for a SE to be generated by exciting
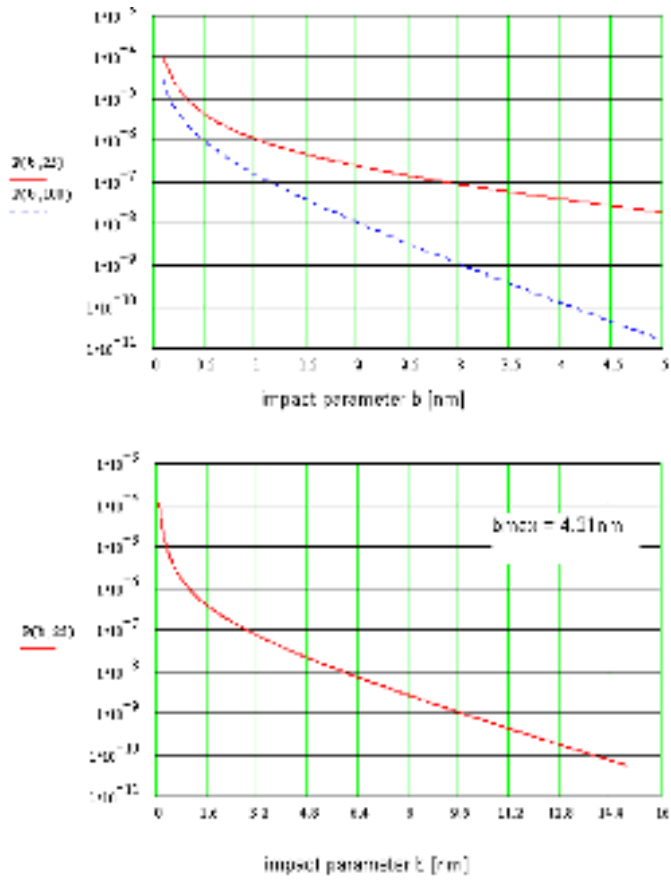
Figure 5-6: The probability to lose an energy E at the impact parameter b for a 100keV electron, P(b,E) (semiclassical approach, the oscillator strength is assumed equal to unity).
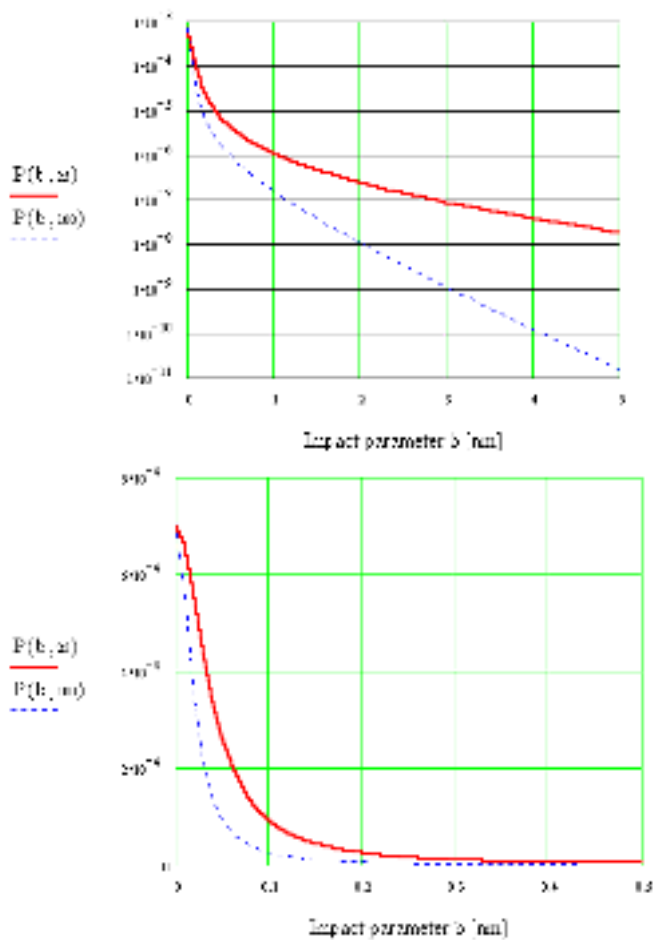
Figure 5-7: The probability P(b,E) for a 100 keV electron to lose an energy E=25eV and E=100eV by exciting an atom situated at a distance b.

a target atom situated at the distance b from the PE inelastic scattering center, denoted P_{SE} (b) (see Fig.5-8).
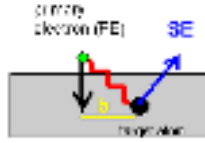

Figure 5-8: The illustration of a delocalized SE generation at an impact parameter b.

As a case study, we consider the EBID performed in a STEM, with a finely focused electron beam accelerated at 100 keV and passing through a thin carbon film. In order to solve the problem of delocalization, we have to choose one of the theoretical approaches 1- 4 described in the section 5.2. The classical approach seems too simple and gives results that do not agree with the experimental observations. We rely then on the statements by Ritchie saying that the fast electrons at 10-100 keV behave like classical particles and quantum corrections are expected to be negligible small [36]. The semiclassical approximation has been used with success by Muller and Silcox to calculate the localization of the EELS signal and the results agreed with the experimentally obtained signal in the case of large collection angles [30]. These reasons make us believe that the semiclassical approach is a right choice to solve the problem of SE delocalization role in EBID.

5.3.2 The spatial extent of the SE generation delocalization treated with the semiclassical approach

We start from the theoretical model described in section 5.2. According to the semiclassical approach, the probability that an atom will transit from an initial state 0 to final state n as result of the incident electron PE passage at distance b, is:

$$P_{(0 \to n)} = \frac{1}{\pi^2 b_{max}^2} \left(\frac{\lambda_0}{a_0} \right)^2 \frac{\hbar^2}{2mE_{n0}} f_{no} \left[K_0^2(b/b_{max}) + K_1^2(b/b_{max}) \right] \tag{5.17}$$

where $\lambda_0 = h/mv$ is the nonrelativistic de Broglie wave length of the incoming electron
a_0 = the Bohr radius
f_{no} = the oscillator strength for the transition $0 \to n$
$K_0(x)$ and $K_1(x)$ = the modified Bessel functions of the second kind
$b_{max} = v\hbar/E_{fi}$ = the Bohr cut-off parameter
E_{no} = the energy lost by the swift electron
We can transform further the expression (5.17) by replacing b_{max} :

$$P_{(0 \to n)} = \frac{E_{n0}}{\pi^2 v^2} \left(\frac{\lambda_0}{a_0} \right)^2 \frac{1}{2m} f_{no} \left[K_0^2(bE_{no}/\hbar v) + K_1^2(bE_{no}/\hbar v) \right]$$
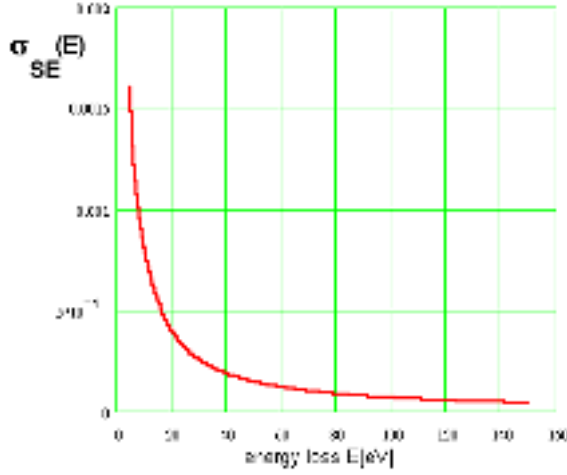
Figure 5-9: The energy loss distribution $\sigma_{SE}(E)$ for a SE generated by a 100 keV primary electron (f_{SE} =1).

If we assume that the excitation of the target atom from state 0 to state n will generate a SE with an energy $E = E_{no}$, then the probability that a SE is generated causing an electron energy loss E at distance b is:

$$P_{\text{SE}}(b, E) = \frac{E}{\pi_{v^2}^2} \left(\frac{\lambda_0}{a_0}\right)^2 \frac{1}{2m} \left[K_0^2(bE/\hbar v) + K_1^2(bE/\hbar v)\right] f_{SE}(E) \qquad (5.18)$$

We observe from the relation (5.18) that the probability P_{SE}(b,E) is a product of a kinematic component, dependent on the incident electron motion, that can be easily evaluated and a component dependent on the material, f_{SE}(E). This is a practically unknown quantity, a kind of oscillator strength for the SE generation or the target probability of absorbing some energy in order to produce a SE.

The integrated probability that a SE will be generated and cause an energy loss E for the incident PE can be obtained by integrating eq(5.18) over all possible b values, considering that only one atom is excited at each interaction [22]:

$$\sigma_{SE}(E) = 2\pi N \int\limits_0^\infty P(b, E) b\, db \qquad (5.19)$$

where N is the atomic density [atoms/unit area].

In the beginning we can assume that f_{SE}(E)=1, as in many microscopy calculations [30, 33] and we obtain an approximate probability that a SE will be generated with an electron energy loss E. $\sigma_{SE}(E)$ is plotted vs. the electron energy loss E in Fig. 5-9.
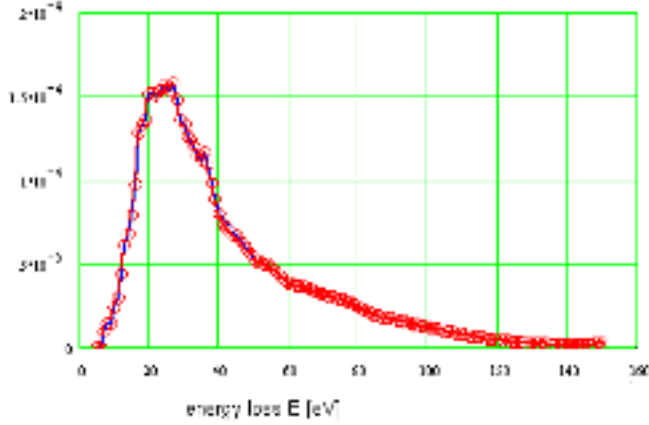
Figure 5-10: The coincidence rates between the electron energy loss and the SE generation events in a 10 nm carbon film irradiated by a 100 kV electron beam (from [34], [11])

An experienced eye can say that the shape of the curve in Fig. 5-9 is not specific for the electron energy loss in inelastic scattering events. It would be useful to check this dependence against a correct energy distribution at least for one particular scattering case.

The physics of secondary emission under electron irradiation has been studied for a long time. Still a very intriguing question is how the energy lost by the incident electron is distributed after the inelastic scattering in the material. It is known that after an inelastic scattering SE are internally generated and that they eventually escape in the vacuum. One knows much less about the mechanisms of SE generation, because more possible excitation channels and steps are possible, like the inter-band transitions, the valence electrons excitation, the ionization of core electrons, plasmon decay. Nowadays a current technique allows to measure the total energy lost by the primary electron passing through a target - the EELS. But what we need now is the distribution of energy losses which produced a SE , i.e. the energy invested by PE only in SE generation. Solutions can be found by simulations using Monte Carlo methods, where by simulating a huge number of collisions, it is hoped to approach the real situation provided that the correct cross sections for each excitation channel are known.

The most reliable answer can be obtained by experimentally measuring the correlation between the secondary emission and the incident electron energy loss events. A few attempts have been made in this direction, contributing to the clarification of the internal mechanisms of secondary electrons generation. [34, 29, 39, 11, 10]. In Fig. 5-10 an experimental EELS - SE coincidence measured spectrum is shown obtained by combining the data reported by Drucker & Scheinfein [11] and Pijper & Kruit [34].

It is obvious that the energy loss distribution curves from Fig. 5-9 and Fig. 5-10 do not look alike and the reason is the assumption we made in the calculation of $\sigma_{SE}(E)$, that $f_{SE} = 1$. At this moment we are able to correct this simplification, and determine the function f_{SE} (E) as a correction factor necessary to fit the calculated to the measured curves. The correction factor $f_{SE}(E)$ determined in this way is plotted in Fig. 5-11.

Going back to eq. (5.18) we can now correct the expression of $P_{SE}(b,E)$ for each energy
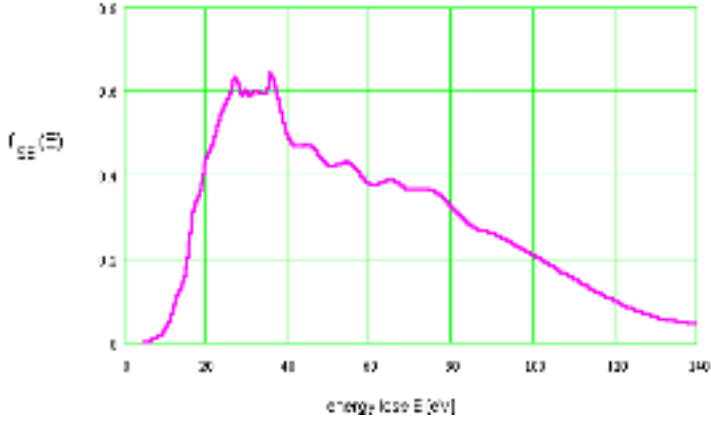
Figure 5-11: The dependence f$_{SE}$ (E) determined as a correction parameter between curves Fig. 5-9 (calculated) and Fig. 5-10.(measured).

loss E. Below in Fig. 5-12 we plot the probability P$_{SE}$ (b,E) to generate a SE with an energy loss of 25 eV at a distance b, corrected to EELS-SE coincidence experimental data.

The final answer to our problem is the SE delocalization profile, obtained by integrating the generation probability P$_{SE}$ (b,E) over all possible energy losses :

$$P_{SE}(b) = \int\limits_{0}^{\infty} P_{SE}(b, E) dE$$

The normalized probability $P_{SE}(b)$ that a SE is generated within an impact radius b from the PE inelastic scattering center is plotted in Fig. 5-13.

Even if a non zero probability exists that a SE is generated at a distance of 1 nm, we see from Fig. 5-13 that the probability decreases very sharply in the region 0-0.05 nm. From the plot of the integral function N50%(x), we estimate the FW50% of the SE delocalization profile to be 0.04 nm and the FW90% to be 0.32 nm.

5.4 The delocalization of surface plasmon generation

In the previous section we analyzed the delocalization of single electron excitation events. In this section we will analyze the delocalization of collective excitations generated in a medium by the passage of a fast electron. A particle approaching a polarizable body can induce collective excitations, including surface plasmons, surface optical phonons, surface excitons, etc. The plasmons are collective oscillations of the valence (conduction) sea of electrons in a material. There can be distinghuished two types of plasmons: volume (bulk) plasmons (VP) and surface plasmons (SP). The surface modes are sometimes named surface polaritrons for general materials, or surface plasmon polaritrons. The volume excitation is dominant when the beam

205
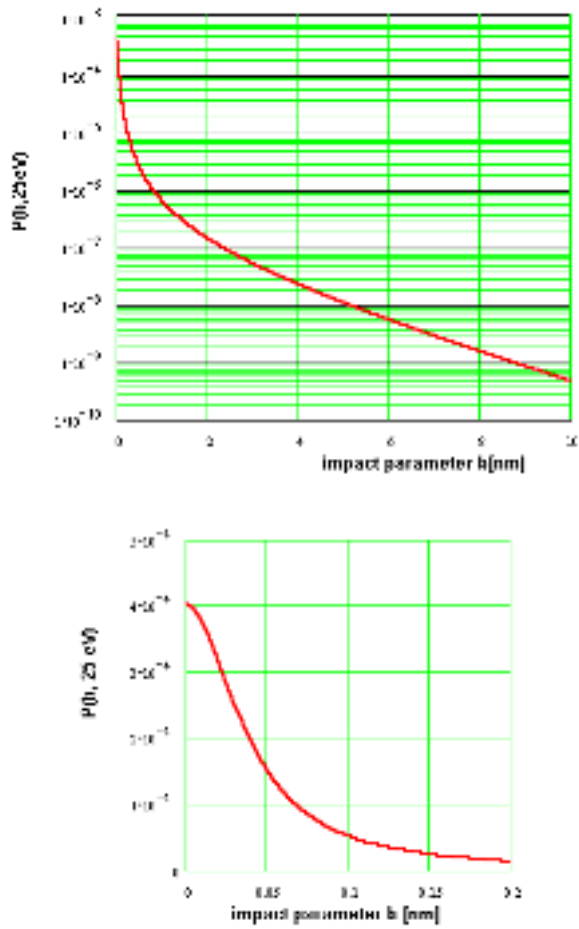
Figure 5-12: The probability P $_{SE}$ (b,E) that a SE is generated causing an energy loss of E = 25 eV within an impact parameter b (corrected to the measured coincidence EELS-SE spectra).
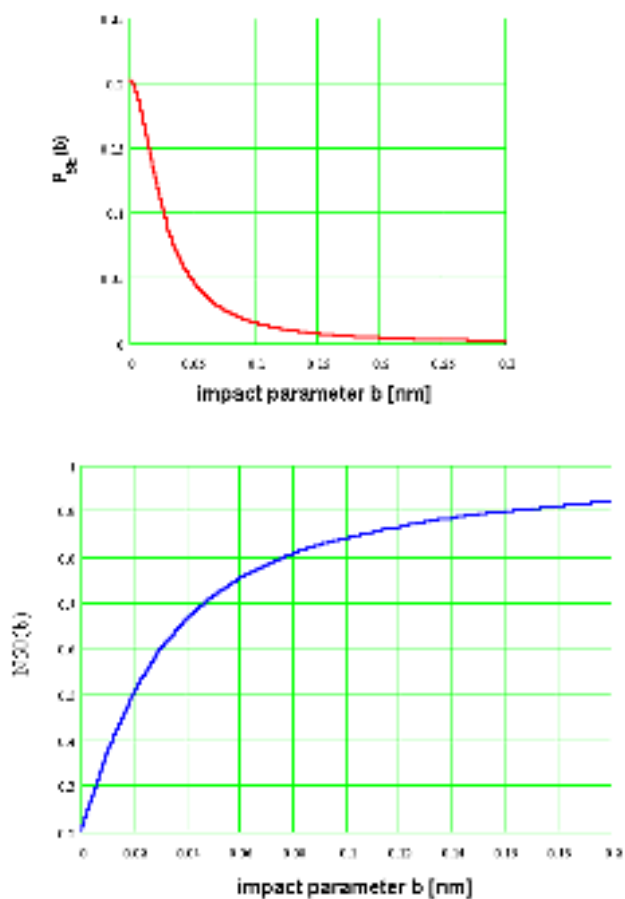
Figure 5-13: The normalized probability that a SE will be generated within an impact parameter b (100 kV electron incident on the 10 nm carbon foil)-upper plot. The lower plot shows the integral function of this probability: the probability that a SE will be generated in a circle of radius b.
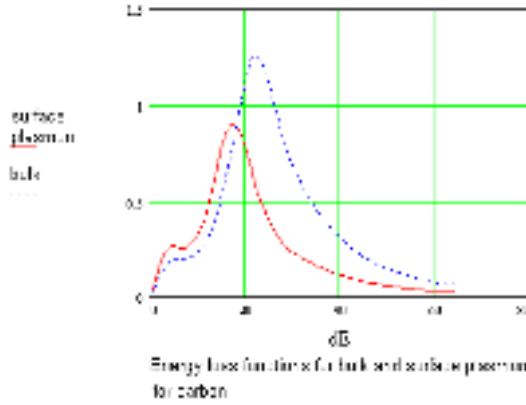
Energy loss functions for bulk and surface plasmon for carbon

Figure 5-14: The energy loss function for carbon calculated from optical data from [2].

penetrates the target, the surface excitation is the only one possible if the beam passes near the surface. The intensity of SP is roughly proportional with the area of the excited object and depends on the object shape.

In the study of plasmons, the free-electron theory has been applied with success for metals and semiconductors. For dielectrics this theory has to be replaced with the dielectric response theory. In the book of Raether a detailed study of plasmons can be found [21]. Sernelius treats in his book the surface plasmons for different object configurations [37].

The eigenfrequencies $\omega_{S,P}$ and energies of the plasma oscillations $E_{S,P} = \hbar\omega_{S,P}$ are known for a large number of materials, from measurements or calculations.

The bulk plasmon eigenfrequency ω_P can be calculated using the Drude model that considers the electrons as free and not bound to the atoms.

$$\varepsilon(\omega) = 1 - \frac{\omega_p^2}{\omega(\omega + i\Gamma)}$$

where $\varepsilon(\omega)$ is the dielectric function of the target material, ω_P is the plasma frequency, and Γ is the damping due to frictional forces proportional to electron velocity.

The resonance excitation of the volume occurs when $\varepsilon(\omega) = 0$. The energy E_s of the surface plasmon is on a flat target [14, 40]:

$$E_s = \hbar\omega_s = \hbar\omega_p/\sqrt{2} = E_p/\sqrt{2}$$

For example for amorphous carbon, the surface plasmon is at 17.7 eV and the volume plasmon is at 20-25 eV. We plot in Fig. 5-14 the energy loss function for surface and bulk plasmons in the case of carbon. Th$\sqrt{}$e dielectric function has been calculated using the optical data from [2].

EELS is normally used to measure the plasmon losses defined as the charge oscillations in a

208

thin film irradiated by an electron beam. EELS with very fine beam can nowadays also register the loss spectra when the beam passes outside or inside a nanometric particle.

The charge oscillations associated with plasmons can reach the entire medium even if the excitation source is a fine electron probe. The plasmon excitation is therefore a long-range excitation and a delocalized scattering process. The plasmons decay creating secondary electrons or giving a part of their energy to the gas molecules, and that is why they might influence the EBID resolution. We aim to estimate as good as possible the implications the plasmon delocalization might have in EBID.

The case of EBID involved an electron beam passing through a thin target and a gaseous precursor adsorbed on the target. Many types of plasmons can be generated and interact with each other, making this case very complicated to study. Because this is a first step in such an analysis we will try to simplify the problem and reduce it to cases already solved and available in literature. Therefore, let us analyze a simpler, practically assessed case, that considers an electron beam passing outside the target. A long-range contamination growth away from the electron trajectory can be easily observed in any electron microscope. The effect has been observed and modeled by Aristov and Kislov, where contamination rods could be grown starting from the edge of a holey carbon foil even when the beam passed through a hole [4, 3]. This effect is also used in electron microscopy as a method of determining the horizontal contamination rate by measuring the time necessary to close a hole of given diameter.

The EELS spectrum measured during the long-range growth gives an information about the mechanism of electron induced processes. The EELS spectrum of the passing 80 keV electron (see Fig.5-15), recorded when a contamination rod has been grown outside the beam trajectories (position 2) has shown a carbon surface plasmon peak (17.7eV). A different spectrum has been recorded during the growth within the beam area (position 1), when the carbon volume plasmon peak (25eV) appeared. It means that the long range growth can be explained with the electron interaction with the precursor molecule or the target via the surface plasmons..
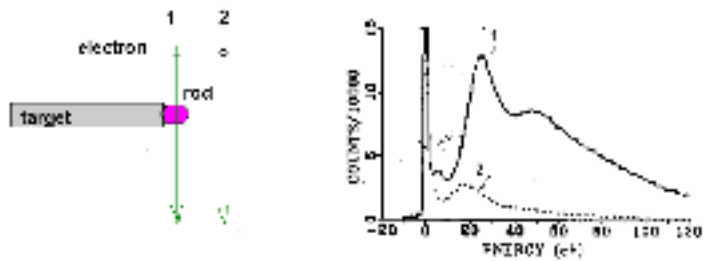

Figure 5-15: The EELS spectra of PE passing through the rod (1-solid line) and outside the rod (2-dashed line) [From Aristov and Kislov]

We consider the surface plasmons as an additional tool the electron beam can use to dissociate molecules. In this context, a complete study of EBID resolution requires an estimation of the delocalization of surface plasmon generation.

To get a first feeling of the dimension of the localization of plasmon generation by fast electrons, we can use a simple classical approach, proposed by Cheng [8]. A plasma is treated

as a system containing many relatively mobile charged particles. The excitation of a plasma is a coherent motion of a very large number of electrons, leading to small density fluctuations as a wave propagates with a certain velocity and can exist for a time in plasma. Considering a wave which moves with a certain velocity and decays in a certain time, the localization distance can then be defined as:

$$L = v_g \tau$$

where v_g is the group velocity and τ is the relaxation time determined from the Heisenberg principle.

The localization distance is then:

$$L = \frac{6}{5} \frac{\hbar^2}{m} \frac{E_F}{E_{plasmon}} \frac{\overline{k}}{\Delta E_{1/2}}$$

where

$E_{plasmon}$ = the plasmon energy

E_F = the Fermi energy of the target material

$\overline{k}$ = average wave vector of the electron

$\Delta E_{1/2}$ = the half width of the plasmon peak in the energy loss spectrum

For example in the case of an aluminium target, the delocalization of a 15 eV plasmon generated by a 100 keV electron is 0.4 nm, a value also obtained from the experiments of Isaacson [23].

The question is now how can a surface plasmon induce a molecular dissociation. The electron can transfer energy and excite a precursor molecule situated some distance away via two channels: One of them is via direct resonant collective excitation of the valence electrons in the gas molecule, i.e. the excitation of surface plasmons on the surface of the molecule. The situation is similar with the surface plasmons excitation on small metal spheres situated at a distance from the electron trajectory. The second process is an indirect one, and involves the surface plasmon generated on the target edge parallel to the electron trajectory . This surface plasmon can transfer a part of its energy to a nearby situated molecule. Both types of energy transfer may produce the dissociation of the molecule, (see Fig. 5-16). Both processes have further a specific cross section in the deposition, practically unknown. The direct excitation of the molecule has probably a larger cross-section in deposition than the indirect process because the SP generated on the target can also enhance the gas desorption which is a process counterbalancing the adsorption and deposition.

Let us first solve the problem of the localization of surface plasmons generation. Two different cases can be distinguished: modes on a planar surface and modes generated on a non planar spherical surface.We can separate two types of surface plasmon mediated electron-molecule interactions:

1. the surface plasmon generation on the vertical edge of the thin target, treated as a single planar surface.

2. the surface plasmon generated on the molecule, treated as a non-planar surface. Both interaction processes are delocalized and have a certain probability to happen depending on the distance of the electron passage. Further we will treat separately these two cases. The
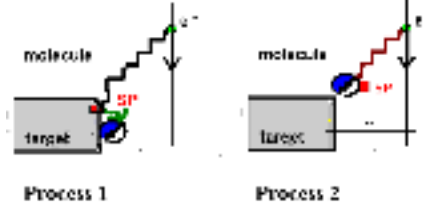
Figure 5-16: Possible mechanisms of long range electron - molecule interaction. Process 1. Indirect transfer: SP on the target edge, Process 2. Direct transfer: SP on the molecule.
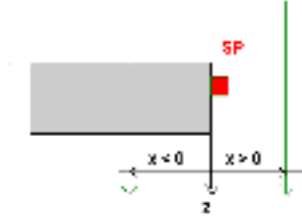

Figure 5-17: An exciting electron passing through or outside a target.

eigenfrequencies of surface modes depend on the geometrical shape of the excited object. For flat objects modeled as a plane bounded medium, a vaste literature exists, while for for spherical or cylindrical symmetric bodies the literature is less extensive.

5.4.1   Process 1. The surface plasmons on a flat surface

The flat interface is the most important type of interfaces. Let us consider an electron moving parallel to the z axis at a distance x from a flat surface. Depending on the distance x, the electron may cross the target or not, see Fig. 5-17.

The plasmon generation on the flat edge (semicontinuous medium) can happen on a certain distance from the electron trajectory with a probability given by [20, 40, 27]:

$$\frac{d^2 P}{d\omega dz} = \frac{e^2}{2\pi\varepsilon_0 \hbar \mathrm{v}^2} \mathrm{Im}\left(\frac{-2}{1+\varepsilon}\right) K_0\left(\frac{2\omega x}{\mathrm{v}}\right) \tag{5.20}$$

if the electron passes parallel outside the surface (x >0).

and by :

211

$$\frac{d^2P(x)}{dzd\omega} = \frac{e^2}{2\pi^2\varepsilon_0\hbar \mathrm{v}^2} \left| \mathrm{Im}\left(\frac{-1}{\varepsilon}\right)\left(\ln\left(\frac{2\pi k_c \mathrm{v}}{\omega}\right) - K_0\left(\frac{2\omega x}{\mathrm{v}}\right)\right) + \mathrm{Im}\left(\frac{-2}{1+\varepsilon}\right)K_0\left(\frac{2\omega x}{\mathrm{v}}\right) \right|$$

$$(5.21)$$

if the electron penetrates into the crystal (x <0).

In the first case only surface plasmons can be excited as these have an electric field which is non zero outside the material.

The first term in (5.21) describes the excitation of the volume plasmon and the second term describes the excitation of surface plasmons.

We consider the case when the electron passes outside the surface (x>0). Integrating over all possible frequencies the expression for the probability that a SP with energy $\hbar\omega$ will be generated at distance x, Aristov and Kislov obtained the full excitation probability of a plasmon on the flat surface at distance x along the electron path z [4]:

$$P_s(x) = \frac{ze^2\Gamma\omega_s^2}{2\pi^2\varepsilon_0\hbar v^2}\int\limits_{\omega_0}^{\infty} K_0\left(\frac{2\omega x}{v}\right)\frac{\omega d\omega}{(\omega_s^2 - \omega^2)^2 + \Gamma^2\omega^2}$$

where v = the velocity of electron

Γ = the damping factor determined experimentally from EELS equal to the width of the SP peak =1.5 x 10^{16} s^{-1}

ε_0 = 8.85 x 10^{-12}F/m, the dielectric constant

z = the length of electron path at a distance x from the surface (the thickness of target)

$\hbar\omega_s$= 17.7 eV the energy of the surface plasmon loss peak for amorphous carbon

If we use a simple threshold model for the precursor dissociation cross-section, only the SP with the energy exceeding the dissociation energy of hydrocarbon molecules (3 eV in average) are interesting. The lower limit of integration is chosen as ω_0=5.331 x 10^{15} s^{-1}. We present in Fig. 5-18 the calculated probability plot for a SP generation at the distance x.

We notice that the surface plasmon excitation happens also when the beam passes at a distance of 1 nm outside the surface. The excitation probability drops quickly when the beam is far from the surface but it still occurs even when the beam is further that 2 nm from the edge.

This result should be coupled with a more accurate cross-section of surface plasmon induced dissociation in order to give a better quantitative contribution of SP delocalization in the EBID rate.

5.4.2   Process 2. Surface plasmons on the spherical gas molecule

We can consider that the gas molecule is a dielectric sphere. The surface plasmon generation on the molecules can be treated similarly with the energy loss of an electron passing near a dielectric spherical particle. At this moment there are quite a few existing theories that treat the particular case of the dielectric spheres imbedded in vacuum and other more general cases. The study of the more complicated case of supported particles is in fast development. If the beam passes through the target surface plasmons will interact with volume plasmons and the situation is very difficult to model. Ouyang issued a formalism which can deal with supported particles
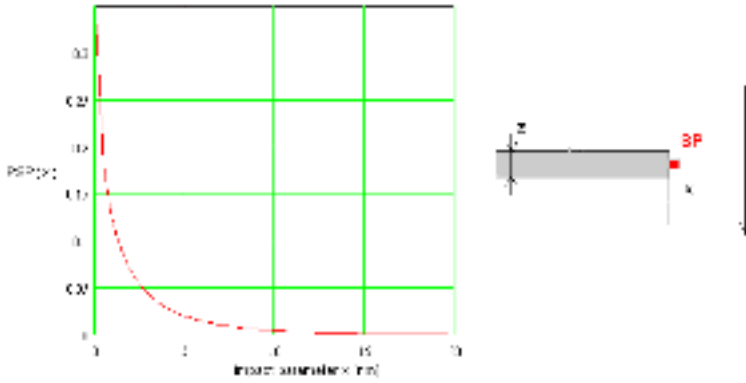
Figure 5-18: The calculated excitation probability across a z=50 nm long carbon thin film edge as function of electron impact parameter x. The energy of the electron is 100 keV.
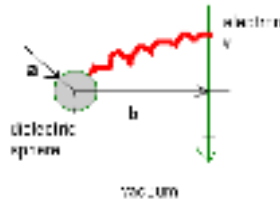

Figure 5-19: A charged particle (electron) moving at impact parameter b >a near a dielectric sphere

with any shape and dielectric constant [32, 31]. Usually simpler situations are analyzed, with particles in vacuum and subtracting the effect of the substrate.

Let us consider a dielectric nanosphere of radius a, situated in vacuum and a fast electron passing with velocity v near this sphere at distance b from its center (see Fig. 5-19).

The passing electron will induce a time dependent electrostatic field. While approaching the object, this field will excite polarization fields in the medium. The polarization induced electrical forces are given in [12].

During the time when the electron passes at a distance b from the molecule (10^{-17}s for a 100 keV electron) it can cause the collective displacement of the molecule valence electrons, without changing the position of its atomic nuclei. These excitations of the valence electrons of the molecule are surface plasmons and they can cause the break of bonds or the ionization of the molecule.

In spherical geometry the excited surface modes are quantized as a function of their angular momentum l.

For spheres, the well-defined surface plasmon modes, have eigenfrequencies given by:

$$\omega_l = \left(\sqrt{\frac{\omega_p^2 l}{2l+1}} \right) \; [1/s]$$

where ω_P is the volume plasmon frequency.

For an organic molecule, the typical plasmon loss can be calculated using free electron theory:

$$\hbar \omega_p = \sqrt{4\pi N Z e^2 / m_e}$$

where N = number of atoms per unit volume

Z= atomic number

m_e = the electron mass

The result is around $\hbar \omega_P$ = 20-25eV [4, 3], for air at NTP : $\hbar \omega_P$ =21 eV, for graphite : $\hbar \omega_P$ =25 eV [24].

The main dipolar mode is associated with $l = 1$ and most calculations restrict themselves to this term. [9, 38]. The dipole approximation equivalent for spherical objects is the solution of electrodynamics for a uniformly moving charge and a harmonically bound charge. Little work has been done for the general case. Acheche has identified the contribution of higher l modes [1]. Smeits used the free electron gas model for dipolar and a few superior l values [38]. Ferell and Echenique proposed a dielectric model that includes all multipole contributions [16].

In general, the probability Q_l to excite the l mode of a SP at the distance b on a sphere of radius a, has a maximum at r = a and for r $\gg$ a only the dipole mode can be excited. The governing factor is a transition factor with the radial dependence [9]:

$$f_l(b) = (b/a)^l, b/a < 1$$
$$= (a/b)^{l+1}, b/a > 1$$

The probability to excite the mode l of a SP on a dielectric sphere with radius a, by an electron passing at a distance b from the sphere center is given by Ferell and Smeits, using the free electron gas model [16, 38]:

$$P_{\omega_l}(b) = \frac{ae^2}{2\pi\varepsilon_0 \hbar v^2} \sum_{l=0}^{\infty} \sum_{m=0}^{l} A_{lm} \omega_l \left(\frac{\omega_l a}{v} \right)^{2l} K_m^2 \left(\frac{\omega_l b}{v} \right)$$

where v = the electron speed, and

$$A_{lm} = (2 - \delta_{om})/(l+m)!(l-m)!$$

δ_{0m}= the Kronecker delta operator
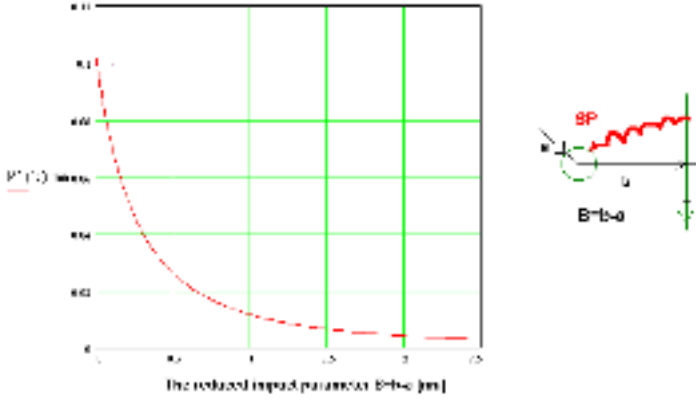
Figure 5-20: Probability of exciting the first mode of a surface plasmon (14.4 eV) on a hydrocarbon molecule with radius a=0.5 nm at the reduced impact parameter B=b-a [nm] for an 100 keV electron.

K_m = the Bessel function of order m

ε_0 =8.854187817 $\times 10^{-12}$ F m^{-1}, the vacuum permittivity

The dipole approximation $l = 1$ is valid only when $\omega a/v \ll 1$, implying for 100 keV that the radius of the sphere is a <1 nm [13]. In many experimental situations however b$\approx a$ and $\omega a/v \approx 1$ and therefore the study needs to include many l values. More than only one mode contribution have to be taken especially for electrons passing close to the sphere.

But a gas molecule has usually a radius smaller than 1 nm, so we can accept in a first approximation only the dipolar contributions.

We can calculate the delocalization of the generation of the first mode SP (l=1, m=0 and m=1) at the distance b from the sphere:

$$P_{\omega_l}(b) = \frac{a}{2\pi\varepsilon_0 \hbar v^2} \left(\frac{\omega_1 a}{v}\right)^3 \omega_1 \left(K_0^2 \left(\frac{\omega_1 b}{v}\right) + K_1^2 \left(\frac{\omega_1 b}{v}\right)\right)$$

The frequency of the first mode is $\omega_{l=1} = \frac{\omega_P}{\sqrt{3}}$=14.4 eV

The probability of exciting a surface plasmon on the typical hydrocarbon molecule by a 100 keV electron is shown in Fig. 5-20 as a function of the reduced impact parameter B=b-a.

5.5   Conclusions

The secondary electrons play the main role in EBID spatial resolution. By using the semiclassical approach we estimated that the delocalization of secondary electron generation can not enlarge their spatial profile with more than 0.5 nm. Another path used by the primary electrons to dissociate molecules is via surface plasmons. We performed a simple calculation of the localization of surface plasmon induced dissociation, considering the case when the substrate is

eliminated. The aloaf fast electrons can generate surface plasmons on the gas molecule surface or on the target edge. The probability to generate a surface plasmon in these two ways has a FW50% of around 1 nm. At distances larger than 2 nm the probability of SP generation drops drastically. The same conclusions have been obtained by Kislov & Aristov and by Han&Cerrina in [4, 19].

Bibliography

[1] ACHECHE, M., COLLIEX, C., KOHL, H., NOURTIER, A., AND TREBBIA, P. Theoretical and experimental study of plasmons excitations in small metallic spheres. *Ultramicroscopy 20* (1986), 99.

[2] ARAKAWA, E., WILIAMS, M., AND INAGAKI, T. Optical properties of arc evaporated carbon films between o.6 and 3.8 ev. *Journal of Applied Physics 48* (1977), 3176.

[3] ARISTOV, V., KISLOV, N., AND I.I.KHODOS. Direct electron-beam-induced formation of nanometer scale carbon structures in STEM. The growth of rods outside the substrate. *Microscopy, Microanalysis Microstructures* (1992), 323.

[4] ARISTOV, V., KISLOV, N., AND KHODOS, I. Direct electron-beam-induced formation of nanometer scale carbon structures in STEM. Nature of long range growth outside the substrate. *Microscopy, Microanalysis Microstructures* (1992), 313.

[5] ATKINS, P., AND FRIEDMAN, R. *Molecular Quantum Mechanics.* Oxford University Press, Oxford, 1997.

[6] BOLTON, J., AND L.M., B. Imaging surface states in the electron microscope: a semiclassical model. *Proc. Royal Soc. Lon. A 428* (1990), 2291.

[7] BUSECK, P. *High resolution transmission electron microscopy.* Oxford University Press, 1988.

[8] CHENG, S. Localization distance of plasmons excited by high energy electrons. *Ultramicroscopy 21* (1987), 291.

[9] COLLIEX, C. An illustrated review of various factors governing the high spatial resolution capabilities in EELS microanalysis. *Ultramicroscopy 18* (1985), 1131.

[10] DRUCKER, J., AND SCHEINFEIN, M. Delocalization of secondary electron generation studied by momentum transfer resolved coincidence electron spectroscopy. *Physical Review B 47* (1993), 15973.

[11] DRUCKER, J., SCHEINFEIN, M., LIU, J., AND WEISS, J. Electron coincidence spectroscopy studies of secondary and Auger electron generation mechanisms. *Journal of Applied Physics 74* (1993), 7329.

[12] ECHENIQUE, P., AND HOWIE, A. Image force effects in electron microscopy. *Ultramicroscopy 16* (1987), 269.

[13] ECHENIQUE, P., HOWIE, A., AND WHEATLEY. Excitation of dielectric spheres by external electron beam. *Philosophical Magazine A* (1987), 335.

[14] EGERTON, R. *Electron energy-loss spectroscopy in the electron microscope.* Plenum Press, New York, London, 1996.

[15] FANO, U. The formulation of track structure theory. In *Charged Particle Tracks in Solids and Liquids* (1970), L. Gray and G. Adams, Eds., p. 1.

[16] FERELL, T. Generation of surface excitations on dielectric spheres by an external electron beam. *Physical Review B 55* (1985), 1526.

[17] GLASS, F. Nanoscale diagnosis in condensed matter with high energy electron beams, 2000.

[18] HAMEKA, H. *Advanced quantum chemistry theory of interaction between molecules and electromagnetic field.* Addison Wesley, Reading, Massachusetts, 1965.

[19] HAN, G., AND CERRINA, F. Energy transfer between electrons and photoresist: its relation to resolution. *Journal of Vacuum Science and Technology B 18* (2000), 3297.

[20] HOWIE, A. Surface reactions and excitations. *Ultramicroscopy 11* (1983), 141.

[21] H.RAETHER. *Excitation of plasmons and interband transitions.* Springer Verlag, Berlin Heidelberg New York, 1980.

[22] INOKUTI, M. Inelastic collisions of fast charged particles with atoms and molecules-the Bethe theory revisited. *Reviews of Modern Physics 43* (1971), 297.

[23] ISAACSON, M., LANGMORE, J., AND ROSE, H. Determination of the non-localization of the inelastic scattering of electrons by electron microscopy. *Optik 41* (1974), 92.

[24] J.D.JACKSON. *Classical electrodynamics.* John Wiley and Sons, New York, 1975.

[25] JOY, D. The theory and practice of high-resolution scanning electron microscopy. *Ultramicroscopy 37* (1991), 216.

[26] JOY, D. High-resolution scanning electron microscopy. *Ultramiscopy 47* (1992), 80.

[27] MARKS, L. Observations of the image force for fast electrons near a MgO surface. *Solid State Coommunications 43* (1982), 727.

[28] MOSS, E. *Advanced molecular quantum mechanics.* Chapman and Hall, London, 1973.

[29] MULLEJANS, H., BLELOCH, A., HOWIE, A., AND TOMITA, M. Secondary electron coincidence detection and time of flight spectroscopy. *Ultramicroscopy 52* (1993), 360.

[30] MULLER, D., AND J.SILCOX. Delocalization in inelastic scattering. *Ultramicroscopy 59* (1995), 195–213.

[31] OUYANG, F., AND ISAACSON, M. Accurate modeling of particle-substrate coupling of surface plasmon excitation in EELS. *Ultramicroscopy 31* (1989), 345.

[32] OUYANG, F., AND ISAACSON, M. Surface plasmon excitation of objects with arbitrary shape and dielectric constant. *Philosophical magazine B 60* (1989), 481.

[33] PENNYCOOK, S. Delocalization corrections for electron channeling analysis. *Ultramicroscopy 26* (1988), 239.

[34] PIJPER, F., AND KRUIT, P. Detection of energy selected secondary electrons in coincidence with energy loss events in thin carbon foils. *Physical Review B 44* (1991), 9192.

[35] REIMER, L. *Scanning electron microscopy*. Springer Verlag, Berlin Heidelberg New York, 1990.

[36] RITCHIE, R. Quantal aspects of the spatial resolution of energy-loss measurements in electron microscopy. *Philosophical magazine A 44* (1981), 931.

[37] SERNELIUS, B. *Surface modes in physics*. Wiley-VCH, Berlin, 2001.

[38] SMEITS, M. Inelastic scattering of fast electrons by spherical surfaces. *Journal of Physics C 14* (1981), 1203.

[39] VOREADES, D. Secondary electron emission from thin carbon films. *Surface science 60* (1976), 325.

[40] WANG, Z. Valence electrons excitations and plasmon oscillations in thin films, surfaces, interfaces and small particles. *Micron 27* (1996), 265.

Chapter 6

An experimental setup for EBID and IBID study

> "Those perfect lines and the incredibly ingenious way in which the difficult construction problems had been solved were quite inconsistent with the style and quality of the Aymara indians' other early possessions. This was inheritance."

> Thor Heyerdahl, "The Ra expeditions"

6.1 Introduction

In this chapter we present some practical steps necessary to build an experimental setup necessary for the EBID or IBID study. The original idea was to build a dual beam instrument (DBI), by combining an electron and an ion beam focused on the same specimen. The main advantage of this type of construction is that two kind of energetic beam-induced lithography processes could be studied and compared in-situ. A second advantage was the possibility to use the less-damaging electron beam for visualization of structures previously fabricated by the ion beam. This type of instruments, despite of their usefulness are only occasionally built. The conventional commercial versions combine a scanning electron microscope with a liquid metal ion gun. The construction of a high-resolution dual beam instrument has been started by P.W.H. de Jager [3]. This DBI system combines a Philips EM 420 STEM and a high-resolution, in-house made focused ion beam column (see Fig.6-1). The complete optical design, together with some of the constructive modifications of the original STEM necessary to accommodate the ion beam column have been described in his thesis. Following the general ideas presented by de Jager, the development of the DBI continued, in order to make it operational and useful in the understanding of gas-assisted lithography processes induced by focused beams. For this purpose, extra imaging facilities have been attached, a computer based pattern generator for the beam deflection over the substrate according to a desired pattern and a gas delivery system based on a capillary nozzle injector have been built. The design of the nozzle injector has been done in close cooperation with dr. J. Bi. Further on we will talk only about the implementation of EBID, but all the described facilities can be directly used for IBID.

A detailed description of these new facilities is presented in the following sections.
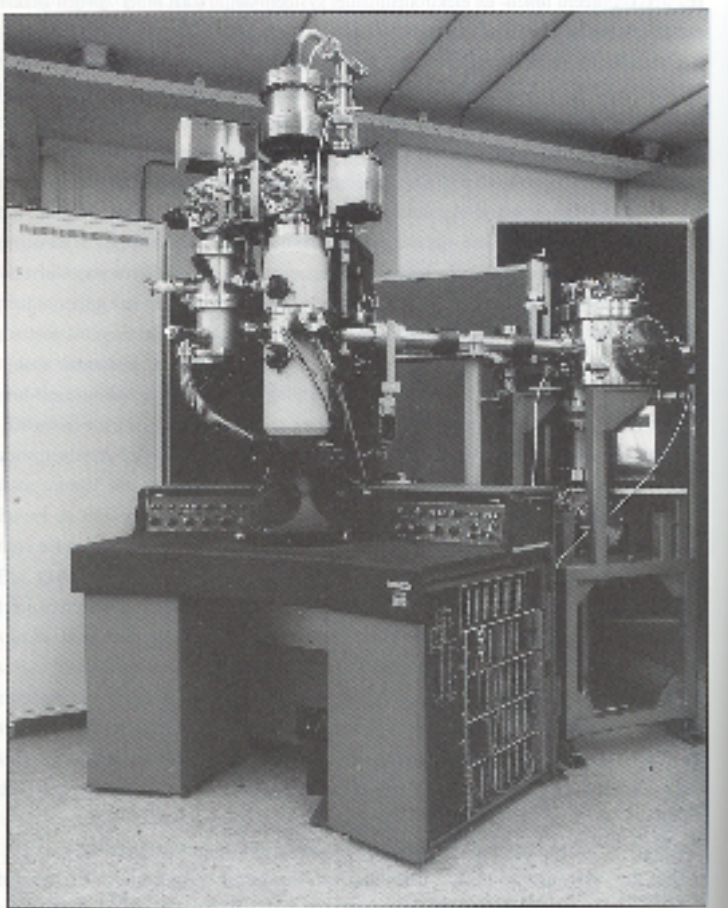
Figure 6-1: The dual beam instrument (DBI) [from [3]]

6.2 The probe forming system

The dual beam instrument is a combination of an electron beam column and a focused ion beam column. The optical systems of both columns are very well described in de Jager thesis [3] (see Fig. 6-2). With two 90 degree deflectors a normal incidence of the ion beam on the specimen is achieved. Between the two deflectors an energy filtering slit is built in, in order to reduce the ion energy spread to 1 eV. The Philips EM420 STEM has a thermionic electron gun with a tungsten filament or a LaB_6 cathode. The ion column has been designed for a Ga^+ LMIS. In order to accommodate the 90 degree deflector of the ion beam, the gun construction has been placed higher than in the original design. A special objective lens has been built for the ion beam focusing on the specimen. The Einzel type objective lens uses the magnetic objective

lens pole piece as one of the electrodes. The other two electrodes are inserted inside this pole piece. Space has been made by eliminating the coils of the auxiliary lens.

1. ion source
2. deflector / stigmator
3. mass filter
4. ion condenser lens
5. 90°-deflector
6. energy spread limiting slit

7. electron source
8. electron pre-deflector
9. electron condenser lens
10. angular limiting aperture
11. pattern generation deflector
12. combined ion and electron objective lens
13. target
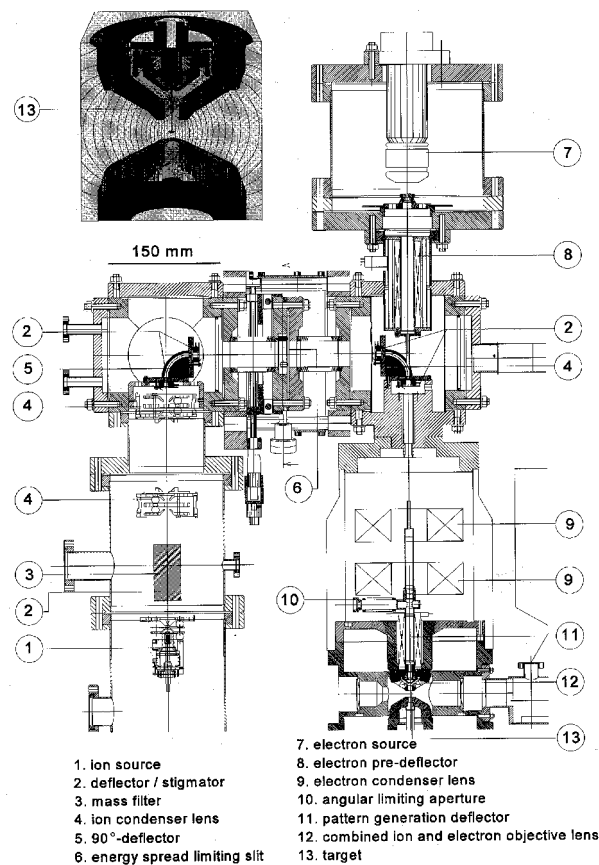
Figure 6-2: The physical design of the combined ion and electron optical instrument [from [3]].

The electronic control of the electron column components is done at this moments using the original equipment. For a future computerization of the control system, a P80 digital modular system has been built. This control system is also designated to supply the medium voltages necessary for the in-house made ion column electrostatic octupoles. Special high voltage supplies with a very good stability were also necessary.

6.3 The precursor delivery facilities

One of the essential elements necessary for a STEM to host EBID is an appropriate precursor delivery system. This system creates and eventually controls the gaseous ambient around

the specimen necessary for EBID to happen. At this moment, existing commercial STEM constructions do not include this facility. This is the reason why we studied the possibilities of extending an original STEM construction with a gas delivery system. As anticipated in Chapter 2, the literature survey on EBID and IBID has been again proven very useful in the dimensioning and operation of this system. The design has been in the first instance adapted to the geometry of DBI host microscope, a Philips EM 420 STEM. After the concept has been tested in this instrument, new demands on higher resolution experiments made us switch to the state-of-the-art STEM, the Tecnai20, where obviously no modifications in the construction could be accepted. This restriction led us to another goal and challenge, a portable environmental cell.

In the following sections, the precursor parameters and the design aspects of two proposed gas delivery constructions, the nozzle injector and the portable gas cell respectively, will be presented.

6.3.1 The precursor parameters

The choice of the precursor used in our deposition system has been influenced by the practical needs expressed by other co-workers at the moment when this project started. The dual beam instrument has been designed to function as one of many workstations in a large nanofabrication system stationed in the NEXT (Nanoscale Experiments and Technology) laboratory [3]. In this laboratory, different nanofabrication and inspection techniques have been implemented, by interconnecting in one UHV system various equipment as: STM's, CVD chambers, etching and preparation chambers, loadlocks, etc. The fabrication techniques implemented in STM could manipulate surfaces on atomic scale and write continuous metal lines but not too fast and not on a large surface. Deposition induced by a finely focused charged particle beam (EBID or IBID) was one of the techniques that promised to achieve better results.

Because the deposited features had to be metallic, the precursor had to be obviously a metal bearing molecule. Because the DBI shared the vacuum system with more workstations, the most accepted metallic "impurity" was tungsten. Tungsten is also a perfect conductor material appropriate for fabrication of wires and field emission tips. In this case the choice was restricted to tungsten hexafluoride WF_6, used on industrial scale in CVD or tungsten hexacarbonyl $W(CO)_6$ used mostly in thermal deposition and in quite a large number of EBID experiments. Both precursors are highly toxic, so the final choice must be the least dangerous one. WF_6 is found in gaseous form at room temperature and it can escape easily without notice from the reservoir. $W(CO)_6$ has a stable chemical composition, and it can be found as a powder that can be safely stored in a tightly closed container. Its disadvantage is that the induced dissociation results in an additional carbon content. This disadvantage is not dramatic as long as we are not interested in high deposit quality but only in high fabrication resolution.

Tungsten hexacarbonyl $W(CO)_6$ (see Fig. 6-3) is a metalo-organic compound, found as a white powder at room temperature and has been supplied with 99 % purity by Sigma Aldrich (CAS# 14040-11-0). The physical properties of the precursor are summarized in Table.6.1.

The vapour pressure dependence with the temperature is given by the relation [4]:

$$\log_{10} P = 11.523 - \frac{3872.0}{T} \tag{6.1}$$

where P is the vapour pressure [torr] and T is the gas temperature [K].

Physical state and appearance	white powder
Density	2.65 g/cm3
Molecular weight M	351.91 g/mole
Vapour pressure	1.2 torr (160 Pa) at 67 °C
Boiling point	451.3 ° C @ 760 torr
Melting Point	170° C
Decomposition Temperature	150° C
Solubility	insoluble

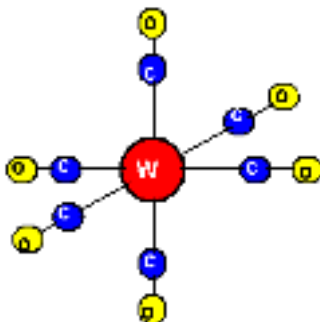Table 6.1: The physical properties of the $W(CO)_6$ molecule
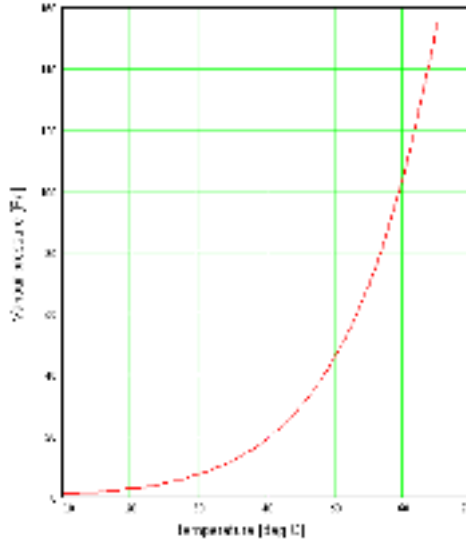

Figure 6-3: The geometry of $W(CO)_6$ molecule

Figure 6-4: The vapour pressure dependence on temperature P $_{vap}$ (θ) for W(CO)$_6$.

A plot of the vapour pressure using (6.1) is shown in Fig. 6-4.

6.3.2 Design considerations for a nozzle based gas delivery system

The design of any gas delivery system connected to an electron microscope is based on a compromise between being effective for EBID and being harmless for the host optical column. For the dual beam instrument we have first chosen for a capillary nozzle based construction. The principle of a nozzle based delivery system is that the vapours of the precursor kept at its constant vapour pressure in a reservoir are introduced through a fine capillary nozzle in close proximity to the sample surface irradiated by the focused beam (Fig. 6-5). The sensitive areas in the microscope like the gun chamber will benefit from such a local gas introduction Knowing the physical parameters of the precursor W(CO)$_6$, the nozzle gas system will be dimensioned to satisfy the throughput demands for EBID to happen, without badly damaging the host vacuum system.

Let us suppose that the gas feedthrough terminates in a fine capillary nozzle with an inner diameter d$_i$ = 0.4 mm and a length L = 10 mm. We have to check if this geometry can supply a satisfactory flux striking the surface and if the pressure in the specimen chamber does not grow up to dangerous levels during gas inlet.

The mean free path of gas molecules at a temperature T and pressure P is approximately given by [1]:

$$\lambda = \frac{kT}{\sqrt{2}\pi P D_{mol}^2}$$

226
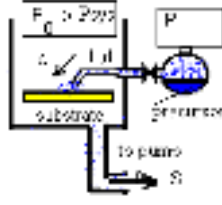
Figure 6-5: The vacuum system of the host microscope connected to the gas reservoir

At room temperature, the mean free path of $W(CO)_6$ molecules with a molecular diameter $D_{mol} = 7.2$ x 10^{-10}m is 0.6 mm at a pressure of 2.7 Pa in the reservoir. Because the mean free path of gas molecules is somewhat larger than the inner dimensions in the tubing, the theory of free molecular flow in a narrow tube and appropriate semi-empirical formulae can be used.

Thus, for zero nozzle outlet pressure (P_0=0), the gas flux or throughput Q from the nozzle is defined by the upstream gas pressure P, the parameters of the precursor molecule and by the geometry of the narrowest terminal part, the capillary [12]:

$$Q = \frac{1}{L} \cdot (2.094 \cdot v \cdot R_i^3) \left(0.0736 \frac{R_i \cdot P^2}{(\lambda P)} + 0.81P + 0.614 \frac{(\lambda P)}{R_i} \ln \left(1 + 3.094 \frac{R_i P}{(\lambda P)} \right) \right)$$

$$v = 4\sqrt{\frac{R_g T}{2\pi M}} \quad ; \quad \lambda P = \frac{kT}{\sqrt{2}\pi D_{mol}^2}$$

Q = the gas flux [Pa m^3/sec]

k = the Boltzmann constant

R_g = the universal gas constant

L = the length of the capillary ,

R_i = the inner diameter of the capillary

v = the average velocity of the gas molecules

l = the mean free path of the gas molecules

M = the precursor molecular weight

P = the precursor reservoir pressure [Pa]

D_{mol} = the diameter of gas molecule

T = the gas temperature in the reservoir [K]

Replacing the temperature dependence of the upstream gas pressure in the reservoir P(T), we can plot the gas throughput dependence on the gas temperature, Q(T) (see Fig.6-6).

The pressure in the system P_{sys} as response to this gas flux Q can be calculated as :

$$P_{sys} = \frac{Q}{S} \text{ [Pa]} \tag{6.2}$$

where

Q is the gas flux [Pa m^3/sec] and S is the pumping speed at the nozzle level [m^3/sec].

Estimating that the pumping speed in the specimen chamber is S = 20 l/sec, we obtain the pressure rise in the system as a result of the gas introduction, plotted in Fig. 6-7.
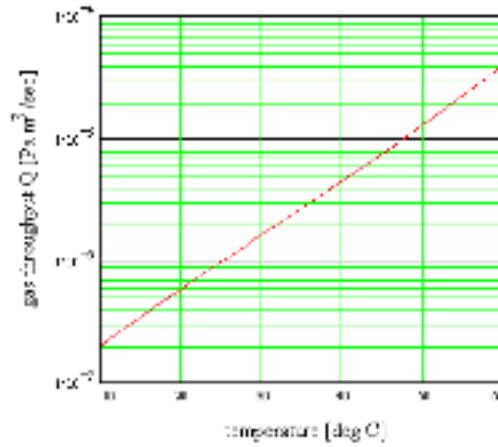
Figure 6-6: The gas flux dependence on the $W(CO)_6$ precursor temperature in the reservoir and in the nozzle.

An essential condition for the good functioning of the host system and for a reduced contamination of the specimen is that the pressure in the specimen chamber should not rise above 10^{-5} mbar (10^{-3} Pa). Then from the Fig. 6-7 an important restriction results, that the precursor temperature in the reservoir should not be larger than 55 °C .

Up to now we calculated that it is safe for the host microscope to operate the precursor within a temperature range from room temperature to 55 °C. But is in this case the gas throughput on the target surface sufficient for EBID to happen in a reasonable time? The answer is given by the molecular density of the gas striking the substrate F, describing the contribution of the gas delivery in the growth rate.

This molecular flow on the surface can be calculated using the relation [20]:

$$F = \frac{1}{kT}\frac{Q}{A} \quad [\text{molecules/m}^2/\text{s}]$$

where
Q = the gas flux $[Pam^3/s]$ (gas throughput)
T = the gas temperature $[K]$
k = Boltzman constant $(1.38 \times 10^{-23} J/K)$
A = the target area covered by gas $[m^2]$

We know from the literature that the molecular flow striking the surface necessary for EBID to happen in a reasonable time is F = 10^{16}...5 x 10^{18} molecules / cm^2/sec if the sticking coefficient is considered equal to one [2, 16, 13, 19, 10].

This condition will dictate the last available degree of freedom, the clearance of the nozzle with respect to the specimen, h and the nozzle inclination angle, α (Fig. 6-8)

The target area covered by precursor A can be calculated using the formula [16]:
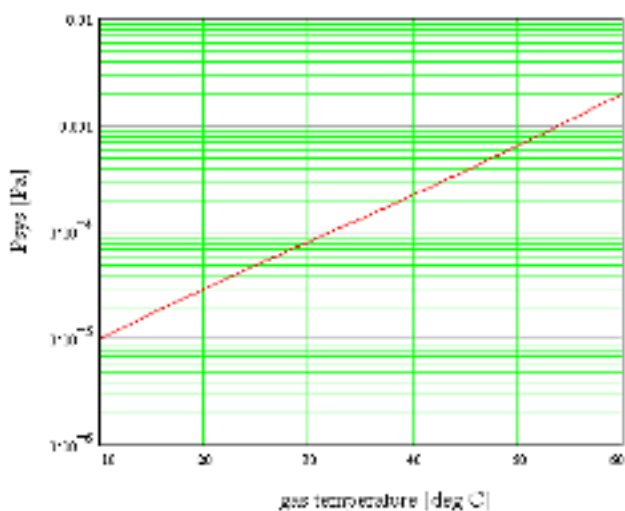
Figure 6-7: The pressure in the specimen chamber dependence on the gas temperature in the reservoir.
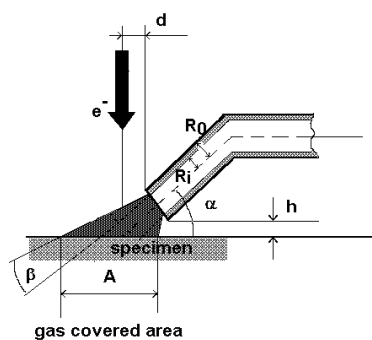
Figure 6-8: The geometry of the nozzle injector.
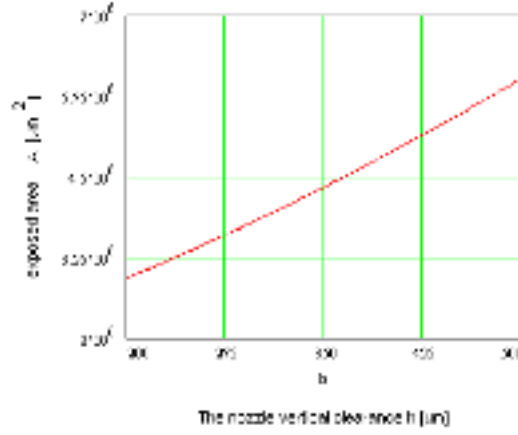
Figure 6-9: The area A [$\mu m2$] covered by precursor as function of the nozzle vertical clearance h [μm].

$$A = \pi \cdot \left(R_o \cdot \cot(\alpha) + \frac{h}{\sin(\alpha)} + \frac{R_i}{\tan(\beta)} \right)^2 \cdot \sin^2(\beta) \cdot C \cdot D$$

$$C = \frac{\sin(\alpha) \cdot \sin(\beta)}{\cos^2(\beta) - \cos^2(\alpha)}$$

$$D = \sqrt{ \left(\frac{\sin(\alpha) \cdot \cos(\beta)}{\cos^2(\beta) - \cos^2(\alpha)} \right)^2 - \left(\frac{\cos(\alpha)}{\cos(\beta) + \sin(\alpha)} + \frac{\sin(\beta) \cdot \cos(\alpha)}{\cos^2(\beta) - \cos^2(\alpha)} \right)^2 }$$

where R_i and R_0 are the inner and outer radii of the cylindrical nozzle.

Taking the inner radius R_i= 200 μm and the outer radius $R_0 = 350$ μm, the spread angle $\beta = 30°$ and the inclination angle $\alpha = 45°$, we can plot the gas covered area A, in function of the nozzle vertical clearance, h, shown in Fig. 6-9.

From Fig. 6-9 we see that the vertical clearance h does not influence very much the gas exposed area on the target. It means that we can calculate an average molecular flux dependance on the temperature in the reservoir $F(T)$ for a typical clearance of $h = 250$ mm, plotted in Fig. 6-10 .

From Fig.6-10 we see that even at room temperature, the molecular flow striking the surface is situated at the lower acceptable limit $\approx 10^{16}$ molec/cm ^{2}/sec. This molecular flux varies strongly with the vapour temperature and it reaches a value of 2 x 10 ^{17} molec/cm ^{2} /sec, situated somewhere in the middle of the recommended range.

We conclude that theoretically the nozzle system defined by the parameters ($D_i = 0.4$ mm, L=10 mm, h = 200-500 μm, $\alpha = 45°$) can produce a satisfactory $W(CO)_6$ throughput for EBID to happen. The heating of the precursor to 55°C can increase the throughput with one decade.

Based on the dimensioning approved by these calculations, a capillary nozzle based gas delivery system has been built for a Philips EM420 STEM (Fig.6-11).

The gas delivery system, shown schematically in Fig.6-11 consists of three parts. One part contains the capillary nozzle and it is inserted inside the deposition specimen chamber, fixed
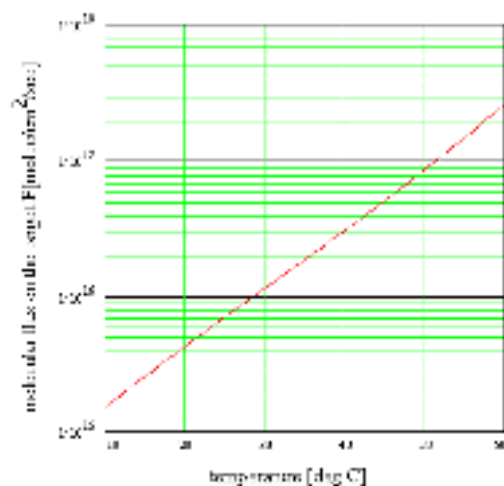
Figure 6-10: The molecular gas flux striking the target surface F [molec/cm^2 /sec] for a vertical clearance of the nozzle h=250 μm.
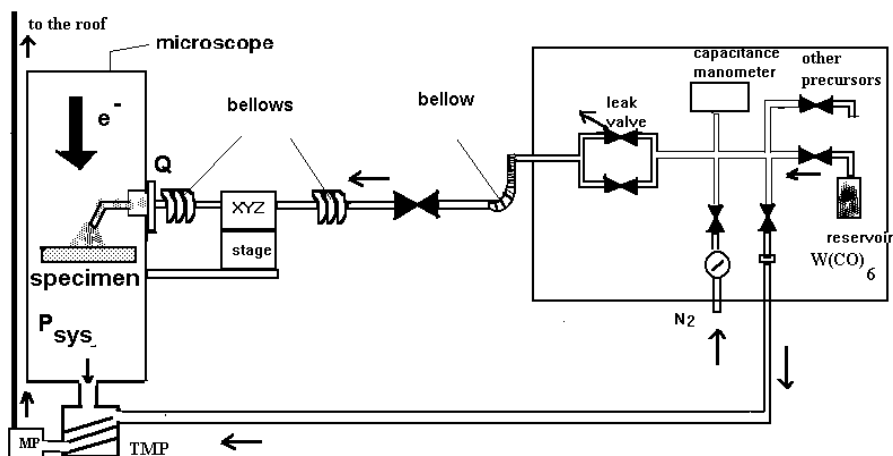

Figure 6-11: The gas delivery system for EM420 STEM.

Figure 6-12: The capillary nozzle and the bellows

on a flange in the goniometer port destined originally for the cold finger anti-contamination device. The nozzle, shown in Fig. 6-12 is made from a nonmagnetic stainless steel material RVS321 to avoid interferences with the electron beam passing in close vicinity. Two flexible bellows allow to move and position the nozzle using a XYZ translation stage having a 10 μm resolution and a range of 10 mm on all three axes.

The precursor reservoir is situated at the other end of the system. This reservoir contains 5 g of $W(CO)_6$, it is made from stainless steel with a UHV compatible glass viewport, for an easy visual quantity check. Above the reservoir is immediately situated a shut-off valve that can be closed when the reservoir is disconnected and taken away to be filled in a special oxygen cabinet. In this way the changing of precursor does not interrupt the functioning of the host system.The vapour pressure above the reservoir is monitored by a 10 Torr capacitance meter type BARATRON, with indications independent of the type of gas sensed. The digital readout of the meter can be eventually used for a feedback control loop for an automatic inlet valve.

A gas feed-through tubing with all-metal NUPRO valves situated in critical points connects the nozzle to the gas reservoir. Facilities to pump the gas tubing using the turbomolecular pump of the microscope (TMP) and to flush the gas system with nitrogen are provided. Also extra gas tubing has been designed, for future extension of precursor types.

Because the precursor is toxic, the exhaust of the system membrane pump (MP) is led outside the laboratory to a safe location on the roof of the building. The necessary exhaust pipe diameter D = 8 mm has been dimensioned in order to protect the pump against overpressure (<100 mbar).

6.3.3   Design considerations for an EBID environmental cell

The dual beam instrument was very useful in testing the nozzle gas delivery system and in general during all the preparation steps necessary to convert a STEM in an EBID setup. Our calculations from Chapter 4 have shown that sub-10 nm EBID resolution is possible provided a very fine beam is used (0.2 nm). Unfortunately such a fine beam is impossible to achieve in the rather obsolete EM420 model used as base for our DBI. The need to perform EBID in a

modern STEM became thus vital for the proof of our theoretical predictions. Obviously any modifications in a commercial STEM are strictly prohibited and the only solution should be to design a small gas cell that can fit in the specimen holder. This is how the idea to design an environmental cell for EBID study in a STEM came up.

The idea of an environmental cell for in-situ electron microscopy studies, where the specimen is kept in a non-vacuum environment, has existed for some time. Another concept coming from recent miniaturization trends in life sciences and chemical analysis is the " laboratory-on-the-chip" The first section presents some useful information about existing constructions of environmental cells for electron microscopy. The next section presents the design of a portable gas cell for the in-situ EBID study in almost any generation of Philips STEM's (EM420, CM20, Tecnai20).

6.3.3.1   Environmental cells in electron microscopy - an historical overview

In order to observe wet specimens, such as biological materials or hydrated clay minerals, or to dynamically observe chemical reactions (oxidation, catalysis), eventually induced by electron irradiation, it is usually necessary to place the specimen in a cell containing a non-vacuum environment. The special cell built for this purpose is called *environmental cell* or *environmental chamber (EC)* [6, 26]. Sometimes the name of gas reaction cell, wet cell or hydration chamber is also used, depending on the kind of phase created around the specimen: gas or liquid.

In electron microscopy practice, depending on the type of separation between the specimen area and the rest of the microscope vacuum, two types of ECs have been developed: film-sealed cells/chambers and differentially pumped chambers. The first type uses thin film windows transparent to electrons to encapsulate the specimen and a small surrounding volume. The second type of EC limits the specimen volume with small apertures (pinholes), to reduce the leakage of gas into the high vacuum regions. The modern commercial low-vacuum SEM's (Wet SEM and Environmental SEM) already accept a gas atmosphere around the specimen, lower than atmospheric pressure, but higher than the water vapor pressure. In this case only an extra separation between the specimen chamber and the rest of the microscope vacuum is needed, using for example a thin film window placed under the objective lens [9].

A very early attempt has been made by von Ardenne (1942) who constructed a reaction chamber in his microscope with open microscopic holes. In 1944, Abrams and McBain separated the specimen of their Stanford microscope using a 60 nm thick nitrocellulose film, vacuum sealed with wax, but problems caused by sudden rupture of the film always occurred. Later, a closed wet cell was built in 1972 by Fullam for a JEOL JEM120 microscope [8]. As separation were used 30-40 nm plastic Formvar and nitrocellulose films covered with a silicon monoxide layer, mounted on 400 mesh copper grids. The films and the specimen were firmly closed with a cap in the specimen holder. The specimen holder bodies could be fit also in other microscopes. Fukami et al. built three types of film sealed environmental cells by modifying a specimen holder or the objective lens pole piece [6, 7]. One is a gas cell , another is an environmental chamber built in the lens area and another is a wet cell combined with an extra droplet injector. The 20-35 nm thin carbon films are resting on a plastic microgrid with 7 μm holes. The maximum pressure difference on the film was 200 torr. For a higher gradient, the seal film rupture has been observed. Physical and chemical reactions and wet biological specimens have been observed.

Keyse, Reynerd and Venables built a side entry oxidation EC integrated in the specimen holder and used crushed indium rings to assure vacuum seals [15]. The separating film used was parylene-N or formvar or pioloform 40 nm thick coated with 20 nm aluminium. Parkinson designed a side entry reaction cell by modifying the specimen holder for a JEOL 200FX TEM.

incorporating in the holder a gas inlet [22]. Green uses a 75 nm thick Si_3N_4 film window to separate the specimen area with atmospheric pressure from the gun chamber in an Amray ESEM [9]. Especially for the EBID study, Koops built a modified specimen chamber in a SEM, with a shutter to let the electron beam in [17]. Lee built a modified gas chamber in a TEM [18]. Folch built a simple gas cell consisting of a sandwich of two apertures and in between the specimen and the liquid $Fe(CO)_5$ [5].

Some EC incorporate also temperature control, heaters or cold stages.

A review of gas reaction cells for EM can be found in articles of Pasons [23] and Turner [26].

In conclusion until now the environmental cells for electron microscopes needed modifications of either the specimen chamber, objective lens area or the specimen holder, sometimes also restricting the specimen tilt possibilities, remaining thus more or less system-dependent and not portable.

6.3.3.2 A portable gas cell for EBID study in a STEM

Based on the concept of lab-on-the-chip, we aimed to build a portable gas cell carrying everything that is needed to study EBID in any generation of Philips and FEI STEM's.

The design of an environmental cell for an electron microscope needs to satisfy some basic requirements. The cell has to be made of materials compatible with normal operation of the host microscope, i.e. nonmagnetic and vacuum compatible. The cell has to fit without modifications in a standard TEM specimen holder with typical sizes of 3 mm diameter and 2 mm high. The cell is not allowed to obstruct the normal functioning of the microscope or to reduce its original performance. An eventual bottom or top foil has to be transparent for 40 keV - 300 keV electrons. The construction has to avoid the contamination of other mechanical parts of the specimen chamber with the precursor powder. The precursor is toxic, so the loading of the cell has to be fast and easy operated in an oxygen cabinet with special gloves. A less strict requirement would be the possibility to re-use the cells and to separate the specimen for further analysis. A valve to control the moment and the flow of the gas inlet should be also a convenient facility.

We designed a simple gas cell that can be still made using classical machining techniques. Because we learned that if the separation material is a thin foil there is always a risk of breaking due to the almost 1 atm pressure shock, we have chosen in our design for a safe solid reservoir construction. The reservoir containing the $W(CO)_6$ powder is designed as a hollow screw, with one end open for filling. A small hole of 0.3 mm diameter serves as a gas valve opening (see Fig. 6-13). After it is filled the reservoir is screwed in a ring holder, so that its other end is also closed (see Fig. 6-14). The assembly reservoir and ring fit in a typical single tilt specimen holder for any electron microscope newer than EM420. (see Fig.6-15) The thin specimen is mounted between the cell and the specimen holder and it is not fixed to the cell. The advantage of such a construction is that after the experiment the specimen can be analyzed separately.

Once the cell is introduced in the deposition vacuum chamber, the vapour will flow out down the pressure gradient (see Fig. 6-16). Some calculations have been made to estimate the time necessary to empty the cell, considering that the cell contains 3 mg $W(CO)_6$ (se Fig. 6-17). We can see that for a hole of 0.3 mm which is on the edge of what is mechanically possible to process, the gas flow will be active for 1.5 hours. We think it is a reasonable time for one experiment.

The gas cell presented here is just a beginning. A lot can be done to improve this construction. An improvement of this construction should be a valve to control the opening of the gas inlet. Microvalves are a modern subject nowadays, especially used in microfluidics.

234

Figure 6-13: The precursor reservoir

Figure 6-14: The assembly gas reservoir and holder ring

Figure 6-15: The gas cell together with the typical TEM specimen and specimen holder.
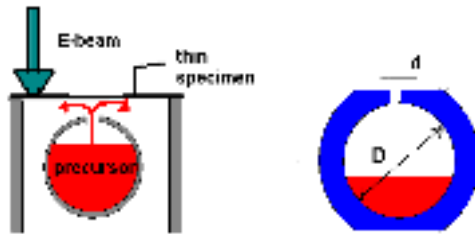
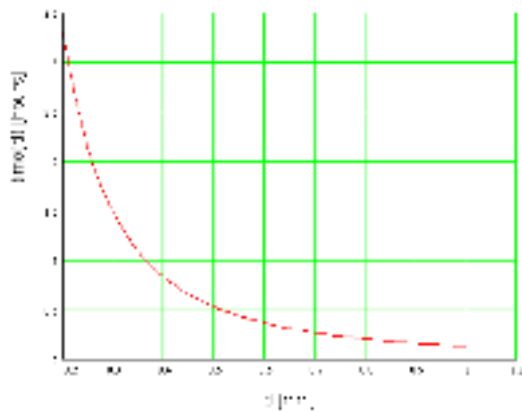Figure 6-16: A cross sectional view of the gas cell during an EBID experiment

Figure 6-17: Evacuation time of the gas cell t [hours] as a function of the valve diameter d [mm].

How can we control the valve after it has been inserted in the microscope and we can hardly access it? The valve can be controlled by varying the temperature, by a pressure gradient, by piezoactuators, by the magnetic field of the objective lens. We propose the idea to use a SMA (shape memory alloy) material that changes its form when heated to a preset form. The material has been used before as a shutter [14]. It is a cheap solution and can be implemented in a heating TEM specimen. A more modern construction should be made by taking advantage of the possibilities of microfabrication and should use MEMS or microvalves to control the gas flow.

6.4 The pattern transfer facilities

After the beam focusing and precursor delivery aspects are solved, the fabrication of a desired pattern still requires the beam to be deflected following this pattern. This will require another construction step - a tool for pattern definition and generation. In this section the deflector construction and a PC controlled pattern generator and its user interface are described.

6.4.1 The beam deflection system

In the DBI an electrostatic deflector unit has been built for the deflection of the ion beam during the specimen patterning. The optical design of the deflecting system is described in de Jager thesis [3]. A double deflector construction has been designed. The advantage of this arrangement is that it introduces a new degree of freedom, the point around which the beam is virtually deflected, the pivot point P. The position of the pivot point on the axis depends on the ratio of excitation applied on the two deflectors. By changing the position of the pivot point, different convenient situations can be realized. For example if the pivot point is chosen in the middle of the objective lens, then the beam will enter the objective lens on axis, reducing the spherical aberrations and improving the probe size. Another convenient situation is a normal beam incidence on the specimen over the whole exposed area, the so-called telecentric beam path (Fig.6-18). The telecentricity is realized by setting the pivot point in the back focal plane of the objective lens.

Each electrostatic deflector is designed as an octupole, made of eight cylindrical electrodes. The construction with eight electrodes offers an electrostatic deflection field in the central region closer to a parallel one than a simple construction with only four electrodes. The whole construction is inserted inside in the lining tube of the condensor part of the EM420 STEM objective lens. Cables making contact with the 16 electrodes are led out of the vacuum system and connected to 0 - 350 V voltage supplies.

Images of the dual octuple deflector construction and the lining tube are shown in Fig.6-19 and Fig. 6-20.

6.4.2 The pattern generator

Usually a pattern generator is a box coupled to a computer that generates the signals necessary to deflect the beam above the specimen according to the desired pattern. A pattern file in a convenient format has to be delivered by the user. Usually the file contains the type of the primitive figure (line, rectangle, box, circle), the coordinates of the reference points of the figure and the exposure times.
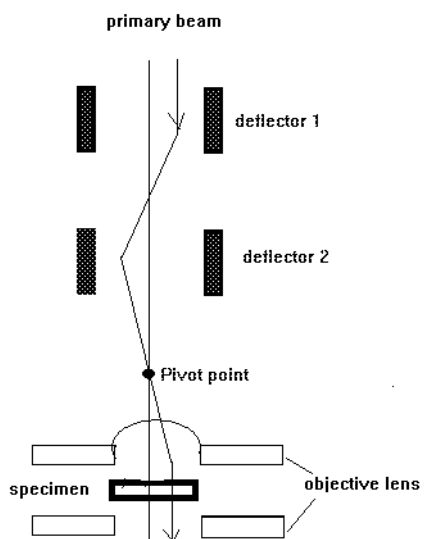
Figure 6-18: The telecentric beam path created by the double deflectors construction
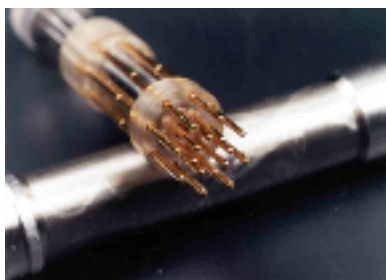

Figure 6-19: A view of the two sets of eight electrodes for the beam deflection.

The hardware is based on the 16 bit digital to analog conversion (DAC) plug-in card from National Instruments, AT 16 MIO DAQ. A large number of bits increases the resolution of conversion, so the distance between two successively exposed pixels can be smaller. The DAC card has two analog outputs X and Y. Two arrays of data have to be send to the DAC. The pattern data is kept in a buffer and send at once with high accuracy. The D/A card has its own internal oscillator that we use as a pixel clock, to trigger each data set generation. The signals from the analog outputs of the DAQ are send to an amplifier and then to the electrostatic deflectors.

We designed a computer program for the pattern generation named DuoLITH, because it can be used with both electron and ion induced patterning in lithography. The software is organized as a menu driven user interface and it has been written in Labwindows programming environment.

An important menu option is the pattern definition, that allows the user to interactively define a pattern on the screen. The user can choose between a few primitives as line, rectangle and filled box. The position and sizes can be directly set by using the mouse. The pattern is saved in an intermediate file. Another option selected by the user will convert this file in a coordinates file with necessary numerical inputs for the DAC card. Here procedures to generate a line when the coordinates of the both ends are given are used like the Bresenheim algorithm.

Another menu option is to send the pattern file to the DAC card, with the possibility to define the dwell time i.e. the exposure per pixel from 1 μs to 1 s , the number of times the pattern has to be repeated and the magnification (distance between pixels). The same pattern defined once, can be scanned with different exposure parameters.

The DAC plug-in cards are commercially available for less that 1500 $ and they are accompanied by easy to handle control software. The same type of data acquisition card has been used with success in direct nanopatterning in STEM by Streblechenko and Scheinfein [25]. We therefore think that this method can be used as a fast solution to generate patterns in beam induced lithography.
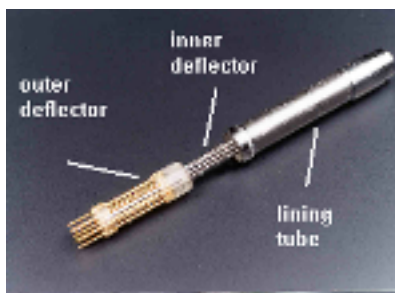
Figure 6-20: The dual electrostatic deflectors construction and their insertion in the objective lens liner tube
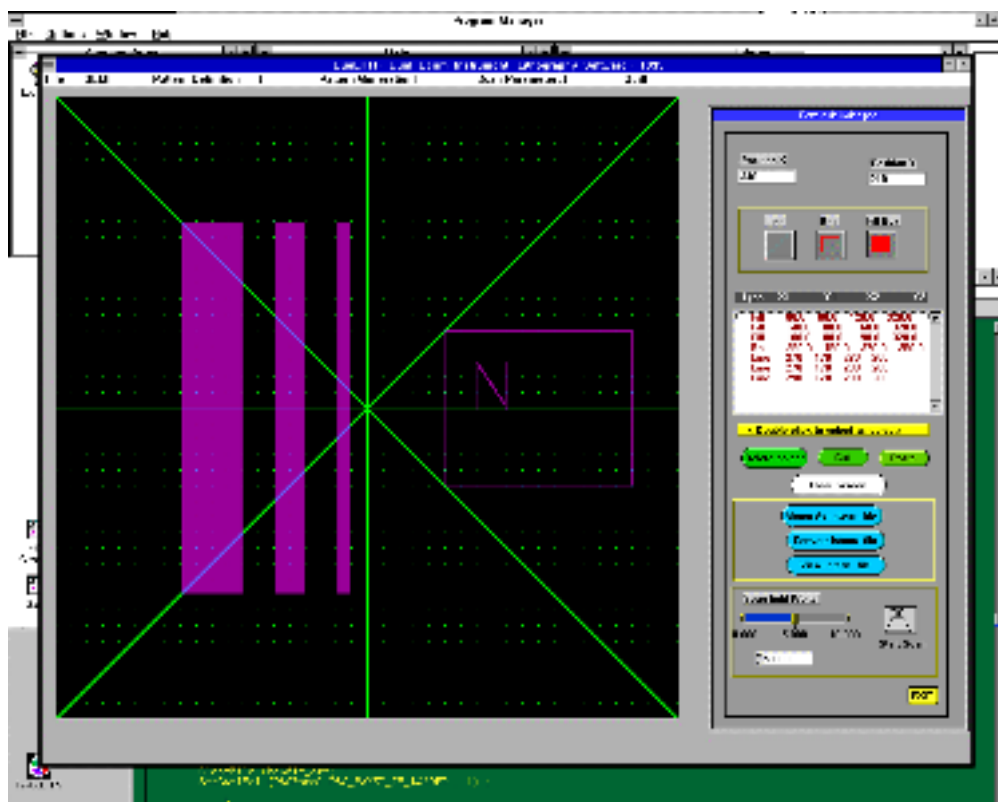
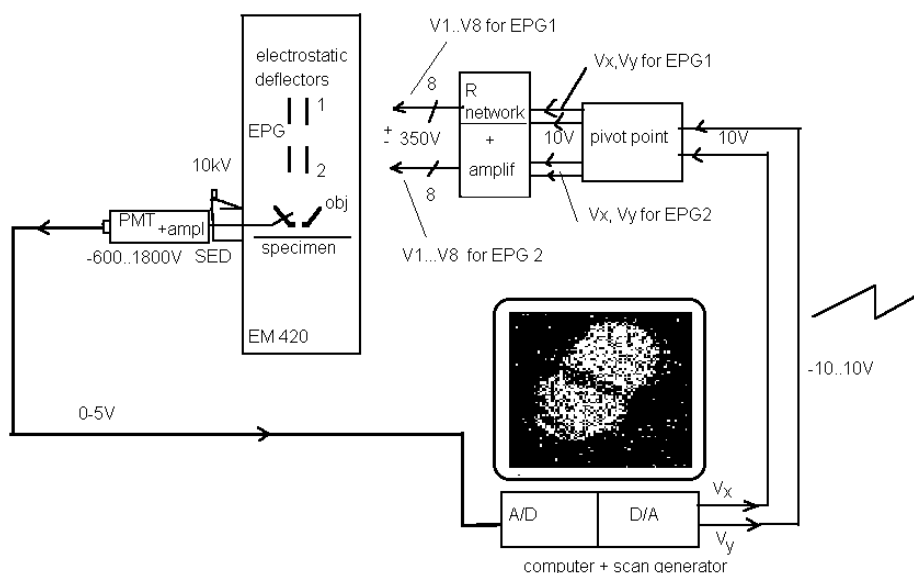Figure 6-21: A hardcopy of the screen during the pattern definition using DuoLith software

Figure 6-22: Arrangement for the secondary electron imaging in the electron beam column

6.5 The imaging facilities

6.5.1 Image formation using the secondary electrons

The detection of the secondary electrons emitted from the irradiated specimen is one of the classical modalities to obtain an image of the specimen. In EBID case, it will also help to assure that the beam is focused on the specimen during patterning.

In the STEM system we arranged (see Fig.6-22), the scanning of the beam across the specimen is done using the electrostatic deflectors built for the ion beam. The advantage of using other set of deflectors than the beam shift from the host microscope is that the alignment information of the beam is not lost during scanning.

A commercial digital scanning system (DISS) is used to scan the beam, register the secondary electrons signal and display a specimen image on a PC. The output signals are two sawtooth signals from -10 to 10V. These signals are fed to a box that establishes the pivot point for the electrostatic deflectors. The signals are then applied to the two sets of deflectors, noted EPG1 and EPG2. The image forming signal comes from a photomultiplier that amplifies the signal from the secondary electron detector (SED). The detector attracts the secondary electrons by 10 keV potential applied to the scintillator. The scintillator is at this moment P47 powder. An idea would be to replace this scintillator with a modern and more robust YAG disk. The scintillator converts the electrons into photons that travel towards the photomultiplier tube through a quartz pipe.

A problem will occur when this arrangement is used for imaging during ion beam experiments. The focusing of the ion beam by the objective lens requires a potential up to 20 kV on

the middle electrode, that creates a strong electrostatic field inside the upper pole piece. This field will obstruct the secondary electrons to arrive at the scintillator and it will be impossible to obtain an image. Solutions have to be found to solve this problem.

One of them, proposed by de Jager, was to use the middle electrode of the Einzel objective lens as scintillator in the secondary electron detection. This electrode could be made from YAG or from glass covered by scintillator powder. Monte Carlo simulations for the conversion efficiency of such a detector have been made by Hoogeboom in his master thesis [11]. Difficulties are encountered in the realization of light transmission from the electrode to the photomultiplier, caused by the high potential of this electrode and the reduced available space. A fixed construction with the light conductor glued to the electrode will make it impossible to disassemble the microscope column. An easier solution would be to avoid any contact and leave a space between the scintillator electrode and the light conductor and hope that the photon detection efficiency will be high enough for a good signal to noise ratio image.

6.5.2 Image formation using the specimen current

Another imaging alternative during ion beam bombardment would be the imaging based on the specimen current measurement [21]. Part of the electron probe current I_p passes through the specimen to ground and it is called the specimen current or absorbed current [24]. All the secondary electrons and backscattered electrons that leave the specimen decrease this current. If $\sigma = \eta + \delta$ is the total yield of SE and BSE, the specimen current becomes:

$$I_S = I_P(1 - (\eta + \delta)) \qquad (6.3)$$

where η and δ are the SE and BSE yields.

A single tilt holder for EM420 STEM has been modified to create an isolated island for the specimen, connected with a wire to the outside world and a current-voltage converter for the current amplification. In this way the specimen can be biased and the adsorbed current can be measured, forming an image reversed to a SEM image.

The method is simple and does not need any modifications in the specimen chamber, but it has the disadvantage that a good signal to noise ratio requires a relatively large (>5 pA) electron probe current.

6.6 The vacuum system

The vacuum system of the EM420 STEM has been modified, by replacing the oil diffusion and the rotary pumps with a turbomolecular - membrane pump assembly. An additional ion getter pump has been attached to improve the vacuum in the gun chamber (see Fig.6-23).

6.7 EBID instrumentation tests

6.7.1 Tests of the gas delivery system

The gas system we designed has been tested at room temperature using a nitrogen source connected in the place of the gas reservoir. The N_2 was introduced in the system through a
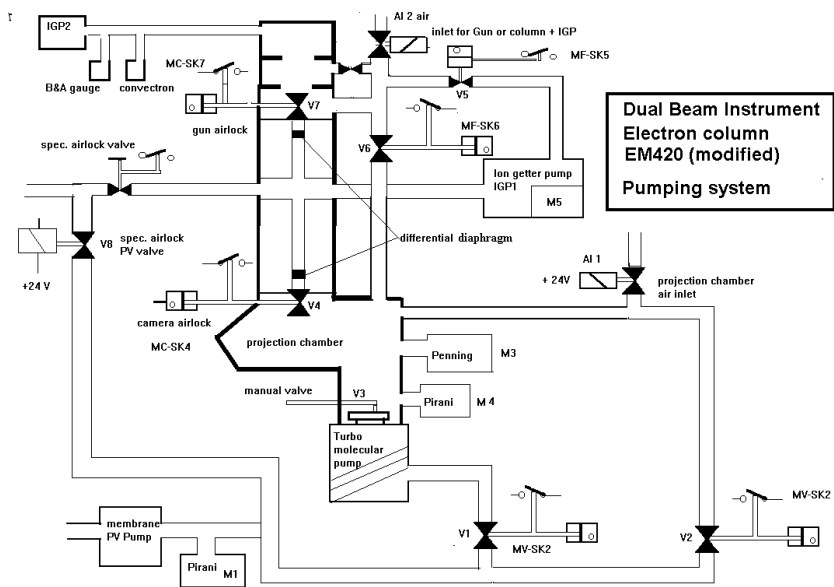
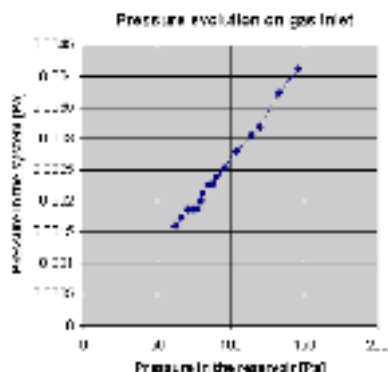Figure 6-23: The vacuum system of the modified EM420 STEM

Figure 6-24: Pressure tests for the nozzle gas delivery system

leak valve, monitoring the gas inlet pressure and the pressure rise in the system. The dependence
of these two pressures is plotted in Fig. 6-24.

6.7.2   Tests of the imaging facilities

The secondaru electron imaging has been tested by using the system described in Fig. 6-22.
The specimen was a holey carbon film, supported by a copper mesh. The diameter of the
copper wire was previously measured with an optical microscope as 10 μm. In Fig. 6-25 we
show a low magnification SEM image of the specimen, where is clearly seen the coipper grid
and a defect in the carbon foil. The maximal field of view is shown in this image, estimated to
be 160 $\mu m \times 160 \mu m$.
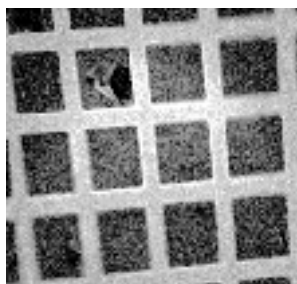
Figure 6-25: SEM image of a holey carbon film supported by a copper grid

The TEM images of the the same specimen have been recorded with an analog TV camera
type Gatan 610 mounted under the microscope. A monochrome frame grabber plugged in a
computer makes possible to digitalize the images and save them as bitmap file on the disk. In
Fig. 6-26 we show the recorded low magnification (x45) image of the same specimen where the

244

copper grid is again visible and a higher magnification image (x 3000) where individual holes estimated at 100 nm diameter in the carbon foil can be distinguished.
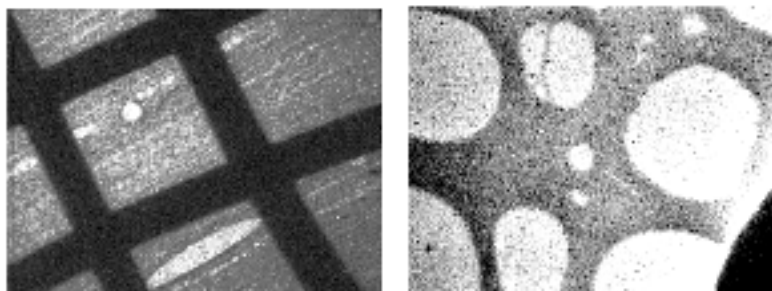
Figure 6-26: Low magnification and high magnification TEM images of a holey carbon foil

6.7.3 Testing the EBID

The first condition to test the EBID is to be sure that the electron beam is focused on the target. For this purpose firstly a sharp SEM image has to be obtained. We estimated that the diameter of our focused electron beam is ca. 10 nm. The first structures to grow are dots, obtained by a stationary beam focused on the target correlated with a $W(CO)_6$ gas introduction in the specimen chamber. After a few minutes, a TEM image with the defocused beam shows the resulted deposition. In Fig.6-27 we show a tilted TEM image of some deposited dots. The diameter of the dots is about 200 nm.

Also lines can be deposited in the same way, by scanning the focused beam over the target surface along a line and by introducing simultaneously $W(CO)_6$ precursor vapours. The pressure of the precursor has been measured by the BARATRON to be ca. 20-30 mtorr as expected from the calculations of vapour pressure at laboratory temperature (25°C).

In Fig. 6-28 we show a 500 nm thick line deposited on the carbon foil from $W(CO)_6$. A thinner line (100 nm) deposited on the foil, as well as a free-standing rod deposited across a hole and a "N" pattern are shown in Fig.6-29.

6.8 Conclusions

All the steps necessary to implement EBID in a STEM have been discussed and solved in the case of a EM420 Philips STEM. EBID has been tested in this instrument, where dots, lines, letters and free-standing structures were deposited on thin carbon and silicon films. The size of the routinely fabricated structures was around 100 nm. High resolution imaging was not possible due to low electron probe currents. A prototype of gas environmental cell useful for EBID study in any similar STEM has been built. This cell will make possible high resolution direct metal deposition in a state of the art STEM with an electron probe size of 0.2 nm.
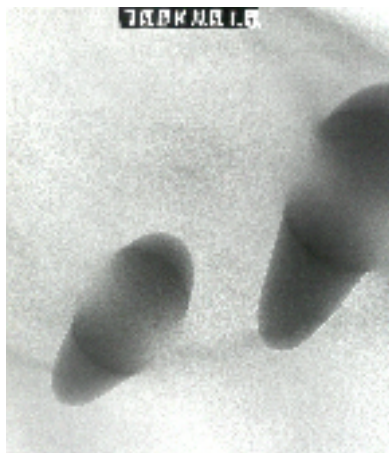
Figure 6-27: High resolution TEM image of EBID dots grown on carbon thin film (the diameter at the base of the tips is ca. 200 nm)
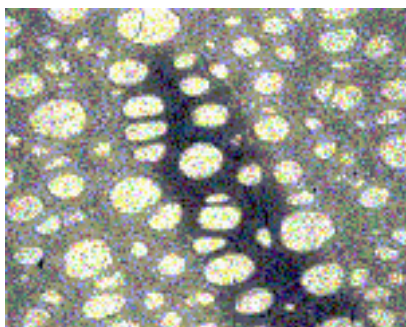

Figure 6-28: A thick line deposited from $W(CO)_6$ on a holey carbon foil

Figure 6-29: Lines, patterns and free standing rods grown by EBID on a thin holey carbon film.

Bibliography

[1] BIGELOW, W. *Vacuum methods in electron microscopy.* Portland Press, London, 1994.

[2] BLAUNER, P., AND RO, J. FIB of submicron gold structures. *Journal of Vacuum Science and Technology B 7*, 4 (1989), 609.

[3] DE JAGER, P. *Design of "the Fancier",an instrument for Fabrication and Analysis of Nanostructures Combining Ion and Electron Regulation.* PhD thesis, Delft University of Technology, 1997.

[4] FELDMAN, J., AND CULLEN, W. Occurence of volatile transition metal compounds in landfill gas. *Environ. Sci. and Technology 31* (1997), 2125.

[5] FOLCH, A., AND SERVAT, J. High-vacuum versus "environmental" electron beam deposition. *Journal of Vacuum Science and Technology B 14* (1996), 2609.

[6] FUKAMI, A., AND FUKUSHIMA, K. Environmental cell: observation of wet specimens. In *Proceeding of European Conference on Electron Microscopy EUREM Budapest* (1984), vol. 1, p. 71.

[7] FUKAMI, A., FUKUSHIMA, K., AND ISHIKAWA, A. Imaging for chemical reaction process of wet specimens using new type of environmental cell with image processing system. In *Inst. Phys. Conf. Series* (1988), vol. I, p. 145.

[8] FULLAM, E. A closed wet cell for the electron microscope. *Review of Scientific Instruments 43* (1972), 245.

[9] GREEN, E., AND KINO, G. Theoretical models for scanning electron microscopy through thin film windows. *Journal of Vacuum Science and Technology B 9* (1991), 3070.

[10] HIROSHIMA, H., SUZUKI, N., OGAWA, N., AND KOMURO, M. Conditions for fabrication of highly conductive wires by electron beam induced deposition. *Japanese Journal of Applied Physics 38* (1999), 7135.

[11] HOOGEBOOM, B. Using an electrode of an electrostatic objective lens as a secondary electron detector. Master's thesis, Delft University of Technology, 1999.

[12] HORWITZ, C. Simple calibrated gas feed system. *Review of Scientific Instruments 50* (1979), 652.

[13] HOYLE, P., CLEAVER, J., AND AHMED. Electron beam induced deposition from $W(CO)_6$ at 2 to 20 kev and its applications. *Journal of Vacuum Science and Technology B 14* (1996), 92.

[14] JARDINE, A., AHMAD, M., CLELLAND, R., AND BLAKELY, J. A simple ultrahigh vacuum shape memory effect shutter mechanism. *Journal of Vacuum Science and Technology A* (1988), 3017.

[15] KEYSE, R. J., REYNERD, G., AND VENABLES, J. An electron microscope helium stage for use with a side-entry windows type environmental cell. *Journal of Physics E 17* (1984), 228.

[16] KOHLMANN, K., THIEMANN, M., AND BRUNGER, W. E-beam induced X-ray mask repair with optimized gas nozzle geometry. *Microelectronic Engineering 13* (1991), 279.

[17] KOOPS, H., WEIEL, R., AND KERN, P. High-resolution electron-beam induced deposition. *Journal of Vacuum Science and Technology B 6* (1988), 477.

[18] LEE, T., AND DEWALD, D. An environmental cell transmission electron microscope. *Review of Scientific Instruments 62* (1991), 1438.

[19] LIPP, S., FREY, L., AND LEHRER. A comparision of focused ion beam and electron beam induced deposition processes. *Microelectronics and reliability 36* (1996), 1779.

[20] MAISSEL, L. *Handbook of thin film technology.* McGraw-Hill Book Company, New York, 1970.

[21] OATLEY, C. Detectors for the scanning electron microscope. *J. Phys. E* (1981), 971.

[22] PARKINSON, G., AND WHITE, D. The application of a controlled atmosphere reaction cell for studying electroactive polymers by TEM. In *Proc XIth Int. Cong. on Electron Microscopy, Kyoto* (1986), p. 331.

[23] PARSONS, D. Structure of wet specimens in electron microscopy. *Science 186* (nov 1974), 407.

[24] REIMER, L. *Scanning electron microscopy.* Springer Verlag, Berlin Heidelberg New York, 1990.

[25] STREBLECHENKO, D., AND SCHEINFEIN, M. Magnetic nanostructures produced by electron beam patterning of direct write transition metal fluoride resists. *Journal of Vacuum Science and Technology A 16* (1998), 1374.

[26] TURNER, J., VALDRE, U., AND FUKAMI, A. Control of specimen orientation and environment. *Journal of Electron microscopy and technique II* (1989), 258.

Chapter 7

Nanometer scale fabrication with EBID

7.1   Introduction

This chapter describes our experimental investigations in the potential of EBID to fabricate small structures situated in the 1 - 10 nm range. The use of electron beams is one of the most promising techniques for high resolution nanolithography. But even for this technique, to fabricate robust sub-10 nm structures is a major challenge, difficult to rebut at this moment. Sub-10 nm fabrication with electron beams is still in its infant times and it is practised at this moment only in research laboratories. Up to this moment, the conventional EBID performed in a SEM could not fabricate structures smaller than 13-20 nm. The PMMA based conventional electron beam lithography reached its fundamental limits at 10 nm. However, occasionally these limits have been broken and electron beam induced processes could induce the fabrication of sub -10 nm structures.

The fabrication resolution in lithography is usually defined as the smallest lateral size achievable for isolated features. For some applications, like high density information storage, the nanostructure density is a more relevant parameter compared to the nanostructure itself.

The proximity effect is the principal enemy of close spacing in lithography. A possible way to improve the resolution and reduce the proximity effect is to use low energy electrons. At low energy (12-50 eV), electron scattering is all but eliminated and proximity effects are no longer a problem. This condition is offered by the scanning tunnelling microscope (STM). The pattern transfer in a STM can be resist-based, like in conventional EBL process, or resistless, using a (metallo)-organic gaseous precursor that can be later evacuated from the chamber. The latter process is actually EBID performed in a STM, known as "STM assisted CVD". The best results of this technique at this moment are individual features as small as 0.8 nm in diameter and 0.7 nm high [6], as well as magnetic material lines of 5 nm FWHM and 2 nm high [3]. Very small spacing between individual dots was obtained, between 1.5 and 3 nm [1]. The drawback of the scanning probe techniques is their low throughput and the incapacity to expose large areas.

Another possible direction to improve the fabrication resolution is to use thin film targets and high energy electron beams that can be focused in very fine spots. Thin films reduce the electron scattering in the substrate and high energy beams pass with less lateral broadening in

the film. These conditions are offered by Scanning Transmission Electron Microscopes (STEM). A method that can produce very high resolution structures in a STEM is the direct sublimation under electron bombardment of a variety of solid inorganic materials, like Al_2O_3 or the self-developing metal halides including $NaCl$, MgF_2, AlF_3 LiF. The high resolution of this technique has been investigated, among others, by Murray & Isaacson who obtained arrays of 4 nm diameter holes and 8 nm spacing, 2 nm diameter and 4 nm spacing [2]. Recently Streblechenko and Scheinfein demonstrated a new high-resolution electron beam sensitive resist, FeF_2 and CoF_2. For example, by using the magnetic fluoride CoF_2 in a VG STEM with 0.5 nm beam and 1 nA current at 100 keV, Co lines with 5 nm FWHM could be writen [5]. The principle of this method is not completely understood, but it seems that the structures are induced by high energy electrons.

In Chapter 4 and Chapter 5 we showed that EBID in a high resolution STEM should be able to fabricate 2-3 nm wide structures. In the following section we will prove experimentally the viability of this idea, by showing images of sub-10 nm size dots and lines grown in a Tecnai 20 STEM with a very stable, sub-0.5 nm electron beam.

7.2 Experimental results

Here we present our high resolution experiments on contamination growth, performed in a state-of-the-art STEM. Contamination study is the first easy to realize step in EBID study with the only difference that the precursor is formed by the hydrocarbon molecules, supplied from the specimen at a much lower rate. But we expect that the spatial results we obtain will create a realistic general image of the EBID resolution. We will show that contamination lines as narrow as 2 nm to 8 nm can be directly deposited on a thin carbon film. The advantage of this approach is that it implements a one-step, maskless and resistless writing method, that does not require resist development, etching or lift-off.

Contamination experiments have been performed in a prototype of the-state-of-the-art STEM, the Tecnai 20. The beam energy was 200 keV, the probe size has been measured to be 0.2 nm FWHM in NANOPROBE mode and 1 nm FWHM in MICROPROBE mode. The probe current could be varied from 5 pA to 20 pA. The TEM micrographs of the deposited structures have been recorded and off-line processed by using the Gatan Digital Micrograph software v. 3.6.1. The common image processing functions used were the profile across a line, obtained by averaging in a rectangle area of the image and filtering of the FFT transform of the image in the frequency domain [4].

First an individual contamination dot has been deposited in 60 seconds on a 12 nm thick holey carbon foil, by a stationary 5 pA beam, focused in a 0.4 nm probe. The TEM top view image of this dot is shown in Fig. 7-1. The intensity of each pixel in this TEM micrograph can be displayed as a gray tone or a RGB color in a 3D surface plot. Such a surface plot of the same dot is shown in Fig. 7-2. The estimated exposure dosis used to grow this dot is 23 000 C/cm^2. We observe that the diameter of the dot is around 20 nm, much larger than the measured beam diameter. This means, according to our model, that we measure the diameter somewhere near the point B in the saturation area of the diameter evolution curve.

To check if this assumption is correct and if the diameter of the dot can be also made smaller, we deposit a series of dots with exposure times increasing from 3 s up to 15 s. The series of dots has been deposited by stagnation of the beam on the same specimen. A TEM top view micrograph, as well as the TEM image of the tilted dots are recorded and shown in Fig. 7-3 and Fig. 7-4. We observe that the shapes of the tilted dots agree with the results of our
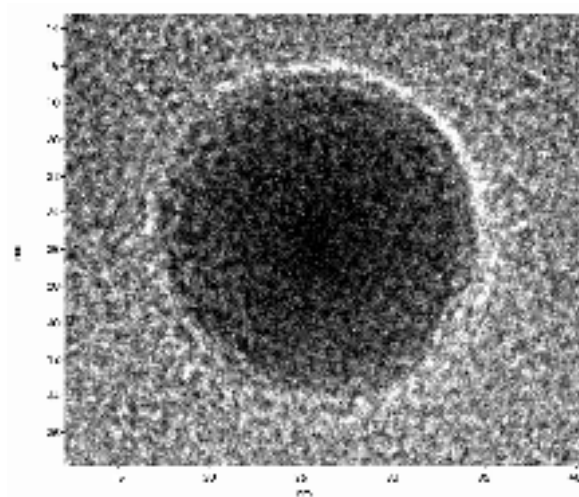
Figure 7-1: TEM micrograph of an individual contamination dot deposited on a 12 nm thin carbon foil, in 60 seconds, by a 0.4 nm diameter beam. The probe current is 5 pA and the beam energy is 200 keV.
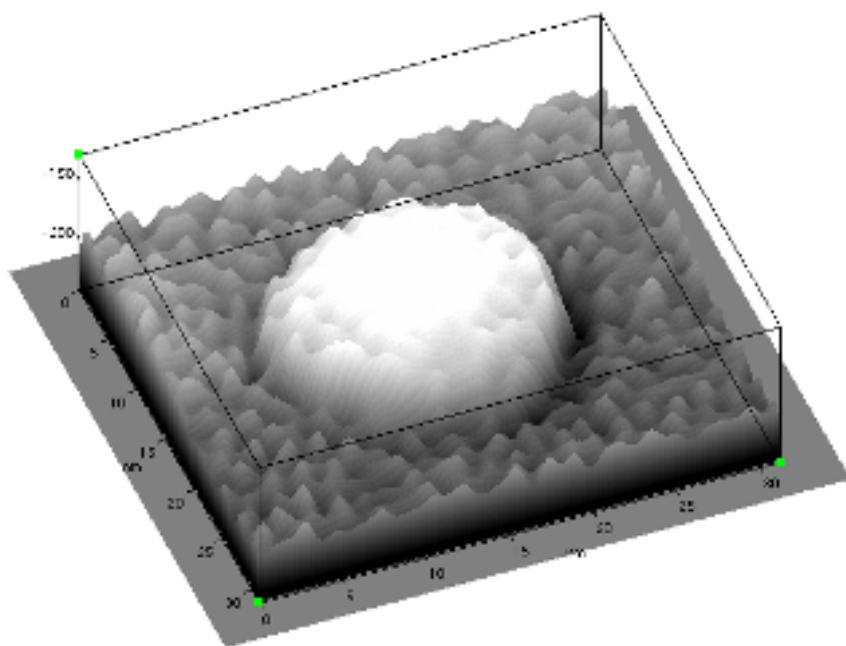

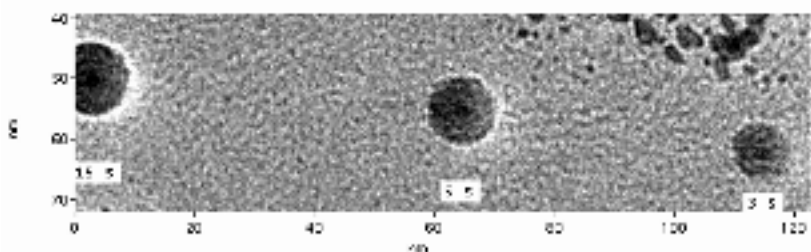Figure 7-2: Surface plot of the individual dot shown in Fig. 7-1.

Figure 7-3: TEM micrograph (top view) of a dot series deposited by a 1 nm beam at 200 keV, on a cross grating specimen. Exposure time varies as 15 : 5 : 3 seconds. The diameters of the dots are estimated to be 13.3 nm, 10.6 nm and 8 nm respectively.
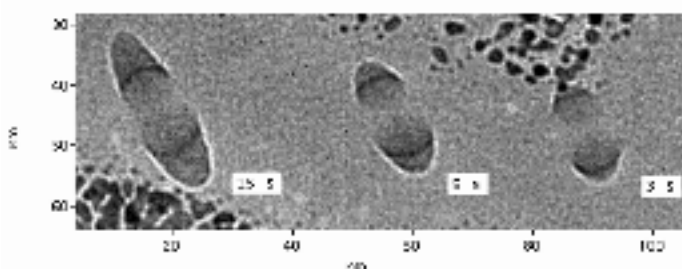
Figure 7-4: TEM image of three dots tilted with 28 degrees.

MC profile simulator, exposed in Chapter 4. The growth times can differ because we neglected in our simulation the time necessary for a hydrocarbon molecule to travel from a source to the wall of the grown tip. In our simulation we expected the walls of the tip to be instantaneously covered by a hydrocarbon monolayer.

From this dot series we observe an obvious increase in the diameter of the three dots from 8 nm to 10.6 nm to 13.3 nm and that the height of the dots is less than 20 nm. We conclude that the diameters of the three dots can be situated somewhere on the segment between A and B on the time evolution curve. Even smaller dots, with diameters closer to the point A and thus to the ultimate resolution could unfortunately not be produced because they contained a very low mass impossible to be visualized in TEM mode, at least not on a carbon foil.

The next step was to deposit lines on the thin carbon foil, by repeated digital scanning of the 5 pA electron beam focused in a 1 nm diameter spot. First line was deposited with high enough exposure time, by scanning the beam 20 times, with a dwell time of 4 ms per pixel, where a pixel diameter equal to the beam diameter. The result was a continuous line, shown in Fig.7-5. A very powerful image processing technique is the spatial filtering in one direction, by performing a profile across the line, averaged over a rectangular area. Such a line profile of the deposited line is shown in Fig. 7-6. We estimate that the linewidth at the base is 8.44 nm and the FWHM of the line is 6.66 nm. This result is better than any linewidth deposited by EBID in a SEM or TEM until now. A surface plot of this line is shown in Fig. 7-7.
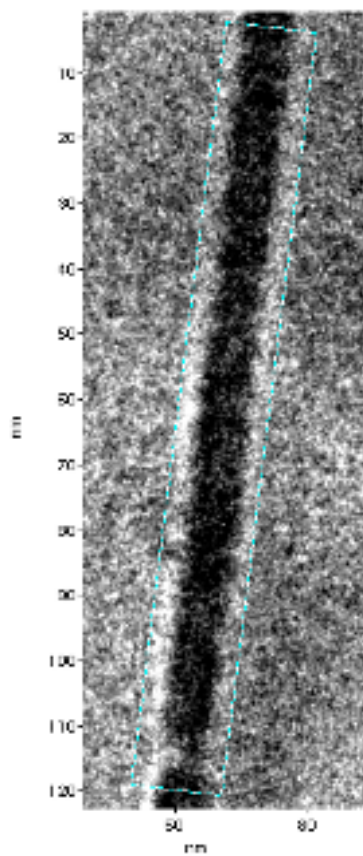
Figure 7-5: TEM micrograph of a contamination line deposited on a 12 nm holey carbon foil. (Probe diameter - 1 nm, 200keV exposure time 20 scans x 4 ms / pixel = 80 ms / pixel, dosis is 50 C / cm^2).
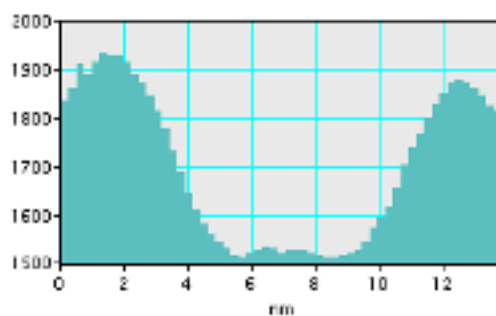
Figure 7-6: An averaged line profile of the contamination line deposited with 20 beam scans. The linewidth at base is 8.44 nm , the FWHM is 6.66 nm.
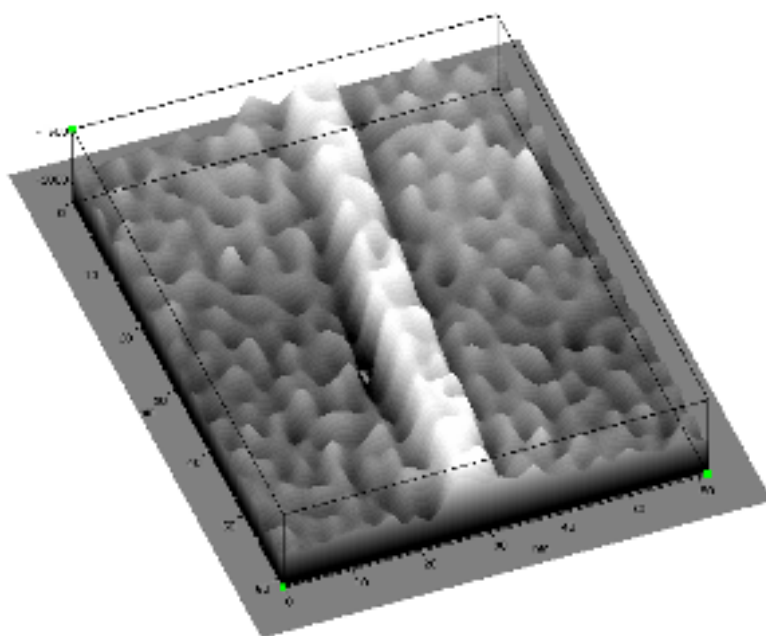

Figure 7-7: A surface plot of the contamination line deposited by 20 scans.

Because we saw that the structures deposited by a lower exposure have narrower features, lines with less scans have been performed. For 5 scans already individual dots caused by the digitalization of the DAC convertor, used to generate the deflection signals, can be distinguished (see Fig. 7-8). The integrated line profile shown in Fig. 7-9 reveals that the interrupted lines have a FWHM of 4 nm. Also two lines written accidentally, with even lower exposure, can be distinguished between the thicker 6 lines only from the integrated cross-profile, as narrow as 1.33 nm FWHM. With some effort these lines can be seen also from the TEM micrograph (see the arrows).
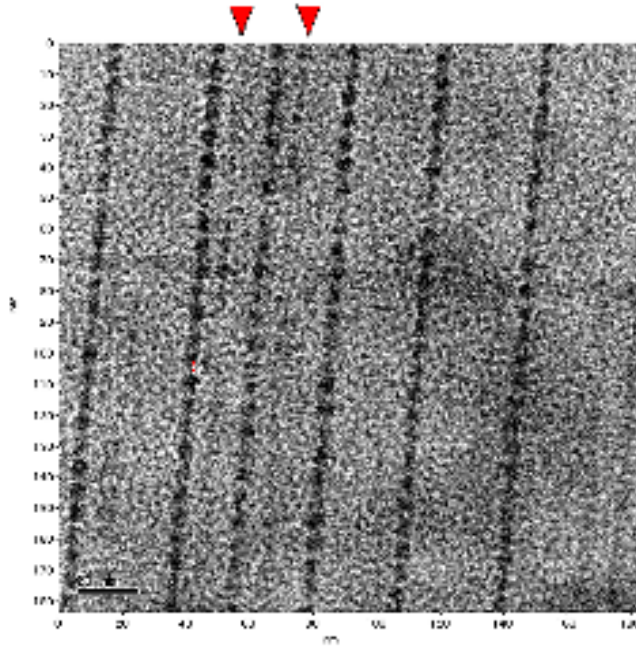
Figure 7-8: TEM micrograph of contamination lines deposited by 5 scans of the 1 nm diameter probe, 5 pA current, 200 keV. Exposure time = 20 ms. Dosis = 12 C / cm^2.

A surface intensity plots of the 5 scans line is shown in Fig. 7-10.

The conclusion after this experiment is that very narrow lines with FWHM of 1.3 nm can be deposited, but they contain not enough material to be decently visualized in TEM mode. Even if the lines are discontinuous, thus not suitable for contact fabrication, this result should not be discarded. The discontinuous lines are actually series of very small dots with a very small spacing and could find a possible application in another field, for example in quantum device fabrication.

The experiment has been further improved, by applying an analog signal to the deflector coils, in order to assure that the deposited lines are always continuous. Even a smaller beam diameter has been used, with a diameter of 0.2 nm. The probe current was 20 pA. A filtered image of a line pattern obtained in this way is shown in Fig. 7-11. The lines have a FWHM of
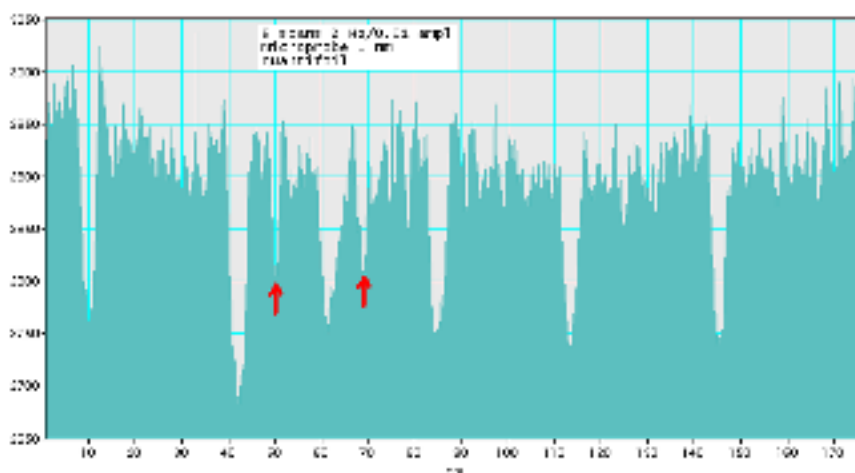
Figure 7-9: The averaged line profile of the lines deposited by scanning 5 times the 1 nm diameter electron beam over a 12 nm thin carbon film. The 6 thicker lines have a FWHM of 4 nm. We also indicate with markers two thinner lines, with FWHM of only 1.33 nm.

3.63 nm. A surface plot of these lines can be seen in Fig. 7-12.

This experiment shows that continuous lines can be deposited with FWHM between 3 and 10 nm. These lines are very narrow and their low mass makes them difficult to image in TEM bright field mode. We estimate that the line height is lower than 10 nm, approaching the thickness of the carbon substrate. The lines are carbon rich, so it is very difficult to get a good contrast in TEM imaging and distinguish them from the carbon substrate. In this case, another in situ imaging technique, available on a Tecnai 20 model we used, the HAADF (high angular annular dark field) imaging, should bring an improvement. An example resulting from his technique is shown in Fig. 7-13.
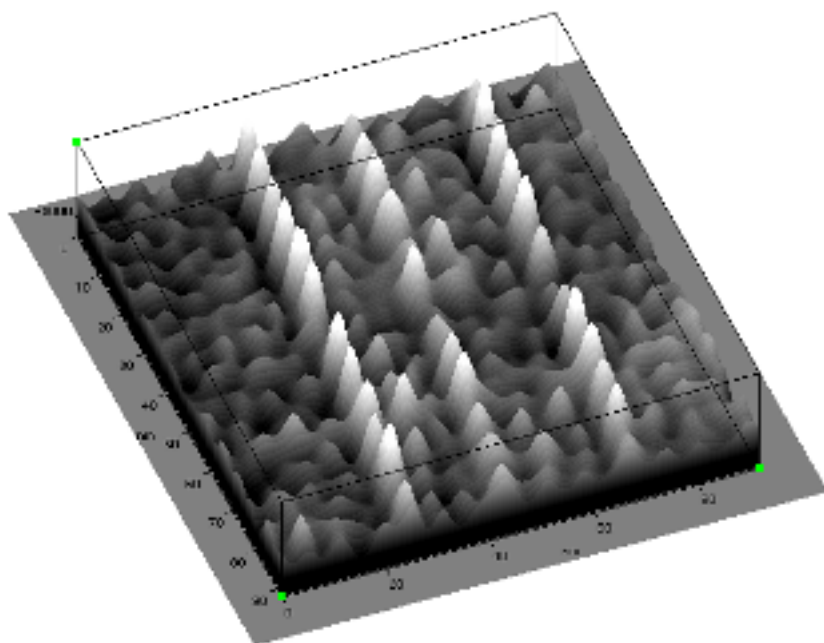
Figure 7-10: Surface plot of the contamination line deposited by 5 scans (Probe current 5 pA, exposure time 5 x 4 ms / pixel = 20 ms / dot ; Dosis = 10 C / cm^2)
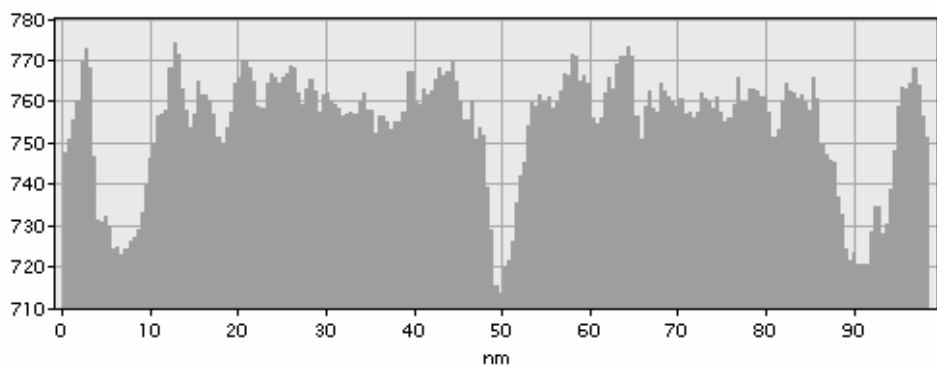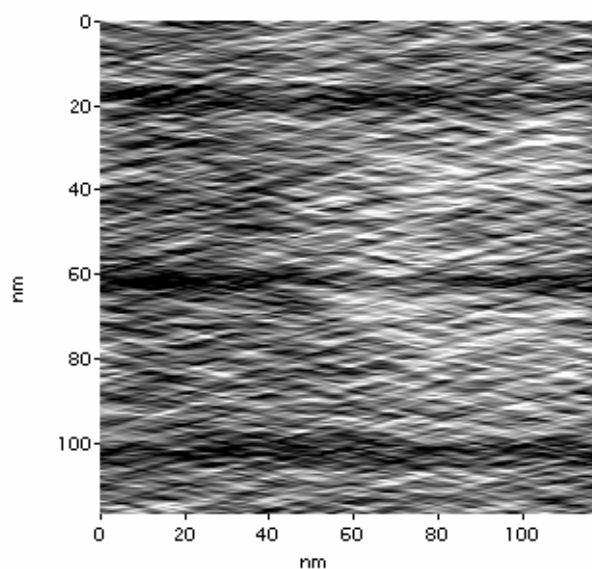
Figure 7-11: A TEM micrograph and the line profile of 3 continuous contamination lines deposited on carbon film by a 0.2 nm diameter electron beam (FWHM = 3.63 nm)
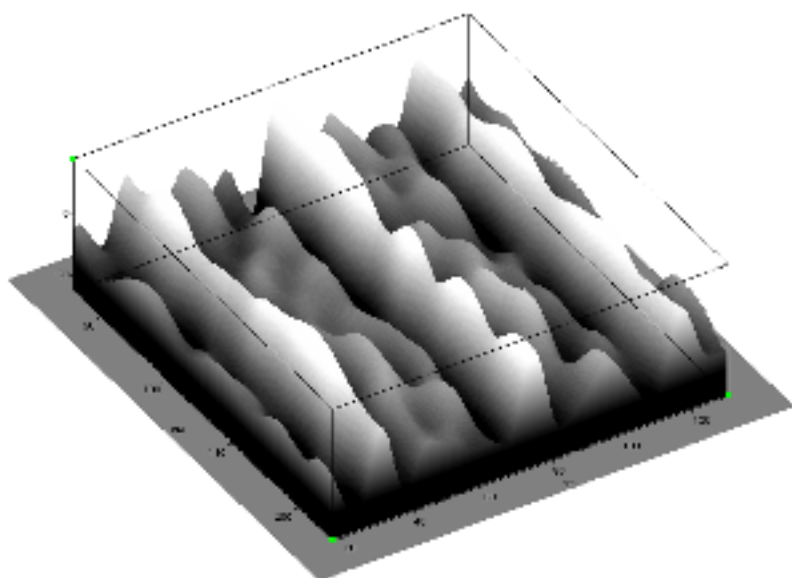
Figure 7-12: A surface plot of three continuous contamination lines deposited by a 0.2 nm diameter electron beam.
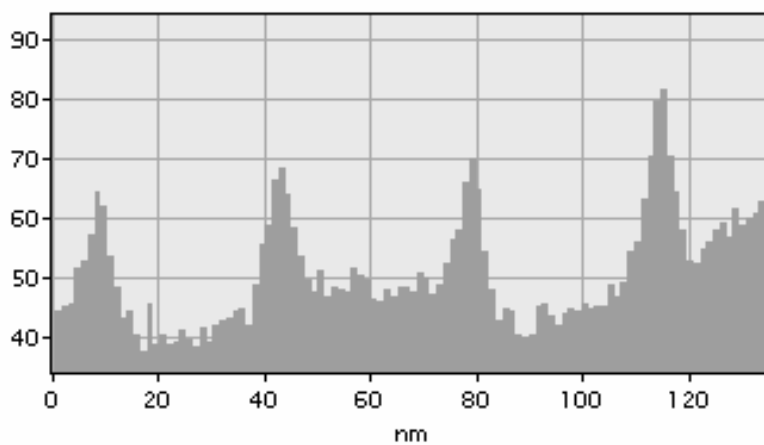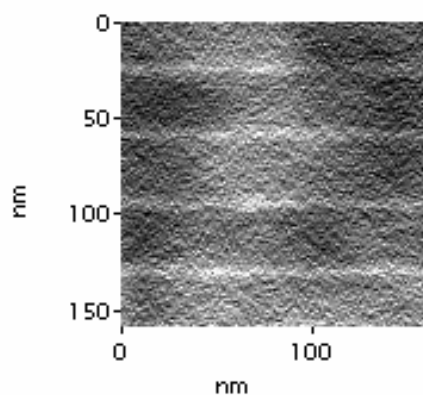
Figure 7-13: HAADF image and the averaged line plot of 4 contamination lines written by a 0.2 nm diameter electron beam at 200 keV on a 12 nm carbon foil. The FWHM of the lines is between 2.2 nm and 2.8 nm.

7.3 Conclusions and future developments

Our experiments demonstrated that EBID performed in a modern STEM can fabricate sub 10 nm structures. Dots and continuous lines with lateral sizes (FWHM) between 2 and 10 nm could be deposited on thin films. These sizes are about 10 times smaller than other reported EBID results in SEM and TEM and comparable with the best results offered by EBID-STM.

We also observed that the shapes of the dots experimentally obtained on a thin film agree with the shapes predicted by our Monte Carlo simulator. It means that our assumption that the SE are the main player in the deposition and that they mainly determine the shape and size of the deposited dots is correct.

We know now how to deposit narrow structures. The lateral size can reach the spatial extent of the SE on the target surface around 2 nm if the beam exposure time is kept very short. The problem is that such narrow structures contain very little mass and are almost impossible to be directly visualized in TEM mode, especially when the target is made of carbon. EBID performed with a metal bearing precursor would create much better contrast. For example the gas cell designed in this thesis filled for example with $W(CO)_6$ powder could be used in the same high resolution STEM. Also other off line imaging techniques should be investigated, like AFM and STM.

What can be done for a future development of EBID in a STEM? First of all, we have to make a distinction between EBID as a laboratory nanofabrication method and EBID as a candidate for nanofabrication at industrial scale.

The first priority is to improve STEM-EBID for the use in the research laboratory. Immediate steps should investigate if even smaller structures can be deposited. If the secondary electrons scattered in the already grown structure are the main influence factor in EBID resolution, then smaller lateral sizes could be obtained if these electrons are prevented to reach the lateral flanks of the tip. Another precursor could be used containing atoms of a metal with a shorter electron inelastic mean free path. Or the precursor should be a gas less sensitive to secondary electrons, with a dissociation cross-section peaked at higher energy values, above the energy of secondary electrons, such that structures can be written with the finely focussed primary electron beam.

New application areas have to be investigated. Such narrow lines and dots can be used to fabricate quantum devices, can serve as masks for metal deposition or etching, as nanocontacts to measure the properties of molecules, proteins or nanocrystals. Another problem to be solved is the interface of the deposited nanostructure with the macro world, necessary to make any application possible or to test the deposit properties. For this purpose, contact pads with micron scale command electrodes have to be fabricated on thin film by other conventional lithography methods, prior to deposition experiments.

A second step should focus on optimizing the EBID process for larger scale applications.

Bibliography

[1] MARCHI, F. Nanometer scale patterning by scanning tunnelling microscope assisted chemical vapour deposition. *Microelectronic engineering 50* (200), 2000.

[2] MURAY, A., ISAACSON, M., AND ADESIDA, I. AlF_3 - a new very high resolution electron beam resist. *Applied Physics Letters 45* (1984), 589.

[3] PAI, W., ZHANG, J., WENDELKEN, J., AND WARMACK, R. Magnetic nanostructures fabricated by scanning tunneling microscope-assisted chemical vapor deposition. *Journal of Vacuum Science and Technology B 15* (1997), 785.

[4] RUSS, J. *The image processing handbook*. CRC Press, Boca Raton, 1995.

[5] STREBLECHENKO, D., AND SCHEINFEIN, M. Magnetic nanostructures produced by electron beam patterning of direct write transition metal fluoride resists. *Journal of Vacuum Science and Technology A 16* (1998), 1374.

[6] UESUGI, K., AND YAO, T. Nanometer scale fabrication on graphite surfaces by scanning tunneling microscopy. *Ultramicroscopy 42-44* (1992), 1443.

Chapter 8

Summary and conclusions

"Or eccomi giunto al nord cap. Che e dire all'extremita di fiunmarka anzi. Pero co'terminata la mia curiosita."
Francesco Negri, 1664

Electron Beam Induced Nanometer Scale Deposition

Miniaturization, micromachining and integration started as a trend in electronics manufacture in the mid-seventies and is still continuing at this moment, extending rapidly to other fields like molecular biology, analytical chemistry and mechanical engineering. Twenty five years ago the resolution requirement for integrated circuits was 10 μm while today it is approaching 100 nm. Structures with sizes between 100-500 nm are fabricated on industrial scale, at throughputs of many wafers per hour, offering fascinating applications. The challenge of large scale manufacturing for the immediate future is to find the right methods to fabricate sub-100 nm features. The promising candidates for the so-called nanolithography are: the extreme ultraviolet lithography, ion and electron projection systems and X-ray proximity printing.

In the research laboratories, another community is exploring the future of nanotechnology. Here the so-called laboratory nanofabrication methods are theoretically investigated or experimented. The main purpose of laboratory activities is to demonstrate that, as R. Feynman would say, "little has been done, but an enormous amount can be done in principle" [1]. At this moment in research laboratories, features between 10 and 100 nm can be fabricated on a day to day basis using electron beam lithography (resist based or electron beam induced deposition (EBID)) at throughputs of ca. 25 - 250 Mpixels per second. The need to control and manipulate things on molecular scale drives the search for methods to fabricate sub-10 nm structures. In scanning probe lithography (STM or AFM) 1 nm features can be fabricated using EBID with a speed of a few Mpixels per second and 0.3 nm size structures can be arranged by atom manipulation, with a speed of ca. 1 atom per minute. However the scanning probe procedures are extremely slow, unacceptable for an industrial process, and even for many research purposes.

Promising alternatives to scanning probe atomic manipulation are the focused energetic beams (photon, ion and electron). Among these techniques, electron beam lithography offers the best resolution. The problem is that the electron beam lithography using a conventional resist (PMMA) has reached its fundamental resolution limits, imposed mainly by the electron scattering in the resist and the resist grain size. This limit is set at 10 nm and this barrier turned out to be very difficult to break with any other nanofabrication method.

265

In this context, we investigate the potential of EBID to fabricate sub-10 nm features. EBID is a resistless, direct writing technique which might suffer less from the proximity effects that gave headaches to PMMA lithography. The driving force is the fact that nowadays electron optical systems with 0.2 nm beam diameter are available. EBID performed in such a Scanning Transmission Electron Microscope (STEM) might be a potential sub-10 nm fabrication technique. This is a less conventional manner to approach nanofabrication with electron beams, because STEM is only known as a commercial tool for high resolution material analysis. STEM offers an environment very favorable for high resolution EBID: a thin substrate, a very fine and stable focused beam (0.2 nm is the state-of-the-art), good control of the beam focus and positioning. This thesis contains the theoretical and practical demonstration of the viability of this idea.

An extensive literature review on electron and ion beam induced deposition has been performed. The results show that in principle EBID can deposit continuous and sufficiently conductive metal lines, both on bulk and thin specimens. The intriguing fact was that even with a 2 nm diameter beam, the smallest structures deposited elsewhere were 13 to 20 nm. A theoretical model that could explain this lateral broadening did not exist at that moment. It is our main goal to estimate the size of structures fabricated with EBID for given beam, target and precursor parameters.

The theoretical estimate of EBID fabrication resolution is a long and complicated procedure. Things would have been easier if only the primary beam would be the main player in EBID. Then structures as wide as the probe size could be fabricated and the use of modern electron microscopes with 0.2-0.5 nm diameter probes would easily fabricate sub 10 nm structures. Unfortunately, a simple experiment shows that even such a fine beam grows on a thin target tips with diameters of 20-30 nm. This is a trivial demonstration that also other factors are playing a role in deposition, some of them influencing its resolution. The problem has been solved using a straightforward strategy: factors that might play a role in lateral evolution of deposited structures are identified and their contribution quantified as accurately as possible.

The secondary electrons (SE) emitted as a result of primary bombardment are the most suspected factor, due to their low energy range overlapping with the dissociation cross section peak for most of gaseous precursors. We developed a procedure to predict the shape of a singular dot grown by EBID in an electron microscope as determined by the secondary electrons.

For this purpose a Monte Carlo simulation program for the electron scattering in a flat solid target has been written. The user friendly interface can be also useful for student presentations, because the process parameters can be changed easily and the electron trajectories are graphically displayed. The results of MC simulations show where the SE emerge and what energies they have. The difference with other MC simulations is that we coupled these results with the electrons power to dissociate molecules. Their contribution to deposition depends on their energy and on the sensitivity of the gas molecule, characterized by the molecular dissociation cross section of the gas molecule, $\sigma_{diss}(E)$. After reading a lot about electron - gas interactions we discovered that this property is very unknown. Even the most simple molecule, hydrogen H_2 creates enough problems to the chemists, and in 2001 still new empirical formulas are issued for its electron impact induced dissociation. The problem is that a large number of possible dissociation paths exists, and this number grows with the complexity of the molecule. EBID unfortunately uses precursor gas molecules with a complicated structure, making this task not trivial.

The results of our simulations show that the SE emerging on the flat surface of the thin target create a dot clustered in an area of 2 nm around the primary beam axis. This is the ultimate limit in EBID, determined by SE.

The question is why in reality a stationary 0.2 nm electron beam still deposits 20 nm diameter dots? Our discovery is that later in time, the SE emitted from the flanks are laterally broadening the tips until a saturation value is reached. The dots shape tracing is necessary also after a structure begins to grow and this is performed by extending the MC for flat surfaces with a profile simulator based on cellular automata. The saturation value is the routinely obtained resolution and agrees with the values reported by many authors. The problem is that structures as narrow as 1 nm can be fabricated, but they will be very thin. Very soon the diameter will expand, so the exposure has to be very low.

The results of this exercise was that we understood the role of SE in deposition and know how to make smaller structures.

Other influences have been also estimated. The delocalization of inelastic scattering happens because an electron can lose energy also at a distance away from its inelastic scattering center. The necessity to study this effect has been suggested by a few authors, but no quantification has been made yet. Only a range is usually given as between 0.1 and 10 nm. It is a difficult problem. We calculated the spatial extent of delocalization of SE. Our results show that the delocalization of SE generation can broaden the SE profile with about 0.1 nm. Other influences, like migration of fragments and electric field effects, have been also investigated.

The first experimental system where we studied EBID is the dual beam instrument, based on a Philips EM 420 STEM and a home made ion column. This system is designed as a workstation in an ambitious project started at Delft University of Technology in cooperation with the FOM foundation, the NEXT laboratory.

The electron beam column has been made operational and additional elements necessary to host EBID have been added. The computer controlled pattern generator and two possible variants for a gas delivery system are described. A nozzle injector gas delivery system has been designed for the Philips EM 420 STEM. It can be used for both electron and ion induced chemistry. EBID has been tested in this system with the conclusion that electrostatic deflectors also work for the positioning of the electron beam and the $W(CO)_6$ precursor operated at room temperature creates enough gas flow to obtain deposition. The limitations of the system were the spot size and the probe current.

In order to perform EBID experiments in another higher resolution STEM, a portable environmental gas cell, that can be used without modifications to the microscope has been designed.

Encouraged by the theoretical estimations that pointed out that sub 10 nm lithography is possible using EBID, we dedicated the last chapter to high resolution experiments. Successful high resolution experiments with contamination in a state-of-the-art STEM have been obtained. Continuous contamination lines with FWHM ranging from 3 to 8 nm have been deposited. Also very thin and narrow lines with FWHM of 1.3 nm could be obtained. Difficulties have been encountered in their visualization because the thickness is less than 10 nm. Other imaging methods as AFM should be tried.

This thesis is organized as follows:

- an extensive literature review on EBID and IBID

- the know-how on Monte Carlo techniques used for simulation of secondary electron emission from a target bombarded by electrons and a computer program to demonstrate their use for EBID profile simulation.

- a literature search on gas-electron interactions and properties of precursors used in contamination lithography and EBID.

- a theoretical model that demonstrates the role of SE in EBID spatial resolution.

- an evaluation of the influence of the delocalization of electron inelastic scattering on EBID

resolution.

- the design of additional elements necessary for the EBID and IBID experimental study in a STEM: a computer controlled pattern generator, imaging facilities and two gas delivery systems (nozzle injector and a gas environmental cell)

- experiments on high resolution line deposition that show that sub 2 nm is possible.

In conclusion we could give a reasonable answer to the questions formulated in the introduction in Chapter 1. We demonstrated theoretically and experimentally that EBID can be used in a STEM and if this STEM is a very high resolution one, it can host sub 10 nm deposition.

We now know that structures smaller than reported before can be obtained with EBID.

We know that the previously observed lateral broadening of the structures is not due to the secondary electrons emitted from the flat substrates. The broadening is caused by the secondary electrons generated in the freshly deposited structure. This effect has been beautifully demonstrated by Monte Carlo simulations.

The shapes of experimentally obtained dots are in agreement with the results of Monte Carlo profile simulations.

In the future efforts have to be made to prevent EBID to remain just a laboratory nanofabrication technique. To be promoted among other nanotechnology methods, an EBID system has to be built that fulfills the strict industrial lithography standards, as patterning at high speed, patterning with low distortion, high linewidth control, reproducibility and high overlay accuracy.

Bibliography

[1] R.P.FEYNMANN. There's plenty of room at the bottom. *APS meeting, California Institute of Technology* (1959).

Chapter 9

Samenvatting en conclusies

Elektronenbundel geïnduceerde depositie op nanometer schaal

Het almaar verkleinen, microfabricage en integratie begon als een trend in elektronikaproduktie medio jaren zeventig en dit schrijdt op dit moment nog altijd voort, waarbij het zich verbreedt naar andere disciplines, zoals molekulaire biologie, analytische scheikunde en mechanica. Vijfentwintig jaar geleden was de benodigde resolutie in integrated circuits (IC's) 10 μm, terwijl dit vandaag de 100 nm nadert. Structuren met afmetingen tussen 100 en 500 nm worden op industriële schaal toegepast met een produktiesnelheid van enkele wafers per uur. Deze bieden fascinerende toepassingen. De uitdaging voor produktie op grote schaal ligt in het zoeken naar de juiste methode om structuren kleiner dan 100 nm te fabriceren. De meest veelbelovende kandidaten voor de zogenoemde nanolithografie zijn: de extreem ultraviolet lithografie, de ionen en elektronen projectie systemen en de Röntgen lithografie.

In verschillende laboratoria is men bezig met onderzoek naar de toekomst van nanotechnologie. Hier wordt laboratorium nanofabricage theoretisch en experimenteel onderzocht. Het belangrijkste doel van deze laboratoriumaktiviteiten is te laten zien, dat zoals R. Feynman [?] zou zeggen: "Er is nog maar weinig gedaan, maar in principe kan er enorm veel gedaan worden". Op dit moment kunnen op laboratoriumschaal op een betrouwbare manier structuren gemaakt worden tussen 10 en 100 nm met behulp van elektronenbundellithografie (gebruikmakend van resists of electronen bundel geïnduceerede depositie (EBID)) met een snelheid van 25-250 Mpixels per seconde. De noodzaak om dingen op molekulaire schaal onder controle te krijgen drijft de zoektocht verder naar methoden om structuren kleiner dan 10 nm te fabriceren. In scanning probe lithografie (STM of AFM) kunnen structuren van 1 nm worden gemaakt met behulp van EBID met een snelheid van enkele Mpixels per seconde en structuren van 0.3 nm met atoommanipulatie met een snelheid van 1 atoom per minuut. De scanning-probe methode is echter nog dermate langzaam dat dit onacceptabel is voor een geïndustrialiseerd proces en zelfs niet geschikt voor veel onderzoeken.

Een veelbelovend alternatief is een methode met gefocusseerde energiebundels (photon, ion en elektron). Van deze technieken biedt de elektronenbundellithografie de hoogste resolutie. Het probleem is dat de elektronenbundellithografie conventionele resists (PMMA) gebruikt en daarmee zijn de praktische grenzen van de resolutie bereikt. Dit wordt met name veroorzaakt door de verstrooiing van elektronen in de resist en de afmetingen hiervan. De grens ligt op 10 nm en deze barrière blijkt met elke methode moeilijk te doorbreken.

In deze context onderzoeken we de mogelijkheden van EBID om structuren te maken kleiner dan 10 nm. EBID is een directe schrijftechniek, zonder een resist laag, en heeft daarom mogelijk

minder last van de effecten die zoveel hoofdpijn hebben veroorzaakt bij de PMMA-lithografie. De drijvende kracht is dat tegenwoordig elektronoptische systemen beschikbaar zijn met bundels van 0.2 nm in diameter. EBID toegepast in een STEM is in potentie een techniek voor fabricage van structuren kleiner dan 10 nm. Dit is een onconventionele benadering van nanofabricage met elektronenbundels, omdat STEM alleen bekend is als commercieel instrument voor materiaalanalyse met hoge resolutie. STEM biedt een goede omgeving voor EBID met hoge resolutie: een dunne preparaat, een kleine en stabiele bundel (0.2 nm is het neusje van de zalm) en een goede controle over de positie en focusering van de bundel. Dit proefschrift bevat een theoretische en praktische demonstratie van de levensvatbaarheid van dit idee.

In eerste instantie is een uitgebreid literatuuronderzoek uitgevoerd over met elektronen en ionen uitgevoerde depositie. De resultaten laten zien dat in principe met EBID continue en voldoende geleidende metalen lijntjes gedeponeerd kunnen worden, zowel op dikke als dunne preparaten. Het intrigerende hieraan is echter dat zelfs met een bundel van 2 nm de kleinste structuren afmetingen krijgen van 13 tot 20 nm. Een theoretisch model dat deze verbreding kan verklaren bestond tot op heden nog niet. Het is ons doel om de afmetingen van de met EBID gemaakte structuren te voorspellen.

De theoretische voorspelling van de resolutie met EBID fabricage is een lange en ingewikkelde procedure. Het zou makkelijker zijn geweest als alleen de primaire bundel de belangrijkste rol zou spelen. In dat geval zouden structuren ter grootte van de bundel kunnen worden gefabriceerd. Gebruikmakend van moderne elektronenmicroscopen met bundels van 0.2-0.5 nm zouden eenvoudig structuren kleiner dan 10 nm gefabriceerd kunnen worden. Helaas laat een simpel experiment al zien dat zelfs met zo'n kleine bundel op een dun preparaat lijnen met een dikte van 20-30 nm ontstaan. Het is een triviale demonstratie die aantoont dat andere factoren een rol spelen in de depositie, waarvan sommige de resolutie beïnvloeden. Het probleem is opgelost op een rect-toe-recht-aan manier: factoren die een rol spelen in de laterale groei van gedeponeerde structuren worden geïdentificeerd en zo goed mogelijk gekwantificeerd.

De secundaire elektronen (SE) die gegenereerd worden door het primaire bombardement zijn vermoedelijk de belangrijkste factor, vanwege hun lage energiebereik dat overlapt met de piek in de dissociatiedoorsnede van de meeste gasmolekulen. We hebben een procedure ontwikkeld die de vorm van een enkele tip, ontstaan door EBID in een elektronmicroscoop, kan voorspelen op basis van de secundaire elektronen.

Voor dit doel is een Monte Carlo simulatieprogramma geschreven voor elektronen verstrooing in een vlak preparaat. De gebruikersvriendelijke interface kan ook gebruikt worden bij presentaties voor studenten, omdat de parameters eenvoudig veranderd kunnen worden en de banen van de elektronen grafisch worden weergegeven. De resultaten van de Monte Carlo simulaties laten zien waar de SE ontstaan en welke energie zij hebben. Het verschil met eerdere Monte Carlo simulaties is dat we de resultaten gekoppeld hebben aan het vermogen van de elektronen om molekulen te dissociëren. Hun bijdrage aan de depositie hangt af van hun energie en de gevoeligheid van het gasmolekuul, gekarakteriseerd door de dissociatiedoorsnede van het gasmolekuul $\sigma_{diss}(E)$.

Na veel gelezen te hebben over elektron-gasinteracties kwamen we erachter dat over deze eigenschappen erg weinig bekend is. Zelfs het meest eenvoudige molekuul, waterstof H_2, creëert genoeg problemen voor de chemici en in 2001 werden nog steeds nieuwe empirische formules ontwikkeld voor de dissociatie als gevolg van impact door elektronen. Het probleem is dat een groot aantal manieren van dissociatie bestaat en dit aantal groeit met de complexiteit van het molekuul. EBID maakt helaas gebruik van gasmolekulen met zeer gecompliceerde structuren, wat onze taak niet eenvoudig maakt.

De resultaten van onze simulaties laten zien dat de SE die ontstaan op het vlakke oppervlak

van het dunne preparaat een vlek creëren ter grootte van 2 nm rond de as van de primaire bundel. Dit is de uiteindelijke limiet in EBID bepaald door de SE.

De vraag is waarom in werkelijkheid een stationaire 0.2 nm brede elektronenbundel 20 nm brede tips deponeert. Onze ontdekking is dat de na enige tijd in de gedeponeerde struktuur gegenereerde SE vanuit de flanken de struktuur in zijdelingse richting doen groeien, totdat een punt van verzadiging optreedt. Het nagaan hoe de vorm van de struktuur zich ontwikkelt is noodzakelijk ook nadat de structuur is begonnen te groeien en dit is gedaan door de Monte Carlo simulaties voor vlakke oppervlakken uit te breiden met een profielsimulator, die is gebaseerd op cellulaire automaten. De verzadigingswaarde is gelijk aan de routinematig verkregen resolutie en komt overeen met waarden die door meerder auteurs zijn gerapporteerd. Een probleem is dat structuren met een breedte van 1 nm kunnen worden gemaakt, maar deze blijven tevens erg dun. Snel zal de diameter toenemen, dus de blootstelling aan de elektronenbundel moet kort zijn.

De resultaten van deze exercities zijn dat we nu de rol van de SE in de depositie kennen en dat we weten hoe kleinere structuren te maken.

Ook andere invloeden hebben wij beschouwd. De delokalisatie van inelastische verstrooiing treedt op, omdat een elektron ook energie kan verliezen op enige afstand van zijn baan. De noodzaak om dit effect te bestuderen is gesuggereerd door een aantal auteurs, maar tot nu toe is geen berekening gemaakt. Meestal wordt een marge gegeven tussen 0.1 en 10 nm. Het is een moeilijk probleem. Wij hebben het effect van de delokalisatie van SE berekend. Onze resultaten laten zien dat de delokalisatie van SE generatie het profiel met ca. 0.1 nm kan verbreden. Andere invloeden, zoals migratie en elektrische veld effecten zijn eveneens onderzocht.

Het eerste experimentele systeem, waarmee we EBID hebben bestudeerd is het 'dual beam instrument', gebaseerd op een Philips EM 420 STEM en een zelf gemaakte ionenkolom. Dit systeem is ontworpen als deel van een ambitieus project begonnen door TU Delft in samenwerking met de Stichting FOM: het NEXT-laboratorium. De elektronenkolom is werkend gemaakt en extra onderdelen om EBID toe te passen zijn toegevoegd. De computergestuurde patroongenerator en twee mogelijke gasinvoersystemen zijn beschreven. Een gasinvoersysteem met behulp van een mondstuk is ontworpen voor de Philips EM 420 STEM. Dit kan gebruikt worden voor zowel de door elektronen als ionen veroorzaakte reacties. EBID is getest in dat systeen met de conclusie dat de elektrostatische deflectoren ook werken voor de positionering van de elektronenbundel. De $W(CO)_6$ precursor gasinvoer op kamertemperatuur creëert voldoende gasstroom om depositie te verkrijgen. De beperkingen van het dual beam instrument zijn echter de grootte van de bundel en de stroom in de bundel.

Om EBID experimenten uit te voeren in een hoge resolutie STEM is een losse gascel ontworpen, die kan worden gebruikt zonder aanpassingen aan de microscoop.

Aangemoedigd door de theoretische voorspellingen die zeiden dat lithografie kleiner dan 10 nm mogelijk is met EBID, hebben we het laatste hoofdstuk gewijd aan de hoge resolutie experimenten. Zeer hoge resolutie met contaminatiegroei in de nieuwste STEM is behaald. Continue lijnen met FWHM tussen 3 nm en 8 nm zijn gedeponeerd. Ook erg dunne en smalle lijnen met FWHM van 1.8 nm kunnen worden bereikt. Probleem is de visualisatie, omdat de lijn dunner is dan 10 nm. Andere methoden voor visualisatie, zoals AFM zouden moeten worden uitgeprobeerd.

Dit proefschrift is als volgt ingedeeld:

-een uitgebreid literatuuroverzicht over EBID en IBID;

-een handleiding voor Monte Carlo technieken, die zijn gebruikt voor simulaties van secundaire elektronenemissie van een preparaat dat wordt gebombardeerd door elektronen en een computerprogramma om het gebruik van Monte Carlo technieken in EBID profielsimulaties te

demonstreren;

-een literatuuronderzoek naar gas-elektroninterakties en eigenschappen van gassen gebruikt in contaminatielithografie en EBID;

-een theoretisch model dat de rol van SE in de plaatsresolutie van EBID demonstreert;

-een evaluatie van de invloed van de delokalisatie van inelastische verstrooiing door elektronen op de EBID resolutie;

-het ontwerp van toegevoegde onderdelen aan een STEM, noodzakelijk voor de EBID en IBID experimentele studie: een computergestuurde patroongenerator, beeldvormende instrumentatie en 2 gasinvoersystemen (monstukinjectie en gascel);

-experimenten met hoge resolutie lijndepositie die laten zien dat 2 nm mogelijk is.

Tot besluit kunnen we een redelijk antwoord geven op de in de inleiding geformuleerde vragen. We hebben theoretisch en experimenteel laten zien dat EBID kan worden gebruikt in een STEM en als deze STEM een hoge resolutie heeft kunnen continue lijnen kleiner dan 10 nm worden verkregen.

We weten nu dat structuren kleiner dan tot op heden gerapporteerd kunnen worden gerealiseerd met EBID.

We weten dat de voorheen reeds geobserveerde verbreding van de structuren niet komt door secundaire elektronen die worden geëmitteerd vanaf het oppervlak van het preparaat. De verbreding wordt veroorzaakt door de secundaire elektronen die worden gegenereerd in de net gedeponeerde structuur. Dit effect wordt mooi gedemonstreerd door de Monte Carlo simulaties.

De vormen van experimenteel verkregen strukturen stemmen overeen met de resultaten van de Monte Carlo profielsimulaties.

In de toekomst zal inspanning moeten worden geleverd om te voorkomen dat EBID slechts een methode voor nanofabricage op laboratoriumschaal blijft. Om naast andere methoden EBID te kunnen promoten moet een EBID systeem worden gebouwd dat tegemoet komt aan de strenge randvoorwaarden uit de lithografieindustrie, zoals patronen schrijven op hoge snelheid, met lage vervorming, goede controle over de lijnbreedte, reproduceerbaarheid en een hoge overlappingsnauwkeurigheid.

List of abbreviations

AES	Auger electrons spectrum
acac	acetyl acetonate
AFM	Atomic force microscope
BSE	Backscattered electrons
CVD	Chemical vapour deposition
EBID	Electron beam induced deposition
EB	Electron beam
EDS	Energy dispersive spectroscopy
EDX	Energy dispersive X-ray analysis
EELS	Electron energy loss spectroscopy
EBL	Electron beam lithography
EBIR	Electron beam induced resist growth
DBI	Dual Beam Instrument
FW50%	Full width 50%
FWHM	Full width at half maximum
FIB	Focused ion beam
FEG	Field emission gun
GAE	Gas assisted etching
GFIS	Gas field ion source
hfac, HFA	hexafluoro acetylacetonate
HREM	High resolution electron microscopy
IMFP	Inelastic mean free path
IBID	Ion beam induced deposition
LCVD	Laser chemical vapour deposition
LMIS	Liquid metal ion source

Me	methyl
MBE	Molecular beam epitaxy
MOCVD	Metalorganic chemical vapour deposition
PMMA	Polymetylmethacrylate
RIE	Reactive ion etching
RS	Raman spectroscopy
QCM	Quartz crystal microbalance
SAM	Self-assembled monolayers
SE	Secondary electrons
SEM	Scanning electron microscope
SET	Single electron transistor
SIMS	Secondary ion mass spectrometry
SPL	Scanning probe lithography
SPM	Scanning probe microscopy
SFM	Scanning Force Microscopy
STM	Scanning tunnelling microscopy
STEM	Scanning transmission electron microscope
TMA	Trimethyl aluminum
TEM	Transmission electron microscope
tfac	trifluoroacetylacetonate
TMP	Turbo molecular pump
$W(CO)_6$	Tungsten hexacarbonyl
XMA	Xray microanalysis
XPS	Xray photoelectron spectroscopy

Acknowledgements

"C'est le temp que tu as perdu pour ta rose qui fait ta rose si importante. Tu as responsable de ta rose." [1]

Antoine de Saint-Exupéry, "Le Petit Prince"

"Promoveren" is like crossing a frozen river. You can walk on the ice if you are a fast and adventurous runner or you can take your time and use your skills to build a bridge. The reward is also well known. The fast ones get their deserved glory, while the slow ones get the hope that others might once use the same bridge. Belonging to the second group, I started in 1997 to build a bridge. First at all, I would like to thank my promotor, Pieter Kruit and my project supervisor, Kees Hagen for the trust they showed in the very beginning, by giving me a chance to work in such a special group and in such a prestigious university. My promotor also for the freedom he gave me, interrupted from time to time with excellent ideas and correction steps that led the project on a good path. And Kees for constantly helping and encouraging me and for reading this thesis as many times it was necessary to make it error free. Peter Leunissen arrived late in our group and left early, but I benefitted from the discussions with him around Monte Carlo simulations. Jim Barth provided me with an overflow of articles that revealed the crazy competition taking place in science. The years passed and a lot of other people have been involved in this project. Patrick de Jager left an experimental setup and a thesis full of ideas and open questions, which served as inspiration source and starting point in my research. Together with Jianhua Bi, at that time postdoc in our group, we continued to develop the dual beam instrument. And this was not possible without the competent help of our technical team, to whom I am thankfull. Jacques Nonhebel who always had time for electronics questions, who could find a word of encouragement in the right moment and who together with Rajes Radhoe saved the microscope each time it was necessary, from a defect diode to real smoke. In our group if there is no vacuum, there is no measurement, and here Jan de Looff and Peter van de Rijken solved our frequent problems and helped to keep the setup running. Thanks to Erik van Straten everything worked fine and smooth with the computers until the last day. Elly v.d. Most kept control of all the secretarial work necessary to finish this thesis in time. The dual beam instrument was built as a workstation in the NEXT laboratory and I am happy I could benefit from its facilities and technical help. Especially Ron Hoogerheide, thank you for helping when nobody was around and for the fast and clever design of the gas delivery system. I worked in this laboratory during its busiest time, when it was built with a lot of enthousiasm by Bart Geerlings, Sven Rogge, Burghard Ilge, George Palasantzas, Christophe Bisch, Norbert

---

[1] "It is the time you lavished on your rose which makes your rose so important. You are responsible for your rose"

Curriculum Vitae

Natalia Silvis-Cividjian

geboren 31 januari 1967 te Craiova, Roemenië

1981-1985 Voortgezet onderwijs aan het bèta Lyceum (wiskunde-natuurkunde) "Fraţii Buzeşti" te Craiova

1985-1990 Universiteit van Craiova, Faculteit Automatisering en Computers, vakgroep software ontwikkeling

1990-1996 Junior docent aan de Universiteit van Craiova, Faculteit Automatisering en Computers, Afdeling Elektronika en Meettechnieken.

1993 Drie maanden Tempus stage in Londen, Middlesex University, Electrical Engineering School

1997-2001 Onderzoeker in opleiding in dienst van stichting FOM, DIMES/s instituut, werkzaam bij de Technische Universiteit Delft, Faculteit Technische Natuurwetenschappen, vakgroep Deeltjes Optica

2001-2002 Toegevoegd onderzoeker in dienst van stichting FOM, werkzaam bij de Technische Universiteit Delft, Faculteit Technische Natuurwetenschappen, vakgroep Deeltjes Optica